

DOCTORAL THESIS NO. 21

# Development of Concentrating Photovoltaic-Thermal Solar Collectors

João Santos Leite Cima Gomes



Gävle University Press

Dissertation for the Degree of Doctor of Philosophy in Energy Systems to be publicly defended on Friday, the 27th of August at 10.15 in Room 13:111, University of Gävle.

External reviewer: Professor Heimo Zinko, Linköping University.

This thesis is based on work conducted within the industrial post-graduate school REESBE (Resource Efficient Energy Systems in the Built Environment). The projects in REESBE are aimed at key issues in the interface between the business responsibilities of different actors in order to find common solutions for improving energy efficiency that are resource efficient in terms of primary energy and, at the same time, low environmental impact.



The research groups that participate are Energy Systems at the University of Gävle, Energy and Environmental technology at Mälardalen University, and the Energy and Environmental Technology at the Dalarna University. REESBE is an effort of close cooperation with the industry in the three regions of Gävleborg, Dalarna, and Mälardalen, and is funded by the Knowledge Foundation (KK-Stiftelsen).

© João Santos Leite Cima Gomes 2021

Cover illustration: C-PVT Prototypes in Maputo, Mozambique (photographer: Henrik Davidsson)

Gävle University Press

ISBN 978-91-88145-67-3

ISBN 978-91-88145-68-0 (pdf)

urn:nbn:se:hig:diva-35411

Distribution:

University of Gävle


Faculty of Engineering and Sustainable Development

Department of Building, Energy and Environmental Engineering

SE-801 76 Gävle, Sweden

+46 26 64 85 00

[www.hig.se](http://www.hig.se)

 Svanenmärkt trycksak, 3041 0736 Kph Trycksaksbolaget 2021

*To my children, with the hope of making  
a better world for them*



## Abstract

Fossil fuels have greatly improved human living standards and saved countless lives. However, today, their continued use threatens human survival, as CO<sub>2</sub> levels rise at an unprecedented pace to levels never seen during human existence on earth.

This thesis aims at gathering knowledge on solar energy in general and photovoltaic thermal (PVT) and concentrating photovoltaic thermal (C-PVT) in particular. This thesis establishes several key research questions for PVTs and C-PVT collectors and attempts to answer them.

A comprehensive market study of solar thermal (ST), photovoltaic (PV) and PVT was conducted to obtain prices and performance. Simulations of the energy output around the world were conducted. A ratio between ST and PV annual output was defined to serve as a tool for comparison and plotted on a world map.

A key issue for PVT collectors is how to encapsulate the solar cells in a way that, amongst other things, protects the cell from the thermal expansion of the receiver, has a high transparency, and insulates electrically while at the same time conducts the heat to the receiver. In order to be useful, this analysis must also consider the impacts on the production processes. Several prototypes were constructed, a test methodology was created, and the analysis of the results enabled several conclusions on the validity of the different silicon encapsulation methods.

This thesis relies heavily on collector testing with 30 different prototypes of C-PVTs being designed and constructed. Most testing was conducted using steady state method but quasi dynamic was also carried out. From this work, several guidelines were created for the design of collectors in terms of reflector geometry, cell size, string configuration, encapsulation method and several other design aspects. These analyses were complemented with thermal simulations (COMSOL & ANSYS), string layout (LT SPICE) and evaluation of existing installations. Two novel design ideas came from this thesis work, which the author will patent in the coming year. Additionally, raytracing work has been conducted and a new reflector geometry more appropriate for C-PVTs has been found to significantly improve the annual performance. Finally, the current and future position of PVTs in the global energy market is discussed.

**Keywords:** Solar Energy, Photovoltaic-Thermal (PVT), Concentration, Collector Testing, Silicon Cell Encapsulation, Ray Tracing, Market Survey, String Layout, Prototype Collectors.

# Sammanfattning

Denna avhandling syftar till att samla kunskaper om solenergi i allmänhet och PVT-hybrider som ger både el och värme i synnerhet. Särskilt stort intresse riktas mot koncentrerande C-PVT-hybrider.

Avhandlingen ställer ett flertal viktiga forskningsfrågor för PVT och C-PVT solfångare och försöker svara på dem. En omfattande marknadsstudie av solvärme (ST), solceller (PV) och PVT har genomförts för att erhålla priser och prestanda.

Studien användes som underlag för energiutbytessimuleringar runt om i världen. Ett förhållande för kvoten mellan energiutbytena för ST och PV definierades för att användas som ett verktyg för en jämförelse mellan systemen och ritades in på världskartan.

En viktig fråga för PVT-solfångare är hur man kapslar in solcellerna på ett sätt som bland annat skyddar solcellen från absorbatorns värmeutvidgning, har hög transparens och isolerar elektriskt samtidigt som den leder värmen till absorbatorn. För att vara användbar måste denna analys också ta hänsyn till produktionsprocesserna. Flera prototyper konstruerades, en testmetod utarbetades och analysen av resultaten möjliggjorde ett antal viktiga slutsatser om funktionen hos de olika silikoninkapslingsmetoderna.

Denna avhandling baseras på verkningsgradstestning av 30 olika prototyper av C-PVT. De flesta testerna utfördes med den statiska testmetoden, men kvasi dynamisk testning har också använts. Från denna testning utarbetades riktlinjer för konstruktionen av solfångarna när det gäller reflektorgeometri, cellstorlek, strängkonfiguration och inkapslingsmetod. Dessa analyser kompletterades med termiska simuleringar (COMSOL & ANSYS), stränglayout (LT SPICE) och utvärdering av befintliga installationer. Ett antal nya designidéer kommer att patenteras under de kommande åren. En ny reflektorgeometri för C-PVT som förbättrar det årliga energiutbytet har utarbetats och testats. Slutligen diskuteras PVTs nuvarande och framtida position på den globala marknaden för solenergisystem.

**Nyckelord:** Solenergi, Fotovoltaisk-termisk (PVT), Koncentration, Solfångarprovning, Inkapsling av kiselceller, Strålgångsberäkning, Marknadsundersökning, Strängdesign, Solfångarprototyper

## Acknowledgements

Welcome to the most read section of a thesis!

This PhD thesis has been carried out within the REESBE programme (Resource Efficient Energy Systems in the Built Environment) and was partly funded by the Knowledge Foundation (KK-Stiftelsen), for which I am grateful.

**Supervisors:** I have first met my PhD supervisor, Björn Karlsson, in a solar course in Praha. Since then, we have been around the world, at CERN in Geneva where I worked, in Lund, around India being blessed by a strange lady, in Maputo testing collectors, in Zurich at the IEA task meeting on PVTs, in Dubai, over the Baltic sea by boat, etc. I would like to thank my supervisor and friend Björn Karlsson, whose overarching view of the world and deep knowledge of physics and solar I admire. I would also like to thank my second supervisor Mats Rönnelid for his kindness and his deep knowledge of concentration physics. To my PhD company supervisor and mentor at Solarus, Göran Lundgren, I would like to say that it was an honor to work for you, I have learned a lot from you. I would like to thank you for all the support as well as your trust, which I hope to have proven worthy of. I am thankful to Bengt Perers for all the great comments and review of my thesis.

**Solarus:** I would like to thank Susanne and Stefan Maston for having welcomed me into Sweden, as if I was their son. I am very grateful and I shall never forget. Furthermore, I would like to thank Stefan for his technological advice and for the opportunity to start at Solarus, which changed my life. Tony, you have been my main mate during this long and defining Solarus adventure. We had our differences along the way, but I am very happy to have shared this adventure with you. The best mechanical knowledge in town! MG is our next adventure! Olle, the man who can change the world with one word! The sharpest tool in the box, hang in there and never forget that it is worth changing the world! Och tack för allt! To all my trainees, to whom I hope to have helped in their path. Having to supervise you has also pushed me forward and I have enjoyed our time together. There isn't enough space to mention everyone but you are remembered. Maidur, you were the first student I supervised back in 2011. Luis Ferreira, Nayeem, Pierre Labrunie (keep that good mood), Jose Moreno (the one who started on the solar lab at HiG), Luc and Carine (the creators of the code that passed on for generations), Jana (Winsun master), Linkesh (The one that can do anything), and Kamala. The great generation of 2014/2015: Assem, Sathish (you remind me of myself. Stay that way, I guess ☺), Christina, Tiffany (merci pour le cartes), Silvio, Franz and Mafalda (Fjärdervägen Power), Luis, and Stefan. To all, thank you for the good times and for the measurements that were important in my path to understanding concentrating PVTs. The same applies to Francho, Caroline, Fabien, Remi, Thomas, Eduardo, Xavier, Gerard, Patrick, Claire, Thomas, Damien, Romain, Rohith, and Ali. Also, Gustaf, Viktor, David, and Paul Dostie (Mate in 4). To the EUREC 2018 generation: Caroline, Rajan, Chacin, João, Harish, Sreemnanth, Pallavi, Gautham, Aparajeet, Behrooz, and Torsten. Also 2019: Abi, Arian, Simon (um abraço!), Yehja, Marvin, Apram, and Tharun.

**REESBE/HiG:** To my colleagues at REESBE for their support during the courses in particular to Harald, Mathias, Jessika, and Corey. And, of course, to Gunnar, I hope to one day, attain even half your knowledge of thermal systems. And to Diogo Cabral, who lived 1 km away my hometown, but I met in Gävle. Chegaste na altura certa à Solarus e fizeste pela vida. Respeito! Foi um prazer. Eureka, RESBUILD, IEA task 60, and much more. And more to come! To Abo, Mazyar, Pouriya, and Hossein, with whom I enjoyed building and testing a unique PVT, as well as visiting Iran. Lastly, to Ulf Larsson for his kindness and financial support in various courses and conferences.

**Maputo:** To the Mozambican group, Henrik, Ricardo, Niko, & Mr Gruffman. Long Live Maputo! And please keep saving the dolphins! Ricardo, we met in a BEST course that truly shaped my whole life, as it was your grant that got me to Lund and I married one of the course organizers! Mr H, The world and beyond, I have travelled the most with you. And with your мать! Spassibo!

**IST Group:** Gostava de agradecer a colaboração com o grupo do Técnico Carlos, Paulo, João, João, Daniel, Pedro, Catarina, and Samuel.

**MG Sustainable Engineering AB:** To Luis, my MG partner, I admire your knowledge and especially your energy. Don't forget listen. Let's move this boat to the moon! To George Pius, my basket/ping-pong nemesis! Slow and steady, you are truly unstoppable! To all the great collaborators at MG, Hamza, Bilal, Adam, Maria, Jubin, Adithya, Andrew, Aravind, Alex, Manali, Arun, Mohamad, Flavio, Nistha, Vengatesh, Shibu, Mahdi, Avip, Juan, Chimba, Chooi (the organizer!), Tutty, Elias, Ahmed, Muhamad, Adeel & Nikita (Mr & Mrs proofreading, Baie Dankie!), Abel, Yannis, Kahlid, Reuben, Nassar, Jacek, Isac, Sahand, et al. Projects: CSP, ABS, RES4Live, RES4Build, PowerUpMyHouse, RES4Community and AfricaSun, the sky is the limit!

**Absolicon AB:** Thank you Joakim for trusting me. And for creating an amazing place to work in! Carlo, Jonatan, Olle again, Puneet, George, and all others in this fantastic place.

**To the Geo gang of Uppsala,** with whom I have spent wonderful times. I can't mention everybody. Iwa, Sunnersta Inn power! Monika, Chris, Magnus, Bojan, Silvia, Fred, Sebastian, Laura, Shunguo (the glorious), Marta, Dragos, etc. Rudi amigo do CERN, sempre p/ a frentex, mantém esse espirito aventureiro.

**Nova Uni:** Za moje Eramus kamo, Sérgio, Pozor: "Ukončete, prosím, výstup a nástup, dveře se zavírají"! Nejlepší rok v životě! Uvidíme brzo, bratr!

**Á Malta da Parede,** pessoal do coração: João Carlos, Liliana, Hugo, Mika (Mr CFD), Sara, Raquel, Pedro, Rita, Joaninha, Nesoca, Primão, JP, Carina, Richie, Hugo, Marisa, Cabrita, Coimbra forever!

**Last but not least,** to my mother whose wisdom, I have always relied on, and my father whose energy I admire. I would not have reached here without all your loving support. To my fantastic sister and brother, whom I am lucky to have and for whom I hope to have been a good influence. Aos meus avós queridos e a toda a minha família. Por fim, obrigado a minha filha por me derreter com apenas uma palavra, e ao menino que aí vem. Și a Gia Gia Gia, a mulher da minha vida que esteve comigo em todos estes momentos que me aturou e apoiou durante estas e todas as outras aventuras dos últimos 12 anos. Te iubesc ad infinitum.



## List of Papers

This thesis is based on the following papers, which are referred in the text by Roman numerals.

### **Paper I - Submitted to Journal “Energy Strategy Reviews”**

**Gomes J.**, Junge J., Lehmann T. et Karlsson B. (2016). Defining an Annual Energy Output Ratio between Solar Thermal Collectors and Photovoltaic Modules. *Presented at IAHS conference. Improved and submitted to Energy Strategy Reviews.*

**Key Message:** Winsun Chapter. A new tool for comparison of ST and PV technologies and a market overview.

### **Paper II - Journal “Energies”**

Gomes J. (2019). Assessment of the Impact of Stagnation Temperatures in Receivers Prototypes of C-PVT Collectors. *Energies, Special Issue Photovoltaics Lifetime Output Improvement: Advanced Monitoring, Failure Detection and Classification and Energy Forecasting, 12(15), 2967.* DOI: <https://doi.org/10.3390/en12152967>

**Key Message:** Silicone chapter. Analysis on the impact of stagnation on solar cells encapsulated by silicone and different methods for impact mitigation.

### **Paper III - Journal “Engineering”**

Bernardo R., Davidsson H., Gentile N., Gomes J., Gruffman C., Chea L., Mumba C. et Karlsson B. (2013). Measurements of the Electrical Incidence Angle Modifiers of an Asymmetrical Photovoltaic/Thermal Compound Parabolic Concentrating-Collector. *Presented at PEEC conference and published in Engineering, Vol. 5 No. 1B, 2013, pp. 37-43.* DOI: [10.4236/eng.2013.51B007](https://doi.org/10.4236/eng.2013.51B007)

**Key Message:** Collector testing chapter (SST). Characterization of the IAM of an early C-PVT prototype.

### **Paper IV - Conference Proceedings “Energy Procedia”**

Gomes J., Diwan L., Bernardo R. et Karlsson B. (2014). Minimizing the Impact of Shading at Oblique Solar Angles in a Fully Enclosed Asymmetric Concentrating PVT Collector. *Presented at Solar World Conference and published in Energy Procedia, Volume 57, 2014, p. 2176-2185.* DOI: <https://doi.org/10.1016/j.egypro.2014.10.184>

**Key Message:** Collector Testing Chapter (SST). Analysis of the impact of shading in different asymmetric low concentration stationary PVT including transparent and opaque sides.

### **Paper V - Journal “Solar Energy”**

Cabral D., Gomes J., Hayati A. et Karlsson B. (2020) Experimental Investigation of a CPVT Collector coupled with a Wedge PVT Receiver. *Solar Energy,*

Volume 215, February 2021, Pages 335-345. DOI: <https://doi.org/10.1016/j.solener.2020.12.038>

**Key Message:** Collector Testing Chapter (SST). Evaluation of a novel bifacial CPVT.

#### **Paper VI - Conference Proceedings “Eurosun”**

Kurdia A., Gomes J., Pius G., Ollas P. and Olsson O., (2018). Quasi-dynamic testing of a novel concentrating solar collector according to ISO 9806:2013. *Presented at Eurosun*. DOI: [10.18086/eurosun2018.12.07](https://doi.org/10.18086/eurosun2018.12.07)

**Key Message:** Collector Testing (QDT). Comparison of the testing results between the Solarus C-PVT and a standard flat plate.

#### **Paper VII - Conference Proceedings “Eurosun”**

Giovinazzo C., Bonfiglio L., Gomes J. et Karlsson B. (2014). Ray Tracing Modelling of an Asymmetric Concentrating PVT. *Presented at Eurosun*. DOI: [10.18086/eurosun.2014.21.01](https://doi.org/10.18086/eurosun.2014.21.01)

**Key Message:** Raytracing Chapter. The Solarus C-PVT collector has been modelled using Tonatiuh to extract a 3D map of the effective solar irradiation of both top and bottom sides of the receiver.

#### **Paper VIII - Journal “Solar Energy”**

Cabral D., Gomes J., et Karlsson B. (2019). Performance and Impact Evaluation of Non-Uniform Illumination on a Transverse Bifacial C-PVT Receiver in Combination with an Ideal Cylindrical Concentrator Geometry. *Solar Energy, Volume 194, December 2019, Pages 696-708*. DOI: [10.1016/j.solener.2019.10.069](https://doi.org/10.1016/j.solener.2019.10.069)

**Key Message:** Ray Tracing Chapter. Evaluation in Tonatiuh of an improved reflector geometry for PVT called DM.

Reprints were made with permission from the respective publishers.

During this thesis work, the author has contributed to a total 40 papers, 27 published in conferences (4 under review) and 13 in journals (1 under review). These papers were, as a whole, very important in shaping this thesis and its research direction. The remaining 32 papers are shown below and in several cases, cited in the thesis text.

#### **Additional Journal Papers:**

**Paper 9:** Nashih S., Fernandes C., Torres J., Gomes J. et Branco P. (2016). Validation of a Simulation Model for Analysis of Shading Effects on Photovoltaic Panels. *Solar Energy Engineering: Including Wind Energy and Building Energy Conservation, Volume 138, Issue*. DOI: [10.1115/1.4033646](https://doi.org/10.1115/1.4033646).

**Key Message:** Validation of an LTSpice model.

**Paper 10:** Alves P., Branco P., Fernandes J., Torres J., Fernandes C. et Gomes J. (2019). From Sweden to Portugal: the Effect of Very Distinct Climate Zones on Energy Efficiency of a Concentrating Photovoltaic/Thermal System (C-PVT). *Solar Energy*. DOI: /10.1016/j.solener.2019.05.038

**Key Message:** FEM study on different receiver channels on the Solarus C-PVT with a performance evaluation.

**Paper 11:** Nasseriyan P., Gorouh H., Gomes J., Cabral D., Salmanzadeh M., Lehmann T. et Hayati A. (2020). Numerical and Experimental Study of an Asymmetric CPC-PVT Solar Collector. *Energies*. DOI: <https://doi.org/10.3390/en13071669>

**Key Message:** Study on heat conduction through the silicone encapsulation.

**Paper 12:** Cabral D., Gomes J., Hayati A et Karlsson B. (2021). Experimental Investigation of a Parabolic Trough Solar Collector prototype coupled with a vertical n-PERT half-size Bifacial Solar Cells. Submitted to *Solar Energy*.

**Key Message:** Evaluation of a bifacial CPV (collectors testing).

**Paper 13:** Davidsson H., Bernardo R., Gomes J., Chea L., Gentile N. et Karlsson B. (2013). Construction of laboratories for solar energy research in developing countries. *Energy Procedia, Volume 57, 2014, Pages 982-988*. DOI: 10.1016/j.egypro.2014.10.081.

**Key Message:** Study on the design and components for a solar lab for research and education in developing countries.

**Paper 14:** Torres J., Fernandes C., Gomes J., Olsson O., Bonfiglio L., Giovannazzo C. et Branco P. (2018). Effect of Reflector Geometry in the Annual Received Radiation of Low Concentration Photovoltaic Systems. *Energies*. DOI: 10.3390/en11071878

**Key Message:** Analysis of different reflector geometries using the soltrace software.

**Paper 15:** Torres J., Nashih S., Fernandes C. et Gomes J. (2016). The effect of shading on photovoltaic solar panels. *Energy Systems, page 1-14*. DOI: 10.1007/s12667-016-0225-5

**Key Message:** LTSPICE study on the shading impact in a PVT.

**Paper 16** Torres J., Fernandes J., Fernandes C., Branco P., Barata C., et Gomes J. (2018) Effect of the collector geometry in the concentrating photovoltaic thermal solar cell performance. *Thermal science, Vol. 22, No. 5*. DOI: 10.2298/TSCI171231273T,

**Key Message:** Ray Tracing analysis and comparison of different geometries.

### **Additional Conference Papers:**

**Paper 17:** Gomes J., Gruffman C., Davidsson H., Maston S. et Karlsson B. (2013). Testing bifacial PV cells in symmetric and asymmetric concentrating CPC collectors. *PEEC Conference and published in Engineering, Vol. 5 No. 1B, PP. 185-190*. DOI: 10.4236/eng.2013.51B034.

**Key Message:** Different low concentration bi-facial PV collector prototypes were built and tested.

**Paper 18:** Gentile N., Davidsson H., Bernardo R., Gomes J., Gruffman C., Chea L., Mumba C. et Karlsson B. (2013). Construction of a small scale laboratory for solar collectors and solar cells in a developing country. *Presented at PEEC conference and published in Engineering, Vol. 5 No. 1B, 2013, PP. PP. 75-80*. DOI: 10.4236/eng.2013.51B014.

**Key Message:** Developing and reducing the cost of components of solar collector testing labs while maintaining the necessary accuracy.

**Paper 19:** Gomes J., Bonfiglio., Giovinazzo C., Fernandes C., Torres J., Olsson O., Branco P. et Nashih S. (2016). Analysis of C-PVT reflector geometries. *17th international conference on power electronics and motion control*. DOI: 10.1109/EPEPEMC.2016.7752175.

**Key Message:** Analysis of the raytracing results of different reflector geometries including a cost/output balance.

**Paper 20:** Gomes J, Bastos S., Henriques M., Diwan L. et Olsson O. (2015). Evaluation of the Impact of Stagnation in Different Prototypes of Low Concentration PVT Solar Panels. *ISES Solar World Congress*. DOI: 10.18086/swc.2015.10.14.

**Key Message:** Analysis on the impact of stagnation on solar cells encapsulated by silicone and different methods for mitigation of the impact.

**Paper 21:** Mantei F., Henriques M., Gomes J., Olsson O. et Karlsson B. (2015). The Night Cooling Effect on a C-PVT Solar Collector. *ISES Solar World Congress*. DOI: 10.18086/swc.2015.10.33.

**Key Message:** Night cooling using glazed C-PVT collectors will work only under very few specific circumstances.

**Paper 22:** Contero F., Gomes J., Mattias G. et Karlsson B. (2016). The impact of shading in the performance of three different solar PV systems. *Eurosun*. DOI: 10.18086/eurosun.2016.08.25.

**Key Message:** Evaluation of the electrical shading at HiG's installation. Comparison between different shading mitigation devices.

**Paper 23:** Gomes J. et Karlsson B. (2010). Analysis of the Incentives for Small Scale Photovoltaic Electricity Production in Portugal. *Eurosun*. DOI: 10.18086/eurosun.2010.08.05.

**Key Message:** Analysis of the impact of the incentive schemes in PV penetration in Portugal.

**Paper 24:** Gomes J. et Karlsson B. (2010). Analysis of Reflector Geometries for Flat Collectors. *Renewable Energy Conference, Yokohama, Japan*.

**Key Message:** Analysis on the best point for truncation for reflectors in concentrating solar thermal collectors.

**Paper 25:** Cabral D., Dostie-Guindon P., Gomes J. et Karlsson B. (2017). Ray Tracing Simulations of a Novel Low Concentrator PVT Solar Collector for Low Latitudes. *ISES Solar World Congress*.

**Key Message:** Comparison between different reflector geometries for a low concentrating PVT using Tonatiuh ray tracing.

**Paper 26:** Fernandes J., Alves P., Torres J., Branco P., Fernandes C., Gomes J. (2017). Energy Efficiency of a PV/T Collector for Domestic Water Heating Installed in Sweden or in Portugal: The Impact of Heat Pipe Cross-Section Geometry and Water Flowing Speed. *12th SDEWES Conference*.

**Key Message:** Simulations were conducted to verify the influence of the flow, losses in electric efficiency, temperature variation, shading effect in the electrical efficiency of a C-PVT in Portugal and Sweden.

**Paper 27:** Fernandes C., Torres J., Nashih S., Gomes J. et Branco P. (2016). Cell string layout in a stationary solar concentrating solar photovoltaic collectors. *Power Electronics and Motion Control Conference (PEMC), IEEE*. DOI: 10.1109/EPEPEMC.2016.7752179

**Key Message:** Simulations using an LTSPICE to predict the shading influence in the electrical output of a C-PVT.

**Paper 28:** Fernandes C., Torres J., Nashih S., Gomes J. et Branco P. (2015). Shading Effects on Photovoltaic Panels. *Conftele Conference*.

**Key Message:** Early shading study with LTSPICE.

**Paper 29:** Lança M., Gomes J. et Abolfazl H. (2018). Numerical Simulation of the Thermal Performance of Four CPC Collectors Prototypes with Bifacial PV Cells. *Eurosun*.

**Key Message:** Thermal study of the receiver temperature of different CPV panel designs.

**Paper 30:** Costeira J., Viera M., Hayati A., Gomes J. et Cabral D. (2018). Development of a compact and didactic solar energy kit using Arduino. *Eurosun*.

**Key Message:** Development of a low cost teaching tool for solar PV.

**Paper 31:** Cabral D, Costeira J. et Gomes J. (2018). Electrical and Thermal Performance Evaluation of a District Heating System Composed of Asymmetric low concentration PVT Solar Collector Prototypes. *Eurosun*.

**Key Message:** Evaluation of wall mounted system with 20 Solarus Collectors at Gävle University.

**Paper 32:** Chacin L., Rangel S., Cabral D. et Gomes J. (2019). Impact study of operating temperatures and cell layout under different concentration factors in a CPC-PV solar collector in combination with a vertical glass receiver composed by bifacial cells. *Solar World Conference*.

**Key Message:** Construction and testing of a CPV collector.

**Paper 33:** Panchal R., Gomes J., Cabral D., Eleyele A. et Lança M. (2019). Evaluation of Symmetric C-PVT Solar Collector Designs with Vertical Bifacial Receivers. *Solar World Conference*.

**Key Message:** Construction and testing of a C-PVT collector with a novel reflector geometry.

**Paper 34:** Gallardo F., Guerreiro L. et Gomes J. (2019). Exergo-economic Comparison of Conventional Molten Salts Versus Calcium Based Ternary Salt Direct HFT-TES in CSP Parabolic Troughs. *Solar World Conference*.

**Key Message:** SAM modeling. Comparison between a binary and a ternary salt in the performance of a CSP plant.

**Paper 35:** Baradey J., Hawlader M., Hrairi M., Hafner A., Gomes J. and Ishaq S. (2020). Innovative Coupling of PVT collectors with electric-driven heat pumps for sustainable buildings. *Mechanical Engineering*.

**Key Message:** Study on a C-PVT and heat pump system.

**Paper 36:** Meramveliotakis G., Kosmadakis G., Krikas A., Gomes J. and Pilou M. (2020). Innovative Coupling of PVT collectors with electric-driven heat pumps for sustainable buildings. *Eurosun 2020*.

**Key Message:** Evaluation of the C-PVT with heat pump systems designed for the RES4Build H2020 project.

**Paper 37:** Housoli S., Cabral D., Gomes J. Performance assessment of concentrated photovoltaic thermal (CPVT) solar collector at various locations. Submitted to Solar World Congress 2021. Submitted to Solar World Congress 2021.

**Key Message:** Summary of the solar collector testing carried out in Greece and Sweden for RES4Build H2020 project.

**Paper 38:** Housoli S., Loris A., Gomes J. Evaluation of solar photovoltaic thermal (PVT) system for dairy farm in Germany. Submitted to Solar World Congress 2021.

**Key Message:** Summary of the PVT market survey carried out for the RES4Live H2020 project.

**Paper 39:** Poursanidis I., Housoli S., Loris A., Lennermo, G. Lança M., Gomes J. Reverse engineering of energy demand profiles in EU livestock farms. Submitted to Solar World Congress 2021.

**Key Message:** A new methodology for estimating the load profiles in livestock farms developed for the RES4Live H2020 project.

**Paper 40:** Loris A., Poursanidis I., Housoli S., Lennermo, G., Gomes J. Evaluation of the use of concentrated solar photovoltaic thermal collectors (CPVT) coupled with other renewable energy sources on livestock farms. Submitted to Solar World Congress 2021.

**Key Message:** System evaluation for livestock farms carried out for the RES4Live H2020 project.





## Abbreviations

AEL	National Laboratory of Cyprus
CPC	Compound Parabolic Concentrator
CPV	Concentrating Photovoltaic
C-PVT	Concentrating Photovoltaic Thermal Collector
CSP	Concentrated Solar Power
DHW	Domestic Hot Water
DM	Double MaReCo
EL	Electroluminescence
EVA	Ethylene Vinyl Acetate (PV standard encapsulation)
HiG	Gävle University
HSAT	Horizontal single axis tracker
HTF	Heat Transfer Fluid
IAM	Incidence Angle Modifier
IEA	Internal Expansion Area
LNEG	National Laboratory of Energy and Geology of Portugal
MaReCo	Maximum Reflector Concentration
MELACS	Micro Energy Logger And Control System
MLR	Multiple Linear Regression
NASA	National Aeronautics and Space Administration of the USA
NOAA	National Oceanic & Atmospheric Administration of the USA
NOCT	Nominal Operating Cell Temperature
PC	Power Collector (last version of the C-PVT produced by Solarus)
PV	Photovoltaic
QDT	Quasi Dynamic Testing
RE	Renewable Energy
REESBE	Resource-Efficient Energy Systems in the Built Environment
SIDA	Swedish International Development Agency
SST	Steady State Testing
SHIP	Solar Heat for Industrial Processes
ST	Solar Thermal
TEA	Total Expansion Area
VT	Vacuum Tube

## Nomenclature

$P$	Collector power (for both thermal or electrical collectors)
$I$	Solar irradiation intensity on the collector plane
$\eta$	Collector Efficiency (for both thermal or electrical collectors)
$\eta_0$	Optical efficiency of the thermal collector
$U_1$	First order heat losses
$U_2$	Second order heat losses
$\Delta T$	Temperature difference
$F'(\tau_{\alpha})$	Zero loss efficiency of the collector for beam irradiation, at normal incidence angle
$K\theta b_{(\theta L, \theta T)}$	Incidence angle modifier for beam solar irradiation. $K\theta b$ varies with the incidence angles $\theta L$ , and $\theta T$
$K_{\theta d}$	Incidence angle modifier for diffuse solar irradiation
$c_1$	Heat loss coefficient at $(t_m - t_a) = 0$ (also mentioned as $U_1$ in literature)
$c_2$	Temperature dependence in the heat loss coefficient (also mentioned as $U_2$ in literature)
$c_3$	Wind speed dependence of the heat losses
$c_4$	Long wave irradiance dependence of the heat losses
$c_5$	Effective thermal capacitance [ $J/m^2 \cdot K$ ]
$c_6$	Wind dependence of the collector zero loss efficiency
$P_{\text{thermal}}$	Thermal power
$P_{\text{electric}}$	Electric power
$P_{\text{electric\_top}}$	Electric power of the top side of the receiver
$P_{\text{electric\_bottom}}$	Electric power of the bottom side of the receiver
$T_{\text{in}}$	Inlet temperature
$T_{\text{out}}$	Outlet temperature
$T_{\text{mid}}$	Average temperature
$T_{\text{amb}}$	Ambient temperature
$dV/dt$	Flow ( $m^3/s$ )
$C_p$	Heat capacity (water) ( $J/kg \cdot ^\circ C$ )
$\rho$	Density (water) ( $kg/m^3$ )
$A_{\text{Hybrid}}$	Total glazed collector area ( $m^2$ )
$A_{\text{active\_elect}}$	Electric active glazed area
$A_{\text{active\_thermal}}$	Thermal active glazed area
$A_{\text{cells}}$	Cell area of one receiver
$T$	Transmittance coefficient of the glass (-)
$R$	Reflectance coefficient of the reflector (-)
$A$	Absorptance coefficient of the solar cells(-)
$C$	Concentration factor of the collector (-)
$\eta_{\text{od}}$	Diffuse efficiency (%)
$\eta_{\text{ob\_thermal}}$	Beam thermal optical efficiency (%)
$\eta_{\text{ob\_electric}}$	Beam electric optical efficiency (%)
$\eta_{\text{cells}(25^\circ C)}$	Cell efficiency at $25^\circ C$ (-)
$a_1$	Heat loss factor ( $W/m^2 \cdot ^\circ C$ )

$a_2$	Temperature dependence of heat loss factor ( $\text{W/m}^2 \text{ } ^\circ\text{C}$ )
$K_{\text{ta\_thermal}}$	Thermal angle of incidence modifier for beam irradiance (-)
$K_{\text{ta\_electric}}$	Electric angle of incidence modifier for beam irradiance (-)
$b_{\text{o\_thermal}}$	Thermal angular coefficient (-)
$b_{\text{o\_electric}}$	Electric angular coefficient (-)
$K_{\text{diffuse}}$	Diffuse incident angle modifier (-)
$K_{\text{T}}$	Electric efficiency temperature dependence ( $\%/^\circ\text{C}$ )
$\theta$	Angle of incidence onto the collector ( $^\circ$ )
$\text{IAM}_{\text{t\_elect.}}$	Electrical transverse incidence angle modifier (-)
$\text{IAM}_{\text{l\_elect.}}$	Electrical longitudinal incidence angle modifier (-)
$\text{IAM}_{\text{t\_thermal.}}$	Thermal transverse incidence angle modifier (-)
$\text{IAM}_{\text{l\_thermal.}}$	Thermal longitudinal incidence angle modifier (-)
$f$	Fraction of useful diffuse irradiation
$Z$	Height
$A_{\text{ptarea}}$	Aperture Area ( $\text{m}^2$ )
$C_i$	Concentration ratio
$\theta_t$	Transverse incident angle
$\text{FF}$	Fill factor
$A_a$	Aperture
$t_{\text{cell,PVT}}$	Cell temperature [ $^\circ\text{C}$ ]
$K_s$	Effective thermal conductivity [ $\text{W/m}\cdot\text{K}$ ]



# Table of Contents

<b>1</b>	<b>Introduction</b>	<b>1</b>
1.1	Background and motivation for this work	1
1.2	Aims and Research Questions	1
1.3	Research Funding Obtained and other activities	2
<b>2</b>	<b>Literature review</b>	<b>4</b>
2.1	The importance of energy	4
2.2	Climate change	5
2.3	Overview of the Energy Sector	7
2.4	Solar Energy: PV and Thermal collectors	9
2.4.1	Solar Electricity	9
2.4.2	Solar Heat	10
2.5	Basics of Solar Energy: Differences between PV & ST	13
2.5.1	Comparing heat and electricity	13
2.5.2	The effect of solar irradiation in PV and ST collectors	13
2.5.3	The effect of temperature in PV and T collectors	15
2.5.4	Influencing factor: local climate	15
2.6	Basics of Concentration in Solar Collectors	17
2.6.1	Concentration factor	18
2.6.2	Compound Parabolic Collectors	19
2.7	Maximum Reflector Concentration Design	20
2.7.1	The stand-alone MaReCo	21
2.7.2	The roof integrated MaReCo	22
2.7.3	The wall MaReCo	23
2.8	PVT collectors: Advantages and Disadvantages	24
2.9	C-PVT collector: Advantages and Disadvantages	25
2.10	The impact of shading and concentration in PV panels and solar thermal collectors	26
2.11	First Look at the Solarus C-PVT	27
2.11.1	The Collector Box	27
2.11.2	Receiver core	29
2.11.3	Systems Integration of the Solarus C-PVT	30
2.12	PVT Market Overview	31
<b>3</b>	<b>Method Overview</b>	<b>35</b>
<b>4</b>	<b>Winsun</b>	<b>42</b>
4.1	Method	42
4.1.1	Definition of the ratio between ST and PV	42
4.1.2	Market survey	42

4.1.3	Winsun Simulations	43
4.2	Results	44
4.2.1	Market Survey	44
4.2.2	Winsun Simulations	46
4.3	Conclusion	49
<b>5</b>	<b>On the Successful Silicon Encapsulation of a CPVT Receiver</b>	<b>52</b>
5.1	Challenges and advantages of silicon encapsulation	52
5.1.1	Distance between solar cell and receiver	54
5.1.2	Manufacturing challenges	54
5.1.3	Material expansion	54
5.1.4	Top & Bottom Silicone Layer	54
5.1.5	Silicone Thermal Conductivity	55
5.1.6	Production process	56
5.1.7	Curing Process & Mixing	57
5.1.8	Material cost	57
5.2	Test Methodology	57
5.2.1	The Prototype Receivers	57
5.2.2	Test Method and Equipment	58
5.3	Silicon Encapsulation Testing Results	60
5.3.1	Electroluminescence Microcrack Evaluation	60
5.3.2	Thermal Stress Test Results	62
5.4	Silicon Encapsulation Testing Conclusions	68
5.5	A Novel Solution for Improved Thermal Contact in PVT receivers: The H-Pattern	69
5.5.1	Design proposal	69
5.5.2	Expansion-inhibiting design pattern	70
5.5.3	Advantages of the H-Pattern	70
5.5.4	Insulation layer	71
<b>6</b>	<b>Collector testing</b>	<b>74</b>
6.1	Collector Testing Method	74
6.1.1	Key thermal parameters of a low concentration C-PVT	74
6.1.2	Key electrical parameters of a low concentration C-PVT	76
6.1.3	Incidence angle modifier	76
6.1.4	Calculation of the theoretical maximum electrical power	77
6.2	Testing at Lund University	78
6.2.1	Description of the prototype collector	78
6.2.2	Method	79
6.2.3	Results	81
6.2.4	Conclusions	85
6.3	Paper III: Testing at Eduardo Mondlane University	85

6.3.1	Description of the prototype collector & laboratory set-up	85
6.3.2	Method	89
6.3.3	Results	93
6.3.4	Conclusions	95
6.4	Paper IV: Testing at Solarus, Gävle and Dalarna Universities	95
6.4.1	Overview of the different laboratory set-ups	96
6.4.2	Indoor testing at the Solarus Laboratory	96
6.4.3	Outdoor Testing	97
6.4.4	Measured Collectors	98
6.4.5	Results	99
6.4.6	Conclusions	103
6.5	Testing at Gävle University of 2014	104
6.5.1	Solar Laboratory at the University of Gävle	104
6.5.2	Measured Thermal and Electrical Parameters	107
6.5.3	Prototype Collectors tested	108
6.5.4	Collector Testing Results	109
6.6	Testing at Gävle University of 2015	114
6.6.1	Prototype Collectors tested	114
6.6.2	Method	116
6.6.3	Collector Testing Results	116
6.7	Paper VI: Testing at Dalarna University of 2016	126
6.7.1	Methodology	126
6.8	Paper V: CPVT with a wedge receiver	131
6.8.1	Methodology	131
6.8.2	Collector Testing Results	133
6.8.3	Conclusions	135
6.9	The RES4Build DM Collector	136
6.9.1	RES4Build project	136
6.9.2	Construction of the DM collector (V10 & V11)	138
6.9.3	New Solar Laboratory at Gävle University	143
6.9.4	Test results from the DM collector	147
6.9.5	Output simulations based on the measured results	149
6.10	Testing in Cyprus, Portugal and Switzerland	155
6.10.1	Methodology and results	155
<b>7</b>	<b>RayTracing Simulations with Tonatiuh</b>	<b>158</b>
7.1	Method	158
7.1.1	Tonatiuh and Matlab	158
7.1.2	Optical properties	159
7.1.3	Software limitations	159
7.1.4	Incidence Angle Modifier	160
7.2	Simulation of an early CPVT prototype	160

7.2.1	The impact of the different collector components in performance	161
7.2.2	Influence of the tilt	163
7.2.3	Flux Homogeneity	165
7.2.4	3D Effective solar radiation	167
7.2.5	Conclusions	169
7.3	Improved Reflector Geometries for C-PVTs	169
7.3.1	The DM reflector geometry	170
7.3.2	Comparison of Incidence Angle Modifiers	174
7.3.3	Electrical and thermal yield	175
7.3.4	Evaluation of non-uniform illumination	176
7.3.5	Conclusion	178
<b>8</b>	<b>Overall Conclusions</b>	<b>179</b>
<b>9</b>	<b>References</b>	<b>190</b>



# 1 Introduction

## 1.1 Background and motivation for this work

This thesis is part of an Industrial PhD done within Resource-Efficient Energy Systems in the Built Environment (REESBE). It was initiated at the company Solarus Sunpower Sweden AB in Gävle and concluded at the company MG Sustainable Engineering AB, a start up from Uppsala, which the author of this thesis has founded in 2014.

This work was aimed at detailing the scientific principles behind concentrating photovoltaic-thermal (C-PVT) solar collectors and its unique features, as well as conducting an unbiased evaluation of the merits of this technology in comparison to other energy-producing technologies. A better understanding of its own product will help the companies to improve the products available for the population. Furthermore, the knowledge generated will increase the scientific understanding about C-PVT panels and hopefully support future researchers in this topic.

## 1.2 Aims and Research Questions

The research questions include both broader solar aspects and specific questions about PVT and C-PVT solar collectors:

1. How does the annual energy output ratio between PV and ST collectors vary around the world? What is relevant to consider when analyzing this ratio?
2. What are the most important parameters that define PVT and C-PVT collector?
3. How does PVT technology compare with standard PV and ST technologies?
4. What are the advantages and disadvantages of using concentrating PVT solar collectors?
5. What are the challenges and requirements of solar cells encapsulation in PVT and CPVT collectors?
6. How can solar cells be encapsulated in PVT collectors? Can PVT and C-PVT collectors use a silicone encapsulation method? What are the advantages and disadvantages? How can these disadvantages be mitigated?
7. Can Tonatiuh be used for reflector design of a C-PVT? Which reflector geometry is the most suitable for a stationary low concentration factor C-PVT?
8. What type of cell string layout is most suitable for a stationary low concentration C-PVT?
9. What types of PVT collectors exist and what is their potential market?
10. Is a PVT better than separate PV + ST systems? Under which situations are PVT or C-PVT collectors a good choice? What can the future hold for the PVT market?

### **1.3 Research Funding Obtained and other activities**

Obtaining funding is an essential part of a researcher's career. This activity becomes even more critical during an industrial PhD within a start-up company with a strained financial capacity such as Solarus.

These circumstances have forced the author to place a great deal of emphasis into obtaining research funding in order to carry essential research projects for the company and the industrial PhD. Table 1 shows the various grants that the author has written on behalf of the different institutions he represents.

This funding has been important for carrying out the scientific developments described in this thesis. Despite the funding, Solarus AB bankrupted in January of 2020. However, MG Sustainable Engineering AB has been founded by the author and is continuing with the line work of this PhD thesis. Both Solarus Sunpower and MG Sustainable Engineering AB have been devoted to developing the field of Solar Energy and, in particular, advancing concentrating PVT and thermal collectors. MG Sustainable Engineering AB is currently expanding activities and growing to a point, where it is expected to employ 12 persons by the end of the 2021.

Furthermore, the author has supervised master 32 thesis projects during this PhD, some of which later became his colleagues at Solarus Sunpower AB and MG Sustainable Engineering AB, and with whom the author shares publications.

Lastly, as a result of the work within this thesis, two patents applications are expected to emerge within the next year. One application pertains to a variation of the H-pattern design which is designed to enhance the output and protect the solar cells, while the other is a novel design for C-PVT collector using bifacial solar cells and a unique method for cooling of these cells.

Table 1. Projects obtained by the thesis author for the institutions he has represented.

Project Name	Project budget (k€)	Received Grant (k€)	Number of Partners	Role in Project	Partners Represented	Project Description
Innovative Collector	200	120	2	Leader	Solarus AB	Install and evaluate the performance 20 concentrating solar thermal collectors in Moldova via
SolarSoft	3000	180	12	Participant	Solarus AB	Develop and evaluate the performance of a softer ribbon for solar cells that allows reduced cell breakage
Solar Laboratory Development	35	20	4	Leader	Solarus AB	Meeting three Indian Universities to develop a solar laboratory suitable for research and education
Solar CPC PVT Production	2684	696	7	Leader	SOL AB & BV	Develop two novel concentrating PVT & T solar collectors and automate their production process
RES4BUILD	5000	521	15	Participant	HiG & SOL AB	Develop innovative systems for buildings, including PVT and magneto caloric heat pumps
IEA task 60 participation	15	15	30	Participant	HiG & SOL AB	Participate in the IEA task 60 on PVT collectors
Friendship	5000	640	10	Main Participant	Absolicon AB	Development of systems with high temperature heat pumps for concentrating solar thermal
RES4Live	6000	727	20	Main Participant	MG SUST AB	Novel energy systems in livestock farms (PVT)
PowerUp MyHouse	300	48	8	Participant	HiG & MG	Education in solar PVT

## 2 Literature review

### 2.1 The importance of energy

Energy is of the utmost importance for humanity. One of the consequences of the improvement in energy access over the past two centuries can be visualized in Figure 1:

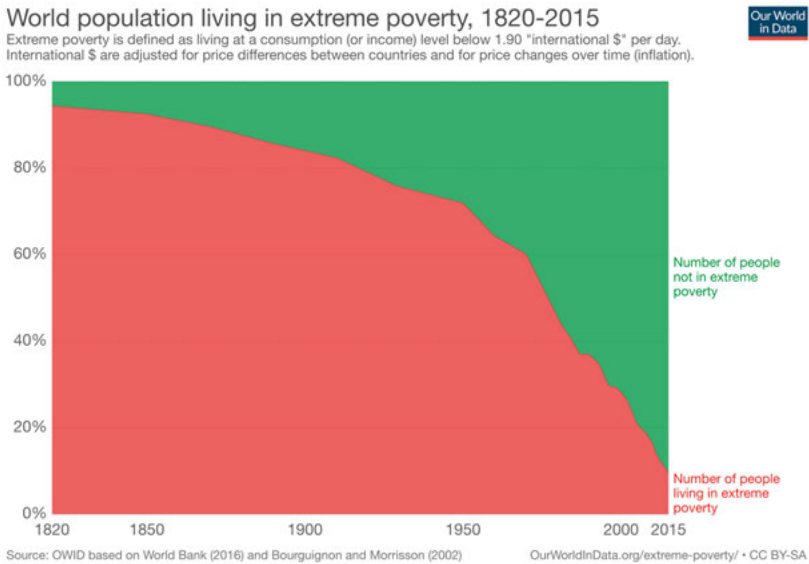


Figure 1. Percentage of the world population living in extreme poverty over 2 centuries.

The percentage of population living in extreme poverty has been reduced from 90 % to 10 % of the world population. And, while 10 % of the world population in poverty is still tragic, this is still a drastic reduction and amazing human progress that has been mostly due to the fantastic properties of fossil fuels.

This progress is an even more extraordinary accomplishment if one considers that this poverty reduction has been achieved during a period of fast population growth, as illustrated by Figure 2. In the past century, the world has seen its fastest population growth spiking in 1968 with 2.1 % annual growth. This population explosion was mainly driven by the fast reduction of child mortality in the same time frame. This was counterbalanced during the second half of 1900 with the average family size falling from six to two children today. In this way, the population quadrupled from 1920 to today at just under eight billion and will stabilize at just under 11 billion by 2100.

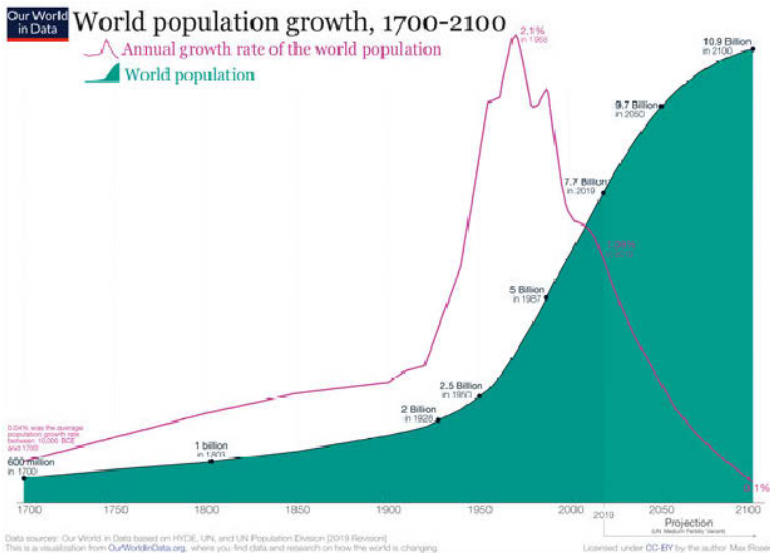


Figure 2. Annual growth and world population size from 1700 to 2100.

## 2.2 Climate change

“Today, like always before, society faces its gravest challenge.”

Although current challenges always appear to be the most pressing as the above quote somewhat cynically postulates, it is nevertheless an objective and undeniable reality that mankind today has an unprecedented capacity to alter the planet which supports its life. And, in its quest to improve its standard of life, mankind has created environmental problems that today threaten its very survival. Climate change is a reality and must be tackled, if humans are to continue to exist.

Figure 3 shows the temperature data from four reputable international scientific institutions. All show rapid warming in the past few decades and that the past decade has been the warmest on record [1].

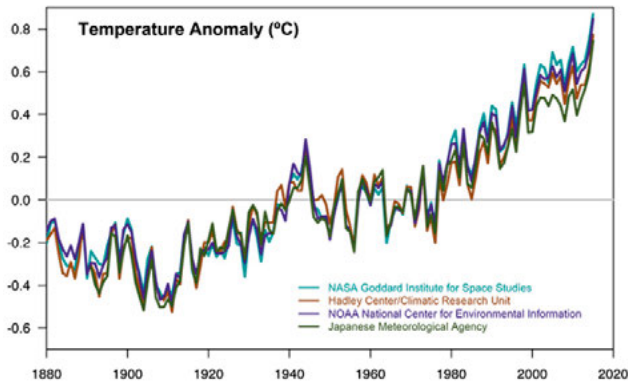


Figure 3. Planetary temperatures over the last 140 years. Sources: NASA's Goddard Institute for Space Studies, NOAA National Climatic Data Center, Met Office Hadley Centre/Climatic Research Unit and the Japanese Meteorological Agency.

Figure 4 clearly shows not only how large the atmospheric CO<sub>2</sub> increase since the Industrial Revolution has been, but also how drastically fast the planetary balance of the last 400,000 years has been disrupted. Figure 4 was made based on the comparison of atmospheric samples contained in ice cores and more recent direct measurements [2].

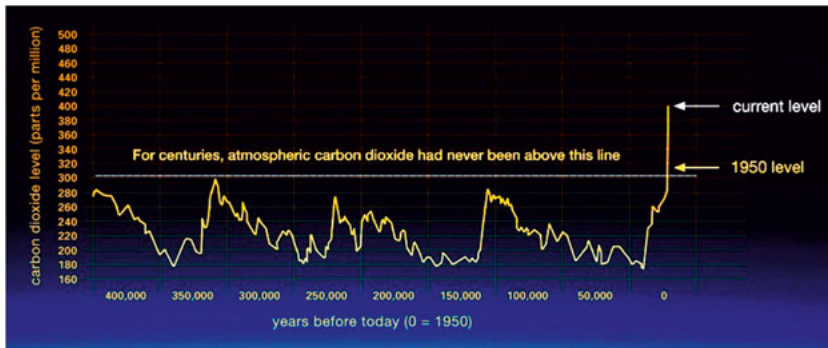


Figure 4. Variation of atmospheric carbon dioxide levels over 400,000 years. Source: Vostok ice core data/J.R. Petit et al.; NOAA Mauna Loa CO<sub>2</sub> record.

Lüthi et al, plotted CO<sub>2</sub> levels during 800,000 years and the cycles still remain between 160 and 300 PPM [1]. As a time reference for comparison, Homo sapiens, the first modern humans, have evolved from their early hominid predecessors about 250,000 years ago; language was developed about 50,000 years ago and the great migration from Africa started about 70,000 years ago [2]. Mankind has always existed within this range of atmospheric CO<sub>2</sub>. Climate change impacts has multiple impacts that range from acidification of the oceans to melting of the polar caps. Furthermore, the greenhouse effect may make planetary and regional temperatures spiral out of control. And while there is no crystal ball to accurately predict the future, we know that the climate

balance that has allowed humans to thrive will be greatly disturbed. At a planetary level, this would be just one of many climate changes, and it is even likely that a percentage of the current species would adapt to survive a major climate shift. However, it is likely that humans are too dependent on the global ecosystem to survive such changes. Regardless, this is definitely a risk that is not worth taking.

### 2.3 Overview of the Energy Sector

Energy use is one of the major contributors to climate change. As a result, humankind needs to convert to low CO<sub>2</sub> emitting energy sources, preferably renewable ones, which are sustainable in the long run.

The world energy consumption can be divided into three categories: 50 % of thermal (heating and cooling), 30 % transport and 20 % electricity [3], as illustrated by Figure 5. These percentages have remained fairly stable for the past two decades. It is important to mention that from the segment with the highest renewable energy (RE) penetration is electricity at 26.4 %. On the other hand, transport is the segment that shows the lowest penetration at 3.3 %.

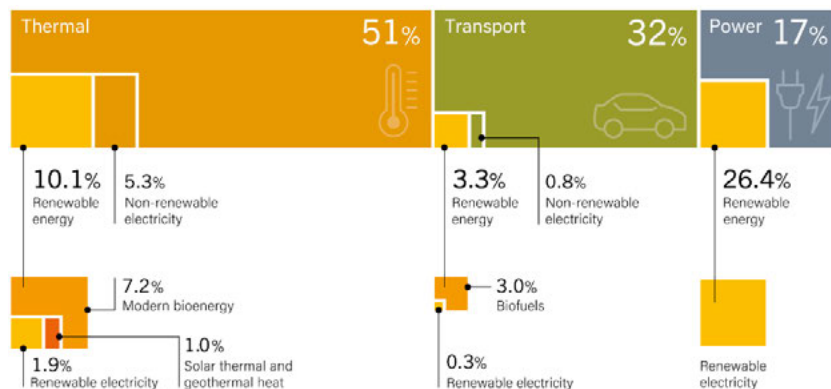


Figure 5. Breakdown of energy consumption and its sources [3].

Energy is used in two forms: heat and electricity. Figure 6 illustrates the shares of the different energy sources in world's final energy consumption.

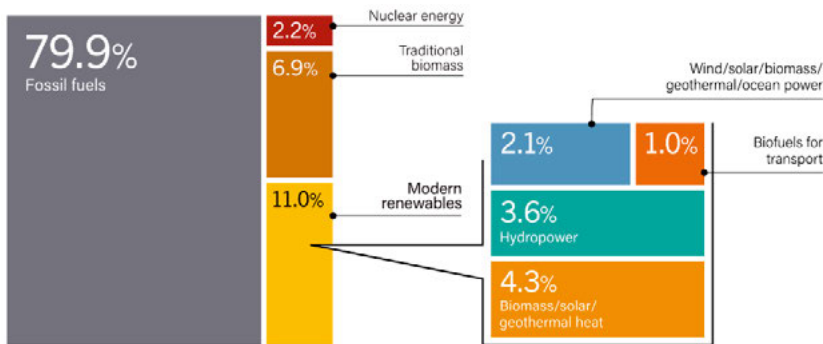


Figure 6. Estimated RE share of global final energy consumption in 2018 [3].

According to the REN21, renewable energy reports, in 2009, the share of renewable energy in the total energy usage of the world was 16 % [4]. In 2018, the same share was 17.9 % [5], this is a very slow progress that will not make it possible to reach the Paris Climate Accords. In the same period, modern renewables accounted for the bulk of the increase, from 6 % to 11 % of the world's energy usage. Traditional biomass relevance has decreased by 3.1 %, from 10 % to 6.9 % [6].

Regarding renewable electricity, the year of 2015 saw the largest increase ever, with 147 GW of total capacity added. This represented an increase of almost 9 % to a total installed capacity of 1849 GW [5]. Both Wind and Solar PV made record additions and together they made up 77 % of all renewable power capacity added in 2015 [5]. A major milestone achieved is the fact that today, the world adds more renewable power capacity annually than what it adds in net capacity from all fossil fuels combined. In fact, since 2015, renewables have accounted for 60 % of all net additions to global power generating capacity [5]. By the end of 2019, renewables featured 2600 MW of power generating capacity, which supplied 26 % of global electricity, with hydropower representing 16 %, as illustrated in Figure 7.

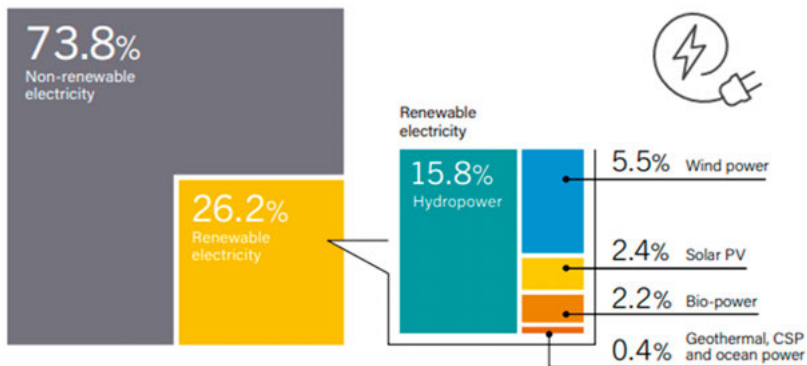


Figure 7. Estimated share of RE in Global Electricity Production in 2019 [3].



By 2040, it is expected that the cumulative growth of renewable energy will contribute to a total primary energy consumption of 50 % [7] [8].

## **2.4 Solar Energy: PV and Thermal collectors**

Energy from solar irradiance can be directly collected in two forms:

1. Solar Electricity
2. Solar Heat

### **2.4.1 Solar Electricity**

Solar Electricity is either produced by the photovoltaic (PV) effect or by the conversion of solar irradiation into high temperature heat, which is then used to drive a turbine that generates electricity. The latter process can only be achieved in large centralized power plants and is called Concentrated Solar Power (CSP).

In 2015, the total installed capacity of CSP was 5 GW, which compares to 227 GW of PV. As a comparison point, in 2015 alone, 50 GW of PV have been installed, which is 10 times the total installed capacity of CSP [5]. Although only 10 years ago, CSP was expected to become the mainstream of solar electricity production method, PV has managed to greatly surpass CSP having reached a total installed capacity that is 45 times higher. This is probably due to the simplicity and modularity of PV installations which overall has much lower capital requirements than CSP. However, thermal storage can help CSP to gain momentum, as it allows CSP to do baseload. In 2016, all CSP plants where built with storage [9].

The growth in PV has been so fast that capacity installed in the world in 2015 is nearly 10 times higher than the cumulative installed capacity of 2005 [8]. Figure 8 shows the top 10 countries in total installed capacity of PV. Germany has been the installed capacity leader for the past decade. However, in 2015, China took the lead [5] and, in 2016, Japan became second [9], making Germany become third. A major shift has also happened in PV production in the world. According to the REN21 2014 report: “Less than 10 years ago, almost all solar panels were produced in Europe, Japan, and the USA. In 2013, Asia accounted for 87 % of global production (up from 85 % in 2012) with China producing 67 % of the world total (62 % in 2012). Europe’s share continue to fall to 9 % while Japan remained at 5 % and the US at only 2.6 %” [10]. Experience from trends in similar technology indicate that such global supply chains are intrinsic for a maturing technology [11].

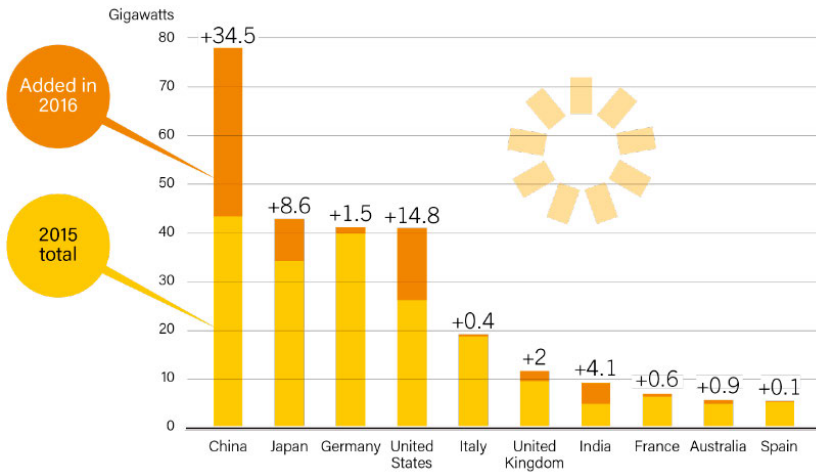


Figure 8. Installed capacity and new additions of PV in 2016 for the top 10 countries [9].

Moreover, it is important to note that several PV technologies exist with very different efficiencies and development stages. However, silicon solar cells are today the dominating PV technology with about 90 % of the PV market. Within this, monocrystalline silicon cells represent about 25 % of the world panel production in 2015 [12] [13] [14] [15].

It is also important to note that “Solar PV saw record additions and, for the first time, accounted for more additional power capacity (excluding decommissioned capacity) than any other renewable technology. Solar PV represented about 47 % of newly installed renewable power capacity in 2016, while wind and hydropower accounted for most of the remainder, contributing about 34 % and 15.5%, respectively” [9].

### 2.4.2 Solar Heat

Solar Heat or Solar Thermal (ST) is the process of converting solar irradiation into heat. A large number of different technologies exists ranging from uncovered flat plate collectors, to vacuum tube collectors or large tracking, concentrating solar collectors. These technologies produce heat at different temperatures and therefore have multiple applications in residential and industrial sectors.

Figure 9 displays the total installed capacity in 2016 of solar heating in the world at 456  $\text{GW}_{\text{th}}$ . For reference, one can compare to the 303  $\text{GW}_{\text{e}}$  of installed capacity PV [9], although it is fundamental to keep in mind that PV and ST have different capacity factors and that they produce energy with different values. The 456  $\text{GW}_{\text{th}}$  of ST are estimated to have produced 375 TWh of heat at different temperatures. At the same time, the 303  $\text{GW}$  of PV produced about 375 TWh of electricity [9].

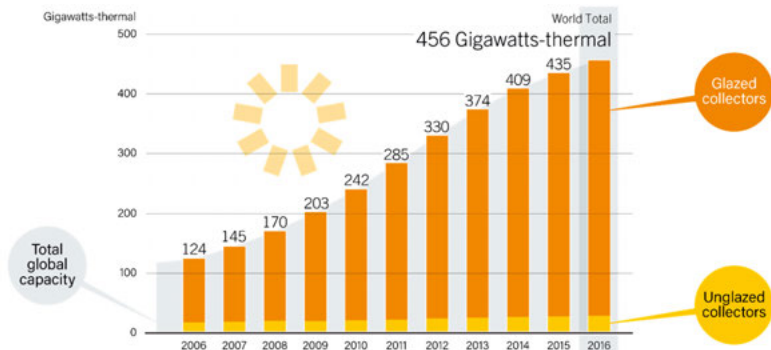


Figure 9. World Installed capacity of ST in 2016 [9].

In 2017, China alone has accounted for 75% of the total new additions. The Chinese market has been undergoing a change from small residential to large installations such as hotels or within the public sector [9]. In 2015, the installed capacity of ST collectors grew by 6.3 % (26 GW<sub>th</sub>) which is a significant growth reduction from previous years. As a comparison point, the installed capacity of PV is record-breaking, as it grew by 28% which corresponds to 50 GW [5].

As illustrated in Figures 9 and 10, over the past 10 years, total installed capacity of ST has roughly quadrupled while PV has been multiplied by a factor 45. However, although there is a difference of an order of magnitude between these two numbers, it is important to point out that PV started with a much lower base number from which it was easier to increase. Figure 10 shows how China is currently also dominating the solar thermal market having an installed capacity that is almost 20 times larger than the second world player, Turkey.

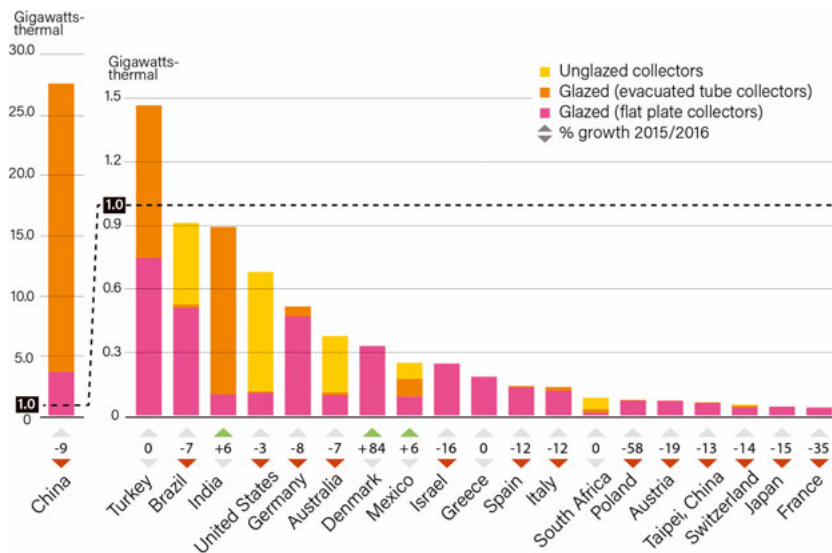


Figure 10. Installed capacity of ST in the top 20 countries in 2015 [9].

Finally, it is important to remember that the heat produced by ST can serve different purposes, as illustrated in Figure 11. Globally domestic hot water production, either for single or multi-family houses, is the main application for ST, although some economic regions install ST for different purposes.

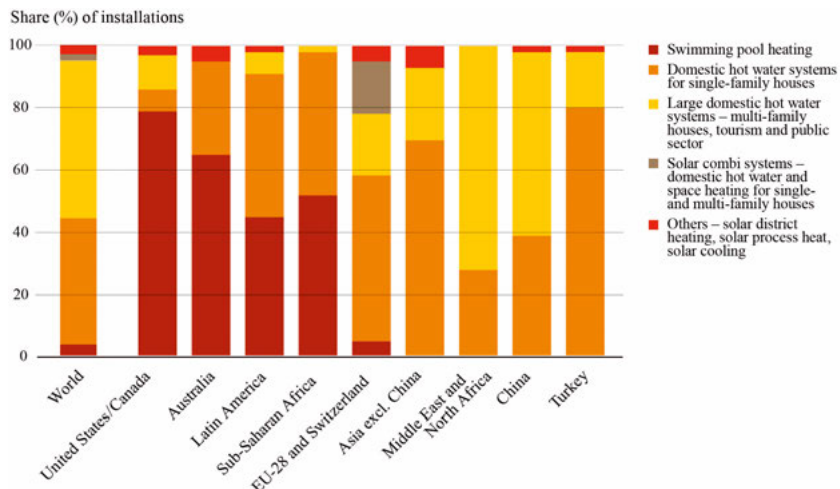


Figure 11. Solar Thermal Applications by economic region in 2015 [16].

## 2.5 Basics of Solar Energy: Differences between PV & ST

### 2.5.1 Comparing heat and electricity

Energy has many forms such as heat and electricity and comparing these different forms is not straightforward. Exergy – or the quality of energy – is of high relevance when discussing primary energy.

According to Carnot [17], if the reference temperature is 0 °C, heat at 75 °C can theoretically be converted to power with the following efficiency:

$$\eta = 1 - \frac{273}{273+75} = 0.216 \quad \text{eq. 1}$$

$$1 \text{ kWh}_{\text{electricity}} = \frac{1}{0.216} = 4.64 \text{ kWh}_{\text{heat}} \quad \text{eq. 2}$$

Similarly, according to Carnot, 1 kWh of electricity can be converted to heat at 75 °C with a heat pump.

$$COP = \frac{T_{\text{high}}}{T_{\text{high}} - T_{\text{low}}} = \frac{273+75}{75} = 4.64 \quad \text{eq. 3}$$

$$1 \text{ kWh}_{\text{el}} = 4.64 \text{ kWh}_{\text{heat}} \quad \text{eq. 4}$$

This is explained by  $COP = 1/\eta$ . However, in a real system, the COP is well below  $1/\eta$ . This means the ratio between the values have different numbers depending on the direction of conversion. This is one of the reasons why it is so difficult to define the values of primary energy factors.

### 2.5.2 The effect of solar irradiation in PV and ST collectors

Figures 12 and 13 show the effect of solar irradiation on both power output and efficiency for photovoltaics panels and solar thermal collectors, which is calculated according to a simplified model using the following formulae:

Photovoltaic panels:

$$P = I \times \eta \quad \text{eq. 5}$$

Solar thermal collectors:

$$P = \eta_0 \times I - ((U_1 + U_2 \times \Delta T) \times \Delta T) \quad \text{eq. 6}$$

where  $P$  is the power from the collector,  $I$  is the irradiance on to the plane,  $\eta$  is the efficiency of the PV panel,  $\eta_0$  is the optical efficiency of the thermal collector,  $U_1$  is the first order heat losses, and  $U_2$  is the second order heat losses. In equation 6, the heat loss value ( $U$ ) is divided into two components  $U_1$  and  $U_2$ .

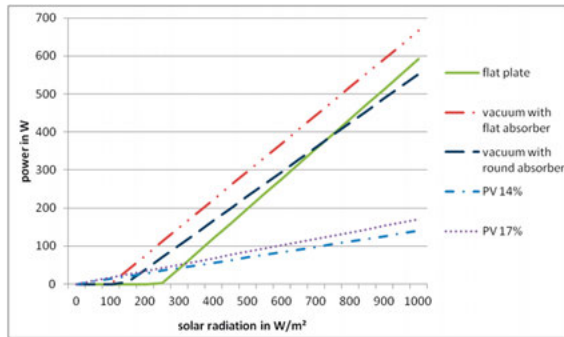


Figure 12. Impact of solar irradiation on power for PV & ST at  $\Delta T$  of 50 °C [1].

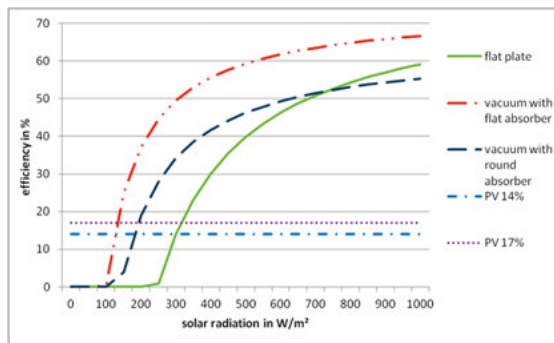


Figure 13. Impact of solar irradiation on efficiency for PV & ST at  $\Delta T$  of 50 °C [1].

The collector values used to plot the graphs in Figures 12 and 13 were taken from the market survey conducted for Paper I, which is shown in the results section. These efficiency values are for a standard thermal collector and are calculated based on the aperture area of collectors working with a  $\Delta T = (T_{med} - T_{ambient}) = 50$  °C, where  $T_{med} = (T_{in} + T_{out}) / 2$ . In this model, only the most relevant factors are taken into consideration. In reality, there are other factors to consider, such as a small efficiency dependence of Si solar cells on irradiation levels and spectral distribution [18] or an increase in the temperature of the solar cells that will lead to a decrease in solar cell efficiency of around -0,35 %/K for monocrystalline solar cells [19]. However, Figure 13 shows that, at a constant temperature, the efficiency of a PV system is almost independent of the solar irradiance, while the efficiency of solar thermal systems is strongly dependent, with the efficiency of a thermal collector often being zero at low solar irradiation intensities. This main point holds true even when the above factors are considered.

Another important point to mention is that system losses such as inverters, cabling, or piping were not considered, neither for ST nor PV.

### 2.5.3 The effect of temperature in PV and T collectors

Figure 14 shows the effect of operating temperature on the efficiency of solar panels, which was calculated using the equations 5 and 6. For PV panels, the cell temperature dependency was taken into account as described below.

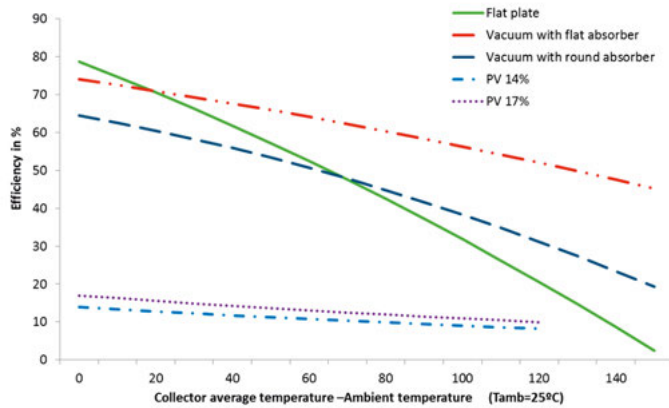


Figure 14. The impact of temperature in efficiency of PV & ST panels at a constant solar radiation of 1000W/m<sup>2</sup> [1].

As mentioned in the author's Paper I, the operational temperature of a PV panel varies according to how much solar irradiation is received and how much heat the panel dissipates, which is greatly influenced by factors like panel construction or type of installation (building integrated vs free standing). The operating temperature of a PV panel is defined by the nominal operating cell temperature (NOCT). In Figure 14, it was accepted that 120 °C was the maximum temperature for the PV panel since many panels stop working above that temperature due to the limitations of Ethylene Vinyl Acetate (EVA), which is the standard encapsulation methods for solar cells in PV [20]. Similar to PV panels, the operational temperature of an ST collector is also a function of solar irradiation and heat losses, however, in ST systems there is also a fluid that is extracting heat from the collector. This fluid can be water, glycol, or a special type of oil for collectors that work at high temperatures. The amount of heat that is transferred to the fluid depends on factors such as the temperature difference between the fluid and the collector, the ambient temperature, the characteristics of the fluid and the flow rate and type of flow [21].

A major difference between PV and ST panels is that in ST panels, the heat is carried from the collector to the tank, while in standard PV panels, the build-up of heat is passively dissipated. A similarity of both types of panels is that the efficiency goes up when the operating temperature is decreased.

### 2.5.4 Influencing factor: local climate

Weather conditions vary widely around the globe. Figure 15 from Paper I shows the variation of beam irradiation around the world, while Figure 16 dis-

plays the annual average temperature. Many other parameters, such as the median daily variation of temperature or the air humidity could be shown to illustrate these large variations. The numbers in Figure 15 show the percentage of beam irradiation out of the total solar irradiation normal to the ground, while the color reflects the total amount of solar irradiation. As it can be observed, the beam fraction is not dependent on latitude, although the total amount of solar irradiation generally increases at lower latitudes. The main influence on the beam fraction is the local climate [22].

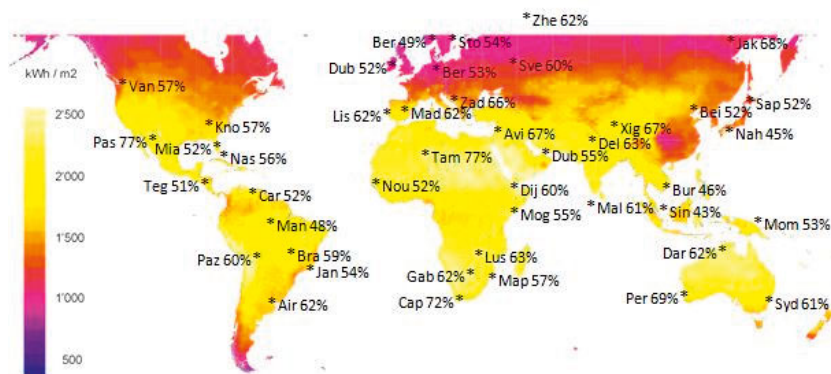


Figure 15: Percentage of beam in the total solar radiation (number) and total solar radiation in different locations (color) [1].

The percentage of beam irradiation in the total irradiation ranges from 43 % in Singapore to 77 % in El Paso and Tamanrasset. Singapore, Naha, Chon Buri, Manaus and Bergen are the only five cities where the diffuse irradiation represents more than 50 % of the annual solar irradiation at 0° tilt. The main reason for this effect is the presence of clouds [5]. Cities in Southeast Asia are affected by monsoons twice a year. Bergen has 200 rainy days over the year and a moderate climate [10]. Manaus, located close to the equator, is affected by a long rainy season which leads to the 48 % of beam in the total solar irradiation. Whereas in desert areas like El Paso or Tamanrasset, the climate is dry, and the ratio reaches up to 77 %. As expected, the countries closer to the equator show the warmest average temperatures around the world which go up to 30 °C. However, there are exceptions like La Paz with 8.2 °C which owes its low annual temperature to the high altitude. At high altitudes, the layer of atmosphere is less dense which leads to both higher temperature variations (the atmosphere has less capacity of retaining the heat) and higher solar irradiation (the atmosphere is less dense and absorbs less solar irradiation). The main cause of low temperatures at higher latitudes is the angle at which the incoming rays are incident on the ground. Although, normal solar irradiance on a perfect sunny day is close to 1000 W/m<sup>2</sup> anywhere in the world at sea level, if the irradiance has a lower angle, that irradiance will be spread over a larger area. This effect is also known as the cosine effect [23].





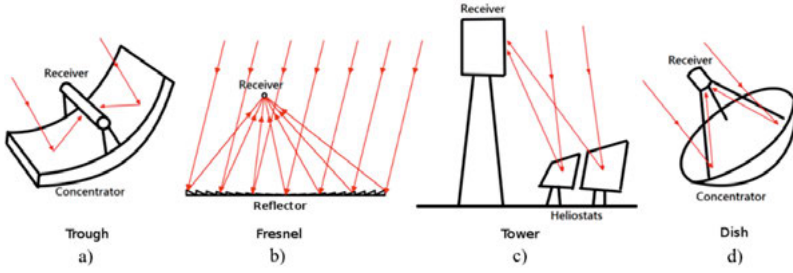


Figure 17. Four technologies for high concentration solar energy. Linear concentrators: Trough (a) and Fresnel (b). Punctual concentrators: Tower (c) and Dish (d) [29].

### 2.6.1 Concentration factor

The concentration factor ( $C_i$ ) is one of the most important parameters for concentrators. It is defined as the ratio between the effective area of the aperture and the area of the receiver.

$$C_i = \frac{\text{Aperture Area}}{\text{Receiver Area}} \quad \text{eq. 7}$$

A collector with no concentration is said to have a concentration factor of 1, while a collector that has an aperture area ( $A_a$ ) that is twice the receiver area ( $A_r$ ) is said to have a concentration factor of 2 [27]. Designs with higher concentrations require tracking the sun, while low concentration designs may dispense tracking. Tracking increases the amount of solar irradiation that reaches the receiver but also increases cost, complexity and may not suit all locations.

The equations below [30] [21] present the relation between the acceptance angle and the geometric concentration ratio for an ideal two-dimensional (linear) non-truncated CPC and for an ideal three-dimensional (circular):

$$C_{linear} = \frac{1}{\sin(\theta_c)} \quad \text{eq. 8}$$

$$C_{circular} = \frac{1}{(\sin(\theta_c))^2} \quad \text{eq. 9}$$

Where  $\theta_c$  is the half acceptance angle of the sun's disk.

According to the laws of thermodynamics, a reflection can never be brighter nor hotter than its original object. The above equations give the maximum concentration factor  $C$  for respectively a linear and a circular concentrator [21].

$$C_{linear\_max} = \frac{1}{\sin \theta_c} \quad \text{eq. 10}$$

$$C_{circular\_max} = \frac{1}{(\sin \theta_c)^2} \quad \text{eq. 11}$$

Since  $\theta_c = 4.65 \text{ mrad}$ , the maximum concentration factor for a linear concentrator is 215 while for a circular concentrator it is 46 248. Additionally, assuming theoretical conditions (assuming no atmosphere, 100% reflectance, etc.), the maximum temperature that these concentrators could reach would be 5 800 K, which is the temperature of the sun. However, it is more common to see the concentration ratio  $C$  being defined by the component properties (eq. 8), since this is simpler.

Another important point to consider is that diffuse radiation is accepted at a ratio of  $1/C$ . This means that for a concentrating of 10, only 10% of the diffuse light will be redirected to the receiver. This means that concentration is not suitable for locations with high shares of diffuse radiation.

### 2.6.2 Compound Parabolic Collectors

This thesis work will focus on CPCs, which are non-imaging type concentrators that do not necessarily require a tracking system due to the ability of reflecting both beam and diffuse irradiation to the receiver. The incidence angle for these concentrators make them attractive due to system simplicity, flexibility, and cost effectiveness [30] [31] [32]. CPC concentrators combine two parabolic reflectors that can be symmetric or asymmetric. Each reflector has its own focal length ( $F$ ) at the lower edge of the other parabola, as shown in Figure 18.

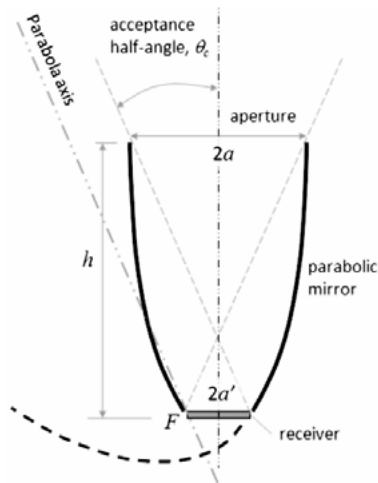


Figure 18. Cross section of a symmetrical non-truncated CPC [15].

The angle between the axis of the collector and the line connecting the focus of one of the parabolas with the opposite edge of the aperture is called acceptance half-angle ( $\theta_c$ ). The relationship between the size of the aperture ( $2a$ ), the size of the receiver ( $2a'$ ) and the acceptance half-angle is expressed through eq. 12.

$$2a' = 2a \sin\theta_c \quad \text{eq. 12}$$

Knowing the concentration ratio, it is possible to obtain the acceptance half-angle [15]:

$$C_i = \frac{2a}{2a'} = \frac{1}{\sin\theta_c} \quad \text{eq. 13}$$

The following equations establish the relation between the focal distance of the side parabola and the acceptance half-angle ( $\theta_c$ ), receiver size, and height of the CPC ( $h$ ) [21]:

$$f = a'(1 + \sin\theta_c) \quad \text{eq. 14}$$

$$h = \frac{f \cos\theta_c}{\sin^2\theta_c} \quad \text{eq. 15}$$

CPC concentrators are designed so that each ray coming into the aperture with an angle smaller than  $\theta_c$  is reflected onto the receiver at the base. However, when the angle of the ray is greater than  $\theta_c$ , the ray will be reflected back to the atmosphere. Figure 19 shows this effect:

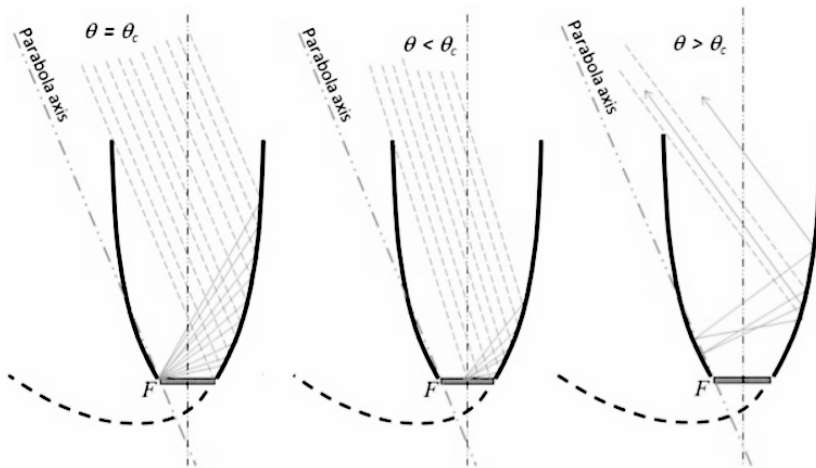


Figure 19. Reflection of the light rays directed to the CPC concentrator at different angles [21].

## 2.7 Maximum Reflector Concentration Design

The Maximum Reflector Concentration (MaReCo) is a patented design that originated from research done at Vattenfall. It is based on an asymmetric truncated CPC collector with a bi-facial flat receiver that is specially adapted for the asymmetric annual solar irradiation profiles of high latitudes. A solar thermal collector with this reflector design will be able to better match the asymmetric heat production profile existent at high latitudes to the nearly constant

annual demand profile of a Domestic Hot Water (DHW) consumption and thus, be able to prevent stagnation damage [33].

The general design of the MaReCo reflector trough consists of two parabolic reflectors with their individual optical axis tilted  $20^\circ$  and  $65^\circ$  from the horizon, collecting all the incoming irradiation between a solar altitude of  $20^\circ$  and  $65^\circ$  as shown in Figure 20 [34] [35].

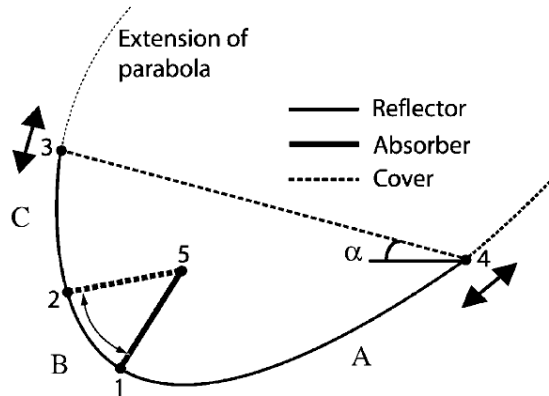


Figure 20. Sketch of the basic MaReCo design [34] [33].

The optical axis from the parabola defines the lower and upper acceptance angles. The reflector is divided in sections A, B, and C. Section A comprises the lower parabola that goes from point 1 to 4. The optical axis is placed along the upper acceptance angle and its focal point on point 5, the upper part of the receiver. Section B is characterized by the circular section between points 1 and 2. Solar irradiation that reaches this reflector is directed towards the backside of the receiver, which is between point 1 and 5 in this case. However, the receiver could be located anywhere in section B, for example a receiver between points 2 and 5 (the dotted line) would also be possible and have the same theoretical performance. Section C is an upper parabolic reflector that reaches between points 2 and 3, with an optical axis along the lower acceptance angle and focus at point 5.

The dotted line that goes between points 3 and 4 defines a truncation point for both parabolas. However, several other truncations points are possible with a considerable impact on the annual performance of the solar collector.

Additional MaReCo design configurations were created for different situations such as stand-alone, roof integrated and wall mounted [31]. These configurations are described below in more detail.

### 2.7.1 The stand-alone MaReCo

Figure 21 shows the stand-alone MaReCo design. This design has a concentration factor ( $C_i$ ) of 2.2, an upper acceptance angle of  $65^\circ$ , a lower acceptance angle of  $20^\circ$  and an aperture tilt of  $30^\circ$ [31].

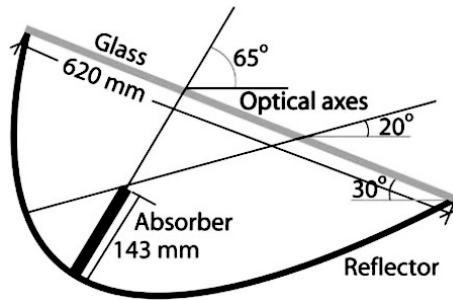


Figure 21. Section of the stand-alone MaReCo for Stockholm conditions, a stationary asymmetrically truncated wedge CPC with acceptance angles between  $20^\circ$  and  $65^\circ$ . Aperture tilt  $30^\circ$  [33] [34].

### 2.7.2 The roof integrated MaReCo

The roof integrated MaReCo design features a cover glass that starts immediately where the circular section of the MaReCo ends, as shown in Figure 22. This MaReCo design has a concentration factor ( $C_i$ ) of 1.5 and is meant for a roof with a tilt of  $30^\circ$  [31]. All the irradiation normal to the cover glass is accepted.

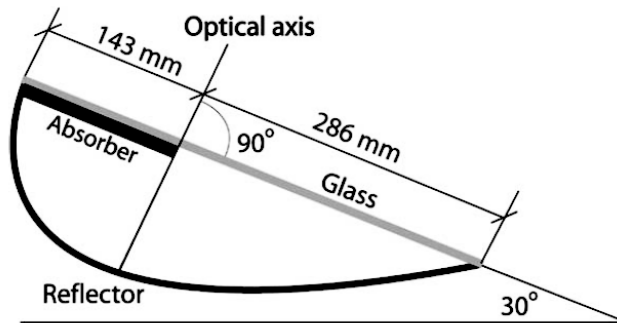


Figure 22. Section of the roof integrated MaReCo design for a tilt of  $30^\circ$  and optical axis  $90^\circ$  from the cover glass [33].

Other roof integrated MaReCo designs were developed, such as the roof MaReCo for east/west and the spring/fall MaReCo. The roof MaReCo for east/west is illustrated in figure 23. It has a  $C_i = 2.0$  and was designed for roof facing west. It accepts irradiation between  $20^\circ$  and  $90^\circ$ , meaning that the optical axis is  $70^\circ$  from the cover glass [31].

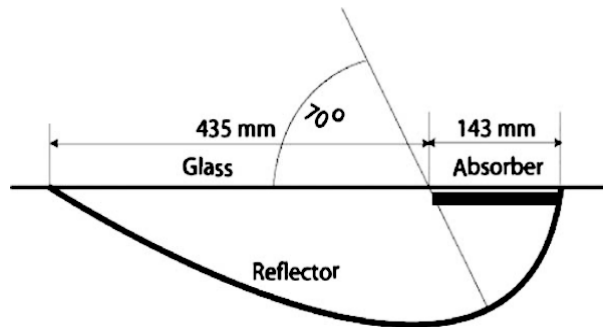


Figure 23. Section of the east/west roof MaReCo [26].

The roof spring/fall MaReCo has been designed for a roof tilted  $30^\circ$  and it has an optical axis at  $45^\circ$  from the horizon. Direct solar irradiation that hits the reflector at an angle smaller than  $15^\circ$  normal to the aperture will be reflected out of the collector, which prevents overheating. This design has a concentration factor ( $C_i$ ) of 1.8 [29] and is displayed in Figure 24.

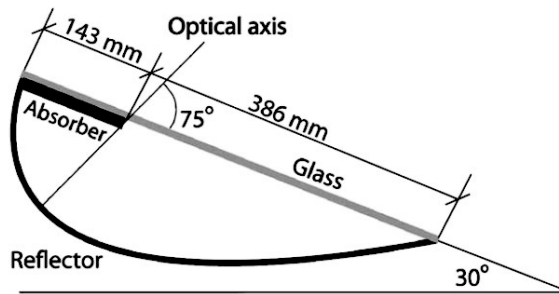


Figure 24. Section of the spring/fall MaReCo [26].

### 2.7.3 The wall MaReCo

This design was developed for a south facing wall, in order to be an alternative to standard installations. Figure 25 shows the design which has a  $C_i = 2.2$ , an optical axis at  $25^\circ$  from the horizon and an acceptance angle between  $25^\circ$  and  $90^\circ$  from the horizon [31].

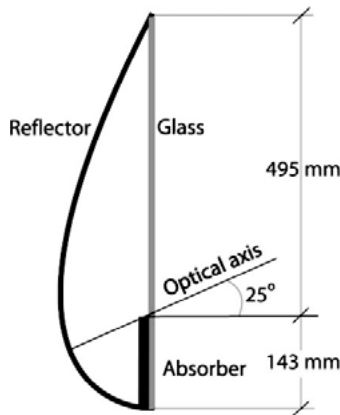


Figure 25. Section of the wall MaReCo [26].

## 2.8 PVT collectors: Advantages and Disadvantages

As mentioned in the author's Papers IV and I, photovoltaic/thermal (PVT) collectors produce both heat and electricity. The main benefits of PVT collectors when compared to standard thermal and photovoltaic (PV) solar collectors are:

- The possibility of increasing cell efficiency by reducing the cell operational temperature, when hot water is extracted at low temperatures. In order for this to be achieved, it is fundamental that the panel design is able to transfer the heat from the cells to the cooling liquid efficiently as well as homogeneously;
- The production of one unit of PVT uses fewer raw materials than an equivalent area of both thermal and photovoltaic panels. This is expected to enable a lower production cost per kWh of annual produced combined heat and electricity;
- Reduction of the installation area, which enables the deployment of more installed capacity per roof area and should also lower the installation costs.

The main disadvantages for PVTs are the higher complexity in both for collector production and installation and the reduced market share, since it requires customers that need both the heat and the electricity. Table 2 summarizes the advantage and disadvantages of PVT collectors.



Table 2. *Advantages and disadvantages of PVT collectors (Vs T and PV).*

Topic	Advantage	Disadvantage
<b>Efficiency</b>	Most PVT designs yield a higher energy output per m <sup>2</sup> compared to PV and T, in particular for low temperatures. Possibility to increase electrical efficiency by cooling.	Heat has more value at high temperatures, but this reduces electrical output.
<b>Collector Cost</b>	Fewer raw materials needed to obtain the same energy output	Early in the Technology curve. Cell Price has greatly decreased making PVT (and T) less attractive.
<b>Production Cost</b>	-	Increased complexity at production level
<b>Installation Cost /Reliability</b>	Lower installation cost can be achieved due to smaller area for the same output	Increased complexity at installation level
<b>Market</b>	-	Niche Market (require need for heat and electricity)

## 2.9 C-PVT collector: Advantages and Disadvantages

As mentioned in the author's Papers IV and I, some PVT manufacturers combine the concept with concentration to reduce the usage of PV cells and thermal absorber material. Concentration carries a penalty due to extra reflection losses from the reflector and a lower Incident Angle Modifier (IAM) profile for stationary collectors. However, at the same time, it reduces the number of expensive components (solar cells, receiver and/or selective surface) [25]. In the end, it is often a trade between the positive effect of lowering the collector cost and the negative effect of lowering output per square meter. The steep decrease in the price of silicon solar cell made C-PV concepts less popular. However, in PVT collectors, the receiver becomes more expensive again, since it features both the thermal absorber and the PV cells.

Concentration also helps to reduce the heat losses by reducing the heat emitting area. This way, concentration also allows higher temperatures to be achieved, although higher temperatures will reduce the efficiency of the solar cells in PVT collectors [25].

Some of the disadvantages of concentration are aesthetics (bulkier), higher stagnation temperatures, which lead to more expensive components, and lower power density [25].

Factors such as simplicity or aesthetics are important for solar costumers; however, in the end, the most important number in solar remains the cost per kWh of heat and electricity produced, including the installation cost [36]. Regarding this, the Table 3 illustrates a list of the factors but does not quantify their importance.

Table 3: *Advantages and disadvantages of C-PVT collectors (vs PVT).*

Topic	Advantage	Disadvantage
<b>Electrical Output/Cost</b>	Concentration can reduce the costs, as it increases the output per cell area	Concentration reduces output per glazed area
<b>Thermal Output/Cost</b>	Concentration reduces heat losses and increases range of possible working temperatures	Higher stagnation temperatures (=more expensive materials or complex systems to cope)
<b>Product Complexity</b>	-	Concentration increases complexity
<b>Aesthetics</b>	-	Concentration can reduce aesthetic value

## 2.10 The impact of shading and concentration in PV panels and solar thermal collectors

Shading can be caused by many factors, such as buildings, trees or other solar panels. As mentioned in the author's Papers IV and I, shading has a considerably different impact on PV panels than on thermal collectors. In PV modules, the solar cells are commonly connected in series, thus one shaded solar cell will reduce the output of the whole string. Bypass diodes can be used to mitigate this effect by allowing current to flow in a different path at the expense of a minor fraction of the total power. However, the introduction of diodes increases both assembly time and material cost, which leads to increased overall costs. On the other hand, diodes also prevent hotspots that can destroy PV panels [37] [38]. In thermal collectors, the decrease in power produced due to shading is approximately proportional to the shaded area. Thus, shading clearly has a much bigger impact on PV panels than thermal collectors [I].

Non-uniform concentration is a feature of all compound parabolic concentrators (CPC) [21] [30] [39]. Its effects are similar to partial shading. For a PV panel, differential illumination levels in the cells increases the series resistance losses. However, the most significant losses are at a string level when at least one of the series connected cells has a lower illumination level which reduces the current in the whole string [39] [I] [IV]. This lower illumination level is often caused by shading from the collectors' box frame or the lack of reflector. In other words, in a stationary CPC, the transversal shading impacts all cells in a string and does not cause one cell to generate more current than another, which means that the losses are almost proportional to the shaded area. On the other hand, the longitudinal shading causes the edge cells to receive lower illumination than the rest of the series connected cells, which greatly amplifies the effect of shading. Hence, non-uniform illumination is considerably more critical for PV panels than for solar thermal.

The analyzed PVT design includes a stationary CPC concentrator. For this reason, the study on shading was mainly focused on the electrical part of an asymmetric compound parabolic concentrating (CPC) photovoltaic/thermal hybrid (PVT).

## 2.11 First Look at the Solarus C-PVT

Over time, Solarus has developed several versions of its C-PVT, which have been analyzed during this thesis. For simplicity, this section will only detail the latest version of the Solarus collector which is called Power Collector (PC) [40]. Figure 26 shows the PC with a gross area of 2.57 m<sup>2</sup>:



Figure 26. The latest version of the Solarus C-PVT, the Power Collector.

However, all versions of the Solarus C-PVT solar collector can be divided into two defining components: The collector box and the PVT receiver, both of which are presented in the next chapters.

### 2.11.1 The Collector Box

Figure 27 shows a breakdown of all components of the collector.

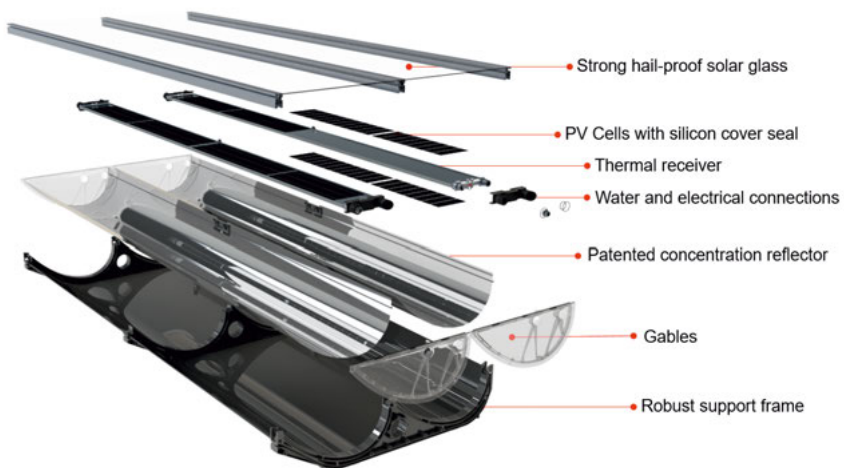


Figure 27. Solarus C-PVT PC components profile.



Figure 28. Profile view of the Solarus C-PVT showing the transparent gable and the black plastic frame.

The collector box has four main components:

- A black plastic solid frame that provides structural support to the reflector;
- A gable with a reported 90% of transparency made from Polymethylmethacrylate (commonly known as PPMA) that seals the collector sides as shown in Figure 25;
- A 4mm tempered solar glass with anti-reflective treatment (on both sides) to reach a 1.5% absorptance and 2% of reflectance per side;
- A 0.4mm aluminium reflector with a total reflectance of 92 % (in the visible range it is 95 %) at an air mass of 1.5, according to the standard ASTM 891-87 (or ASTM E1651 for the visible range). Specular reflectance was 91 %, tested according to the ISO 7668;
- The reflector geometry is a variation of the roof integrated Maximum Reflector Concentration (MaReCo), as illustrated in Figure 29. The concentration factor is 1.7.

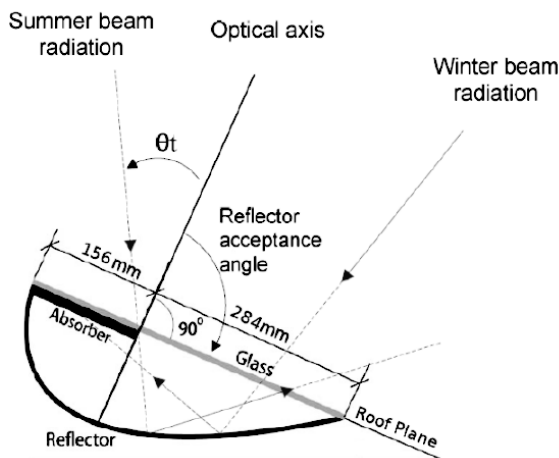


Figure 29. Cross section of the MaReCo collector [29].

### 2.11.2 Receiver core

The receiver core is the heart of the Solarus C-PVT. It is 2321 mm long, 165 mm wide and 14.5 mm thick. As seen in Figure 30, there are solar cells on both sides of the Aluminium receiver. These solar cells are encapsulated by highly transparent silicon with a reported transparency of 97%.



Figure 30. Solarus bifacial receiver.

The receiver consists of an Aluminium receiver with eight elliptical channels as shown in Figure 31. The cooling fluid flows through eight channels in order to extract heat from the collector. The core is made of extruded Aluminium.

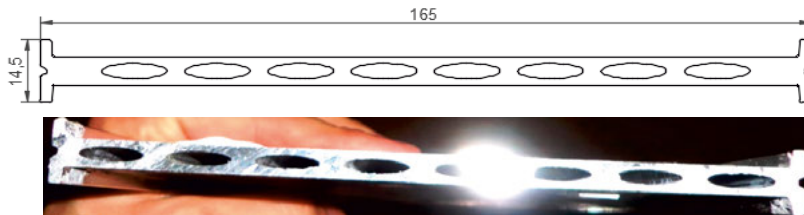


Figure 31. Side view of the receiver core with the elliptical channels. Dimensions in mm.

The collector uses standard monocrystalline solar silicon cells with an efficiency of 19.7%. The cell string layout consists of four cell strings on the bottom and four on the top of the receiver (Figure 32).

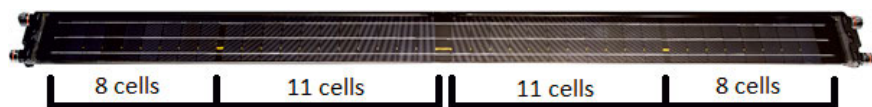


Figure 32. Receiver, showing 4 cell strings and its distribution in the receiver.

Each side of the receiver has 38 cells, and the receiver in total has 76 cells. Each collector has two receivers, and 152 cells. The dimension of each cell is 52 mm long, 156 mm wide, and 0.2 mm thick, with a nominal efficiency of 19.7%. The manufacturer obtains these cells by cutting standard size cells (156mm\*156mm) into three pieces of the same size. The reason for this is to

reduce the current in the strings, which reduces the resistance losses. The resistance losses in ribbons that connect the cells is particularly important for the performance. Lastly, Figure 33 illustrates an overview of the collector, the position of the cells and the thermal receiver, as well as how the sunlight reaches both the front and back side of the receiver.

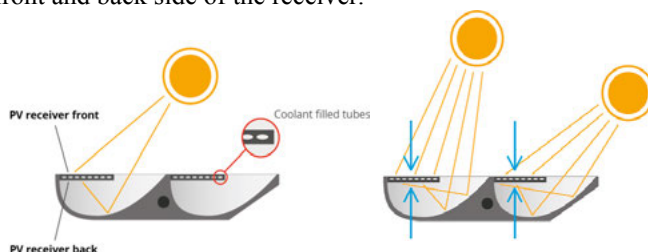


Figure 33. Key features of the Solarus C-PVT technology [40].

### 2.11.3 Systems Integration of the Solarus C-PVT

The Solarus C-PVT collector produces heat and electricity, therefore, only costumers that have a need for both are suitable. The most common system in which a Solarus collector can be utilized is in a hotel using the heat to cover the DHW demand and feeding the electricity to the grid for a fee. Solarus is currently focusing mainly on this market. However, other systems are possible. Figure 34 shows a system that can produce heat, cooling and electricity.

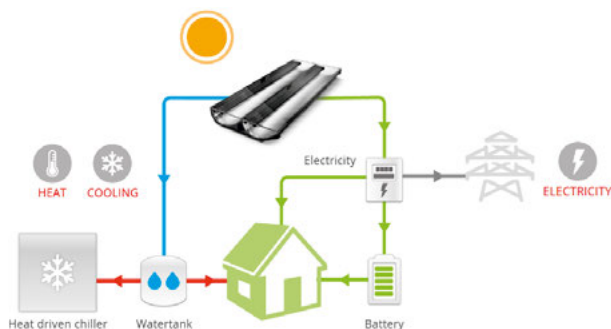


Figure 34. Sketch of a possible Solarus system providing heat, cooling and electricity to a household [40].

Besides these three applications, the manufacturer is looking into options to provide four other applications: (i) steam; (ii) desalination; (iii) water purification; (iv) pool heating.



Figure 35. Possible applications for the PC [40].

## 2.12 PVT Market Overview

Within this thesis, a large market study to the available PVT technologies has been carried out and is displayed in Tables 4 to 7.

Table 4. Overview of the PVT market, detailing brands, dimensions and price in 2018.

Technology	Company & panel model	Country	Price [€/m <sup>2</sup> gross]	Size (m <sup>2</sup> )			Thickness (mm)
				Gross	Aperture	Absorber	
C-PVT	SOLARUS - PC	SE	253	2.57	2.31	0.65	241
PVT w/airgap	Solimpeks - Volter powertherm	TR	243	1.43	1.42	1.40	105
PVT w/ airgap	Grammer SolarTwinSolar Compact 2.0	DL	705	2.01	1.60		138
PVT w/ airgap	Ecomesh by EndeF	ES	366	1.63			104
PVT w/out air-gap	SOLAIRE 2G S.A.S DualSUN - DS250M	FR	436	1.64	1.58		45
PVT w/out air-gap	Fototherm - Module FT220Cs	IT		1.61	1.59	1.59	41
PVT w/out air-gap	Fototherm - Module 235 Cs	IT		1.61	1.59	1.59	41
PVT w/out air-gap	Fototherm - Module FT250Cs	IT		1.61	1.59	1.59	41
PVT w/out air-gap	Fototherm - Module 255 Cs	IT		1.61	1.59		41
PVT w/out air-gap	Fototherm - Module 260 Cs	IT		1.61	1.59		41
PVT w/ airgap	Fototherm - Module 265 Cs	IT		1.61	1.59		41
PVT w/out air-gap	Fototherm - FT295AL	IT	299	1.64	1.58		51
PVT w/out air-gap	Fototherm - FT310AL	IT	302	1.64	1.58		51
PVT w/out air-gap	Solator GmbH - PVTHERMAU 280	AT		1.64			40
PVT w/out air-gap	Solator GmbH - PVTHERMAU 300	AU		1.64			35
PVT w/out air-gap	Solvis	HR		1.65	1.48		
PVT w/out air-gap	FDE Solar	IT	222	1.65	1.48		40

Table 5. Overview of the PVT market, detailing brands, dimensions and price in 2018 (Continuation).

Technology	Company & panel model	Country	Price [€/m <sup>2</sup> gross]	Size (m <sup>2</sup> )			Thickness (mm)
				Gross	Aperture	Absorber	
PVT w/out air-gap	Meyer Burger Hybrid 260/900	CH		1.64			
PVT w/out air-gap	Solimpeks - Volther powervolt	TR	263	1.37	1.36	1.30	90
PVT w/out air-gap	MillenniumSolar - MSS-MIL-PVT-195W-M03	IL	166	1.28			40
PVT w/out air-gap	RES Energy - RES-PV++300	DL	364	1.65			40
PVT	TESZEUS (240P, 250P, 280P, 300P)						50
PVT (w/heat pump)	Triple Solar	NL		1.97	1.91		58
PVT	Solimpeks Volther PowerHybrid	TR					
PVT	Helios Technology Module I3A235P	IT		1.63	1.60	1.49	
PVT	Helios Technology Module I3A225P	IT		1.63	1.60	1.49	
PVT	Helios Technology Module I3A250P	IT		1.63	1.60	1.49	
PVT	TES Solar	CN		1.69	1.60	1.57	
PVT	3S Photovoltaics Meyer Burger	CH		1.65			
PVT	Sun System	BG		1.63	1.62		
PVT	Minimise Generation Power Hybrid (240,200,180)	UK		1.29	1.26 56	1.26	
PVT	Naked Energy	UK		0.65	0.64		
PVT	Smart Clima Solar PVT	SI		1.66			
PVT	Ensol	PL	198	2.02	1.86		
PVT	SunDrum	USA	Variable	Variable			
Thermal	TVP Solar - MT-Power	CH		1.96	1.84		



Table 6. Overview of the PVT market from 2018, detailing brands, PV & ST performance parameters and weight. Note: Bolded values are taken from the solar Keymark database, while the remaining values are taken from the manufacturer's website.

COMPANY & PANEL MODEL		PHOTOVOLTAIC PART							THERMAL PART							Weight (kg)			
		Cell type		Current (A)		Voltage (V)		Power peak (W)	Efficiency (%)	Absorber	Pressure (bar)	Stagnation Temperature (C)	Gross area parameters				Aperture area parameters		
				Isc	Imp	Voc	Vmp						$\eta_0$	$a_1$ (W/m <sup>2</sup> K)	$a_2$ (W/m <sup>2</sup> K <sup>2</sup> )		$b_u$ (s/m)	$b_1$ (W/m <sup>2</sup> K)	$b_2$ (W/m <sup>2</sup> K)
Solarus Power Collector	Front	3.1	2.8	48.1	40	270	12.0	Al	10	180	47	3.40	0.03				65		
	Back	4.5	3.9	48.1	40.0														
Solimpeks - Volter powertherm	Mono	5.6	5.2	45.2	32.7	180	16.0	Cu	10	135	48.6	4.0	0.07				34		
Grammer SolarTwinSolar 2.0										130		3.2	0.03				45		
EndeF Ecomesh	Poly	8.6	8.0	36.7	28.9	240	14.4	Cu	6			2.6	0.01				45		
DualSUN DS250M	Mono	9.3	8.8	38.9	32.0	280	17.2	Cu	12	75	47.5	9.1	0	0.028	12.1	1.84	33		
Fototherm - Module FT220C's	Poly	8.1	7.5	36.6	29.2	220	15.5	Al		85	55.9	9.1	0				27		
Fototherm - Module 235 Cs	Poly	8.5	7.9	36.9	29.8	235	15.5	Al		85	55.9	9.1	0				27		
Fototherm - Module FT250C's	Poly	8.9	8.3	37.2	30.1	250	15.5	Al		85	55.9	9.1	0				27		
Fototherm - Module 255 Cs	Poly	9.0	8.4	37.4	30.2	255	15.8	Al		85	55.9	9.1	0				27		
Fototherm - Module 260 Cs	Poly	9.1	8.6	37.5	30.4	260	16.2	Al		90	55.9	9.1	0				27		
Fototherm - Module 265 Cs	Poly	9.2	8.7	37.7	30.6	265	16.5	Al		90	55.9	9.1	0				27		
Fototherm - FT295AL	Mono	9.9	9.4	39.3	31.3	295	18.0	Cu		94	51.4	7.5	0	0.035	6.1	1.47	32		
Fototherm - FT310AL	Mono	10.0	9.6	39.4	31.2	310	18.3	Cu		94	51.4	7.5	0	0.035	6.1	1.47	32		
Solator GmbH - PVTHERMAU 280	Mono	9.6	9	38.5	31.2	280	17.1	Cu	3 to 6	80	49.9	11.8	0	0.067	10.7	1.10	28		
Solator GmbH - PVTHERMAU 300	Mono	9.9	9.4	39.5	32.2	300	18.5	Cu	3 to 6	80	49.9	11.8	0	0.067	10.7	1.10	28		
Solvis										90				0.035	8.2	1.55			
FDE Solar										90				0.035	8.2	1.55			
Meyer Burger Hybrid 260/9000	Poly	8.8	8.3	37.7	30.0	250	15	Cu/Al		69	57.6	14.1	0	0.064	12.5	1.63			
						260													

Table 7. Overview of the PVT market from 2018, detailing brands, PV & ST performance parameters and weight (Continuation). Note: Bolded values are taken from the solar Keymark database, while the remaining values are taken from the manufacturer's website.

COMPANY & PANEL MODEL	PHOTOVOLTAIC PART						THERMAL PART						Weight (kg)				
	Cell type	Current (A)		Voltage (V)		Power peak (W)	Efficiency (%)	Absorber	Pressure (bar)	Stagnation Temperature (C)	Gross area Parameters			Aperture area Parameters			
		Isc	Imp	Voc	Vmp						$\eta_0$	$a_1$ (W/m <sup>2</sup> K)		$a_2$ (W/m <sup>2</sup> K <sup>2</sup> )	bu (s/m)	b1 (W/m <sup>2</sup> K)	b2 (W/m <sup>2</sup> K)
Solimpeks - Volther powervolt	Mono	5.6	5.2	45.2	36.5	200	17.8	Cu	10	101	47.6	8.4	0.59				24
MillenniumSolar - PVT-195W-M03	Mono	5.7	5.6	48.6	36.1	195	17.4										23
RES Energy - RES-PV++300	Mono	9.7	9.2	39.9	32.5	300	18.2										23
TESZEUS 240P	Poly	8.5	8.0	37.0	30.2	240		Cu/Al		60							
TESZEUS 250P	Mono	9.5	8.4	36.5	29.8	250		Cu/Al		60							
TESZEUS 280P	Poly	8.4	7.8	44.3	36.1	280		Cu/Al		60							
TESZEUS 300P	Mono	8.9	8.1	44.5	37.1	300		Cu/Al		60							
Triple Solar	Mono	9.5	9.1	48.0	37.6	340	17.5		6	50							32
Solimpeks - Volther PowerHybrid	HIT	5.9	5.5	52.4	43.7	240	21.6	Cu		101							26
Helios Technology - I3A235P	Poly	8.3	7.7	37.3	30.7	235	14.4	Al	2 to 10	70							
Helios Technology - Module I3A225P	Poly	8.1	7.6	37.2	29.6	225	13.8	Al	2 to 10	70							
Helios Technology - Module I3A250P	Poly	8.6	8.0	37.7	31.3	250	15.3	Al	2 to 10	70							
TES Solar	Mono	5.3	4.9	59.9	50.8	250	17.7	Cu/Al		85	52.2						28
3S Photovoltaics - Meyer Burger	Mono	9.7	9.1	39.8	31.4	285	17.4		6	80							29
Sun System	Poly	8.5	7.8	37.2	30.6	240	16.4	Cu/Al		85		9.1	0				28
Minimise Generation Power Hybrid	Mono	5.9	5.5	52.4	43.7	240	19.0	Al	10	93	53.4	8.4	0.59				26
Naked Energy	Mono	12.0	11.5	8.0	6.2	71					37.6	1.3	0.006				
Smart Clima Solar PVT	Poly	9.0	8.1	37.4	30.7	250	16	Al		85							30
Ensol	Poly	8.8	8.2	45.3	36.8	300		Al	6	≤60							
SunDrum	Any	They use an attachable thermal case which can fit at the back of a traditional PV module (the module length is adjustable). The nominal thermal power mentioned is 400W.															

### 3 Method Overview

A combination of complementary methods was used in order to answer the research questions.

The main method utilized was collector testing on a large number of different C-PVT collector prototypes that were built for this thesis. The testing results were complemented with four types of simulations:

- Winsun, in order to obtain annual output;
- Raytracing with Tonatiuh, for characterizing the current reflector and comparing different reflector geometries;
- LTSpice, for analyzing the impact of different string layouts;
- Thermal simulations using software such as COMSOL and ANSYS, which were mainly used for determining heat conduction and convection but also to investigate thermal expansion.

The papers on LTSpice and thermal simulation are included in the extended paper list of the author, but are not covered in detail in this thesis due to space limitations, although their results are present in Chapter 5, 6 and 8. Furthermore, a novel methodology for assessing the impact of the electrical shading in solar panels using a combination of Tonatiuh and Matlab has been developed and will be published in future work. This method uses the limiting cell to estimate the output of the panel.

A market survey was conducted for PV, and ST, and a new ratio was defined, as a way to compare different collectors. Additionally, a large PVT market survey has been carried out and presented in Section 2.12.

Furthermore, several analyses of C-PVT installations were carried out by the author. Papers 12, **31**, 26, 36, 37, 38, and 40 [41], [42] evaluate different types of PV, ST and PVT systems. However due to space limitation in the thesis, these analysis are not included in the thesis, although this work influenced the perspective of the author.

Tables 8 to 13 detail most of the full size prototypes built, tested or analyzed by the author over the past years. Since the number of tested prototypes reached 29, it is not possible to discuss all the results individually in this thesis, however the analysis of the measurement results from these prototypes has influenced the direction of this thesis as a whole.

Table 8. Overview of all tested collector prototypes within the PhD framework.

Location of test		Lund	Maputo, MZ	Gothenburg	Arizona, US	Älvkarleby
Name in	Thesis	<b>V0</b>	<b>V1</b>	-	-	-
	Paper/ report	<b>Hybrid</b>	<b>Hybrid</b>	T	Hybrid	Bifacial
Collector Area (m <sup>2</sup> )		<b>2.31</b>	<b>2.31</b>	2.39	2.39	1.20
Reflector Geometry		<b>MaReCo</b>	<b>MaReCo</b>	MaReCo	MaReCo	MaReCo
Collector Box		<b>Initial version with wood</b>	<b>Initial version with wood</b>	Initial version with wood	First plastic version	First plastic version
Collector Side Frame		<b>Large</b>	<b>Large</b>	Large	Large	Large
Receiver Core Type		<b>Hollow Aluminium</b>	<b>Hollow Aluminium</b>	Sunstrip Sputtered Absorber	Solid Aluminium	Glass
End Gables		<b>Reflective</b>	<b>Reflective</b>	Reflective	Reflective	Reflective
Soldering Process		<b>Manual</b>	<b>Manual</b>	-	Manual	Manual
Connection between	Strings	<b>Parallel</b>	<b>Parallel</b>	Series	-	-
	Receiver Sides	<b>Parallel</b>	<b>Parallel</b>	Series	Series	-
Trough 1	N of strings/ receiver side	<b>2</b>	<b>2</b>	-	2	1
	Diodes/ receiver side	<b>0</b>	<b>1</b>	-	2	0
	Cell Type	<b>Mono</b>	<b>Mono</b>	-	Mono	Bifacial Mono
	Cell Size (mm)	<b>70*145</b>	<b>26*148</b>	-	26*148	26*148
	String Layout	<b>26-26</b>	<b>38-38</b>	-	38-38	12
	Silicone	<b>Transparent</b>	<b>Transparent</b>	-	Transparent	Transparent
Trough 2	N of strings/ receiver side	<b>2</b>	<b>2</b>	-	2	-
	Diodes/ receiver side	<b>0</b>	<b>1</b>	-	2	-
	Cell Type	<b>As T1</b>	<b>As T1</b>	-	Mono	-
	Cell Size (mm)	<b>As T1</b>	<b>As T1</b>	-	26*148	-
	String Layout	<b>As T1</b>	<b>As T1</b>	-	38-38	-
	Silicone	<b>As T1</b>	<b>As T1</b>	-	Transparent	-

Legend: Collectors in bold are considered to be the most relevant for this thesis.

Table 9. Overview of all tested collector prototypes within the PhD framework (Continuation I).

Location of test		Älvkarleby	Dalarna	Gävle	Gävle	Dalarna
Name in	Thesis	V2	V3	V4	V5	-
	Paper/ report	V1	V2	V3	-	T
Collector Area (m <sup>2</sup> )		2.39	2.39	2.39	2.39	2.39
Reflector Geometry		MaReCo	MaReCo	MaReCo	MaReCo	MaReCo
Collector Box		First plastic version	Improved Version	Improved Version	Improved Version	Improved Version
Collector Side Frame		Large	Thinner	Thinner	Thinner	Thinner
Receiver Core Type		Hollow Aluminium	Solid Aluminium	Solid Aluminium	Solid Aluminium	Sunstrip
End Gables		Reflective	Transparent/ Reflective	Transparent	Transparent	Transparent
Soldering Process		Manual	Manual	Manual	Manual	-
Connection between	Strings	Parallel	Parallel	Parallel	Parallel	-
	Receiver Sides	Parallel	Parallel	Parallel	Parallel	-
Trough 1	N of strings/ receiver side	2	2	2	2	-
	Diodes/ receiver side	2	2	2	2	-
	Cell Type	<b>Mono 18.6%</b>	<b>Mono 18.6%</b>	<b>Mono 18.6%</b>	<b>Mono 18.6%</b>	-
	Cell Size (mm)	<b>26*148</b>	<b>26*148</b>	<b>26*148</b>	<b>52*148</b>	-
	String Layout	<b>38-38</b>	<b>38-38</b>	<b>38-38</b>	<b>19-19</b>	-
	Silicone	<b>Transparent</b>	<b>Transparent</b>	<b>Transparent</b>	<b>Transparent</b>	-
Trough 2	N of strings/ receiver side	2	2	2	2	-
	Diodes/ receiver side	2	2	2	2	-
	Cell Type	<b>As T1</b>	<b>As T1</b>	<b>Mono 18.6%</b>	<b>Mono 18.6%</b>	-
	Cell Size (mm)	<b>As T1</b>	<b>As T1</b>	<b>52*148</b>	<b>26*148</b>	-
	String Layout	<b>As T1</b>	<b>As T1</b>	<b>19-19</b>	<b>38-38</b>	-
	Silicone	<b>As T1</b>	<b>As T1</b>	<b>Transparent</b>	<b>Transparent</b>	-

Legend: Collectors in bold are considered to be the most relevant for this thesis.

Table 10. Overview of all tested collector prototypes within the PhD framework (Continuation II).

Location of test		Dalarna	Gävle	Gävle	Gävle	Lisbon, PT
Name in	Thesis	-	V6	V7	V8	-
	Paper/ report	PVT	PVT	PVT	PVT	PVT
Collector Area (m <sup>2</sup> )		2.39	<b>2.39</b>	<b>2.39</b>	<b>2.39</b>	2.39
Reflector Geometry		MaReCo	<b>MaReCo</b>	<b>MaReCo</b>	<b>MaReCo</b>	MaReCo
Collector Box		Improved Version	<b>Improved Version</b>	<b>Improved Version</b>	<b>Improved Version</b>	Improved Version
Collector Side Frame		Thinner	<b>Thinner</b>	<b>Thinner</b>	<b>Thinner</b>	Thinner
Receiver Core Type		Solid Aluminium	<b>Solid Aluminium</b>	<b>Solid Aluminium</b>	<b>Solid Aluminium</b>	Solid Aluminium
End Gables		Transparent	<b>Transparent</b>	<b>Transparent</b>	<b>Transparent</b>	Transparent
Soldering Process		Manual	<b>Manual</b>	<b>Manual</b>	<b>Automatic</b>	Automatic
Connection between	Strings	Parallel	<b>Parallel</b>	<b>Parallel</b>	<b>Parallel</b>	Parallel
	Receiver Sides	Parallel	<b>Parallel</b>	<b>Parallel</b>	<b>Parallel</b>	Parallel
Trough 1	N of strings/ receiver side	2	<b>2</b>	<b>2</b>	<b>4</b>	4
	Diodes/receiver side	2	<b>2</b>	<b>2</b>	<b>4</b>	4
	Cell Type	Mono 18.6%	<b>Mono</b>	<b>Mono</b>	<b>Poly</b>	Mono
	Cell Size (mm)	26*148	<b>26*148</b>	<b>52*148</b>	<b>52*148</b>	52*148
	String Layout	38-38	<b>38-38</b>	<b>19-19</b>	<b>4-15-15-4</b>	8-11-11-8
	Silicone	Transparent	<b>Red</b>	<b>Red</b>	<b>Transparent</b>	Transparent
Trough 2	N of strings/ receiver side	2	<b>2</b>	<b>4</b>	<b>4</b>	4
	Diodes/ receiver side	2	<b>2</b>	<b>4</b>	<b>4</b>	4
	Cell Type	Mono 18.6%	<b>Mono</b>	<b>Mono</b>	<b>Mono</b>	Mono
	Cell Size (mm)	26*148	<b>52*148</b>	<b>52*148</b>	<b>52*148</b>	52*148
	String Layout	38-38	<b>19-19</b>	<b>4-15-15-4</b>	<b>5-14-14-5</b>	8-11-11-8
	Silicone	Transparent	<b>Red</b>	<b>Red</b>	<b>Transparent</b>	Transparent

Legend: Collectors in bold are considered to be the most relevant for this thesis.

Table 11. Overview of all tested collector prototypes within the PhD framework. (*Continuation III*)

Location of test		Dalarna	Gävle	Gävle	Gävle	Gävle
Name in	Thesis	<b>V9</b>			<b>V10</b>	<b>V11</b>
	Paper/ report	<b>PC</b>	Prototype	Prototype	<b>Prototype</b>	<b>Prototype</b>
Collector Area (m <sup>2</sup> )		<b>2.57</b>	0.91 Top & 1.22 Bottom	2.42	<b>2.57</b>	<b>2.57</b>
Reflector Geometry		<b>MaReCo</b>	PP 1.2 & 1.6	PP 1.66 & 1.25	<b>DM 1.6 &amp; 1.4</b>	<b>DM 1.6</b>
Collector Box		<b>Improved Version</b>	Wooden Prototype	Wooden Prototype	<b>Wooden box w/ open back</b>	<b>Wooden Prototype</b>
Collector Side Frame		<b>No frame</b>	No frame	No frame	<b>No frame</b>	<b>No frame</b>
Receiver Core Type		<b>Solid Aluminium</b>	Solid Aluminium	Glass	<b>Solid Aluminium</b>	<b>Solid Aluminium</b>
End Gables		<b>Transparent</b>	Transparent	Transparent	<b>Transparent</b>	<b>Transparent</b>
Soldering Process		<b>Automatic</b>	Automatic	Manual	<b>Automatic</b>	<b>Automatic</b>
Connection between	Strings	<b>Series</b>	Series	-	<b>Series</b>	<b>Series</b>
	Receiver Sides	<b>Parallel</b>	Parallel	Series	<b>Parallel</b>	<b>Parallel</b>
Trough 1	N of strings/ receiver side	<b>4</b>	4	1	<b>4</b>	<b>4</b>
	Diodes/receiver side	<b>4</b>	4	0	<b>4</b>	<b>4</b>
	Cell Type	<b>Mono</b>	Mono	Bifacial Mono	<b>Mono</b>	<b>Mono</b>
	Cell Size (mm)	<b>52*156</b>	52*156	39*156	<b>52*156</b>	<b>52*156</b>
	String Layout	<b>8-11-11-8</b>	8-11-11-8	24	<b>8-11-11-8</b>	<b>8-11-11-8</b>
	Silicone	<b>Transparent</b>	Transparent	Transparent	<b>Transparent</b>	<b>Transparent</b>
Trough 2	N of strings/ receiver side	<b>4</b>	4	3	<b>4</b>	<b>4</b>
	Diodes/ receiver side	<b>4</b>	4	0	<b>4</b>	<b>4</b>
	Cell Type	<b>Mono</b>	Mono	Bifacial Mono	<b>Mono</b>	<b>Mono</b>
	Cell Size (mm)	<b>52*156</b>	52*156	156*156	<b>52*156</b>	<b>52*156</b>
	String Layout	<b>8-11-11-8</b>	8-11-11-8	3-6-3	<b>8-11-11-8</b>	<b>8-11-11-8</b>
	Silicone	<b>Transparent</b>	Transparent	Transparent	<b>Transparent</b>	<b>Transparent</b>

Legend: Collectors in bold are considered to be the most relevant for this thesis.

Table 12. Overview of all tested collector prototypes within the PhD framework (*Continuation IV*).

Location of test		Lisbon, PT	Nicosia, CY	Nicosia, CY	Nicosia, CY	Nicosia, CY
Name in	Thesis	<b>V18</b>	-	<b>V15</b>	<b>V16</b>	<b>V13</b>
	Paper/ report	<b>Thermal</b>	Thermal	<b>Thermal</b>	<b>Thermal</b>	<b>1S Inlay</b>
Collector Area (m <sup>2</sup> )		<b>2.57</b>	2.57	<b>2.57</b>	<b>2.57</b>	<b>2.57</b>
Reflector Geometry		<b>MaReCo</b>	MaReCo	<b>MaReCo</b>	<b>MaReCo</b>	<b>MaReCo</b>
Collector Box		<b>Improved Version</b>	Improved Version	<b>Improved Version</b>	<b>Improved Version</b>	<b>Improved Version</b>
Collector Side Frame		<b>No frame</b>	No frame	<b>No frame</b>	<b>No frame</b>	<b>No frame</b>
Receiver Core Type		<b>Solid Aluminium with glue selective surface</b>	Solid Aluminium with glue selective surface	<b>Solid Aluminium sputtered</b>	<b>Solid Aluminium anodized</b>	<b>Solid Aluminium with glue selective surface</b>
End Gables		<b>Transparent</b>	Transparent	<b>Transparent</b>	<b>Transparent</b>	<b>Transparent</b>
Soldering Process		-	-	-	-	<b>Automatic</b>
Connection between	Strings	-	-	-	-	<b>Series</b>
	Receiver Sides	-	-	-	-	-
Trough 1	N of strings/ receiver side	-	-	-	-	<b>4</b>
	Diodes/receiver side	-	-	-	-	<b>4</b>
	Cell Type	-	-	-	-	<b>Mono</b>
	Cell Size (mm)	-	-	-	-	<b>52*156</b>
	String Layout	-	-	-	-	<b>8-11-11-8</b>
	Silicone	-	-	-	-	<b>Transparent</b>
Trough 2	N of strings/ receiver side	-	-	-	-	-
	Diodes/ receiver side	-	-	-	-	-
	Cell Type	-	-	-	-	-
	Cell Size (mm)	-	-	-	-	-
	String Layout	-	-	-	-	-
	Silicone	-	-	-	-	-

Legend: Collectors in bold are considered to be the most relevant for this thesis.



Table 13. Overview of all tested collector prototypes within the PhD framework (*Continuation V*)

Location of test		Nicosia, CY	Nicosia, CY	Nicosia, CY	Rapperswill, CH
Name in	Thesis	<b>V12</b>	<b>V14</b>	<b>V17</b>	<b>V19</b>
	Paper/ report	<b>1S Sputtered</b>	<b>PC</b>	<b>PC</b>	<b>Thermal</b>
Collector Area (m <sup>2</sup> )		<b>2.57</b>	<b>2.57</b>	<b>2.57</b>	<b>2.57</b>
Reflector Geometry		<b>MaReCo</b>	<b>MaReCo</b>	<b>MaReCo</b>	<b>MaReCo</b>
Collector Box		<b>Improved Version</b>	<b>Improved Version</b>	<b>Improved Version</b>	<b>Improved Version</b>
Collector Side Frame		<b>No frame</b>	<b>No frame</b>	<b>No frame</b>	<b>No frame</b>
Receiver Core Type		<b>Solid Aluminium sputtered</b>	<b>Solid Aluminium anodized</b>	<b>Solid Aluminium anodized</b>	<b>Solid Aluminium with glue selective surface</b>
End Gables		<b>Transparent</b>	<b>Transparent</b>	<b>Transparent</b>	<b>Transparent</b>
Soldering Process		<b>Automatic</b>	<b>Automatic</b>	<b>Automatic</b>	-
Connection between	Strings	<b>Series</b>	<b>Series</b>	<b>Series</b>	-
	Receiver Sides	-	<b>Parallel</b>	<b>Parallel</b>	-
Trough 1	N of strings/ receiver side	<b>4</b>	<b>4</b>	<b>4</b>	-
	Diodes/receiver side	<b>4</b>	<b>4</b>	<b>4</b>	-
	Cell Type	<b>Mono</b>	<b>Mono</b>	<b>Mono</b>	-
	Cell Size (mm)	<b>52*156</b>	<b>52*156</b>	<b>52*156</b>	-
	String Layout	<b>8-11-11-8</b>	<b>8-11-11-8</b>	<b>8-11-11-8</b>	-
Silicone		<b>Transparent</b>	<b>Transparent</b>	<b>Transparent</b>	-
Trough 2	N of strings/ receiver side	-	<b>4</b>	<b>4</b>	-
	Diodes/ receiver side	-	<b>4</b>	<b>4</b>	-
	Cell Type	-	<b>Mono</b>	<b>Mono</b>	-
	Cell Size (mm)	-	<b>52*156</b>	<b>52*156</b>	-
	String Layout	-	<b>8-11-11-8</b>	<b>8-11-11-8</b>	-
Silicone		-	<b>Transparent</b>	<b>Transparent</b>	-

Legend: Collectors in bold are considered to be the most relevant for this thesis.

## 4 Winsun

### 4.1 Method

#### 4.1.1 Definition of the ratio between ST and PV

Although PV and ST produce different types of energy, they are often competing among themselves. This is not only because the investment capacity is limited, but also because of other limiting factors such as energy demand and roof space. Additionally, as mentioned earlier, electricity can be converted into heat and vice-versa. However, electricity can be converted into heat at an efficiency of almost 100 % while heat conversion into electricity has a much lower efficiency and requires more complex equipment". [43]

The previously described large global climate variations, lead to significant differences in the performance of solar systems around the globe. Moreover, each type of solar system has a different response to these variations. Therefore, it makes sense to develop a ratio that quantifies the difference in annual energy output between standard solar thermal collectors and PV panels for different locations. This ratio can be useful, for example, to support the decision between installing ST or PV, when combined with other local information such as the value of heat and electricity for a specific location and application, the system complexity and efficiency, and even factors such as the knowledge of local installers or the available offer. This way, the ratio was defined, as following:

$$\begin{aligned} & \text{Ratio Between ST and PV} \\ & = \frac{\text{Annual Energy Output per m2 of ST collector}}{\text{Annual Energy Output per m2 of PV panel}} \end{aligned} \quad \text{eq. 16}$$

This ratio was calculated for the different solar systems based on the results obtained from a market analysis. Two types of PV panels were considered: average monocrystalline and polycrystalline panels. Two main types of ST panels were considered: Flat Plate and Vacuum Tube. Additionally, for ST collectors, the following average collector temperatures were investigated: 30 °C, 50 °C and 80 °C.

The annual energy outputs used to calculate the above ratio were obtained through Winsun simulations.

This ratio was then calculated and plotted on the world map for a clear visualization. The three above mentioned temperatures were plotted but only the middle temperature (50 °C) is shown since it was found to be the most relevant.

#### 4.1.2 Market survey

A detailed two step market survey was carried out to investigate the prices and standard panel characteristics for both PV and ST. The first assessment was carried in 2013 while the second step was carried out in 2021. The ST survey included a total of 90 collectors of three types: flat plate, vacuum tube with flat absorber, and vacuum tube with round absorber. This survey comprised of 43

companies in 16 countries. All collectors in this study passed the standard EN 12975 [26] and an average for the test results available in the solar Keymark website was made. The PV survey looked into 150 different PV panels from 35 companies from nine countries. Additionally, the 10 largest cell manufacturers were also analyzed and the average efficiency.

#### 4.1.3 Winsun Simulations

Winsun is a TRNSYS based solar simulation software that was developed by Bengt Perers and Björn Karlsson at Lund University [I]. Winsun can simulate both the annual performance of an ST and PV panel. The inputs and outputs of the program are described in Figure 36. A new collector file was made for Winsun based on the market survey findings regarding the standard collector characteristics per aperture area. The values for efficiency and heat losses were taken from the market study and are presented in the results. For all performed simulations, the collector was stationary at a tilt equal to the latitude of the selected city. Simulations were performed for 66 cities around the world in a range of different latitudes and climatic regions in order to obtain a good visualization of the variation of the ratio in the world map.

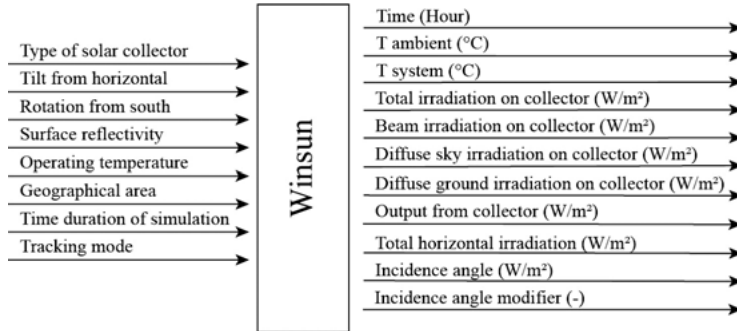


Figure 36. Winsun's inputs and outputs [44].

Winsun was used to simulate the performance of PV and ST panels over the year and provide the annual output per m<sup>2</sup> of aperture area.

The following formulas are used by the Winsun to calculate the annual output [21]:

$$Q = \eta_{0b} \times K_b(\theta) \times G_b + \eta_{0b} \times K_{diffuse} \times G_d - U_1(T_m - T_a) - U_2(T_m - T_a)^2 \quad \text{eq. 17}$$

$$K_b(\theta) = 1 - b_0 \times \frac{1}{\cos(\theta) - 1} \quad \text{eq. 18}$$

## 4.2 Results

### 4.2.1 Market Survey

A detailed two-step market survey was carried out to investigate the prices and average panel characteristics for both PV and ST. The first assessment was carried in 2013, while the second step was carried out in 2021. The ST survey included a total of 90 collectors of 3 types: flat plate, vacuum tube with flat absorber, vacuum tube with round absorber. This survey comprised 43 companies in 16 countries. All collectors in this study have undergone testing under the standard EN 12975 [26] and an average for the test results was made based on the available data from the solar keymark website. This average is displayed in Table 14.

Table 14. Values for different  $T$  collectors expressed per absorber area, aperture area and gross area [1].

Type of Panel	ABSORBER			APERTURE			GROSS		
	$\eta_0$ (%)	U1 (W/m <sup>2</sup> K)	U2 (W/m <sup>2</sup> K)	$\eta_0$ (%)	U1 (W/m <sup>2</sup> K)	U2 (W/m <sup>2</sup> K)	$\eta_0$ (%)	U1 (W/m <sup>2</sup> K)	U2 (W/m <sup>2</sup> K)
Flat Plate	80.3	3.967	0.009	78.6	3.877	0.008	71.3	3.526	0.008
Vacuum with round absorber	74.1	2.088	0.009	64.4	1.809	0.008	39.9	1.117	0.005
Vacuum with flat absorber	82.0	1.626	0.004	74.0	1.468	0.003	54.9	1.085	0.003

The PV survey looked into 150 different PV panels from 35 companies of 9 countries. Additionally, the ten largest cells manufacturers were also analyzed and the average efficiency is shown in Table 15.

Table 15. Average efficiency for monocrystalline and polycrystalline modules [1].

Type of PV panel	Efficiency
Monocrystalline	16.5%
Polycrystalline	14.6%

Finding out the price of the ST and PV panels at customer level proved to be a more complex process than expected and some uncertainty lingered, as the price variations between obtained quotes were considerably large. Another important factor to take into account is the size of the order, as prices tend to go down with larger volumes. In the present market study, the ST order size is two panels, while the PV size is 50 panels. Tables 16 to 18 describe the prices

that were found in the market study. In Table 16, the costs of system components, installation and VAT relates to the Swedish market (both for PV and ST).

Table 16. Price of a ST collector in € per gross and aperture area [1] (at system level).

Type of ST panel	Flat Plate		Vacuum Tube (Flat absorber)		Relative difference FP to VT	
	2013	2021	2013	2021	2013	2021
Sale with VAT (consumer) in €/m <sup>2</sup> gross	158	141	166	154	5 %	9 %
Sale with VAT (consumer) in €/m <sup>2</sup> aperture	187	167	275	255	32 %	34 %
Relative difference gross to aperture area	15 %	15 %	40 %	40 %	-	-

Table 17. PV Price from cell to panel in €/Wp [1] (not including system & installation).

Type of PV panel	Cost in 2013 (€/Wp)		Cost in 2020 (€/Wp)		Price Decrease	
	Poly	Mono	Poly	Mono	Poly	Mono
Cell price	0.27	0.31	0.09	0.12	3	2.6
Panel sale price with VAT	0.52	0.56	0.17	0.21	3	2.5
Price increase from cell to panel	1.9	1.8	1.9	1.8	-	-

Table 18. Price comparison PV to ST (including system components, installation and VAT) at consumer level in EU (custom cleared) [1].

Type of Solar panel	Price €/m <sup>2</sup> aperture		Comparison to Poly		Comparison to VT	
	2013	2021	2013	2021	2013	2021
ST Flat Plate	187	167	61 %	67 %	68 %	65 %
ST Vacuum Tube with flat absorber	275	255	89 %	102 %	100 %	100 %
PV Polycrystalline	282	212	100 %	100 %	103 %	83 %
PV Monocrystalline	308	250	91 %	85 %	112 %	98 %

The survey shows that in a space of less than 8 years, the efficiency of PV cells and panels has increased by roughly 20 %. More striking is what happened in terms of price on both PV panels and cells, which have gone down drastically in terms of €/Wp. This is a factor 3 reduction for polycrystalline and around 2.6 for Monocrystalline cells. Monocrystalline cells enjoy a higher market demand, and this might be the reason why the reduction is less pronounced for mono when compared to poly. It is also important to point out that the PV price reduction on a per m<sup>2</sup> basis is not so pronounced as in €/Wp, as the increase in efficiency offsets partially the cost reduction in €/Wp. Both the cost reduction and efficiency increase for ST are far less pronounced.

#### 4.2.2 Winsun Simulations

For all locations and for a working temperature of 50 °C, the ST panel always produces more energy than PV. As expected, this is also true for a ST operating temperature of 30 °C. However, at an operating temperature of 80 °C, there were two locations in this study (in Russia and Norway) where the flat plates performed worse than PV. Unlike flat plates, vacuum tube performed better than PV in all simulated locations and temperatures. This was due to a lower heat loss factor. Additionally, globally, vacuum tubes normally outperform flat plate collector per aperture area for temperatures of 50 °C and 80 °C. However, for a temperature of 30 °C, the flat plate sometimes outperformed the vacuum tube with flat absorber, especially in warm locations. This is due to the fact that flat plates have 5 % higher peak efficiency.

The ratio between PV and ST ratio was then plotted on a world map for a clear visualization. Since the most commonly used ST temperature is 50 °C, only this temperature was plotted. This way, four world maps were created. The maps show how much more energy ST produces compared to PV. In general, the ratio increases when the latitude decreases. Some examples of this ratio are shown in Table 19 for three cities at three different latitudes: close to the Equator, the Tropic of Capricorn and the Arctic Circle.

Table 19. Irradiance (kWh/m<sup>2</sup>), panel outputs (kWh/m<sup>2</sup>) and ratios ST/PV [1].

City and Country	Tilt (°)	Solar Radiation (kwh/m <sup>2</sup> )		Output (kwh/m <sup>2</sup> )				Ratio			
		Total	Beam	PV14,6%	PV16,5%	Flat Plate at 50°C	Vacuum Tube with flat absorber at 50°	Flat Plate 50°C to PV14,6%	Flat Plate 50°C to PV16,5%	Vacuum 50°C to PV14,6%	Vacuum 50°C to PV16,5%
Nairobi, Kenya	1	1930	1089	259	293	950	1141	3,7	3,2	4,4	3,9
Rio de Janeiro, Brazil	23	1771	953	236	267	893	1054	3,8	3,3	4,5	3,9
Umea, Sweden	64	1273	600	163	185	429	629	2,6	2,3	3,8	3,4

As shown in the Table 19, the ratio between a flat plate working at 50 °C and a polycrystalline PV panels varies considerably around the world. In Nairobi, a flat plate will produce 3.7 times more energy than a polycrystalline PV panel, while for Rio de Janeiro this ratio is 3.8. These two cities are an example that the ratio does not always increase when moving towards the equator. In Umea, the ratio is considerably lower at 2.6.

Figure 37 to 40 illustrate how the ratio varies throughout 66 locations all over the world. All legends have the same scale for the next four maps. The scale goes from green (stronger ST location) to blue (weaker ST location). The black color is an extreme case, which only happens in two specific situations in northern Russia.

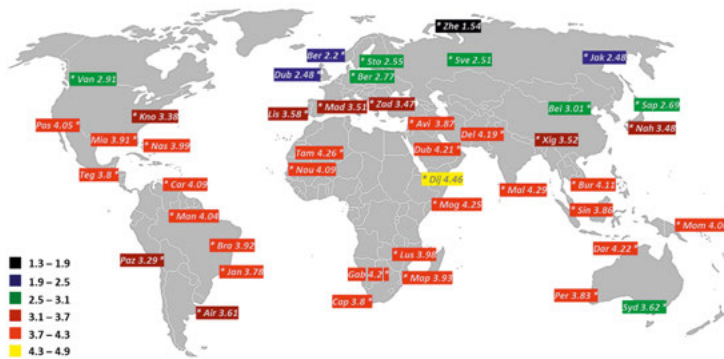


Figure 37. Ratio Flat plate 50 °C to PV polycrystalline [1].

Figure 37 shows the ratio between a flat plate collector working at an average temperature of 50 °C and a polycrystalline PV. The lowest ratio of 1.54 at the coldest place with the highest latitude. On the opposite end, the city of Djibouti at latitude of 12° reaches a ratio of 4.46 signaling a high over performance of ST facing PV.

Singapore is an exception, since it has a considerably lower ratio than the other cities at similar latitudes. This is mostly caused by a long, cloudy rain season, which also lowers the ratio of beam to total irradiation as shown previously. All four maps show that for locations with high diffuse irradiation or low ambient temperature, the ratio goes down which means that ST is producing less energy in comparison to PV.

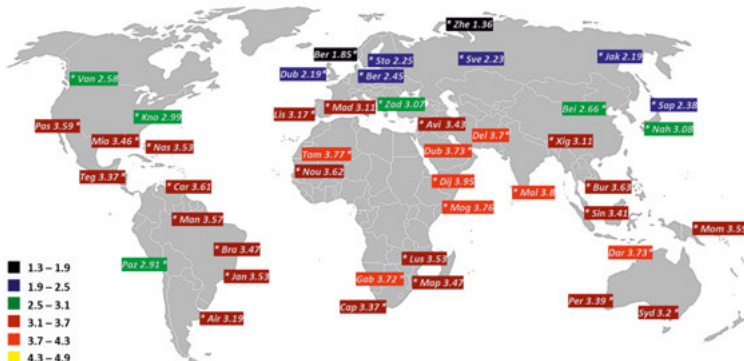


Figure 38. Ratio Flat plate 50 °C to PV monocrystalline [1].

Figure 38 shows the annual energy output ratio between a flat plate working at 50 °C and monocrystalline PV. The ratios in Figure 38 are lower than those in Figure 37, since monocrystalline modules have a higher efficiency than the polycrystalline. The ratio from ST to monocrystalline is always around 88 % of the ratio of ST to polycrystalline. This happens for both vacuum tubes and flat plates collectors.

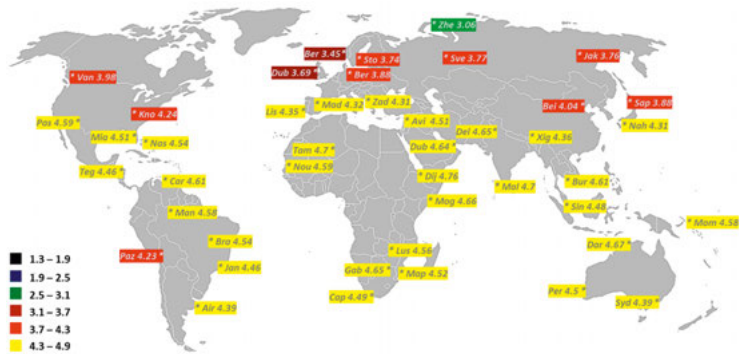


Figure 39. Ratio Vacuum tube with flat absorber 50°C to PV polycrystalline [1].

As expected, the ratio between vacuum tube with flat absorber and the polycrystalline modules shows the highest values in all four maps. For an ST working temperature of 50 °C, the highest ratio value was found to be 4.76 in Djibouti, a city located close to the equator with a warm average temperature of 30 °C [23]. The lowest ratio in Figure 39 is 3.06, which is considerably higher than the lowest ratio found in Figure 37. This is mainly explained by the extremely low temperatures in this location combined with the fact that vacuum tubes have lower heat losses than standard flat plates. In between latitudes of 40° N and 40° S, all ratios in Figure 39 are above 4.2.



Figure 40. Ratio Vacuum tube with flat absorber 50 °C to PV monocrystalline [1].

From the four maps shown in the paper, Figure 40 has the smallest variation between the highest and lowest ratio. This variation is 1.5. The highest ratio found was 4.21, which is lower than the highest ratio between flat plate to poly which is 4.46. In all maps, the lowest ratio is always Cape Zhelaniya (Russia) while the highest ratio of the graph is in Djibouti.



### 4.3 Conclusion

A two-step market survey was conducted that determined the average performance and price values for various types of ST and PV panels. From 2013 to 2021, PV cell efficiency has increased by 20 % and cost reduction on a €/W basis has decrease by a factor three for polycrystalline cells and a factor 2.6 for monocrystalline cells. PV panels have followed similar trends. Both the efficiency improvement and cost reduction on solar thermal show in comparison a negligible improvement during the same time period. The performance values obtained from the survey were then used to simulate the annual energy output of each type of panel using the TRNSYS based software Winsun. This was the basis for establishing a qualitative comparison between ST and PV panels, the annual energy output ratio. In order to facilitate the interpretation of those results, several world maps were drawn to graphically display the differences in annual energy production of the different solar technologies in different locations.

On a world scale, this ratio tends to increase at lower latitudes, which is clearly visible in the world maps. This happens despite large variation being introduced by local climate. The higher ratios at low latitudes mean that ST panels are performing comparatively better than PV and the inverse for higher latitudes. Two main factors are responsible for this:

- The efficiency of a PV panel is reduced with the increase of air temperature while in solar thermal the opposite effect takes place;
- Under low intensity solar irradiance, the efficiency of a PV panel is maintained while a solar thermal collector might not reach the required operating temperatures and have an output of zero;

The ratio maps allow reaching the following conclusions:

- For all locations and for a working temperature of 50 °C, the ST panel always produces more energy than PV;
- Around the world, vacuum tubes with flat absorber normally outperform flat plate collectors per aperture area for temperatures of 50 °C and 80 °C. However, the price per aperture area of vacuum tube with flat absorber is also 32 % higher than flat plate. This means that, assuming that the installation cost is the same for both ST technologies, vacuum tubes should be preferred only if its annual output is higher than a flat plate annual output by 32 %;
- For a temperature of 30 °C, the flat plate is sometimes outperforming the vacuum tube with flat absorber, namely in warm locations;
- All four maps show that for locations with high diffuse radiation or low ambient temperature, the ratio goes down meaning that ST is producing less energy in relation to the PV;
- For latitudes lower than 66°, the ratio of flat plate at 50 °C to PV ranges from 1.85 to 4.46 while the ratio between vacuum tube at 50 °C and PV ranges from 3.05 to 4.76. These numbers can be an important tool when making the decision between PV and ST. However, it is important not

to forget that the dimensioning of ST installations is of utmost importance in order to ensure that there is sufficient heat demand, so that the collectors are working at a high efficiency, which is key to generate good revenue from projects;

- The ratio was also calculated for ST operating temperatures of 30 °C and 80 °C. As expected, the ratio goes up for 30 °C (meaning that it is more favourable to ST) and goes down for 80 °C (meaning that it is less favourable for ST);
- The ratio for ST to monocrystalline is always around 88 % of the ratio of ST to polycrystalline. This happens for both vacuum tubes and flat plate collectors.

Nowadays, due to the steep decrease of the cost of PV modules, there are discussions regarding the competitiveness of ST [45] [18]. Although, the simplicity of the system, the higher value of the energy produced or the possibility to combine PV with heat pumps are very strong arguments in favour for PV [46], it is likely that ST will remain a strong and valuable energy source, especially in warm countries where the annual energy ratios are more strongly in favour of ST, as shown in the world maps presented. Additionally, in warmer countries, the ST system design can be simpler (thermosiphon) which has great impact for the domestic market [47]. This ratio provides a metric to support such investigations.

However, other favourable arguments for PV exist. Presently, there are commercially available PV back contact Si panels achieving efficiencies of upwards of 24 % [48] and these novel technologies will become mainstream in the coming years [49]. Furthermore, the systems losses are often lower for PV than ST. On the other hand, ST benefits more from larger installation size than PV, since it has benefits in both performance and cost [47]. Additionally, there should be more room for a decrease in the costs of system equipment and panel production in ST modules, when comparing to PV, since PV cost has already decreased by 90 % since 2009 [50] due to larger production volumes and heavy research investment.

There has also been research into the merits and possibilities of exporting solar thermal electricity from tropical region to elsewhere like from Northern Africa to Europe [51]. According to the European Solar Thermal Technology Platform, energy consumption worldwide is divided as 20 % electricity, 30 % transport and 50 % heating and cooling. Although, there is a current trend for electrification (i.e. electric cars), when taking a holistic approach, the authors consider that it is not a good idea to use electricity to produce low temperature heat, as there are more efficient alternatives for this segment than for other energy segments. Furthermore, enlarging the grid is costly and time consuming and it is not likely that the world will manage to build an electricity grid that is able to cope with an electrical consumption that is about five times higher. Furthermore, solar thermal is expected to become an essential complement to achieve net zero emission targets worldwide [52]. Thus, it is the author's opin-

ion that both technologies ST and PV will continue to co-exist in a very competitive market, as both technologies are essential in order to meet climate targets and have specific advantages and disadvantages.

For an upcoming work, the authors plan to plot on the world map a new ratio that will be consisting of:

$$New\ Ratio = \frac{Annual\ Energy\ Output\ per\ m2\ of\ ST}{Annual\ Energy\ Output\ per\ m2\ of\ PV} \times \frac{(ST\ collector\ price+installation\ cost\ ST+system\ cost)}{(PV\ collector\ price+installation\ cost\ PV+system\ cost)} \times \frac{avg\ system\ losses\ ST}{avg\ system\ losses\ PV} \quad eq. 19$$

The annual energy ratio will favor ST, while the collector price, the installation cost and the system losses should favor PV. The complete ratio would then be above 1 (higher ST output) or below 1 (higher PV output). To finalize, the user should then multiply the new ratio by an additional ratio which considers the local value of heat and electricity. Furthermore, this ratio should be created for a few typical installation types and technologies, similar to that which has been done in this paper. The authors believe that this ratio has the potential to become a useful decision tool for domestic home owners, for example.

## 5 On the Successful Silicon Encapsulation of a CPVT Receiver

The most critical part in the manufacture of a PVT collector is widely considered to be the receiver [53] [54]. A major technical design difficulty for PVT collectors is to find a material for encapsulating the solar cells that is able to effectively conduct the heat from the solar cells to the receiver while still maintaining a number of critical characteristics such as high electrical insulation, high transparency, low cost, ability to cope with thermal stress in order to protect the solar cells, resistance to moisture penetration, resistance to UV. This difficulty is even more pronounced in CPVT collectors, which face higher stagnation temperatures. Ensuring good thermal contact between solar cells and receiver, while being able to avoid cell cracking from thermal expansion and contraction are significant design considerations in PVT collector development. Improving cell-receiver thermal contact is performed by choice of material and its method of application during the manufacturing process.

In addition to the aforementioned performance and cost considerations, another key aspect in solar collector design is durability. Solar collectors must survive at least 20 years outdoors with an acceptable power output reduction over the period in order for owners to be able to profit from the installation. This carries long-term implications on UV and temperature resistance, for example. The stagnation temperature of a collector is reached, when the heat losses are equal to the energy received from the sun. This means that all incoming solar radiation is transferred to the surrounding environment either as heat losses or as optical losses. A particularly important disadvantage of concentration is the increase of the stagnation temperature, which can cause damage to the materials of the collector, in particular to the solar cells. Paper II, XI and XVI study the survivability of the solar cells under stagnation conditions for several specific PVT designs covering in this way one of the major goal of this thesis, which is to study whether encapsulation of solar cells with silicone was possible for low and medium temperature solar applications. Further studies to these issues are also conducted in Papers 10 [55] and 19 [56].

A number of additional challenges exist such as:

- **Technical:** Adhesion to receiver substrate, adhesion between different encapsulant layer, and suitability for large-scale low cost production;
- **Economic:** Material costs, production times and production costs.

### 5.1 Challenges and advantages of silicon encapsulation

Silicone has favourable material properties to address these aforementioned challenges due to its properties of elasticity, thermal resistance, transparency, electrical insulation properties, and production possibilities. The specific design challenges associated with using silicone are described below:

1. A minimal thermal conductivity from the cell to the cooling fluid (normally water), while ensuring no conductivity of electricity. This represents

a significant challenge, since normally, if a material is not electrically conductive, it is also not thermally conductive;

2. A high transparency in the top part of the silicone to ensure that as much solar radiation as possible reaches the PV cell. A minimal value of 90 % is considered as a base requirement however, a value such as 97 % would be desirable;
3. A level of adhesion between the silicone and the receiver substrate (aluminium in this case) that is strong and durable enough to withstand a minimal of 20 years on both the front side and bottom side of the receiver. Since the studied design features a bifacial PVT receiver, the adhesion must be strong enough to overcome gravity;
4. A process for the silicone encapsulation of the receiver that is compatible with the requirements for industrial mass production. Important factors are the speed of production (in the process and the curing time) as well as reliability of the process (low rejection rate from the process). The viscosity level of the silicone plays a crucial role in this. The viscosity is closely related to the filler which in turn affects both electrical and thermal conductivity values;
5. The ability to absorb tension created by the differential thermal expansion of the aluminium receiver and the silicon solar cell. Another option is to reduce the pressure associated with the thermal expansion, which is addressed by the new H-pattern mesh design created during this thesis (further details below);
6. The ability to resist higher temperatures than standard Ethylene Vinyl Acetate (EVA). Normal materials, such as EVA, cannot operate over 80 °C. Some improved EVAs can cope with 110 °C, however these temperatures are still not enough for the glazed PVT applications since the stagnation temperatures are generally above 110 °C;
7. The requirement of competitive pricing. The chosen solution cannot have a cost that is significantly more than the commonly used alternatives, such as EVA;
8. The requirement to be able to survive the solar Keymark and IEC 61215 standards, which are required for PVT certification. Certification is a requirement to sell in most markets;
9. The need for low moisture penetration. Typically, when silicone heats up it collects moisture, and this needs to be prevented. Otherwise, collected moisture will lead to hazardous short circuits;
10. Several other aspects relevant to consider: stickiness; drying time (liquid); water leakage around the connection cable; mixing process and adequate mixing rates, in case the silicone is poorly mixed, it will have soft spots; and the need for a primer.

This list highlights the multiple issues that need to be balanced in the choice of a suitable encapsulant for the considered CPVT design.

### **5.1.1 Distance between solar cell and receiver**

Alongside with the thermal conductivity of the chosen silicone, the distance between the solar cell and the receiver core has a major impact on cell temperature and thus on its performance. Therefore, it is desirable to keep the solar cell as close to the receiver core as possible. However, cell-receiver proximity creates problems associated with insulation and thermal expansion (e.g. cell cracking), as well as manufacturing difficulties.

### **5.1.2 Manufacturing challenges**

The receiver core consists of a 2.3 m extruded aluminium profile, which is straightened by stretching after extrusion. This process results in manufacturing tolerances that have an impact on the straight surface, making it difficult to pour the silicone. These manufacturing tolerances, combined with tolerances in the assembly line, are expected to obtain tolerances at a magnitude of tenths of a millimeter.

### **5.1.3 Material expansion**

Material thermal expansion is omnidirectional. While the expansion coefficient is a fixed value that depends on the material, its dimension affects the total expansion. By comparison, a small piece of aluminium will have a smaller total expansion compared to a large piece of the same aluminium, provided they are subject to the same temperature.

### **5.1.4 Top & Bottom Silicone Layer**

The considered CPVT design features a bifacial receiver with a top and a bottom side. Each of these receiver sides have both a bottom and top layer of silicone. The bottom layer is between the cell and the receiver and the top layer is between the cell and the air in the collector box. These layers were found necessary due to production process.

The silicone top layer will protect the cells against the air in the box while insulate against heat losses, thus a low heat conductivity is beneficial in this layer. This layer must absolutely be of high transparency.

The silicone bottom layer will protect the solar cells against the expansion and contraction movements of the aluminium receiver. This layer requires a high dielectric insulation, as no current can pass through to the heat transfer fluid (HTF). However, a high thermal conductivity is also beneficial. This layer does not require transparency.

Furthermore, the adhesion of the bottom layer on the bottom side of the receiver requires a strong adhesion to the aluminium substrate. The weight of the silicon, the cells, diodes and busbar is approximately 1.1 kg.

The required specifications for each layer are detailed in Table 20.

Table 20. *Silicone material requirements for top and bottom layers of the receiver.*

Required specification	Bottom Layer	Top Layer
<b>High dielectric resistance.</b> 5 kV between the cells/diode busbar and 1.2 kV between cells and diode busbar.	✓	✓
<b>Withstand a wide range of temperatures.</b> During normal collector operation, the silicon temperature will range between -30 and 120 °C however, the temperature will occasionally rise to 200 °C.	✓	✓
<b>High thermal conductivity.</b> It is important that the cells have a similar temperature to the receiver.	✓	✓
<b>Durability.</b> Needs to survive with good performance for a minimal of 20 years.		✓
<b>Excellent light transmittance.</b> Especially important for the PV absorption range.		✓
<b>Excellent adhesion to aluminium.</b> The silicone must hang upside down on the bottom side of the receiver.	✓	
<b>Viscosity.</b> Air bubbles must not occur during production.	✓	
<b>Surface interfaces.</b> Must not be pierced easily by busbars / or cell.	✓	
<b>UV resistant.</b> The material will be exposed to sunlight.		✓
<b>Low Stickiness.</b> Dust must not adhere to the silicone.		✓
<b>Expansion resistance.</b> The thermal expansion of the receiver must not damage the solar cells.	✓	

### 5.1.5 **Silicone Thermal Conductivity**

The silicone used has a fairly low thermal conductivity, which is similar to other transparent materials: 0.2 [W/m·K]. As a comparison point EVA, the most common encapsulant of crystalline solar cells, has a very similar thermal conductivity. However, one important point is that the thermal conductivity is highly depend on the thickness. EVA layers can be very thin but this is far harder to achieve in silicone layers.

State-of-the-art silicone has other favourable properties: it is very fluid with a viscosity close to that of water during the manufacturing process, which enables it to float-form an even insulation layer at the bottom of the receiver and encapsulate the cell without collecting air bubbles under the cell.

If silicone with a higher thermal conductivity is desired, then a filler material must be selected and included in the silicone composition. The use of filler materials changes the fundamental properties of the silicone, which tend to, for example, result in reduced or no transparency or increased viscosity (which results in a higher shore number after curing and can damage the cells). These are properties that must be avoided for the top layer of the silicone and carefully used in the bottom layer. In addition, unfortunately, the increase in thermal conductivity is relatively small with the addition of a filler. Moreover, silicone tends to become more difficult to dispense with the addition of filler and loses its transparency while appropriating the colour of the filler material. The

addition of a red or black filler material produces a red or black silicone, respectively.

Another method of increasing thermal conductivity is by reducing thermal resistance. This can be achieved by moving the solar cell closer to the receiver core surface. However, this increases risks of expansion and can result in insulation problems, if not carefully managed.

### **5.1.6 Production process**

One problem that has proved difficult to handle with liquid silicone is that the substrate (the aluminium receiver core) requires very precise tolerances. This implies that the production equipment must also have extremely high precision: Extruding a 2300 mm long aluminium profile and building a production line to apply a low viscosity bottom layer while maintaining accuracy within a few tenths of a millimetre is a major challenge. Greater tolerances result in worse thermal conductivity, as the thickness silicon layer needs to be increased to maintain electrical insulation over the full area (Insulation failures renders the collector useless and thus have priority over all any thermal performance aspect).

The aforementioned issue is exacerbated when increasing the proportion of filler material in the silicone, since it increases viscosity of the silicone, which then does not flow so easily by gravity. Furthermore, a mechanical mean must be utilized in order ensure an even layer. Although not an impossible challenge, neither machine suppliers nor silicone manufacturers have been able to present a good solution for this and the development of this extra solution would represent an additional cost for a PVT production line.

Silicone has a higher viscosity than water, which means that it does not easily flow into a smooth and even layer. Neither silicone manufacturers, nor the manufacturers of machine equipment have presented any simple solution to mechanically spread silicone over a large surface, as mentioned above. The tools would require cleaning at regular intervals, as the silicone begins to harden with the passage of time. For this reason, a low viscosity (lighter liquid) silicone is preferred.

After testing several manufacturers and a vast number of silicone types, we found that doing the cell encapsulation in a two layer process was the best method in order to maintain the best compromise between high reliability, affordable cost, reduced production/curing time and good performance. The chosen supplier has been Wacker. A bottom layer of 1 mm is located between the receiver aluminium core and the solar cells. And a top layer of 1 mm located between the solar cells and the air inside the collector box. In the prototypes created for the tests, two types of silicone gels are used:

A highly transparent and electrically insulating silicone (Elastosil 3201), which can be used both for the top layer and bottom layer. Thermal conductivity is 0.2 W/m·K.

A reddish-brown silicon (RT 740) that has the two times higher electrical insulation properties as 3201 and an 2.5 times improved thermal conductivity 0.5 W/m·K, which would allow more heat to be transferred from the cells to



the receiver over the thin layer of silicon. It is important to note that this silicone can only be used in the bottom layer, since it is not transparent and if used on the top layer, it would block the sunlight from reaching the cells. Another important point is that the red silicone is considerably stiffer than the transparent silicone, and thus transmits more thermal stress to the cells when the receiver experiences thermal expansion. This latter point was discovered when making the first prototype collectors and confirmed during the stagnation tests.

### **5.1.7 Curing Process & Mixing**

The curing time and procedure differs significantly according to the type of silicone chosen. For example, a one-component silicone often uses evaporation curing, while a two-component silicone may require different types of catalysts to start the curing process. These different catalytic methods include curing, when mixing at room temperature, curing by heating and curing by UV irradiation.

Incomplete mixing can cause soft spots, which are points where the silicone is not completely cured. These points can cause isolation issues, stickiness (causing the dust to adhere) and visual problems.

Furthermore, silicone is a material that is sensitive to the influence of a number of chemicals, adhesives and even solid materials, which contain various solvents that can interfere with the curing process. Additionally, excess flux in string soldering is a phenomenon that has been shown to cause problems with silicone. The silicone will not be fully cured, if the catalyst in the silicone is disturbed, which will reduce the efficacy of the silicone encapsulant layer.

### **5.1.8 Material cost**

The material cost of silicone has a significant impact of the receiver cost, being around 25% of the receiver cost for the current design. The material cost remains high, even with high volume. Reducing the amount of silicone per receiver has a great potential to significantly reduce material cost of the PVT, however this would imply the use of other technical solutions for implementation of the thinner layer of silicone.

## **5.2 Test Methodology**

Paper II describes in detail the performance and electroluminescence (EL) testing of several different prototypes PVT receivers encapsulated with silicone.

### **5.2.1 The Prototype Receivers**

Eight prototype small receivers were manufactured to study the durability and performance impact at high temperatures of PVT receivers encapsulated with silicone. Table 21 summarizes the characteristics of each small receiver.

Table 21. Characteristics of the eight tested receivers [11].

Receiver	Cell Size	Cell Number	Cell Gap	Soldering	Silicone Layers	Tabbing Strip
Receiver 1	1/6	7	No	Line	Red -Transparent	Straight
Receiver 2	1/6	6	No	Line	Both transparent	Straight
Receiver 3	1/6	6	Yes	Line	Red -Transparent	Strain Relief
Receiver 4	1/6	6	Yes	Line	Both transparent	Strain Relief
Receiver 5	1/6	6	Yes	Two Points	Both transparent	Strain Relief
Receiver 6	1/6	7	No	One Point	Both transparent	Straight
Receiver 7	1/3	4	Yes	Line	Both transparent	Strain Relief
Receiver 8	1/3	4	No	One Point	Both transparent	Straight

The eight receivers were identical with the exception of the six parameters that were varied: Cell size, cell gap, number of cells, type of soldering, type of silicon used, and existence of a strain relief. Four of this six parameters are further explained below:

- Two cell sizes were used: 1/3 (52 × 148 mm) and 1/6 (28 × 148 mm);
- The cell gap is the space between the cells. The word “No” means that the small standard cell gap of 0.5mm was utilized, while “Yes” means a longer gap (triple of the standard gap);
- The strain relief is an exaggerated “s” shape bent in the tabbing strip between each cell. The goal is that this shape absorbs the thermally induced mechanical stress, instead of the cells.
- As mentioned earlier the silicone is applied in two layers. An initial bottom layer that is placed on the aluminium receiver before the cells and a top layer that is placed at the same time as the solar cells, after the initial bottom layer of silicone has already solidified. Two types of silicone were used, as described earlier.

### 5.2.2 Test Method and Equipment

Electroluminescence (EL) is a powerful tool commonly used to control the quality of the PV cell strings, which is used both in research and industry. Using this technique, it is possible to identify defects that are not visible to the naked eye such as microcracks and black (or so called “dead”) areas. These two types of defects are the principal causes of power loss in cell strings. This can be confirmed in the IV-Curve test [57].

The testing procedure consisted of submitting each receiver to eight rounds of gradually increasing temperatures inside an oven for a duration of one hour. In the first round the receiver temperature was raised from room temperature to 60 °C, and in the next rounds from room temperature to 80 °C, 100 °C, 130 °C, 150 °C, 180 °C, 200 °C, and finally, to 220 °C. This process was repeated in exactly the same manner for all receivers. Table 22 describes the heating rounds.

Table 22. *The heating rounds for the receivers (Each round consisted of 1 h inside the oven and 3h of cooling at room temperature).*

<b>Baseline (Round 0)</b>	<b>Receiver at Room Temperature</b>
Round 1	60 °C
Round 2	80 °C
Round 3	100 °C
Round 4	130 °C
Round 5	150 °C
Round 6	180 °C
Round 7	200 °C
Round 8	220 °C

It is important to point out that this collector design is expected to have a stagnation temperature of 180 °C. Nevertheless, the tests at 200 °C and 220 °C give interesting results in order to determine a safety margin.

Before and after each thermal cycle round, the following parameters were recorded:

- Electroluminescence Test: IR photograph of the cells on the receiver was made using a Digital Rebel XTi Black Canon Camera without an IR filter. The system features an image size of (3888 × 2592) in RAW format with 10 megapixels. The test was done in a completely dark chamber. Cells were in forward bias with a current close to 4A. This test allowed the team to spot micro cracks that would otherwise not be visible to the naked eye;
- Diode Function test, which yielded a response of working or not working;
- Visual Inspection, which consisted in a simple visual check to the overall condition of the cells, discoloration of the silicone or any other potential issue;
- IV Curve test with an IV tracer in a solar simulator. The following parameters were measured: Short circuit current ( $I_{sc}$ ), open circuit voltage ( $V_{oc}$ ), current at maximum power point ( $I_{mp}$ ), voltage at maximum power point ( $V_{mp}$ ), maximum power point ( $P_{max}$ ) and fill factor (FF).

The indoor solar simulator shown in Figure 41 was utilized for the IV-curves. It consists of two rows of eight halogen light bulbs each with 1000 W of power. As in many solar simulators, the light distribution and spectrum can be a drawback, since it is understandably hard to simulate the energy coming from the sun, a stellar object that is a nearly perfect sphere of hot plasma with a diameter of 1.39 million kilometers and a mass that is about 330,000 times that of Earth. Regardless, for the objective of the comparative measurements between receivers, this solar simulator is well suited.

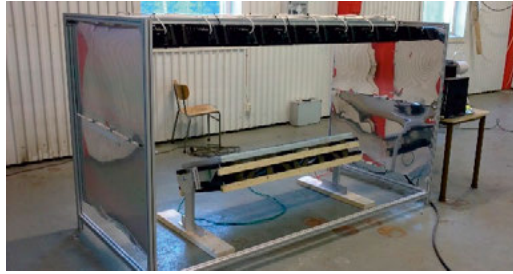


Figure 41. The solar simulator for the indoor measurements.

An important consideration about these eight prototype receivers is that the cells were manually soldered, which means that some microcracks arise from the production process that would not occur in automatic cell soldering production. This means that the baseline round was a fundamental check to account for damages that were not caused by the stagnation.

### 5.3 Silicon Encapsulation Testing Results

#### 5.3.1 *Electroluminescence Microcrack Evaluation*

Figure 42a shows the baseline scenario (ambient temperature) of receiver 1 and the red circles highlight small microcracks that are caused by manufacturing, while Figure 42b shows how these initial microcracks have expand in size after being heated in successive rounds, until the round with a temperature of 130 °C. Additionally, Figure 42b shows that new microcracks have appeared, although the majority of the cracks come from the expansion of initially existing cracks.

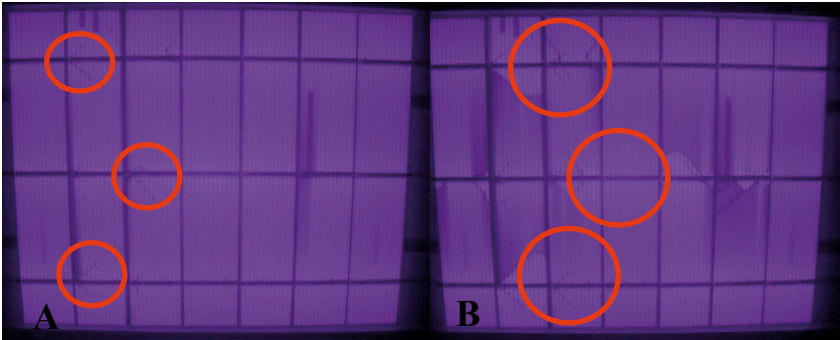


Figure 42. EL test of receiver 1: (A) Baseline (ambient temperature); (B) After the round at 130 °C.

Figure 43 shows the status of receiver 1 after the round 200 °C. Adding to the microcracks, there is also a completely black cell highlighted in orange, which means that there is a short circuit between top and bottom of the cell, potentially caused by the top and bottom ribbon coming into contact through the broken cell.

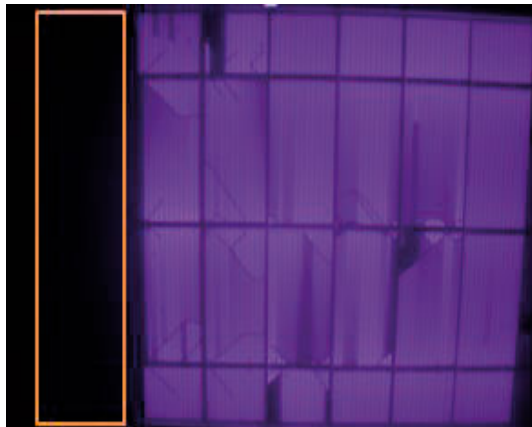


Figure 43. EL test of receiver 1 after the round at 200 °C.

Figure 44 shows receiver 5 at the baseline and at 200 °C. The red circles show again microcracks caused by the manual production process and their expansion when heated up, although in this receiver the cracks take longer to expand. The yellow circle shows the small flaws in the cell, potentially caused during the production process of the cell or the cell wafer. These flaws seem to influence the appearance of new micro cracks.



Figure 44. EL test of receiver 5. (A) Baseline (ambient temperature); (B) After the round at 200 °C.

It was the author's expectation that receiver 1 would be the receiver design least capable to withstand stagnation, while receiver 5 was expected to be one of the most successful designs, which the above images confirm.

This way, three main types of issues were identified:

1. Microcracks caused by manual soldering (Figure 42);
1. Short circuit in one cell (Figure 43);
2. Flaws from cell production (Figure 44).

### 5.3.2 Thermal Stress Test Results

Eight receivers were built, and stress tested at different temperatures over eight rounds. Each of the following figures show an image of the receivers, four EL test images and a graph with the parameters of the tested receiver. For all receivers, the visual inspection did not provide additional information. An example of an IV curve can be visualized in appendix B of Paper II.

Four of the stress tests results are presented. A complete summary of all results can be found in Paper II.

The first test receiver tested had design characteristics that were expected to lead to a substantial amount of microcracks. This way, as expected, after round 5 (exposure to 150 °C which is number 3 in Figure 45), the image from the EL test showed that the string had dark areas and a large number of microcracks, which led to a power decreases shown in graph. Raising the temperature in following heating rounds has significantly increased the number of dark areas and microcracks. In the last round, one cell became completely black, which is most likely caused by a short circuit between the top and bottom of the cell. The reason for the short circuit has not been determined but a

likely explanation is that the solder on the top ribbon melted (or simply became in contact) through a crack and reached the bottom ribbon.

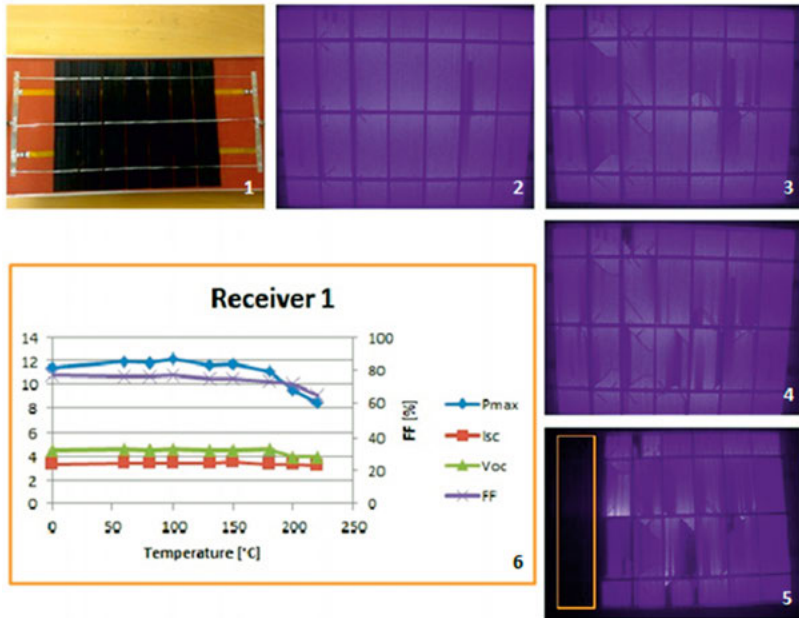


Figure 45. 1) Receiver 1; 2) Baseline; 3) Round 5 (150 °C); 4) Round 6 (180 °C); 5) Round 8 (220 °C); 6) Parameters of the IV curve at different temperatures (Isc shown in the left Y axis).

The only difference between the first and second receivers is the bottom silicone layer. In receiver 2, transparent silicone was used on both layers. From the 5 rounds of EL tests shown in Figure 46, it is possible to see a large increase in microcracks after round 6 (180 °C). Despite this, the IV curve basic parameters remain more or less constant throughout the eight rounds with only a minor power decrease. The number of microcracks in receiver 1 is higher than in receiver 2 for all temperatures, despite the baseline test (image 2 of Figure 46) having a slightly higher number of microcracks.

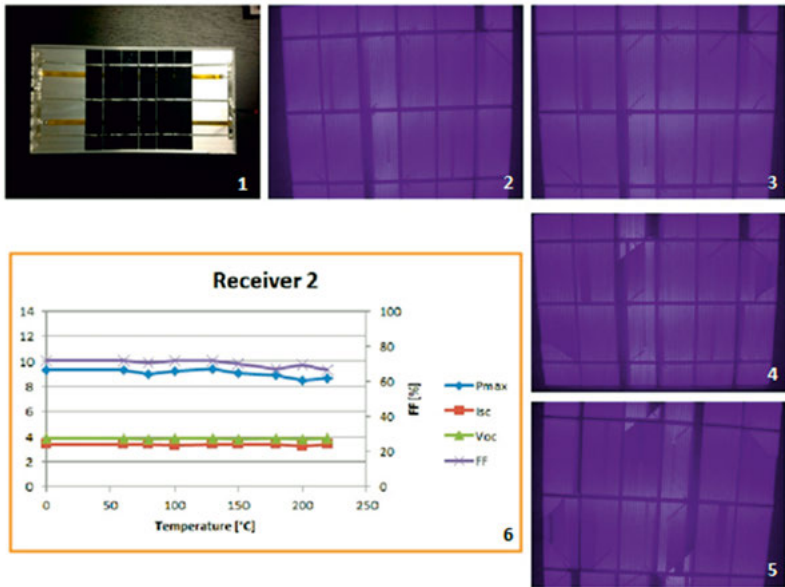


Figure 46. 1) Receiver 2; 2) Baseline; 3) Round 5 (150 °C); 4) Round 6 (180 °C); 5) Round 8 (220 °C); 6) Parameters of the IV curve at different temperatures (Isc shown in the left Y axis).

The main goal of building receivers 3 and 4 was to evaluate the impact of the thermal expansion of the ribbon on the cell. This way, a strain relief bend was inserted before and after each cell. In order to isolate the impact of the different types of silicones two receivers were made with this type of strain relief ribbon: One with red silicone (receiver 3) and another with transparent silicone (receiver 4). The results from receiver 3 can be seen in Figure 47 and from receiver 4 in Figure 48.



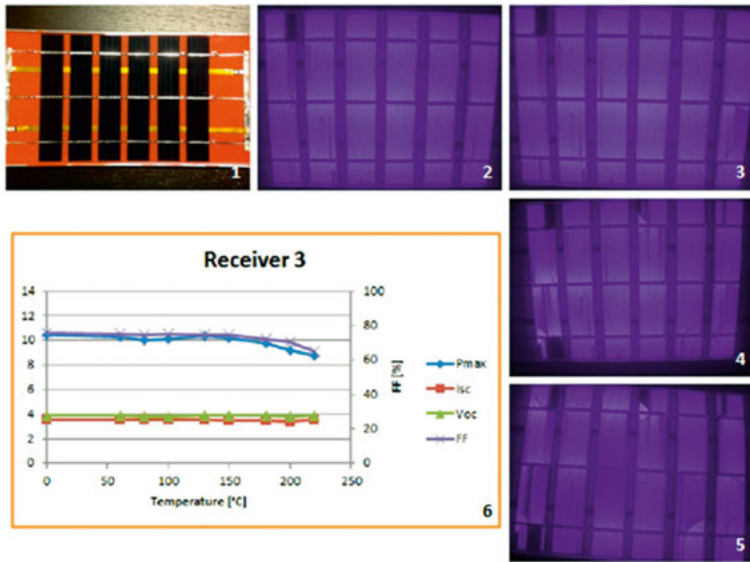


Figure 47. 1) Receiver 3; 2) Baseline; 3) Round 5 (150 °C); 4) Round 6 (180 °C); 5) Round 8 (220 °C); 6) Parameters of the IV curve at different temperatures ( $I_{sc}$  shown in the left Y axis).

The EL tests in Figure 47 show that in a receiver with red silicone, even with the strain relief between the cells, a large number of microcracks appear when exposed to high temperatures (180 °C). Compared with receiver 1, receiver 3 exhibits a smaller power drop, albeit still displaying a significant power drop in the last two rounds.

The cells of receiver 4, shown in Figure 48, have no significant damage along the eight rounds, representing a clear improvement from the results obtained with receiver 2. However, receiver 4 showed one black cell in the last round likely due to the same reason as in the receiver 1. The same black cell, which appeared in round 7 (200 °C), is also responsible for the sharp 15 % drop. Excluding that effect, the power remains considerably constant.

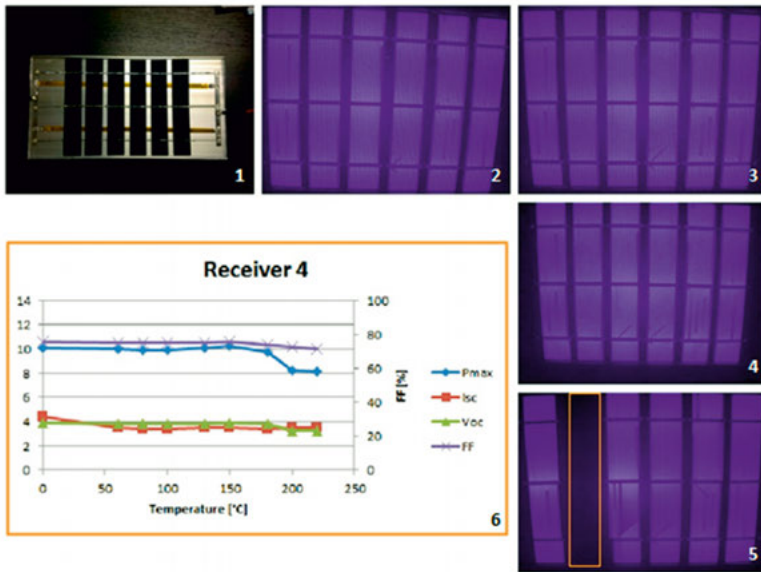


Figure 48. 1) Receiver 4; 2) Baseline; 3) Round 5 (150 °C); 4) Round 6 (180 °C); 5) Round 8 (220 °C); 6) Parameters of the IV curve at different temperatures (Isc shown in the left Y axis).

Figure 49 illustrates that the Pmax of receiver 5 has one initial decrease at 50 °C. This drop is due to the two broken cells shown in image three. If this effect is excluded (likely human error), the Pmax remains relatively stable. It is interesting to note that only at 220 °C one extra microcrack appears. The one-point soldering has much smaller electrical contact between the busbar and the cell than the line soldering but this shows no consequences in term of measurement power output, due to the fact that the current through the cells is low.

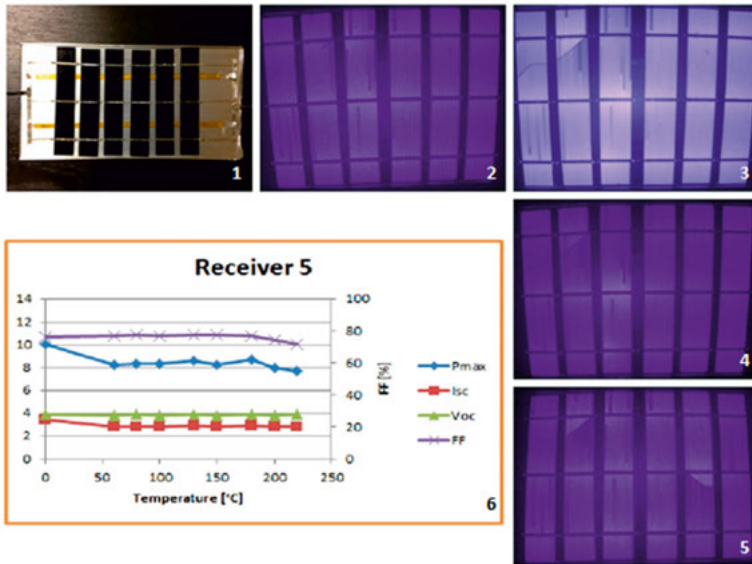


Figure 49. 1) Receiver 5; 2) Baseline; 3) Round 5 (150 °C); 4) Round 6 (180 °C); 5) Round 8 (220 °C); 6) Parameters of the IV curve at different temperatures (I<sub>sc</sub> shown in the left Y axis).

Figures 50 and 51 compare the decrease in  $P_{\max}$  of the different receivers at different temperatures rounds with and without the strain relief. Receiver 2 shows the most stable  $P_{\max}$  across all temperatures. Receiver 5 is also fairly stable if the handling problem on round 1 is excluded. Receiver 1 shows an increase of power that is difficult to explain and is assumed to have been a human measurement error, potentially combined with the small variation in the power provided by the solar simulation. Overall, receivers with red silicone have the highest power decrease, when external factors are excluded. The existence of gaps seems to reduce the number of microcracks. No prototype receiver loses more than 30 % of its initial power, despite the large cell breakage shown by some of the prototype receivers in the EL imaging results.

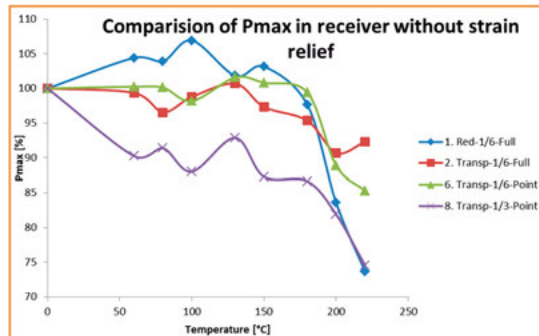


Figure 50. Comparison of  $P_{\max}$  decrease in receivers without strain relief

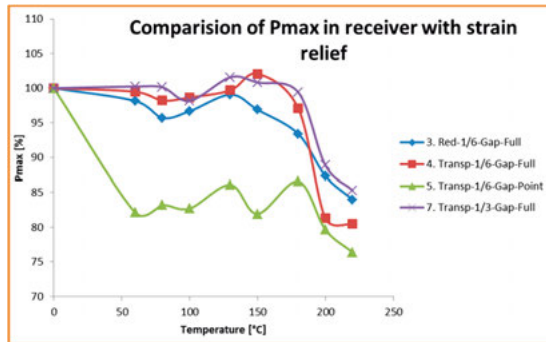


Figure 51. Comparison of  $P_{\max}$  decrease in receivers with strain relief.

## 5.4 Silicon Encapsulation Testing Conclusions

Eight receivers have been built and were successfully tested to assess the impact of reaching high temperatures in the performance and cell structural integrity.

The EL testing allowed identifying two main types of problems in the solar cells which are represented by black areas in the cell EL image. One is the irregularly shaped areas, which are due to microcracks, and the other is regular rectangular areas which are due to broken finger contacts on the front of the cell. It was also noted that the majority of the microcracks were initiated at the soldering points, which is understood to happen due to the different expansion coefficients between the copper ribbon and the silicon solar cell. A third problem was also detected which is due to flaws in production process at either wafer or cell production. These three issues are highlighted in the images show earlier.

From the figures displayed in the results section, it is clear that receivers built with transparent silicone show far less cracks and power degradation after being exposed to stagnation temperatures. This is understood to be due to two main reasons: (1) the transparent silicone is not as stiff as the red silicone and thus further absorbs the mechanical stress of thermal expansion in the aluminium receiver; (2) the red silicone, due to its lower viscosity, normally leads to a thinner layer, which further penalizes its ability to absorb mechanical stress.

No prototype test receiver lost more than 30 % of its initial power, despite the large cell breakage shown in the EL imaging of some receivers. However, further expansion and contraction cycles would likely raise this power drop further. For the receivers with red silicone, further cycles would reduce the power output to zero, as is known from field operation experience.

After eight rounds of testing in eight receivers with different designs, it was possible to conclude that the diodes were working perfectly at all temperatures, despite the diode specifications stated a maximum junction temperature of only 200 °C.

Larger cells are more prone to develop microcracks due to thermally induced stresses. From the tests that have been made, point soldering seems to lead to a reduction in the number of microcracks and black areas, especially in

receivers with larger cells ( $148 \times 52\text{mm}$  instead of  $148 \times 26\text{ mm}$ ). However, the impact of microcracks in the Pmax of receivers with point soldering is also larger due to the smaller contact area between the ribbon and the cell.

From the EL images, the receiver presenting the lowest amount of microcracks after round 8 (at  $220\text{ }^\circ\text{C}$ ) is receiver 5. This receiver was made with point soldering and a strain relief between each cell. Receiver 4 and receiver 6 also exhibit low amounts of microcracks, but both have a full black cell, possibly caused by the top and bottom ribbon becoming in contact through a cell crack or a melted ribbon. Receiver 2 shows the steadiest Pmax across all temperatures. Receiver 5 is also fairly stable, if the human handling error is excluded.

This study also allows to conclude that existing microcracks tend to grow in size into larger cracks. The EL imaging taken during our experiment leads us to conclude that it is far easier for existing cracks to expand than for new cracks to appear.

A limitation of this work was the absence of a fully automatic tabbing machine. Since this is expensive equipment that was not available at the time of these experiments, our team was forced to use manual soldering. However, by setting a baseline scenario for comparison, this limitation was sufficiently addressed.

It is important to point out that the thickness of the bottom silicone layer is of the utmost importance in reducing the transference of thermally-induced stress to the cells. The impact of the variations in the thickness of silicone in the thermal stress suffered by the cells has not been evaluated in this paper and should be addressed in a future study since it is a very relevant aspect for cell survival of stagnation.

## **5.5 A Novel Solution for Improved Thermal Contact in PVT receivers: The H-Pattern**

As the previous section demonstrates, a one-silicone, two-step encapsulate solution provides a working solution for glazed PVT collectors but has room for improvement in both heat transmissivity and cost reduction. During this thesis, a novel solution was developed that has the potential to tackle both of the above, while at the same time increasing electrical insulation and reducing the thermal stress on the cells. This design is called the H-Pattern.

### **5.5.1 Design proposal**

The idea is to replace the filler material inside the silicone with a filler material consisting of an electrically insulated metal sheet (aluminium) with a hole pattern to prevent thermal expansion. By placing the cell as close as possible to an aluminium surface with thermal conductivity of about  $200\text{ [W/m}\cdot\text{K]}$ , the expected result can be compared to the addition of filler material to the silicon. An increase in heat conductivity between the cell and the heat transfer fluid is expected to be of an order of magnitude of 10, while keeping the transparent attribute of silicone.

### 5.5.2 **Expansion-inhibiting design pattern**

The purpose of this design is to allow thermal expansion material in all directions (by expand into its own cavities), thus creating a smaller total expansion in any single direction, which in turn is expected to drastically diminish the risk of cell cracking. Using a metal in thermal applications can bring problems of higher thermal expansion, but these can be addressed by the expansion cavities of the H-pattern.

### 5.5.3 **Advantages of the H-Pattern**

There are three main advantages of the H-pattern.

- **The possibility to use a high electrical pre-insulation that allows the cells to be kept closer to the metal improving heat conduction.**

Since the H-pattern aluminium sheet will have a high electrical pre-insulation, the solar cells can simply rest against the H-pattern without compromising the bottom layer's insulation. This simplifies the production process, since one only needs to pour the silicone on top of the H-pattern and the cells to complete the encapsulation. This activity is in line with the automated production process for the PVT receiver that has already been developed in parallel with the PhD activities.

- **Reduction of costs: The H-pattern will be considerably cheaper than the transparent silicone.**

This would likely symbolize that the cost of silicone per receiver would be cut by a third, which is a significant reduction in one of the most expensive receiver components (representing 25 % of the receiver cost).

- **Thermal expansion is designed-for, thus improving the survivability of the receiver.**

The pattern would be divided into two different areas: Internal Expansion Area (IEA) and Total Expansion Area (TEA). Internal Expansion Area (IEA) is the part of the design pattern where the expansion is counteracted by the design geometry. While one leg expands in one direction, the other leg expands in the other direction. In this way, the total expansion will not be affected, when expansion occurs in this area of design pattern. Total Expansion Area (TEA) is that part of the design pattern where the expansion affects the total expansion. By controlling the value of this area in comparison to the total area, the value of the total expansion can be determined.

Longer "legs" in the "H-shaped hole pattern" (longer holes) will give less total expansion. The sheet pattern can be stamped and pre-insulated easily by several companies working in this field. Any other preparation can be done outside the assembly line and the extra time for placing the H-pattern in the receiver will not necessarily affect the overall process time on the receiver assembly line. This sheet pattern can be made in lengths of a cell, a cell string or a full receiver, depending on what it is expected to be achieved. Figure 52 shows the potential dimensions of the H-pattern.

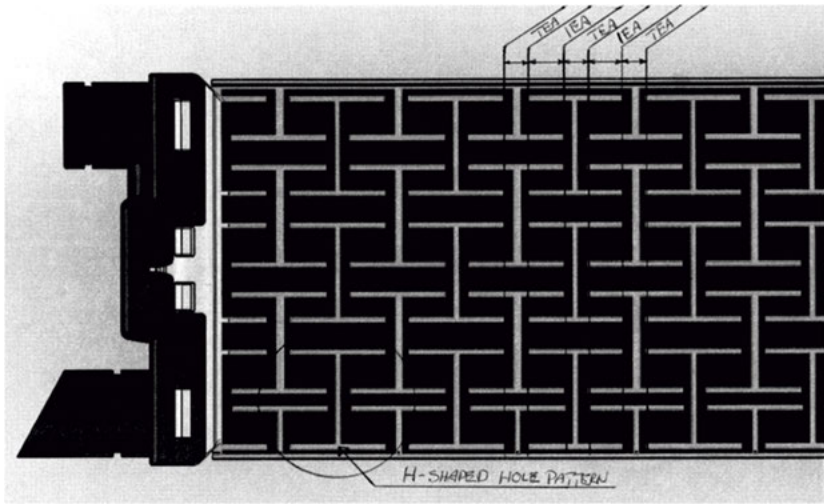


Figure 52. A potential design of the H-Pattern with dimensions.

#### 5.5.4 Insulation layer

Adding a highly electrically pre-insulated aluminium pattern in the bottom layer of silicone is expected to increase the electrical insulation. With the right insulation layer between, the cell should be able to rest directly against the electrically insulating sheet maximising its thermal conductivity, while at the same increasing the safety margin on the insulation side. It is important to note that during production any receiver that does not meet the insulation must be discarded. This must be avoided, as it represents an extra cost and thus this additional safety factor provided by the pre-insulated sheet is a significant improvement. Figure 53 illustrates how the placement of H-pattern on the PVT receiver.

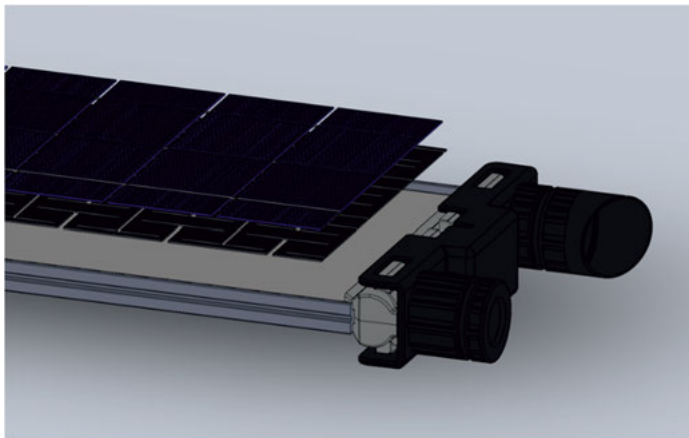


Figure 53. Solidworks drawing of the H-pattern integrated with the PVT receiver.

The insulation layer can be of a UV resistant Powder coating, or possibly a stamped or full-size sheet laminated with the cell string (like gluing a laminated cake to the receiver core). If the expansion problem can be minimised, it would provide the opportunity to use laminate overall. Figure 54 illustrates the expansion vacancies of the H-pattern.

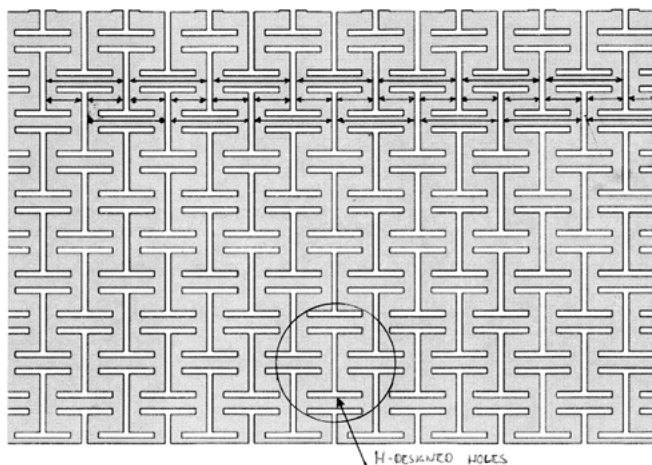


Figure 54. H-pattern sketch with expansion vacancies.

The thickness of the aluminium sheet should be as thin as possible while providing satisfactory properties for production, while being able to withstand the expansion of the thick receiver core. Both thickness of 0.5 mm and 1 mm of the aluminium pattern will be simulated for comparison studies in further work. This is expected to be a minor difference in their thermal conductivity values. However, larger differences are expected which result from the silicone thickness, which has a lower thermal conductivity by factor of approximately 1000 (Silicone 0.2 W/m·K vs Aluminium approximately 200 W/m·K).

A qualified guess regarding the layer thickness requirements for the H-pattern design starting from the water channel and out to the solar cell is presented below and illustrated in Figures 55 and 56:

1. Receiver core with water channels
2. 0.2 mm Elastosil 2205 silicone layer (for gluing H-pattern to receiver core)
3. 0.5 mm H pattern of aluminium.
4. 0.02 mm black Resicoat powder coating.
5. 0.5 mm Elastosil 2205 silicone layer.
6. 0.4 mm solar cell.
7. 1 mm Elastosil 2205 top cover layer.



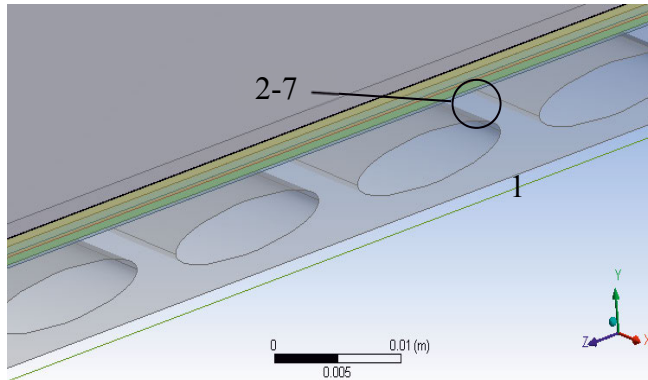


Figure 55. PVT Receiver with an H-pattern sheet for expansion inhibition purposes.

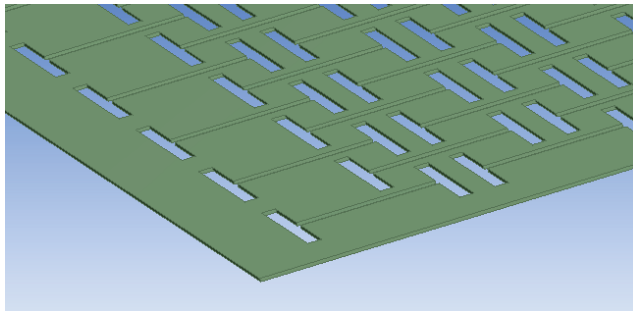


Figure 56. Isometric model of the H-pattern Aluminium sheet.

## 6 Collector testing

Testing is an essential step in order to evaluate solar collectors. This section describes the different collector prototypes that were tested as well as the equipment at the different locations where the collectors were tested, and the tests that were conducted at each location.

### 6.1 Collector Testing Method

#### 6.1.1 Key thermal parameters of a low concentration C-PVT

Solar collector characterization relies on two main testing methodologies: Quasi Dynamic Testing (QDT) and Steady State (SST). During this thesis, both methods were used to characterize the different prototypes that were tested.

According to Petterson et al. [58], QDT method offers the following advantages over SST:

- “It allows for accurate characterization of a wide range of collector types;
- It allows for testing under a wide range of operating and ambient conditions;
- It gives a more complete characterization of the collector through an extended parameter set as compared to steady state testing.”

However according to Afonso et al. [59], “*applying QDT can be difficult in other locations where the weather is very stable or where diffuse fractions are constantly very low*”. Other sources such as Fisher et al. [60] or Carvalho et al. [61] et al concur with the above statements.

In the QDT method, some of the boundary conditions parameters are kept strictly steady (flow rate and inlet temperature), while other parameters are left freely dynamic with only minor limit constraints. Paper VI utilizes QDT to characterize a standard flat plate thermal collector and the Solarus C-PVT, while Papers III, IV, V, 12, 13, 15, 16, 17, 32 use the SST method. The equation utilized in paper VI was adapted from the ISO 9806:2013 and is detailed below:

$$\begin{aligned} \frac{\dot{Q}}{A} = & F'(\tau\alpha) \times K_{\theta_b(\theta_L, \theta_T)} \times G_b + F'(\tau\alpha) \times K_{\theta_d} \times G_d \\ & - C_1(t_m - t_a) - C_2(t_m - t_a)^2 \\ & - C_3u(t_m - t_a) + C_4(E_L - \sigma T_a^4) - C_5 \frac{dt_m}{dt} \\ & - C_6uG \end{aligned} \quad \text{eq. 20}$$

The required input variables for a successful characterization using the above formula are: total irradiation; beam irradiation fraction; diffuse irradiation fraction; mean temperature of the collector; ambient temperature; wind speed; long wave irradiation; mean collector temperature change over time; and the power output of the collector per unit of collector area.

For the case of glazed collectors, however, it is often recommended that the wind speed and the long wave irradiation are omitted since their impact on the absolute losses and gains is negligible. In paper VI, two of the input parameters have been kept steady throughout the testing, the flow rate and the inlet fluid temperature (in different constant levels), while the rest were allowed to change freely.

The tool generally used for parameter identification is Multiple Linear Regression (MLR). This statistical model identifies the equation factors that best describe the collector based on how closely the produced equation can reproduce the collector power output accurately. Per definition, the parameter set + model gives zero error, in the *sum of energy*, over the chosen test period and selected data points. This method can be compared to stationary testing, when the model error in *efficiency* at clear sky conditions is minimized. This mathematical difference means that the parameter identification can give slightly different results even with perfect testing.

The following list summarizes the main terms commonly used to define a solar thermal collector:

- $F'_{(\tau\alpha)}$ : zero loss efficiency of the collector for beam irradiation, at normal incidence angle;
- $K\theta_{b(\theta_L, \theta_T)}$ : incidence angle modifier for beam solar irradiation.  $K\theta_b$  varies with the incidence angles  $\theta_L$  and  $\theta_T$ ;
- $K_{\theta_d}$ : incidence angle modifier for diffuse solar irradiation;
- $c_1$  : heat loss coefficient at  $(t_m - t_a) = 0$  (also mentioned as  $U_1$  or  $a_1$  in literature);
- $c_2$  : temperature dependence in the heat loss coefficient (also mentioned as  $U_2$  or  $a_2$  in literature);
- $c_3$  : wind speed dependence of the heat losses;
- $c_4$  : long wave irradiance dependence of the heat losses;
- $c_5$  : effective thermal capacitance;
- $c_6$  : wind dependence of the collector zero loss efficiency;
- $A$  : Collector area. This can be absorber, aperture or gross area.

SST testing, on the other hand, keeps all parameters in near steady state under a narrow range (the solar radiation can never be completely constant, even in perfect clear sky weather, as the sun moves continuously in comparison to the collector position). The Elforsk report [62] carried out by the author utilizes the SST method to characterize the first C-PVT prototype built by Solarus, which was tested by the author at Lund University. The following formula was used to obtain the thermal power from the measured collector:

$$P = (T_{out} - T_{in}) \times C_p \times \rho \times \text{Flow} / \text{Area of collector} \quad \text{eq. 21}$$

Where  $C_p$  is the specific heat capacity of the fluid in the collector, and  $\rho$  is the density of the fluid used in the test loop (normally water).

An important parameter for collectors is the stagnation temperature. Stagnation temperature is often defined, as the temperature reached by the solar thermal collector without flow, 1000W/m<sup>2</sup> of solar irradiance and ambient temperature of 40 °C. At stagnation, all incoming absorbed solar irradiation becomes heat losses from the collector. This number is often used to define the heat resistance properties that the solar collector and materials must possess in order to survive stagnation. Stagnation commonly occurs after the malfunctioning of a pump or controller or loss/leak of fluid in a solar thermal system during a sunny day.

### 6.1.2 **Key electrical parameters of a low concentration C-PVT**

The most important electrical parameter to describe a PV panel are peak power ( $P_{mp}$ ). Cell temperature dependence is usually given by the manufacturers, but it can also be measured. Parameters such as short circuit current ( $I_{sc}$ ), maximum power current ( $I_{mp}$ ), maximum power voltage ( $V_{mp}$ ) or open circuit voltage ( $V_{oc}$ ) are also important. As of 2018, common peak power of a silicon module, range between 200 to 350W for an area of 1.6m<sup>2</sup>. The cell temperature dependence characterizes the variation in power, efficiency, current or voltage, that a solar cell or PV panel undergoes with a change of temperature. For efficiency, in a silicon solar cell, this coefficient often ranges +0.3 %/K to +0.5 %/K [20].

Both the standard for flat PV panels (IEC 61215) and the standard for concentrated panels (IEC 62108), specify that peak power of a PV panel must be measured at Standard Test Conditions (STC) which are defined as ambient and cell temperature of 25°C, 1000W/m<sup>2</sup> of solar irradiance, air mass of 1.5 and zero wind speed.

These tests are generally performed outside, but they can also be done in a solar simulator. However, it is difficult to accurately simulate the solar spectrum since the sun is a very distant mass at a very high temperature and the transparency of the atmosphere is wavelength dependent. A problem with outdoor testing is that cells increase in temperature rapidly under sunlight and a cell temperature of 25 °C often exist only for a brief period after illumination. Indoor a flash test can assure this temperature condition is met however, this bring the drawback that the spectrum will not be perfect.

### 6.1.3 **Incidence angle modifier**

The incidence angle modifier (IAM) is a key parameter to define for any stationary collector, but it is especially important for concentrating collectors and even more relevant for stationary asymmetric concentrating collectors, such as the Solarus Power Collector.

According to Carvalho et al. [61], for a standard flat plate solar thermal collector, the IAM is commonly defined by the following equation:

$$K_{\theta b}(\theta) = 1 - b_0 \left( \left( \frac{1}{\cos \theta_i} \right) - 1 \right) \quad \text{eq. 22}$$

As mentioned above, other collectors such as vacuum tube or stationary concentrating collectors have more complex IAM profiles that need to be characterized with additional detail. A common resolution for IAM testing is in intervals of 5°. Namely, the Solarus C-PVT has specific characteristics that are important to consider when measuring the IAM.

The IAM can be electrical or thermal. In order to measure the IAM, the collector's electrical or thermal power, is measured at different incidence angles, while making sure that the irradiation and the cell temperature remain constant. For the thermal IAM, the measurements must be spaced out in time to account for the thermal mass.

Further details on the measuring methods of the IAM are given in chapter 5.3.2 and in Papers III and IV.

#### 6.1.4 Calculation of the theoretical maximum electrical power

This chapter presents a numerical example of a theoretical calculation of the maximum electrical power of the collector. The calculations below represent an improvement over the calculations done in Paper III by adding further information, like the transparency of silicone and the average number of bounces (reflections on the reflector):

$$P_{electric\_max} = P_{electric\_top\_max} + P_{electric\_bottom\_max} \quad \text{eq. 23}$$

$$P_{electric\_max} = 110.5 + 159 = 269.5 \text{ W}$$

$$P_{electric\_top\_max} = A_{cells\_top} \times \tau_{silicone} \times \tau_{glass} \times \eta_{cells\_25^\circ\text{C}} \times G_{max} \quad \text{eq. 24}$$

$$P_{electric\_top\_max} = 0.617 \times 0.97 \times 0.945 \times 0.197 \times 1000$$

$$P_{electric\_top\_max} = 110.5 \text{ W}$$

$$P_{electric\_bottom\_max} = P_{electric\_bottom\_beam} + P_{electric\_bottom\_diffuse} \quad \text{eq. 25}$$

$$P_{electric\_max} = 149.2 + 9.8 = 159 \text{ W}$$

$$P_{el\_bot\_beam} = C \times A_{cells\_bot} \times \tau_{silicone} \times \tau_{glass} \times (\tau_{ref} \times \text{avg}_{bounce}) \times \eta_{cells\_25^\circ\text{C}} \times G_b \quad \text{eq. 26}$$

$$\begin{aligned}
& P_{electric\_bottom\_beam} \\
& = 1.7 \times 0.617 \times 0.97 \times 0.945 \times 0.92 \times 0.883 \times 0.197 \\
& \times 900
\end{aligned}$$

$$P_{electric\_bottom\_beam} = 149.2 \text{ W}$$

$$\begin{aligned}
P_{el\_bot\_dif} = C \times \frac{1}{C} \times A_{cells\_bot} \times \tau_{silicone} \times \tau_{glass} \times (r_{ref} \\
\times avg_{bounce}) \times \eta_{cells\_25^\circ C} \times G_{dif} \quad \text{eq. 27}
\end{aligned}$$

$$\begin{aligned}
& P_{electric\_bottom\_diffuse} \\
& = 1.7 \times \frac{1}{1.7} \times 0.617 \times 0.97 \times 0.945 \times 0.883 \times 0.197 \\
& \times 100
\end{aligned}$$

$$P_{electric\_bottom\_diffuse} = 9.8 \text{ W}$$

## 6.2 Testing at Lund University

This section summarizes the testing of the first ever version of the Solarus C-PVT as well as a comparison to a stationary concentrating thermal collector also from Solarus. A full description can be found on the Elforsk report [62]. Throughout this thesis, this prototype version will be referred to as V0.

### 6.2.1 Description of the prototype collector

Figure 57 describes the V0 prototype C-PVT collector that was tested.



Figure 57. The first Solarus C-PVT Prototype (V0) installed at Lund University.

The glazed area of this prototype was 2.3 m<sup>2</sup>, which is a significant difference from the current version (PC). Effective solar thermal area was 2.18 m<sup>2</sup>. Each receiver had 26 solar cells on each side of the absorber. Each cell had the dimensions of 0.07 m by 0.145 m. This means that a string of 26 cells has an area of 0.264 m<sup>2</sup>. The total cell area of the two receivers in the above figure totals:  $4 * 0.264 = 1.06 \text{ m}^2$ . The effective glass area for electricity production equals  $2 \text{ trough} * 3 * 0.264 = 1.58 \text{ m}^2$ . The number 3 comes from the overall collector concentration factor of 1.5. The cells were soldered manually. Manual soldering causes more micro cracks than machine soldering as shown in Paper II.

The backside and the front side PV cells were connected in parallel. The top and the bottom receiver sides were also connected between themselves in parallel.

The geometric concentration factor of this reflector design is 3; however, since there are solar cells on the front and back of the absorber the real concentration factor was 1.5. Concentration ratio for the front is 1, while the cells on the back receive 2 suns.

The four Solarus stationary concentrating thermal collectors displayed in Figure 58 were compared to the C-PVT prototype and are thus named reference collectors. Both the reference and the C-PVT collectors have the same box with the same reflector geometry as well as glazed area. The absorber of the reference collector has selective surface on both sides and was produced by the company Sunstrip.



Figure 58. Four Solarus stationary concentrating thermal collectors installed at Lund University.

## 6.2.2 Method

Testing was conducted at the solar laboratory at Lund University. The main testing period was between 7<sup>th</sup> of May to 30<sup>th</sup> of May. Collector tilt was set to 30° for both C-PVT and reference thermal collectors.

### 6.2.2.1 Thermal Testing:

The thermal testing method was SST, which was described in the previous chapter. The flow was set to  $11 \text{ l/6minutes} = 3.06 * 10^{-5} \text{ m}^3/\text{s}$  and kept constant

throughout the full duration of the tests. This is for a collector with an area of  $2.57 \text{ m}^2$ , meaning a flow of  $0.71 \text{ l/m}^2$ , in conformity with the solar collector standard for testing (ISO 9806:2017).

In order to produce the thermal efficiency curves, it was necessary to select two periods without any clouds, so that the solar irradiation remains constant. Figure 59 and 60, show the solar radiation during the two selected periods. Additionally, these two periods have to be large enough to ensure that a thermal equilibrium point has been reached.

Furthermore, extra power measurements were taken during the night, using high and low inlet water temperatures. This measurement is a common technique for estimating the U-value of a collector, since the U-value is equal to the slope of the thermal efficiency curve.

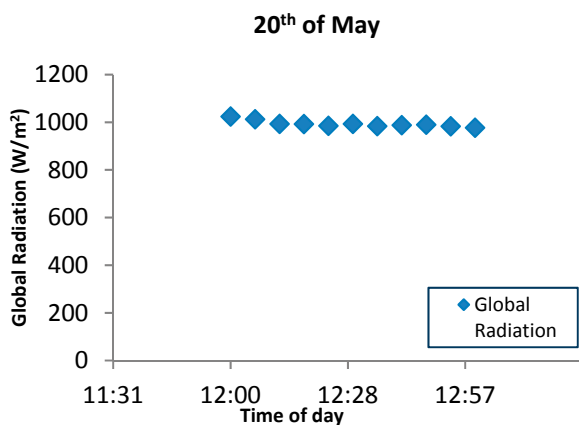


Figure 59. Global Solar Irradiance on the day of the measurements.

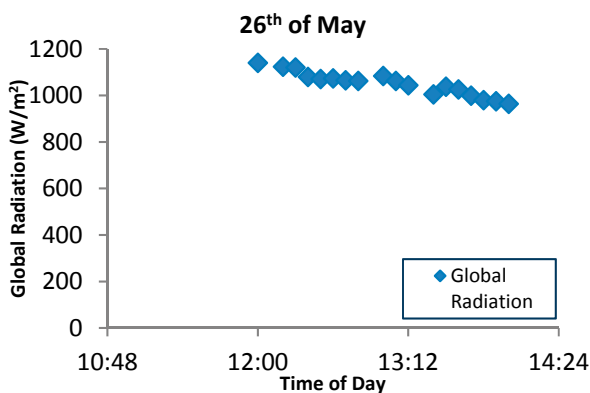


Figure 60. Global Solar Irradiance on the day of the measurements.



### 6.2.2.2 Electrical Testing:

The C-PVT V0 has two receivers as shown in Figure 58. On the bottom receiver, the measured values were for both the back side and the front side simultaneously. On the top receiver, the cables were reconnected in order to perform individual measurements to investigate exclusively the backside or exclusively the front side.

IV curves were continuously measured and recorded with a Campbell Scientific CR1000 logger. With each IV curve,  $P_{max}$ ,  $I_{sc}$ ,  $I_{mp}$ ,  $FF$ ,  $V_{mp}$  and  $V_{oc}$  were stored. These values were averaged over six minute intervals.

## 6.2.3 Results

### 6.2.3.1 Night heat loss measurements:

Figures 61 and 62 are based on all available night data and allow making an estimation of the U-value for both V0 and the reference thermal collector.

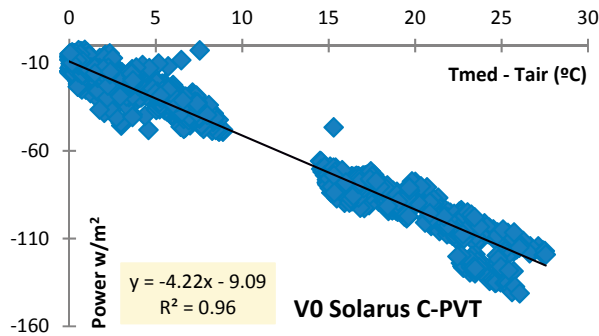


Figure 61. Heat loss measurement during night time for the C-PVT V0.

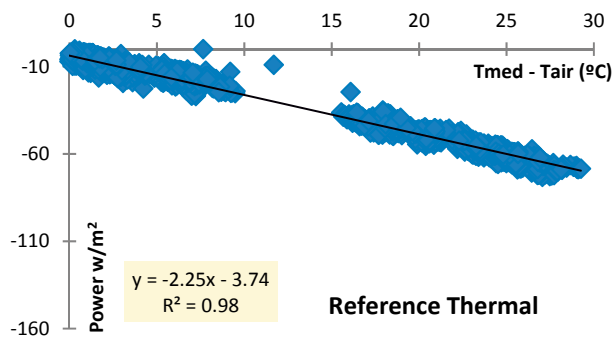


Figure 62. Heat loss measurement during night time for the reference thermal.

### 6.2.3.2 Thermal efficiency curves:

Using the sunniest hours, it was possible to obtain the following thermal efficiency graphs. These results are displayed in Figures 63 and 64.

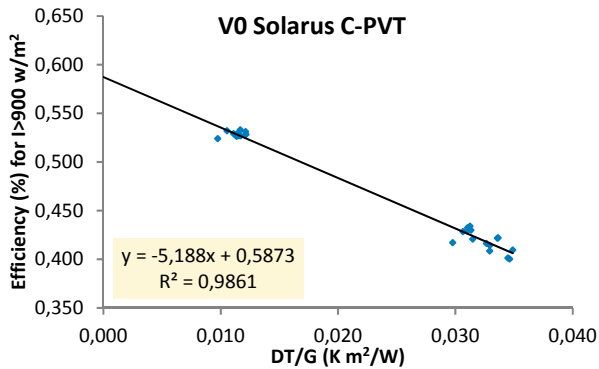


Figure 63. Thermal Efficiency of the Solarus C-PVT V0 at  $>900\text{W/m}^2$ .

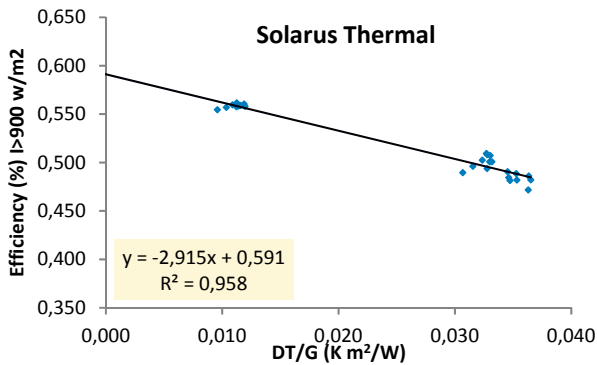


Figure 64. Thermal Efficiency of the Solarus thermal collector at  $>900\text{W/m}^2$ .

It is possible to extract the optical efficiency and the global heat loss coefficient (U-value) of both collectors from Figure 63 and 64. The optical efficiencies of both collectors were fairly identical. This is due to the silicon cells and the black selective absorber having both high solar absorptivity, even if the selective surface has typically a higher solar absorptivity. On the other hand, heat loss shows a large difference between both collectors, which is particularly visible at higher temperatures.

It is relevant to note again, that the only difference between both collectors is the receiver. However, while V0 C-PVT possesses a non-selective string of PV cells encapsulated on a reflective Aluminium receiver, while the reference collector has a black selective absorber that greatly reduces the thermal radiation heat losses. This is the reason why the reference collector has a U-value of only about half of the C-PVT V0.

Table 23. Optical efficiency and measured heat losses of tested collectors

	Solarus Thermal	C-PVT (V0)
Optical Efficiency (%)	59.1	58.7
Global (day) U-value (W/m <sup>2</sup> , K)	2.92	5.19
Night U-value (W/m <sup>2</sup> , K)	2.25	4.22

### 6.2.3.3 Daily Thermal Power Curves:

Figures 65 and 66 shows the daily output and the mean fluid temperature of the reference thermal collector and the Solarus C-PVT V0 as well the global irradiation.

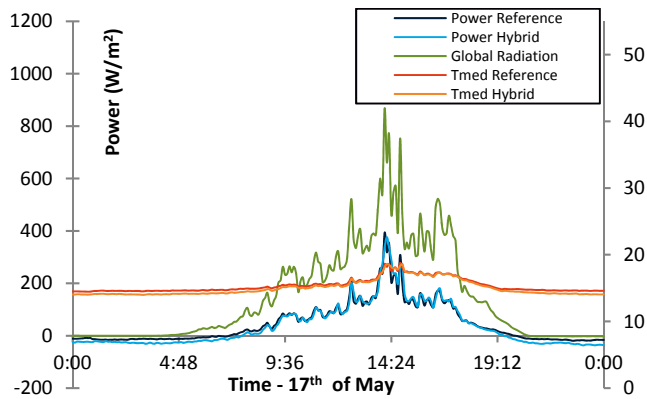


Figure 65. Global irradiation and average collector temperature plus power output for the Reference and V0 collector on the 17th.

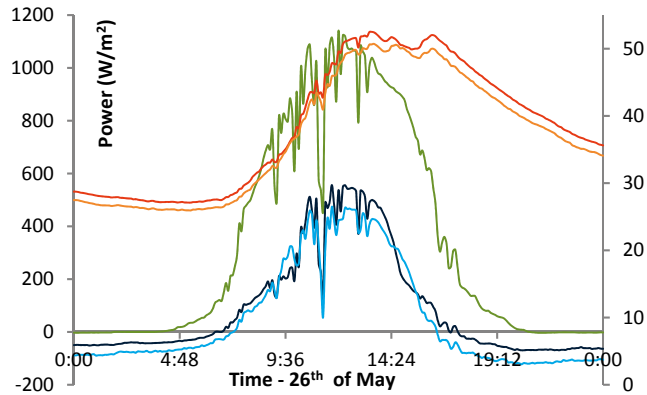


Figure 66. Global irradiation and average collector temperature plus power output for the Reference and V0 collector on the 26th of May.

#### 6.2.3.4 Daily Electrical Power Curve:

A large number of electrical measurements have been conducted and analyzed. Figure 67 shows the electrical power from the front and the back side of the V0 collector during a fully sunny day.

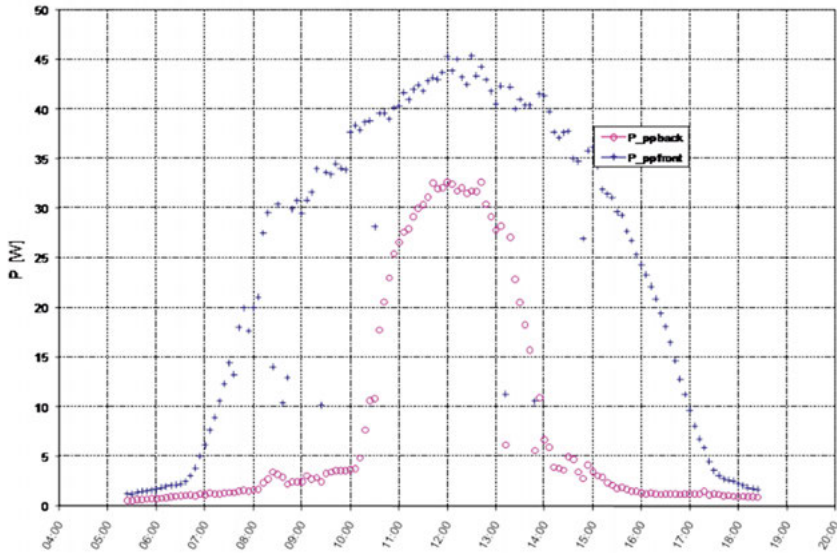


Figure 67. Electrical power from the front and back side of the V0 collector during a clear day with high fraction of beam irradiance.

The IV-curves in the figure above show that the front cells are working as expected at midday:

$$\eta = 45 / (1000 \times 0.264) = 17.1 \%$$

The output of the backside is low at solar noon and decreases rapidly outside of this period. The efficiency in the middle of the day is:

$$\eta = 32.5 / (2 \times 1000 \times 0.264) = 6.2 \%$$

In order to calculate the efficiency of the backside cells, it is important to take into account the backside concentration of 2. The low efficiency at solar noon is due to optical losses in the reflector, uneven illumination and current capacity issues. Outside of solar noon, power production falls rapidly, as the side gables cast a shadow on the outermost cells, which causes the whole string to stop working since the cells are series connected between themselves.

An analysis of the IV curves of the front cells results in a fill factor of 75%. This indicates that the absorber is able to successfully cool the cells. However, the IV-curve for the backside cells at 12:24 when there is no shading due to the

side gables, results in a fill factor of 60%. The lower fill factor should be a result of uneven illumination of the cells. The focus line of an ideal reflector creates varying irradiance over the cells but with the same overall irradiance on each cell. However, in reality, reflectors are not ideal and, thus, create different overall irradiance on the cells. Both these effects reduce the fill factor. The varying total irradiation between the cells has the greatest negative impact on the fill factor and performance. In addition, it is likely that the current capacity of the backside cells is reducing the backside output due to resistivity losses.

#### **6.2.4 Conclusions**

Solarus C-PVT V0 has been tested. Thermal performance has been quantified and compared to a reference thermal collector. The overall optical efficiency of both collectors is relatively low; however, the heat loss factor is also low. As expected, the optical efficiencies of both collectors are similar, but the heat losses are significantly different due to the lack of selective surface on the C-PVT V0. The higher heat losses will lead to a lower stagnation temperature, which in turn improves survivability and reduces material requirements. Due to the heat losses, the V0 collector is best suited for low to medium temperature applications. The V0 receiver also seems to have a higher inertia since its thermal power output tends to drop slower during the afternoon. Electrical measurements show the front side cells are working well which indicates that the receiver is able to successfully cool down the cells. Reflector losses and high current in the cells leads to a low peak power for the backside cells. Furthermore, the side shade from the gables has a very large impact on the daily electric power output from the collector and needs to be prevented. Either some cells are removed for the edge of the strings or diodes are placed to bypass these cells outside of peak sun.

Lastly, the packing density should be increased to maximize the total electricity output.

### **6.3 Paper III: Testing at Eduardo Mondlane University**

Together with colleagues from Lund University, the author has built from scratch a solar laboratory at Eduardo Mondlane University, in Maputo, the capital of Mozambique. The construction of this solar laboratory is described in full detail in Papers 13 [63] and 18 [64]. The test results from this laboratory are described in its fullest extent in Paper III and in report [65].

#### **6.3.1 Description of the prototype collector & laboratory set-up**

As a part of a project funded by the Swedish International Development Agency (SIDA) and the Gulbenkian Foundation of Portugal, a small solar laboratory was constructed. The equipment installed at this laboratory is described in detail in Paper 18 [64] and summarized below:

1. Data Loggers:

- **Campbell CR1000 DataLogger.** Analog, digital and pulse inputs are suitable for the adopted scientific data logger. For the mean voltage input range  $\pm 2.5\text{V}$ , maximum resolution is  $0.67\text{ mV}$  and measurable through up to 16 single-ended ports. High accuracy, versatility and reliability allowed this product to be spread worldwide for scientific application. The price is approximately 1500 USD.
- **MELACS®.** It enables stand alone data logging and remote collection through the built in web server. Connection of multiple loggers (e.g. to increase the number of ports) is possible through the Ethernet port. Voltage input range is fixed to  $\pm 3.3\text{V}$ , corresponding to  $0.8\text{ mV}$  of resolution and measurable through 8 channels. Pulse and digital channels are also available. It works with open-source GPL software. Current price is about 260 USD.

2. Water temperature sensors:

- **PT100 Class A.** High precision temperature measurements were carried out through a PT100 sensors with an immersed insert. The Class A definition guarantees the accuracy of  $\Delta T = \pm(0.15 + 0.002 \cdot |T|)$ , where  $|T|$  is the absolute temperature in degrees Celcius ( $^{\circ}\text{C}$ ). Pentronic AB was the chosen manufacturer, which supplied and tested 30 sensors according to EN10204. In order to have similar offset in measurements, the two PT100 sensors with closer response during the test were chosen for the  $\Delta T$  measurements. Despite the benefit of fluid immersed measurement, appropriate plumbing adaptation is required as show in the Figure 68. Adaptors are rather expensive, approximately 60 USD.
- **LM35CZ.** LM35CZ are precision integrated-circuit temperature sensors produced by National Semiconductor Corporation. Voltage output is linearly proportional to temperature (in Celcius) with  $0\text{ mV}$  as set point for  $0^{\circ}\text{C}$  and  $+10.0\text{ mV}/^{\circ}\text{C}$  scale factor; nonlinearity typically below  $\pm 1.4^{\circ}\text{C}$  is guaranteed over the full range of  $55$  to  $150^{\circ}\text{C}$ . Accuracy is  $\pm 0.4^{\circ}\text{C}$ , hence  $\pm 4\text{ mV}$ , at  $25^{\circ}\text{C}$ , up to a typical value of  $\pm 0.8^{\circ}\text{C}$  in extreme conditions. The price is approximately 5 USD each. Copper paste on the surface and good insulation around the pipe must be carefully provided to have good thermal contact and low heat losses. Indeed, the sensor could record the air temperature in the proximity of the pipe instead of the pipe surface temperature as shown the in the Figure 68. Since the device is not specifically designed for water temperature measurements, it can be successfully used for other applications.

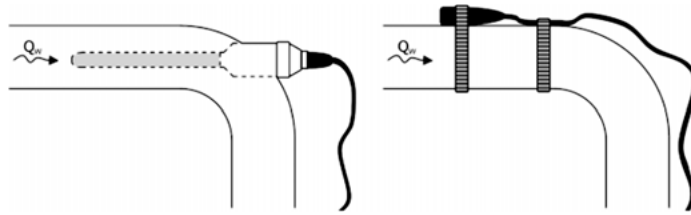


Figure 68. Sensor positioning for PT100 (left) and LM35 (right).

3. Solar irradiation:
  - **Kipp&Zonen CMP 11.** Scientific pyranometer calibrated after purchase according to the technical regulations of World Meteorological Institute. Estimated combined expanded uncertainty for the used device is  $\pm 1.4\%$ , corresponding to  $8.67 \mu\text{V}/\text{Wm}^2$  of sensitivity at normal incidence on a horizontal pyranometer. Commercial price is about 4,000 USD.
  - **Finsun SRS1000.** Basic pyranometer with sensing element made of single crystal Si-cell. The output voltage is 100 mV when exposed to  $1000 \text{ W}/\text{m}^2$  solar irradiance. Sensitivity, offset and ageing tests were performed. Commercial price is approximately 115 USD.
4. **Flow meter.** Kamstrup 10EVL-MP110 energy and flow meter was adopted. No cheaper flow meter was tested.
5. **Concentrating thermal (reference) and C-PVT collectors.** It is important to mention that this version of the C-PVT solar collector is named V1 in this thesis.
6. **Solar tracker.** A horizontal single axis tracker (HSAT) was installed. The tracker is based on an electric motor driven by a Melacs® logger. The software controls the position of solar panels using time and location as input. This solution allows a correct positioning without the use of additional photodiodes-based trackers, thus cutting costs and maintenance.
7. **IV tracer.** The IV tracer used had the capacity to perform IV curves with the limits of 30V and 10A.

Figures 69-71 illustrate several aspects of the equipment of the solar lab such as the solar tracker, the two installed collectors, the tank, the pump, the logger, the flowmeter, the Melacs® loggers, as well as the set-up for both the longitudinal and transversal IAM measurements.



Figure 69. The C-T and C-PVT solar collectors installed in the solar tracker (left) and the installation equipment inside the laboratory housing.

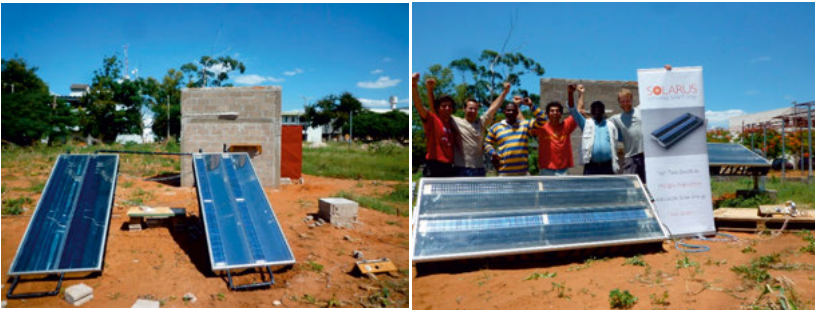


Figure 70. The collectors installed for the transversal IAM measurements (left) and the team celebrating the success of the longitudinal IAM measurements (right).



Figure 71. Detailed view of the C-PVT V1 and the pyranometers

Figure 72 illustrates the electrical arrangement of the solar cells PVT V1.



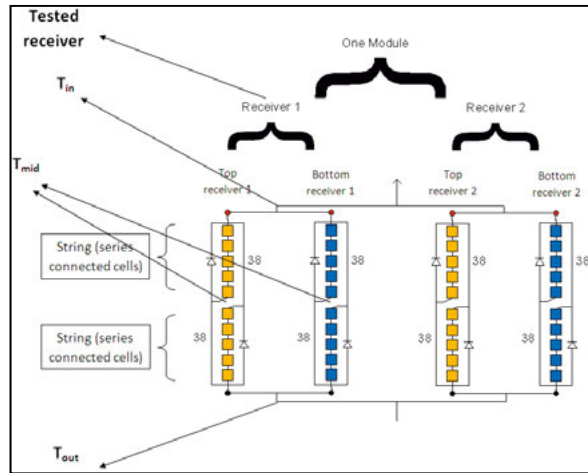


Figure 72. Electrical diagram of the PVT V1.

Table 24 details the areas used to calculate the efficiency of the collector.

Table 24. Different areas used to calculate the efficiency of PVT V1.

$A_{\text{cells}}$ of one receiver ( $\text{m}^2$ )	0.577
$A_{\text{effective reflector electrical}}$ ( $\text{m}^2$ )	0.869
Effective Concentration Factor (-)	1.506

### 6.3.2 Method

As discussed previously in Chapter 6.1, there are a number of factors that influence the performance of a C-PVT solar collector. Due to this, performance measurements should be conducted in a specific order. The first step was to determine the efficiency of the solar cells and its relation to the temperature of the working fluid. This test was performed in an incidence angle that maximizes the electrical output, i.e., close to normal incidence, but not normal, due to the asymmetric curvature of the reflector. Once the temperature dependence was determined, the angular dependence or, more accurately, the incidence angle modifiers could be measured.

Normally, when testing the output of a PVT panel, it is expected that an electric load is permanently connected to the PV cells and electric power is continuously extracted at maximum power point. However, the presented method of instantaneous IV curve measurements simplifies the whole test procedure significantly. These results are less expensive and less time consuming to achieve while still maintaining a good level of accuracy. If an electric load were continuously connected, the absorber would be colder since a part of the incoming irradiation would be converted to electricity. This would mean lower temperatures and thus slightly lower thermal losses. This difference is however small and has little impact on the results [66]. Since the cell is encapsulated in

silicone, it was not possible to measure the cell temperature directly. Instead, the temperature of the outlet water was measured. In a series connected string, the cell producing the lowest output will be limiting the string output. In general, the warmest cell tends to be the cell with the lowest output; however, this may not always be the case, as there are efficiency differences between each cell due to the production process.

**Incidence Angle Modifier testing method:**

As mentioned previously, the transverse incidence angle modifier ( $IAM_t$ ) is defined by the reduction in electrical efficiency for a given irradiation caused by the increase of the incidence angle between the sun and the normal to the collector in the transverse direction ( $\theta_t$ ). This is exemplified in Figure 73. When the sun is normal, for transversal angles, from  $0^\circ$  to  $+90^\circ$  the sun's direction is inside the acceptance angle of the reflector and outside from  $0^\circ$  to  $-90^\circ$ . However, for longitudinal angles, the front part of the receiver accepts light coming in from  $-90^\circ$  to  $90^\circ$ . The  $IAM$  measurements are a combination of all angular effects such as decrease of transmission in the glazing for high incidence angles and shading effects by edges, etc.

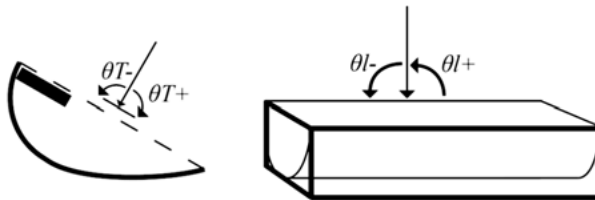


Figure 73. Transversal incidence angle to the left and longitudinal incidence angle to the right.

To be able to measure  $IAM_t$  for different transverse angles the longitudinal angle had to be kept equal to zero. This was measured by facing the collector towards the solar azimuth for various tilt angles. This is illustrated in Figure 74:

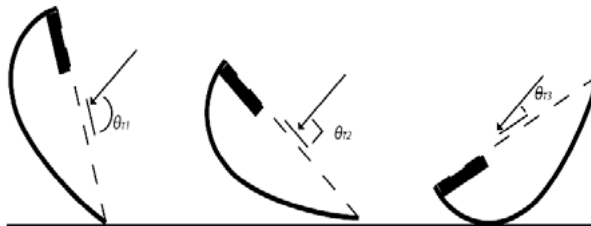


Figure 74. Tilting the collector to achieve different transverse incidence angles.

The incidence angle modifier applies for the direct irradiation only. However, even during clear days, there is always a percentage of diffuse light that contributes to the measured power output, and while, in a clear day, this percentage

can be around 10%, in less sunny days, this percentage can reach 100%. This way, the diffuse contribution becomes relevant for low concentrating collectors such as the Solarus one.

The fraction of useful diffuse irradiation for a concentrating collector, relative to the total diffuse irradiation on the glazed cover of the collector is described in Figure 75. The pyranometer, labelled as (A), will see  $(1 + \cos(\beta))/2$  of the full sky. This is the same as for the front side of the receiver, which is labelled (B). It is correct to assume they see the same part of the diffuse sky when a non-concentrating collector is tested. This is however, not the case for the backside of the receiver. The acceptance angle for the reflector blocks a substantial part of the sky. This part is indicated with red arrows. The irradiation that will reach the backside of the receiver is labelled (C), and is equal to the irradiation measured by the pyranometer minus half the sky due to the acceptance angle. This is true for a positive tilt, i.e. the left collector shown in the figure below. The collector on the right hand side of the figure shows the case for tilting the reflector backwards. The pyranometer (D) and the front side (E) of the receiver are unaffected. However, the backside radiation (F) will be half of the sky as long as the tilt  $\beta$  is less than  $90^\circ$ . This happens since the part outside the acceptance angle is now facing the ground. Thus, the part of the diffuse radiation inside the acceptance angle is always half of the sky.

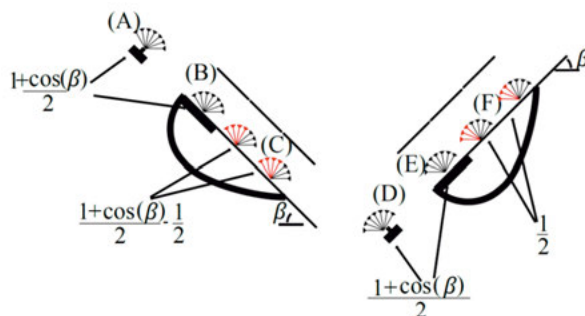


Figure 75. Fraction of useful diffuse radiation for different transverse incidence angles.

The fraction,  $f$ , of the diffuse irradiation that is useful for the collector can be calculated by summing the contributions from the front side and the backside of the receiver and dividing this by the diffuse radiation measured by the diffuse pyranometer. The front side of the receiver accounts for one third of the total glazed area, while the backside, via the reflector, accounts for two thirds of the total glazed area. If the collector is rotated as in the left side of Figure 75,  $f$  will be:

$$f = \frac{\frac{1}{3}\left(\frac{1+\cos(\beta)}{2}\right) + \frac{2}{3}\left(\frac{1+\cos(\beta)}{2} - \frac{1}{2}\right)}{\frac{1+\cos(\beta)}{2}} \quad \text{eq. 28}$$

If the collector is rotated as in the right side of the figure 75,  $f$  will be:

$$f = \frac{\frac{1}{3}\left(\frac{1+\cos(\beta)}{2}\right) + \frac{2}{3}\left(\frac{1}{2}\right)}{\left(\frac{1+\cos(\beta)}{2}\right)} \quad \text{eq. 29}$$

However, this is true for an infinitely long trough without any shading from the edges. This is not the case for the investigated collector. The front side of the receiver will be only slightly affected by shading and the shading effect is thus omitted. The shading of the backside will be more relevant. This is illustrated to in Figure 76.

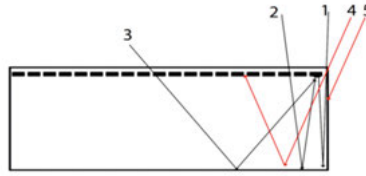


Figure 76. Shading of the PV cells due to the gables of the collector.

The black arrows hit the edge cells while the red arrows miss the cell. The arrow labelled 1, close to normal incidence will be reflected to the outermost PV cell. So will all rays coming from an even lower angle, e.g. rays labelled 2 and 3. For radiation with a higher incidence angle, the rays will be either reflected to hit another cell or will be stopped by the edges. This means that the outermost cell can only see roughly half of the diffuse sky. The problem is identical for the left side of the collector. This will reduce the contribution from radiation to the backside of the receiver, i.e. (C) and (F) in Figure 51 by approximately 50%. This will change eq. 8 and eq. to:

$$f = \frac{\frac{1}{3}\left(\frac{1+\cos(\beta)}{2}\right) + \frac{2}{3}\left(\frac{1+\cos(\beta)}{2} - \frac{1}{2}\right)}{\left(\frac{1+\cos(\beta)}{2}\right)} = \frac{1+2\cos(\beta)}{3(1+\cos(\beta))} \quad \text{eq. 30}$$

$$f = \frac{\frac{1}{3}\left(\frac{1+\cos(\beta)}{2}\right) + \frac{2}{3}\left(\frac{1}{2}\right)}{\left(\frac{1+\cos(\beta)}{2}\right)} = \frac{2+\cos(\beta)}{3(1+\cos(\beta))} \quad \text{eq. 31}$$

Measurements of the  $IAM_t$  were carried out by varying the tilt  $\beta$  from  $-30^\circ$  to  $+30^\circ$  as shown in Figure 74 and Figure 75. Figure 77 shows a plot of eq. and eq. 31731. The variation in the fraction of the useful diffuse irradiation is small for this tilt interval. Hence, the fraction of useful diffuse irradiation was set to be the average of its value and equal to 50%. The longitudinal incidence angle

modifier ( $IAM_t$ ) was measured while keeping a constant  $\theta_t$  which corresponds to the measured maximum value of  $IAM_t$ .

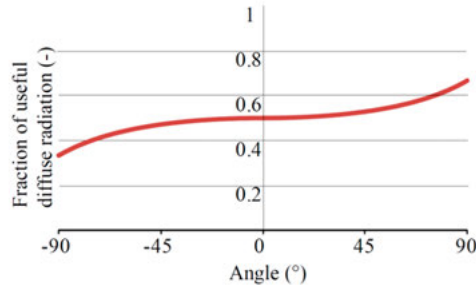


Figure 77. The fraction of useful diffuse radiation as a function of the collector tilt.

### 6.3.3 Results

Figure 78 shows the measured electrical efficiency per cell area for the V1 PVT collector at 25 °C, which is 20.9 %. Expressed per active glazed area this efficiency is 13.9 %. This means that the maximum electrical power output for this collector is 241 W or 139 W/m<sup>2</sup> active glazed area. As expected, this number is 11 % lower than the optimum output of 269.5 W for a perfect optical efficiency.

The dependence of electrical efficiency on cell temperature ( $K_T$ ) is -0.41 %/K, which is in good agreement with values commonly described in literature [20].

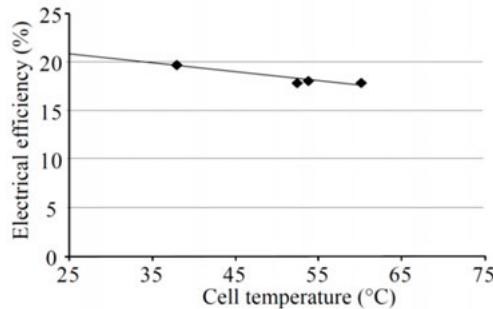


Figure 78. Dependence of the electrical efficiency on temperature.

Figure 79 shows the electrical transverse and longitudinal incidence angle modifiers for the beam irradiation,  $IAM_t$  in blue and  $IAM_l$  in red. The measured values are adjusted for temperature variations. The sharp increase/decrease around 0° for the  $IAM_t$  is due to the irradiation shifting from outside to inside of the acceptance angle. The separate  $IAM_l$  for the front side and backside receivers/cells is shown in yellow and green respectively. The sum of the back and front  $IAM_l$  is equal to the  $IAM_l$  (red in the Figure). Figure 79 shows that the front side receiver behaves very similarly to a flat plate solar panel. The

backside receiver is mainly responsible for the efficiency drop during low incidence angles in the longitudinal direction due to the series connection of the cells.

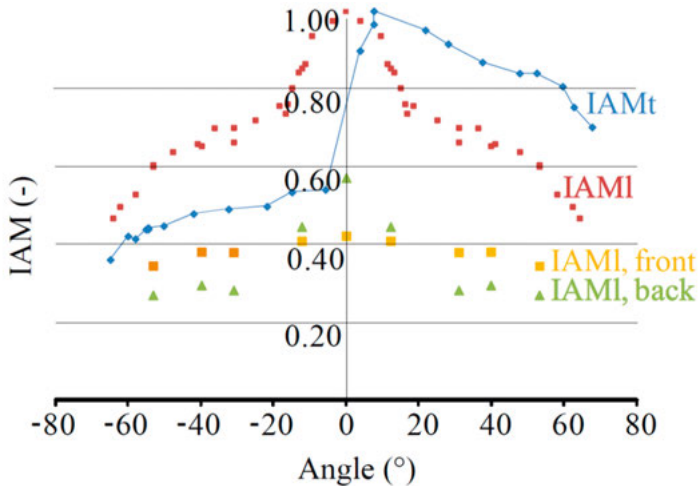


Figure 79. Electrical transverse incidence angle modifier (IAMt) for beam radiation in blue and the longitudinal incidence angle modifier (IAMl) in red. The IAMl for the backside and the front side of the receiver are shown in yellow and green respectively.

By analysing Figure 79, it is possible to conclude that, if the collector was tracking the sun around an axis aligned in the East-West direction, it should maintain the projected solar height over the day close to  $10^\circ$  in order to maximize the annual output. The drop in the longitudinal incidence angle modifier is due to the shading caused by the reflector edges. When  $0^\circ < \theta_i < 30^\circ$  the decrease in the IAMl is quite steep. This corresponds to partial shading on the first cell placed at the edge of the backside receiver, as described in the previous chapter. At around  $\theta_i = 30^\circ$  the cell on the edge on the backside is totally shaded, eliminating almost completely the production of that string. Shading more cells when  $\theta_i > 30^\circ$  will not induce a further production decrease on that string and thus, the total efficiency decrease slows down. Without the diode installed on the string, the drop would be double, since the strings are connected in series. I.e., the total IAM would drop to about 0.5 and not just to the 0.75, as seen Figure 55. This is even more obvious, when analysing the backside of the absorber, where the output drops from 0.58 to 0.29, i.e. a 50% reduction. As can be seen from the same figure, the front side is much less affected by the shading. The IAMt shown in Figure 55 is in agreement with previous measurements for the thermal production of a solar thermal collector with the same geometry [67].

This PVT collector (V1 and remaining designs) are made of two different parts. A front part where the solar cells behave like a standard flat plate solar panel with no concentration and a back part under concentration using a reflector. Since there is no synergic effect from combining non-concentrating solar cells with concentrating solar ones, only one of these alternatives should be the

most cost-effective way of building a solar collector rather than a combination of both. The choice between a concentrating or non-concentrating system depends on the concentration factor, the fraction of diffuse to beam irradiation in the geographical location, the compactness needed for the collector, the temperature of the application and many other factors, as discussed in the previous Chapters.

The reflector part of the collector concentrates the irradiation two times on the back side receiver. If the optical efficiency is around 50%, meaning that, under optimum conditions, the collector produces the same electrical output as a flat plate solar panel for the same temperature. This conclusion would change significantly, if the concentration factor were increased and the optical efficiency maintained. Hence, the concentration factor has an important influence on the output per cell area. One way of increasing the concentration could be to reduce the cell area on the backside of the receiver while using a tracking system. This can be done by cutting the cells in half or in thirds in the parallel direction of the busbars. The effect of the radiation profile after reflection should be further investigated.

As shown in Figure 78, a limitation of this study is the reduced amount of measured data for the dependence of efficiency on the temperature. Measurements were also carried out with cheaper sensors in order to verify the possibility of building low investment scientific solar laboratories in developing countries. The overall accuracy of measurement with such sensors was lowered by 9%, but with a cost reduction of above 90%, as showcased by the Paper 18 [64].

#### **6.3.4 Conclusions**

The optical properties of PVT V1 were determined. These include the electrical transverse and longitudinal incidence angle modifiers, taking into account edge effects, by-pass diodes, acceptance angle and diffuse radiation contribution. The measured electrical efficiency at 25 °C outlet water temperature was 20.9 % per cell area and 13.9 % per active glazed area during peak hours. During a large period of the day the output is significantly reduced by the reflector edges, as shown by the IAM measurements. This represents a big margin of improvement for the collector. By removing the cells on the edge, turning the edge cells 90°, dividing the string into three or four parts or even tracking the collector around an axis oriented in the North-South direction, the collector performance can be significantly improved. Hence, the annual production can become competitive with a flat plate solar panel while, at the same time, producing hot water.

### **6.4 Paper IV: Testing at Solarus, Gävle and Dalarna Universities**

Paper IV deals with the measurements on PVT V2, V3 and V4. It is important to note that the notation of the thesis and Paper IV are different. In Paper IV, these are called V1, V2 and V3, meaning that V4 in the thesis is V3 in the paper.

### 6.4.1 Overview of the different laboratory set-ups

For practical reasons, during this study, the different versions of the PVT collectors were tested in various locations in Sweden at different times, as shown in Table 25, in Figure 80 and in Figure 81. Table 25 also shows the equipment used at each of the locations. All locations have similar latitude and longitude.

Table 25. Overview of measurement locations of Paper IV.

Location	Solarus factory in Älvkarleby	Dalarna University	Gävle University	
Type	Indoor Simulator	Outdoor	Outdoor	
IV tracer	Same for all measurements			
Solar Radiation	Reference Cell	Reference Cell	K&Z CM11	Reference Cell
Temperature recording	Not needed	LM35	PT100	Not available
Flowmeter	Not needed	Kamstrup 9EVL-MP115 flowmeter	Krohne Optiflux 5000	Not available
Data Acquisition	Not needed	Melacs®	National Instruments	Custom software



Figure 80. Outdoor measuring for Paper IV: (a) Solarus Factory PVT V2; (b) Dalarna University PVT V3; (c) Gävle University PVT V4.

### 6.4.2 Indoor testing at the Solarus Laboratory

The indoor solar simulator consists of two rows of eight 1000 W halogen light bulbs. The indoor solar laboratory was used for testing the shading impact on the strings using the Solarus custom-size cells. As in many solar simulators, the light distribution is a drawback, since it does not match perfectly with the sun. However, this limitation is mitigated when performing comparative testing. This way, the indoor solar laboratory was used for testing the shading impact on the strings using the Solarus cell size.



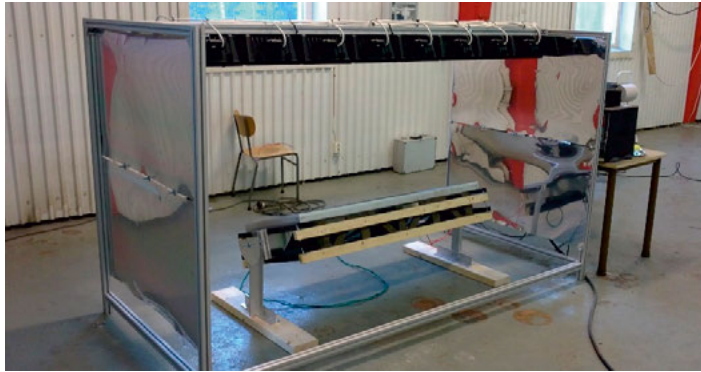


Figure 81. The solar simulator for the indoor measurements.

### 6.4.3 Outdoor Testing

The Outdoor Solarus laboratory is illustrated in Figure 80. IV Tracer is a custom made device, interfacing with the COM interface on a standard PC. A custom Excel macro logs the data periodically or on demand. The IV Tracer uses a current generator to measure the performance; it ramps up the current from zero to maximum, taking voltage and current samples in the process which lasts less than a second. Each IV curve, with values of  $I_{mp}$ ,  $I_{sc}$ ,  $V_{mp}$ ,  $V_{oc}$ ,  $P_{max}$ , FF is saved as a separate CSV file. The device was found to have a resolution of 0.008 V and 0.002 A, just like in Chapter 5.3 and 5.2. This IV tracer is used throughout this thesis.

The reference cell is from the European Standard Testing Institute and is calibrated to be linear from zero to 28.7 mV at 1000 W/m<sup>2</sup>. This reference cell had two outputs: one for data and one for temperature correction. The CM6 in Dalarna measured hemispherical irradiance with a total accuracy of 2% of the measured value. The CM11 measured diffuse irradiance and has an accuracy of  $\pm 1\%$ .

LM35 temperature sensors were used for measuring the inlet and outlet temperatures in Älvkarleby, with a measurement range of -55 °C to +150 °C and accuracy 0.5 °C at 25 °C. These were placed against the copper pipe on the outside of the collector with copper paste being used to ensure a good thermal connection. In Dalarna, the sensors used were PT100s inserted inside the pipe, for water temperature, and in the shade behind the collectors for ambient temperature. These sensors have an accuracy of  $\pm 0.3$  °C at 0 °C. In Älvkarleby, the Melacs® was used to log data. The Melacs® (Micro Energy Logger And Control System) is a device built around a PIC16F microcontroller. It was used as a standalone data logger to read data from thermal sensors and the reference cell. It accepts eight analogue voltage inputs in the range  $\pm 3.3$  V with a resolution of 0.8 mV. In Dalarna, data was logged via a National Instruments Data Acquisition Unit using LabView. A Kamstrup 9EVL-MP115 flowmeter was used in Älvkarleby, which sends 5760 pulses per litre flow, with precision varying from  $\pm 1.5$  % at 2 °C to  $\pm 0.5$  % at 120 °C. The Dalarna setup had an

Optiflux 5000 flowmeters from Krohne, which were accurate to  $\pm 0.1\%$  of the measured value.

#### 6.4.4 Measured Collectors

Solarus is committed to continuous development and as such, has produced a large number of collector prototypes for research. Differences between the tested PVT versions are shown in Table 26. It is important to bear in mind that the numbering of the different collector versions are not the same in the thesis and in the papers.

Table 26. Differences between the tested PVT versions.

Version (Thesis number)	PVT V2	PVT V3	PVT V4
Collector Box	Earlier version	Improved version	Improved version
Receiver Type	Hollow Aluminium core	Solid Aluminium core	Solid Aluminium core
End Gables	Reflective	Transparent	Transparent
Cell Size	All cells were 1/6 of the size of a standard cells	All cells were 1/6 of the size of a standard cells	One trough with cell strings of 1/3, and the other trough with 1/6

**Collector Box:** The collector box has been improved from PVT V2 to PVT V3. The new collector box is sturdier and has improved water insulation.

**Receiver Type:** The receiver design has been improved from PVT V2 to PVT V3. The V2 consisted of a number of parallel pipes of about 5mm diameter, laminated with two thin sheets of metal on either side, while V2 is a massive aluminium extrusion a patented cross-section. This receiver should be more effective at cooling the solar cells, thus producing a more even heat distribution, which in turn reduces the  $F'$  value (basically, there is a better heat transfer or “thermal contact” from cell to fluid).

**End Gable:** The end gable makes part of the box structure and its transmittance (or reflectance) properties are important for the collector performance.

**Cell Size:** PVT V4 was specially built to evaluate the difference between collectors using standard cells cut into 1/3 and 1/6 of the original size. Strings with these types of cells were expected have different power performances over the day.

With emphasis on minimizing the impact of the longitudinal shading, the PVT collectors were constructed and tested. The main differences relevant to this study are displayed in Figure 82.



Figure 82. Differences between PVT V2 and PVT V3.

## 6.4.5 Results

### 6.4.5.1 Indoor Testing

Figure 83 shows the power reduction as well as the behavior of  $V_{mp}$ ,  $V_{oc}$ ,  $I_{mp}$  and  $I_{sc}$  during shading and that the shading greatly influences the current (A) but not the Voltage (V). Three shading tests were conducted: whole string and single cell (both parallel and perpendicular to the cell busbar). It is important to notice that the percentage of shading applied the cell or string is not exact.

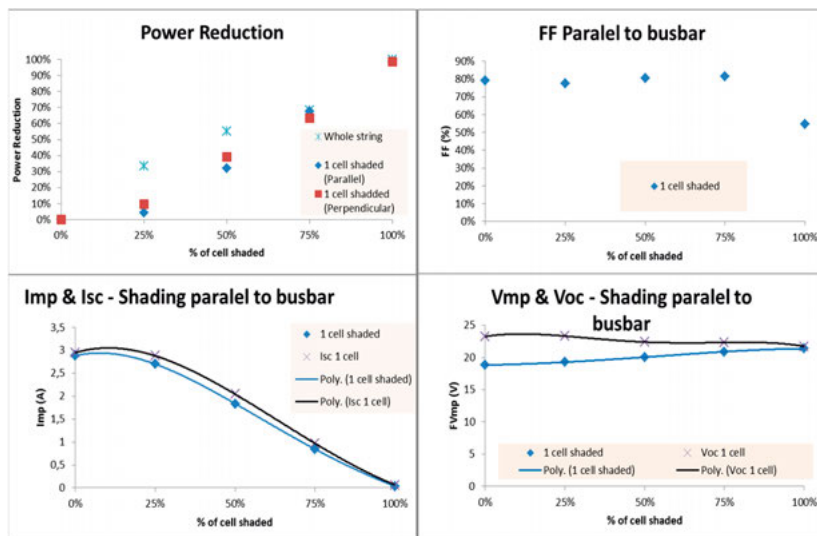


Figure 83. (a) Power Reduction; (b) Shading impact on FF; (c) Shading impact on  $V_{oc}$  &  $V_{mp}$ ; (d) Shading impact on  $I_{sc}$  &  $I_{mp}$ .

#### 6.4.5.2 Outdoor Testing:

PVT V2 was tested in Älvkarleby at Solarus on the 1<sup>st</sup> of April while V3 at Dalarna University on the 16<sup>th</sup> of May. Figure 60 shows the electrical power output of one trough (both front and reflector sides of the receiver) for both V2 and V3 over stable sunny days. The collector tilt was selected to maximize output for the location and the time of the year in which the measurements took place. Cell temperature is assumed to be the same as the average water temperature which, during the day, varied between 10 and 20°C for V2 and 20 and 40°C for V3.

Figures 84 and 85 show sharp increases and decreases of electrical power output for both PVT V2 and V3 due to the reflector side of the receiver having one string (out of the two strings) not working. Since the cells are connected in series, as soon as the first cell becomes shaded, the power of the whole string is reduced. Unshaded power production occurs only for little over 1 hour for V2 while in V3, it lasts for over 2 hours, which is double of the duration. This is because V2 was an early prototype, so the cells strings were longer, causing the shading to begin earlier when compared to V3. The cell strings were longer because the spaces between each cell were larger (number of cells is maintained). The peak power of V2 is 117 W (for one trough) while V3 shows 89 W (for one trough). This difference is mainly justified by the difference in cell operating temperature and by the reflectance of snow in front of the collector. The findings for V2 match the results from Paper IV, which were based on a similar PVT prototype.

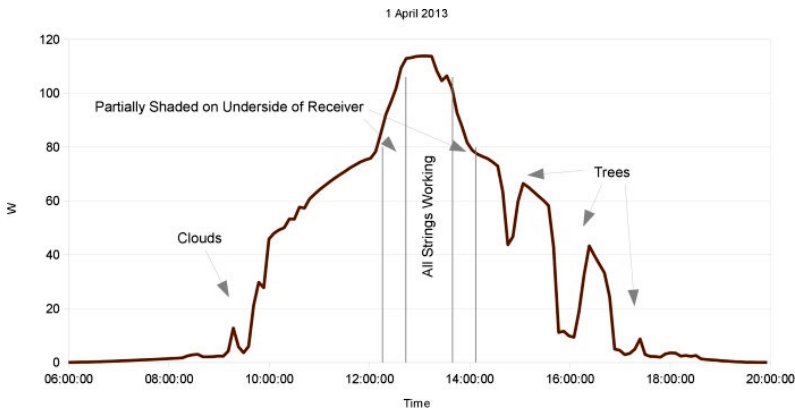


Figure 84. Electrical Power measured in PVT V2 measured in Älvkarleby.

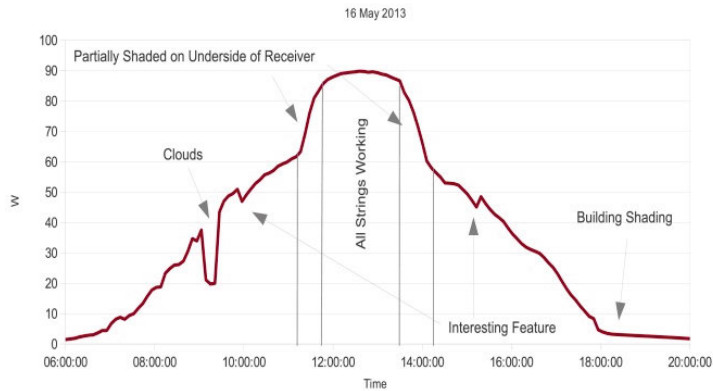


Figure 85. Electrical Power measured in PVT V3 at Dalarna University.

The power profile marked as “interesting feature” in Figure 85 was found to be caused by the combination of the movement of the shade caused by the aluminium frame and the shade caused by the end of the reflector. This was not visible in the graph on the left side of Figure 84 since V2 has reflective end gables, while V3 has transparent end gables.

This effect is further described in Figure 86, which shows how the shading caused by the Aluminium frame varies over the day. The arrows show the movement of the shade produced by the frame on both the reflector trough and the reflector underside, as the sun moves from horizon to zenith. This evaluation is coherent with previous research on similar issues [67], as well as the finding of Paper III.

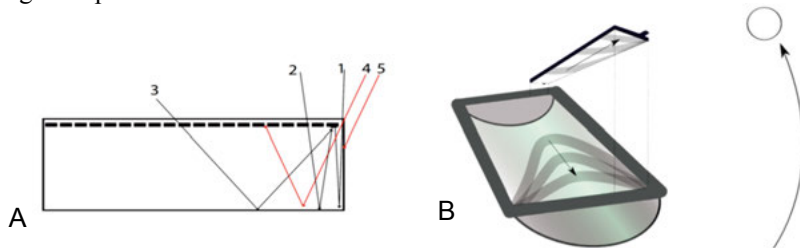


Figure 86. Effect of the shading of the aluminium frame on a PVT with: (a) reflective end gables; (b) transparent end gables.

After a full day of testing, the PVT V3 was modified and the transparent end gables were replaced by a reflective one. The collector was then tested again in the next day which was also a stable sunny day. This way, all collector properties were exactly the same and the only difference that is measured is the effect of the end gable being transparent or reflective. For comparative purposes, the power output of V3 with reflective end gables was normalized to the solar irradiation of the day of test in the V3 with transparent gables. This is shown in Figure 87.

Figure 88 shows the power from the reflector side of the experimental trough in the PVT V4. This trough contains strings with cells 1/3 of the standard size and was tested at Gävle University with perfectly stable solar conditions. Since, at this time, there were still no means to control the collector temperature at this location, the collector was kept fairly constant at stagnation (around 120 °C when the pipes allow air to circulate through the receiver). The time duration of no shading on the reflector side was seen to be considerably longer than in V2 and V3, lasting more than 3.5 hours. This happens because the strings with cells of 1/3 the standard size are shorter, since these strings have only half of the number of spaces between the cells.

Furthermore, also for V4, the “interesting feature” is again seen due to the combination of the shading caused by the aluminium frame and the end of the reflector. These measurements were tested twice for confirmation. Figure 89 A shows the power on the lower side of both troughs of the PVT V4 on a day with perfect and stable solar conditions and collector temperature maintained at stagnation.

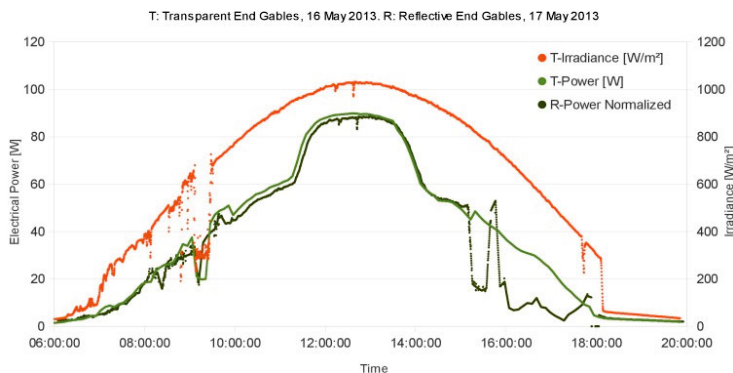


Figure 87. Electrical power output comparison between the same collector with the only change being side gables (transparent or reflective);

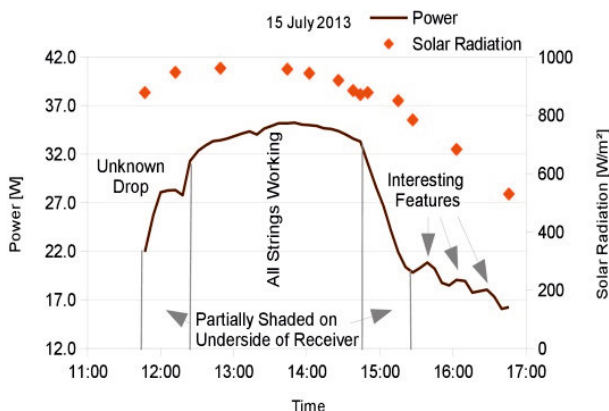


Figure 88. Electrical power output from the back side of the receiver PVT V4 (with 1/3 solar cells) measured at Gävle University on the 15th of July.

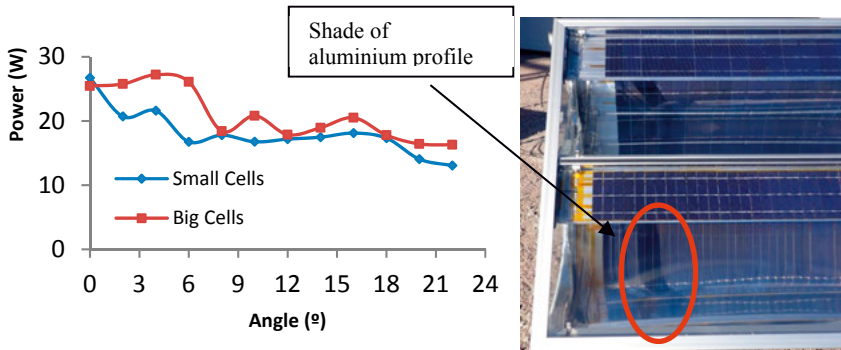


Figure 89. (a) Power output comparison between two V2s with 1/3 and 1/6 cell sizes (left); (b) Picture of PVT V3 showing a band of shading for the troughs with different cell sizes of V4 (right).

At (0,0) on the Figure 89a, two electrical power readings were taken when neither of the troughs had any shading, but just before the shading commenced; Point (0,0) in the figure is not when the sun is normal to the collector. The collector was rotated about  $3^\circ$  relative to the sun in order to provoke shading. For each angle, the two power readings were taken almost simultaneously from both troughs. Figure 89a shows that when there is no shading, the trough with smaller cells produces slightly more power, but the longitudinal shading also starts much before, which is a much more relevant effect for the annual output. The trough with larger cells produces more power even under shading since a larger part of the cell remains unshaded, as seen in Figure 89b, which roughly corresponds to a  $15^\circ$  angle in Figure 89a.

#### 6.4.6 Conclusions

The indoor solar laboratory tests showed that shading a cell parallel or perpendicular to the cell busbar had a similar impact in terms of power reduction. When 25 % and 50 % are covered, the power decrease is larger for the whole string than for a single cell shaded. The whole string experiences a power decrease close to the percentage of the area that is shaded while a single cell has a smaller decrease in power. Interestingly, having 75 % of the whole string shaded or 75 % of one solar cell resulted in a similar decrease in power. As expected, shading one whole cell or string yields a very similar result, with the power output very close to zero. The FF was observed to increase, as the shading increased from 0 % to 75 %.

For the latest PVT version, at  $25^\circ\text{C}$  and  $1000\text{ W/m}^2$ , the collector efficiency was found to be 13.7 % yielding 237 W. The efficiency per cell area was found to be 20.3 %. At peak sun, the reflector side of the receiver produced 58 % of the total power in accordance with measurements done by the author in Paper III.

The testing on the three PVT versions showed clearly that the longitudinal shading caused by the frame represents a window of opportunity for the improvement of this PVT design, in terms of power production optimization. The

results also show clearly that the string length has a significant impact on the duration of peak power with V2 having 1 hour, V3 having 2 hours and V4 having more than 3.5 hours. The study shows that using cells with 1/3 the standard size gives better performance than smaller cells. Although larger cells show decrease in power production of 4 % during peak power, peak power also lasts for a considerably longer period. Overall, the net result will be a gain in power production over the day. Larger cells will also reduce the production costs by halving much of the work required. Further work includes investigating the extent of the benefits of using different cell types and sizes. Using cell strings with cells that are half the standard size and have four busbars instead of three is an option that should be evaluated. The additional busbars increase the efficiency of the cell by reducing the resistivity losses [20].

To minimize the effects of longitudinal shading, it is recommended to build the PVT collector with a transparent or much thinner frame. Reducing the frame shadow by half is expected to make a significant difference. Other measures like having less cells per string should also be evaluated. Alternatively, other reflector geometries for the presented PVT concept can also be studied.

The metal receiver holder also creates a shade that is visible in the reflector. It is likely that this effect is not significant, but this should be further investigated, as it can further increase the output of the PVT.

Although previous tests have unequivocally shown that transparent end gables perform better at large incidence angle than opaque, the results show no clear difference between having transparent or reflective end gable in the PVT, which is unexpected. The difference however may lie within the measurement error. More testing is required for the larger incidence angles. If larger cells were used, the transparent end gables collector should perform better.

## **6.5 Testing at Gävle University of 2014**

### **6.5.1 Solar Laboratory at the University of Gävle**

An outdoor test rig laboratory was built at University of Gävle (HiG) by the author with the help of master students. The site is located at latitude 60° 40' North and longitude 17° 6' East.

#### **6.5.1.1 Solar Thermal Test Equipment**

The thermal rig circulation system was developed for thermal collector testing by a company named Finsun Inresol AB. The goal of this system is to regulate the temperature and flow of water to the thermal collectors in order to determine the thermal efficiency of solar collectors.

This system has connected at HiG in 2013 with the following components: a control unit (Melacs®), feed water pump, flow meter, mixing tank, heating apparatus, expansion tank, automatic flow control valve, LM35 temperature sensors, and a plate heat exchanger as illustrated in the Figure 90.



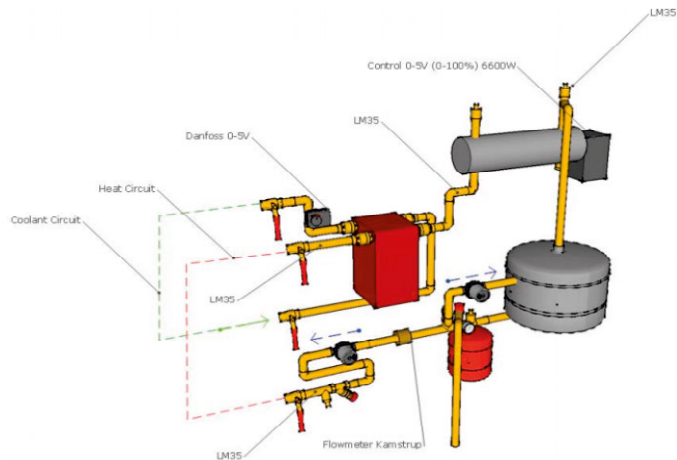


Figure 90: Schematic drawing of the test rig. Source: Finsun AB.

The system features two independent thermal circuits: a closed one, with insulation, that feeds the solar collectors to be tested, and an open one, with grid water, that is used for cooling the closed circuit through a heat exchanger. The system uses two circulation pumps for transport of heat.

Two P.I.D algorithms, one for cooling water valve control and one for heater intensity, were created to maintain the desired system temperature. The Melacs® (Micro Energy Logger and Control System) unit controls the thermal rig. Four temperature sensors LM35 from Texas Instruments are placed on the test rig, as shown in Figure 90. They are only used for control of the rig. According to Texas Instruments, these sensors measure temperatures between -55 °C and 150 °C with an accuracy of 0.5 °C at 25 °C.

The expansion tank is used to protect the closed circuit from pressure above 1.5 bar. To simplify the analysis of the measurement results, whenever the weather conditions allowed, the heat-transfer fluid used has been water.

This system was later adapted to test the Solarus concentrating PVT solar collector. Together with a company called Insitu AB, the following upgrades were made:

- The flow to the collectors was divided into two, so that two collectors (or troughs) could be tested simultaneously;
- New and more accurate (+/- 1%) magnetic flowmeters were installed (Omega FMG82) in both collector inlets;
- A scientific logger (CR1000 from Campbell Scientific) was installed to record all measurements, as well as to control the timing of the measurements;
- Temperature sensors (PT100 from Pentronic) were installed. Four of them measured the inlet and outlet water temperature of the collector, while a fifth measured the ambient temperature. They have an accuracy of  $\pm 0.15$  °C at 0 °C. (Pentronic, s.d.).

In addition, all sensors were calibrated by the company In Situ Instrument AB, before the testing period started.

#### 6.5.1.2 *Solar Electrical Test Equipment:*

The IV Tracer used was the same as described in the previous subchapter (6.4.3). The program of the CR1000 was set to perform one IV curve every 7.5 seconds, after which it moves on to the next receiver side. In total, 4 measurements are taken every 30 seconds.

#### 6.5.1.3 *Solar Radiation Equipment and Collector Stand*

Two Kipp&Zonen pyranometers are used: one for the global irradiance (CMP6) and one for the diffuse irradiance (CMP3). To measure the diffuse irradiance, the pyranometer is combined with a reclining shadow ring. Both pyranometers are mounted in the plane of the collector.

Initially, a very basic wooden collector stand was built that only had the capacity to regulate the tilt, which is shown in Figure 91.



Figure 91. Early collector stand at HiG with the two pyranometers.

However, in 2015, a rotating stand was built with the specific purpose of facilitating the measuring of the IAM. This stand could also adjust the tilt as desired by lifting the collector and locking it into the new tilt. The collector rotates on itself up to  $-90^{\circ}$  to  $90^{\circ}$ , which greatly simplifies the IAM measurements. Figure 92 and 93 illustrate the collector stand.

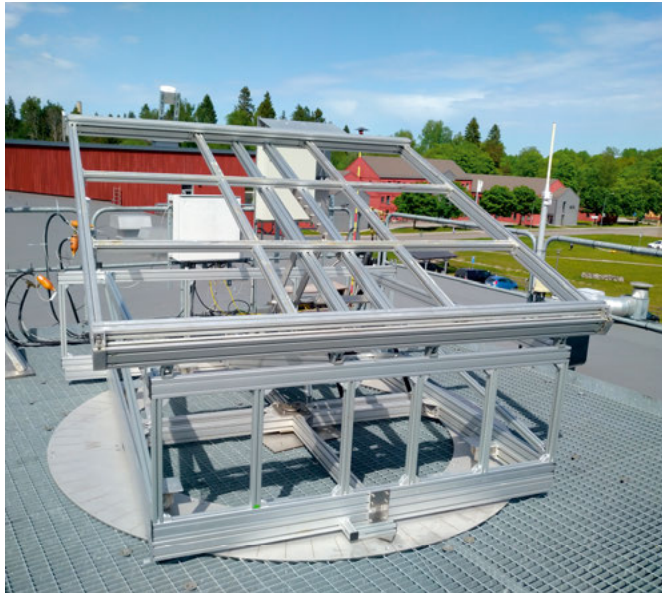


Figure 92. New collector stand at HiG's solar laboratory.

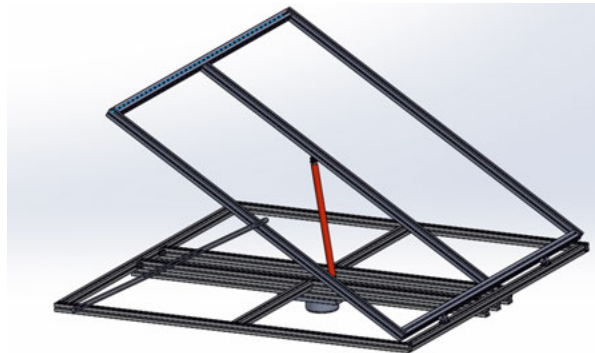


Figure 93. 3D image of the collector stand including the hydraulic arm.

### 6.5.2 Measured Thermal and Electrical Parameters

For the thermal efficiency curve, the steady state method was utilized. The curve was plotted based on several thermal efficiency points measured at different temperatures, such as  $T_{\text{Collector}} = 25\text{ }^{\circ}\text{C}$ ,  $40\text{ }^{\circ}\text{C}$  and  $60\text{ }^{\circ}\text{C}$ . The curve was then extrapolated to obtain peak efficiency and stagnation temperature. All data for the thermal efficiency curve was taken under a constant irradiance that was greater than  $800\text{ W/m}^2$ .

Table 27 describes the parameters that were measured during the testing period, the logging and measuring equipment and the time interval between two measurements.

Table 27. Measured parameters for testing the electrical and thermal part of the PVT collector.

Parameter	Equipment	Unit	Comments
$I_{mp}, I_{sc}, V_{mp}, V_{oc}, P_{mp}$	CR1000 IV tracer	[A, V, W]	Instantaneous electrical measurements are made by performing four different IV curves every 30 seconds.
$T_{in}, T_{out}$	CR1000 PT100	[°C]	Inlet and outlet temperature of the collector. Measured every 7.5 seconds. Two pairs of measurements, one for each trough.
$T_a$	CR1000 PT100	[°C]	Ambient temperature. Measured every 7.5 seconds.
$I_G$	CR1000 CMP6	[W/m <sup>2</sup> ]	Global irradiance. Measured every 7.5 seconds.
$I_D$	CR1000 CMP3	[W/m <sup>2</sup> ]	Diffuse irradiance. Measured every even 7.5 seconds. Pyranometer with shadow ring.
$\dot{V}_1, \dot{V}_2$	CR1000 Flowmeters	[l/min]	Water flow at each trough of the solar collector. Measured every 7.5 seconds.

The following formulas were used to evaluate the thermal performance of the collector:

$$T_{med} = \left( \frac{T_{in} + T_{out}}{2} \right) \quad \text{eq. 32}$$

$$\Delta T = \frac{T_{out} + T_{in}}{2} - T_{amb} \quad \text{eq. 33}$$

$$P_{thermal} = \rho \times \dot{V} \times C_p \times (T_{out} - T_{in}) = \dot{m} \times C_p \times \Delta T \quad \text{eq. 34}$$

$$P_{thermal} = P_{Total} - P_{el} \quad \text{eq. 35}$$

$$Efficiency_{thermal} = \left( \frac{P_{thermal}}{Solar\ radiation} \right) \quad \text{eq. 36}$$

$$\eta_{thermal} = \frac{P_{Th}}{A_{Aperture} \times I_G} \quad \text{eq. 37}$$

$$\eta_{total} = \frac{P_{Total}}{A_{aperture} \cdot I_G} = \eta_{ob} - U \times \frac{\Delta T}{I_G} \quad \text{eq. 38}$$

Where  $T_{med}$  = Average collector temperature,  $T_{in}$  = inlet temperature,  $T_{out}$  = Outlet temperature,  $P_{total}$  = Total collector power (electrical and thermal combined),  $P_{electrical}$  = Electrical power,  $P_{thermal}$  = Thermal power,  $M$  = Mass,  $C_p$  = Specific heat capacity of water in Joules/Kg.□,  $\rho$  = specific density of water,  $A$  = aperture or gross area of the collector,  $\eta_{thermal}$  = Thermal efficiency and  $\eta_{total}$  = Total efficiency.

### 6.5.3 Prototype Collectors tested

The PVT V5 is similar to PVT V4. The only significant different is that the receivers were swapped from outer trough to inner and vice versa, in order to assess the impact of position in both thermal and electrical performance of each of the troughs.

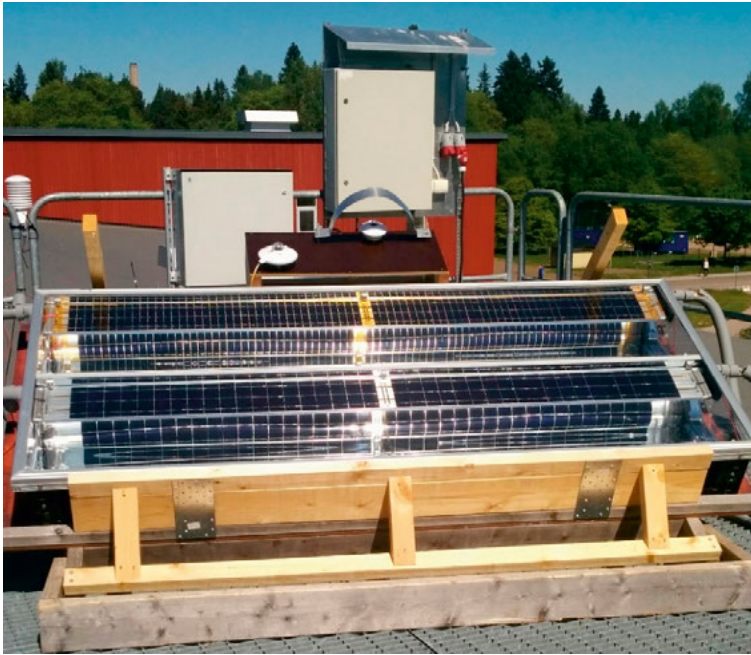


Figure 94. PVT V5 mounted at HiG's solar laboratory.

#### 6.5.4 Collector Testing Results

Figure 95 and 96 presents the electrical parameters of the V5 collector divided into the top, bottom and both sides. Figure 96 showcases how the electrical power is affected by temperature, while Figure 95 displays the power, fill factor,  $V_{oc}$ ,  $V_{mp}$ ,  $I_{sc}$  and  $I_{mp}$ .

The voltage curve is fairly constant throughout the day, while power and current follow a very similar pattern between themselves. Power and current curves commonly follow irradiance. For the topside, these two curves behave similarly to the irradiance curve, however, this is not the case for the bottom side due to the internal shading discussed in Paper IV, which is illustrated in Figure 95 and Figure 96 by the steep drop outside the peak sun period. Additionally, it is possible to discern that, under peak solar radiation, the 1/6 cells have a slightly higher power output. This is due to the fact that the cells with 1/6 size solar cells, produce half the current, which reduces the resistivity losses that scale upwards with the increase of the current. Furthermore, it is possible to observe that the 1/3 cells have both a slightly longer unshaded period at midday and also a less steep output drop, since the 1/3 cells are farther away from the edge of the collector. These findings confirm the results of Paper IV.

It is also relevant to mention also that the 1/3 cells have about double the current and half of the voltage of the 1/6 cells, which leads to very similar power outputs.

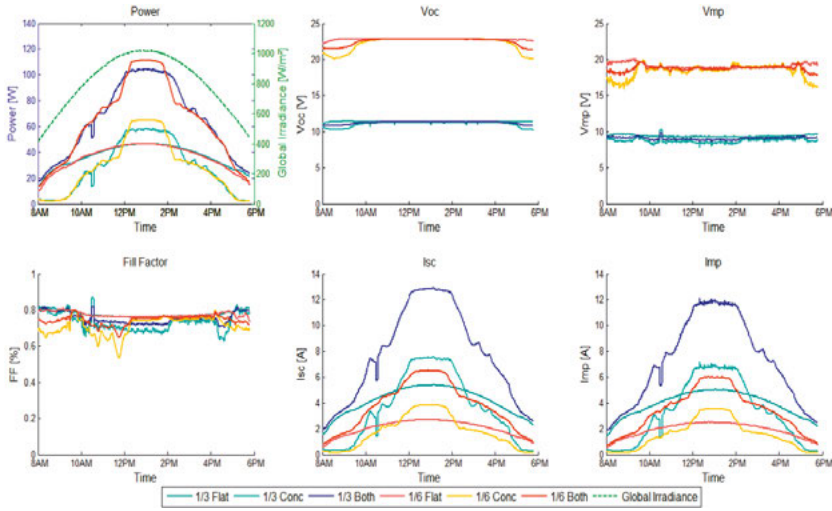


Figure 95. Comparison of the different electrical parameters of collector V5 different into top side (flat), reflector (conc) and both sides simultaneously.

Figure 96 highlights the decrease in electrical efficiency with the increase in inlet temperature over three very sunny summer days. For all temperatures, the bottom side of the receiver (concentrated) is only outperforming the top side on a small time window of about 2h30.

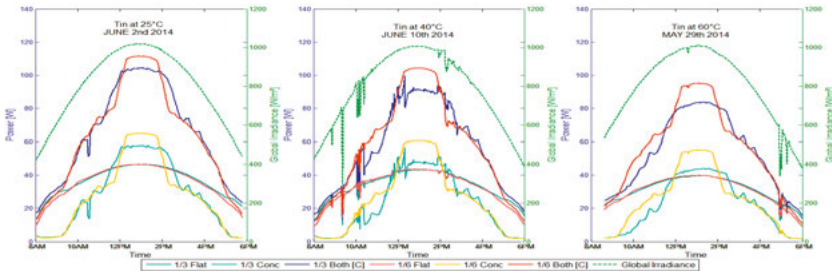


Figure 96. Electrical power variation with temperature for the V5 prototype collector.

Figure 97 plots the relative performance of the bottom and top sides of each trough of the V5 collector based on the formula shown below, where flat is the top side of the receiver and concentration is the bottom side of the receiver:

$$Ratio\_Concentrated = \frac{P_{mp\_Concentrated}}{P_{mp\_Flat} + P_{mp\_Concentrated}} \quad \text{eq. 39}$$

This figure shows that, for the measured day in June, the top side of the receiver (flat) over-performs the concentrated side for the majority of the time. However, it must be said that the solar intensity is higher during peak power, which means that those hours are the most relevant. It can also be seen that the time window in which the bottom side (concentrated) over-performs the top side is

higher 1/6 by 35 minutes. On the other hand, it can also be seen that the bottom side of the 1/6 cell receiver relative performance is slightly higher than the 1/3 receiver. This is due to lower resistivity losses caused by lower currents, as discussed earlier.

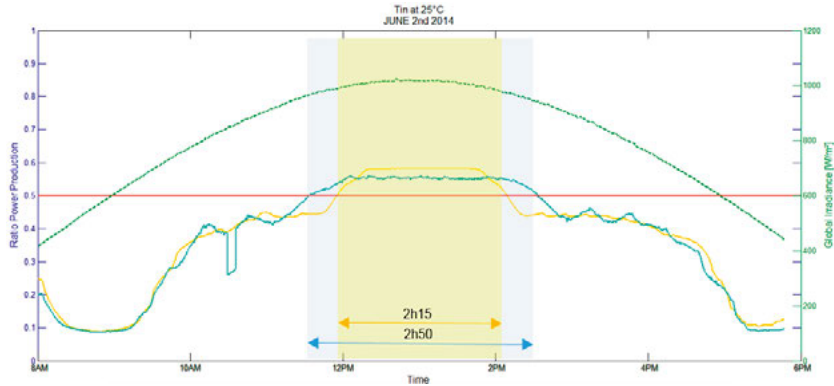


Figure 97. Power ratio between top and bottom sides of each trough of the V5 collector. (legend: in yellow: 1/6 cell receiver; in blue: 1/3 cell receiver; in green: solar radiation)

Figure 98 displays the daily electrical output for a full day (2<sup>nd</sup> of June). This analysis showcases that the bottom side is over the whole day producing less electricity as the top side, despite having a concentration factor of 2. Since during this day, all incoming light is within the acceptance angle and the output of the bottom side is not significantly superior to the front side, it stands to reason that over the year the bottom side will have a lower output than the front side since when the sunlight is not always within the acceptance of the reflector throughout the whole year.

It is also important to note that the electrical output of 1/3 and 1/6 cell receivers is fairly similar, which means that it is better to use the 1/3 cells that are slightly cheaper since they need less cell cutting as well as easier and less time consuming to handle in production.

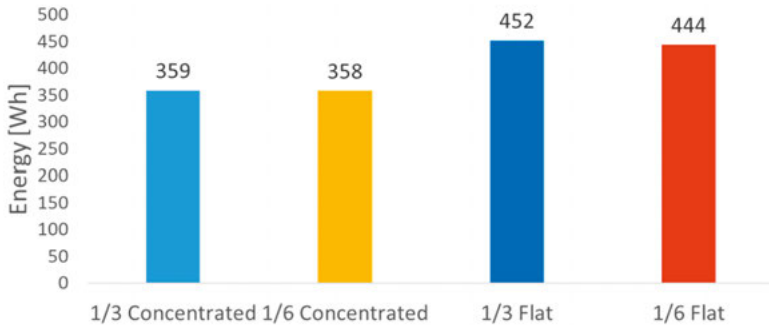


Figure 98. Daily electrical output of the different receiver sides (2<sup>nd</sup> of June)

Figure 99 showcases the thermal performance of V5 on three different days under three different operating temperatures. As expected, the thermal performance is reduced with the increase in inlet temperature and the thermal power correlates very closely with the solar radiation curve. Furthermore, it is possible to observe that the three selected days had perfect weather conditions with high and steady solar radiation throughout the whole day.

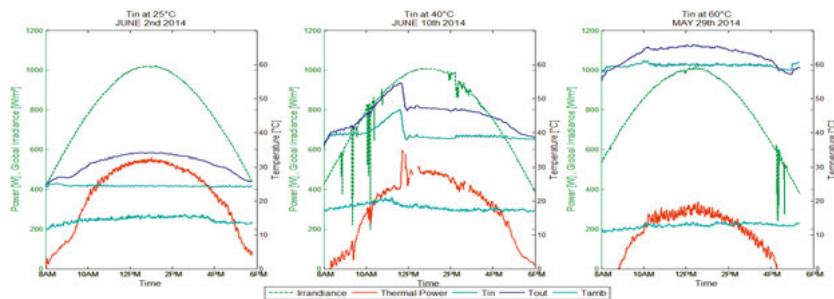


Figure 99. Thermal performance of collector V5 on three different days and operating temperatures.

Figure 100 shows the thermal, electrical and combined efficiency of V5 over three days and under different operating temperatures. This graph illustrates the efficiency reduction at higher temperatures. Electrical efficiencies are around 10 % over the day, while thermal efficiencies surpass 50 % for a temperature difference to the environment of 15 °C. On the other hand, on sunny days, when the difference between the collector average temperature and the ambient temperature is close to 50 °C, the thermal efficiency is just over 20 %. The combined efficiency is the sum of both thermal and electrical output, and is a measured value. On the other hand, the thermal efficiency has been calculated by subtracting the electrical from the combined output.

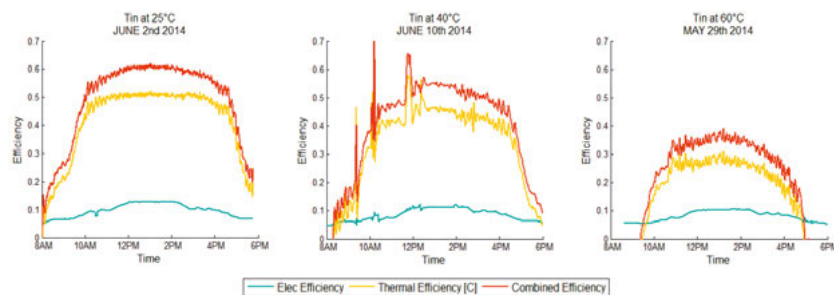


Figure 100. Thermal, electrical and combined efficiency of V5 over three days.

Figure 101 displays the thermal, electrical and combined power curve for the top trough of the V5 prototype collector. This curve is based on measurements done at different temperatures over four days with a solar radiation above 1000W/m<sup>2</sup>. The values used to calculate the electrical and combined power



curves are measured, while the values for thermal curves were calculated. The combined curve represents the thermal efficiency of the collector, while not extracting electricity, basically using the PVT, as if it were a thermal collector. On the other hand, the efficiency curve named “thermal curve” represents the thermal efficiency of the V5 PVT prototype when electricity is being extracted, which is the situation for which the PVT collector is design to operate.

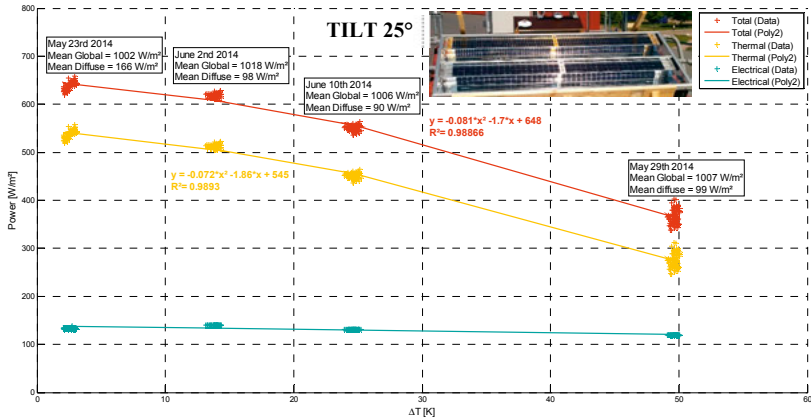


Figure 101. Thermal, electrical and combined power curve of V5 (top trough).

Figure 102 displays the thermal, electrical and combined power curve for the bottom trough of the V5 prototype collector. This curve is based on measurements done at different temperatures over four days with a solar radiation above 1000W/m<sup>2</sup>. It also important to note that each trough was measured separately being that Figure 101 represents the top trough and Figure 102 represents the bottom trough. The goal of measuring each trough separately was to assess how the heat movements impacted differently each trough. It is also important to mention that the top trough had 1/6 size cells while the bottom trough had 1/3, although was not expected to influence the thermal results.

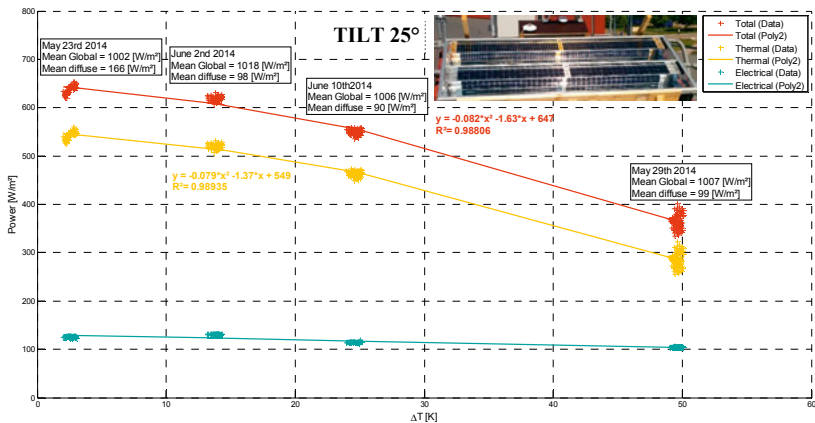


Figure 102. Thermal, electrical and combined power curve of V5 (bottom trough).

Lastly, Table 28 displays the thermal properties of the collector, while extracting electricity (thermal curve) and while not extracting electricity (combined curve). Testing did not show any major difference between the troughs.

Table 28. *Thermal properties of the V5 prototype collector.*

Trough	Extracting Electricity?	Optical Efficiency	a1	a2	U Value at $\Delta T = 30^{\circ}\text{C}$
Top	No	64.8%	1.70	0.081	4.13
	Yes	54.5%	1.86	0.072	4.02
Bottom	No	64.7%	1.63	0.082	4.09
	Yes	54.9%	1.37	0.079	3.74

## 6.6 Testing at Gävle University of 2015

### 6.6.1 Prototype Collectors tested

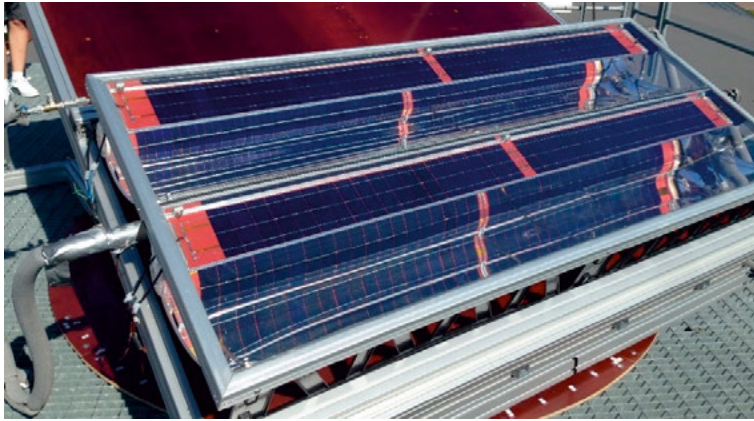
Three prototypes C-PVT solar collectors were constructed and are named V6, V7 and V8. These collectors were made with different top and bottom receivers to increase the number of tests that could be performed and conclusions that could be drawn. All prototypes had identical collector boxes. The receivers were also identical with the exception of five parameters that were varied: Number of strings, cell size, fabrication method, bottom silicone layer and type of silicon cells. Table 29 shows the main characteristics of these prototypes:

Table 29. *Characteristics of the receivers of the prototypes.*

Name	Trough	Strings number (number of cells)	Cell Size	Fabrication Method	Bottom Silicone Layer	Cell Type
V6	Top	2 (38-38)	1/6	Hand-made	Red	Monocrystalline
	Bottom	2 (19-19)	1/3	Hand-made	Red	Monocrystalline
V7	Top	2 (19-19)	1/3	Hand-made	Red	Monocrystalline
	Bottom	4 (4-15-15-4)	1/3	Hand-made	Red	Monocrystalline
V8	Top	4 (4-15-15-4)	1/3	Machine-made	Transparent	Polycrystalline
	Bottom	4 (5-14-14-5)	1/3	Machine-made	Transparent	Monocrystalline

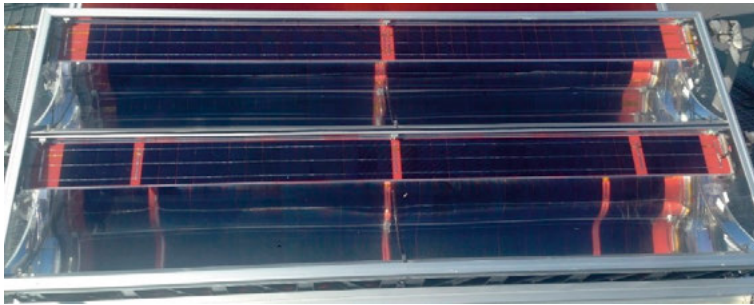
The receivers of the prototypes had two or four strings with different numbers of solar cells. Two cell sizes were used: 1/3 (52 \* 148 mm) and 1/6 (28 \* 148 mm). The fabrication process of the solar cell strings was either hand-made or machine-made. The manual soldering process tends to create considerably more micro-cracks in the cells. One receiver had 18.2 % efficiency polycrystalline cells from the Lithuanian manufacturer Solimpeks, while all other receivers featured monocrystalline Taiwanese cells which provided by AKW with 19.3% efficiency. Each cell string possessed one bypass diode to mitigate shading issues.

Figure 103 shows Prototype V6 that was used to compare the performance of receivers with one third cells and one sixth cells, in order to confirm the results of previous testing. Both receivers are fully identical with the exception of the cell size. Total cell area is the same on both receivers, 0.293 m<sup>2</sup> per receiver side.



*Figure 103. Prototype CPVT V6.*

Prototype V7, shown in Figure 104, was constructed to compare the performance of receivers with two and four strings. Both receivers are fully identical with the exception of the number of strings and the number of bypass diodes.



*Figure 104. Prototype CPVT V7.*

Prototype V8 is the only machine-made receiver. The top receiver is composed by four cell strings: two with four cells and two with 15 cells, just like the bottom receiver of prototype V6. The bottom receiver also has four strings but with two strings of five cells and two strings of 14 cells. The cells in the top are polycrystalline, while the bottom is monocrystalline. Unlike prototypes V6 and V7, cell encapsulation is made only with transparent silicon layers, as it is noticeable in Figure 105.



Figure 105. Prototype 3 CPVT V8.

### 6.6.2 Method

Prototypes V6, V7 and V8 were constructed at Solarus, where two main tests were conducted: Electroluminescence to check for the existence of microcracks following the procedure described in section 5.2.2 and receiver performance under the indoor solar simulator, whose procedure is described under section 6.4.2.

Following these tests, the prototypes were transported to the solar laboratory at Gävle University where they were tested outdoor. The solar laboratory set-up has been described in section 6.5.

Additionally, IV-curves were plotted for all receiver sides.

### 6.6.3 Collector Testing Results

Prototype V6 was designed to compare cells cut into 1/3 and 1/6. IV curves were measured at HiG and are shown below in the Figure 106 and 107.

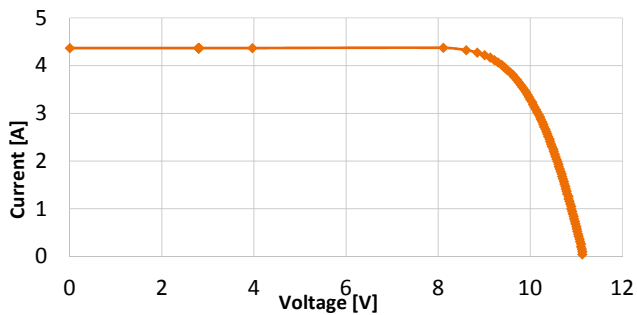


Figure 106. IV curve of the front side with 1/3 cells of V6.

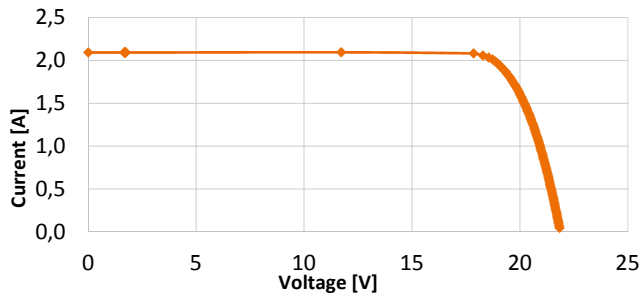


Figure 107. IV curve of the front side with 1/6 cells of V6.

Figure 108 shows the electroluminescence test results on the V6 prototype:

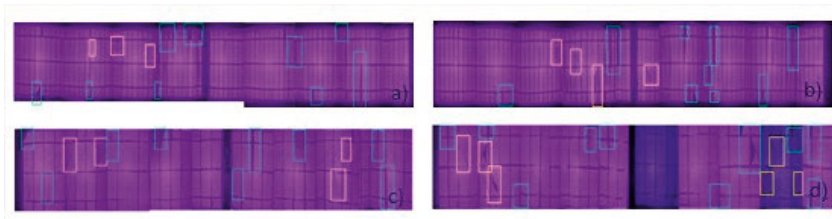
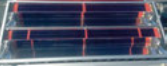


Figure 108. EL testing of receivers of V6: a) Top trough front side 1/6; b) Top trough front side 1/6; c) Bottom trough front side 1/3; d) Bottom trough back side 1/3.

The electrical parameters obtained from the indoor testing are shown in Table 30:

Table 30. Indoor simulator testing results of the receivers of prototype V6.


	Top Trough (1/6)		Bottom Trough (1/3)	
	Front	Back	Front	Back
$P_{max}$ (W)	87.6	83.7	84.7	87.0
$I_{mp}$ (A)	4.0	3.8	7.7	8.0
$I_{sc}$ (A)	4.1	4.0	8.0	8.3
$V_{oc}$ (V)	24.7	24.6	12.4	12.4
$V_{mp}$ (V)	22.2	22.2	11.0	10.9
FF (%)	86	86	85	85
Electrical efficiency (%)	15.1	14.4	14.6	15.0

(Testing conditions: irradiation = 2000 W/m<sup>2</sup>, T<sub>amb</sub>= 20 °C, Note: no glass on this test)

The indoor testing was carried out on the receiver (before the receiver is inserted into the collector box which holds the reflector). This way, the back side and front side of the receiver are expected to produce similar power, which indeed occurs. The indoor simulator test and the electroluminescence allow concluding that there are no major cracks on the cells, despite the manual hand soldering process.

The electrical parameters obtained from the outdoor testing are shown in Table 31. These values were measured on the 4<sup>th</sup> of August at 11:05, with a solar irradiance of 921 W/m<sup>2</sup> and an ambient temperature of 21.9 °C. Tilt was 30°.

Table 31. Results of the outdoor electrical measurements of the prototype collector V6.

	Top Trough (1/6)		Bottom Trough (1/3)	
	Top	Back	Top	Back
$P_{max}$ (W)	37.3	47.3	37.6	39.4
$I_{mp}$ (A)	2.0	2.7	4.1	4.2
$I_{sc}$ (A)	2.1	3.1	4.4	4.3
$V_{oc}$ (V)	21.8	22	11.1	11.1
$V_{mp}$ (V)	18.6	17.5	9.1	9.4
FF (%)	82	69	77	82
Electrical efficiency (%)	13.8	17.6	14	14.6
T <sub>in</sub> (°C)	39.3	39.3	39.6	39.6
T <sub>out</sub> (°C)	41.9	41.8	41.8	41.8

(Testing date and conditions: 04/08 at 11:05, solar radiation = 921 W/m<sup>2</sup>, T<sub>amb</sub>= 21.9 °C)

Prototype V7 was designed to compare troughs with two strings and four strings. The number of strings and diodes is expected to have a minimal impact at the ideal angle but a significant impact at non-ideal angles, which can be visualized through IAM curves.

Just like for prototype V6, some microcracks are present due to the manual manufacturing process but this does not shown a significant impact in the output. The electroluminescence test results of prototype V7 are shown the results in Figure 109.

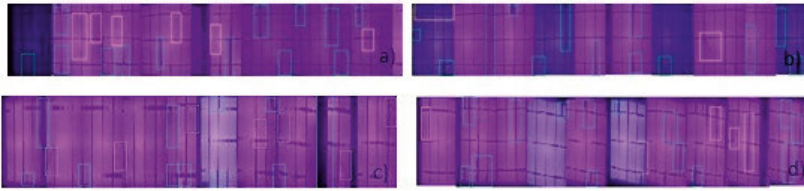


Figure 109. EL testing of receivers of V7: a) Top trough front side 2S; b) Top trough back side 2S; c) Bottom trough front side 4S; d) Bottom trough back side 4S.

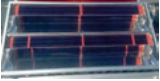
The solar simulator results are shown in Table 32:

Table 32. Indoor simulator testing results of the receivers of prototype V7.

	Top Trough (2S)		Bottom Trough (4S)	
	Front	Back	Front	Back
$P_{max}$ (W)	87.4	86.3	82.7	82.4
$I_{mp}$ (A)	8.0	8.2	4.3	3.7
$I_{sc}$ (A)	8.3	8.4	6.2	6.1
$V_{oc}$ (V)	12.4	12.1	24.2	24.7
$V_{mp}$ (V)	11.0	10.6	19.1	22.4
FF (%)	85	85	55	55
Electrical efficiency (%)	16.6	16.4	15.7	15.6

The outdoor collector testing of V7 was carried out on the 13<sup>th</sup> of August at 12:30, with a solar radiation of 968 W/m<sup>2</sup>, an ambient temperature of 17.8 °C and a tilt of 30°. These results are displayed in Table 33:

Table 33. Results of the outdoor electrical measurements of the prototype collector V7.

	Top Trough (2S)		Bottom Trough (4S)	
	Top	Back	Top	Back
$P_{max}$ (W)	35	45.5	36.3	46.7
$I_{mp}$ (A)	4.0	5.2	2.0	2.7
$I_{sc}$ (A)	4.3	5.5	2.5	3.3
$V_{oc}$ (V)	10.6	10.9	21.7	21.2
$V_{mp}$ (V)	8.8	8.8	18.2	17.6
FF (%)	77	76	67	66
Electrical efficiency (%)	12.3	16.1	12.8	16.5
$T_{in}$ (°C)	48	48.1	48	48
$T_{out}$ (°C)	49	48.6	48.8	48.9


Again, the backside performs better than the topside due to the concentration. It is important to note that the electrical efficiency is given per cell area, otherwise the back would normally have a lower efficiency than the topside of the

receiver. Also, as expected, there is no significant power difference between 2 or 4 strings at peak sun.

Prototype V8 was the first receiver made by the testing team with the use of a tabbing stringer. Automated cell soldering reduces significantly the number of microcracks. Testing this receiver was intended to verify how much the manual solar cell process was affecting the initial peak power of the different receiver sides. Furthermore the top trough receiver was composed by four strings (4–15–15–4) of polycrystalline cells while the bottom trough receiver contains four strings (5–14–14–5) of monocrystalline cells.

The outdoor testing took place on the 14<sup>th</sup> of August at 12:06, with a solar radiation of 964 W/m<sup>2</sup>, an ambient temperature of 22.1 °C and the tilt was 30°.

Table 34. Results of the outdoor electrical measurements of the prototype collector V8.

	Top Trough (poly)		Bottom Trough (mono)	
	Front	Back	Front	Back
$P_{max}$ (W)	44.2	53.4	40.1	53.7
$I_{mp}$ (A)	2.4	3	2.2	3.1
$I_{sc}$ (A)	2.5	3.3	2.4	3.4
$V_{oc}$ (V)	22.9	22.8	22.3	22.2
$V_{mp}$ (V)	18.5	18	18.3	17.4
FF (%)	76	72	76	72
Electrical efficiency (%)	15.6	19	14.2	19
$T_{in}$ (°C)	31.6	31.6	31.7	31.7
$T_{out}$ (°C)	33.6	33.5	33.4	33.5

Polycrystalline cells have lower efficiencies, but this is not highlighted in the output of the front sides, with the poly crystalline cells producing about 10% more power. This was due to a defective batch of mono cells, which was confirmed by electroluminescence testing.

Table 35 compares the electrical results of the outdoor testing of three C-PVT prototypes. One clear conclusion is that the receivers with machine-made cells strings performed significantly better. This conclusion is not surprising, since in the handmade prototypes, the solar cells are soldered manually which inevitably means that some microcracks will occur during the production process. These issues occur significantly less during the machine cell soldering production processes, since machines can be far more precise and constant than humans.



Table 35. Comparison of the outdoor electrical measurements results for prototype collector V6, V7 and V8.

Front Receiver Side (Top trough)							
Receiver Description	V <sub>oc</sub> (V)	I <sub>sc</sub> (A)	P <sub>max</sub> (W)	V <sub>mp</sub> (V)	I <sub>mp</sub> (A)	FF (%)	η <sub>el</sub> (%)
Handmade 2 strings	10.6	4.3	35.0	8.8	4.0	77	12.4%
V8 Machine-made poly 4 strings (4-15-15-4)	22.9	2.5	44.2	18.5	2.4	76	15.6%
Handmade 1/6	21.8	2.1	37.3	18.6	2.0	82	13.8%
Front Receiver Side (Bottom Trough)							
Receiver Description	V <sub>oc</sub> (V)	I <sub>sc</sub> (A)	P <sub>max</sub> (W)	V <sub>mp</sub> (V)	I <sub>mp</sub> (A)	FF (%)	η <sub>el</sub> (%)
Handmade 4 strings	21.7	2.5	36.3	18.2	2.0	67	12.9%
Machine-made mono 4 strings (5-14-14-5)	22.3	2.4	40.1	18.3	2.2	76	14.2%
Handmade 1/3	11.1	4.4	37.6	9.1	4.1	77	14.0%
Reflector Receiver Side (Top Trough)							
Receiver Description	V <sub>oc</sub> (V)	I <sub>sc</sub> (A)	P <sub>max</sub> (W)	V <sub>mp</sub> (V)	I <sub>mp</sub> (A)	FF (%)	η <sub>el</sub> (%)
Handmade 2 strings	10.9	5.5	45.1	8.7	5.2	76	16.0%
Machine-made poly 4 strings (4-15-15-4)	22.8	3.3	53.4	18.0	3.0	72	19.0%
Handmade 1/6	22.0	3.1	47.3	17.5	2.7	69	17.6%
Reflector Receiver Side (Bottom Trough)							
Receiver Description	V <sub>oc</sub> (V)	I <sub>sc</sub> (A)	P <sub>max</sub> (W)	V <sub>mp</sub> (V)	I <sub>mp</sub> (A)	FF (%)	η <sub>el</sub> (%)
Handmade 4 strings	21.2	3.3	46.7	17.6	2.7	66	16.5%
Machine-made mono 4 strings (5-14-14-5)	22.2	3.4	53.7	17.4	3.1	72	19.0%
Handmade 1/3	11.1	4.3	39.4	9.4	4.2	82	14.6%

Figure 110 shows the longitudinal IAM of the V7 collector. As expected, both front sides have very similar performance at all angles, which means that there is no performance impact in the front side of having 4 or 2 strings.

More importantly, it can be observed that the reflector side of the 4 string receiver drops in efficiency before the one with 2 string. This is because of extra space occupied by the separation between the strings that pushes the cells close to the edge of the receiver, where shading at non ideal angles occurs earlier. However, the efficiency drop on the 2 string receiver is only 13%, since there are only 4 cells in the edge strings, which are bypassed by the diode. On the other hand, the 2 string receiver has the first efficiency drop later but it is a much larger drop of about 40%. Overall, this leads to the 4 string receiver having a higher output than the 2 string receiver during the day, which can be confirmed by analyzing the areas under the curve IAM curves.

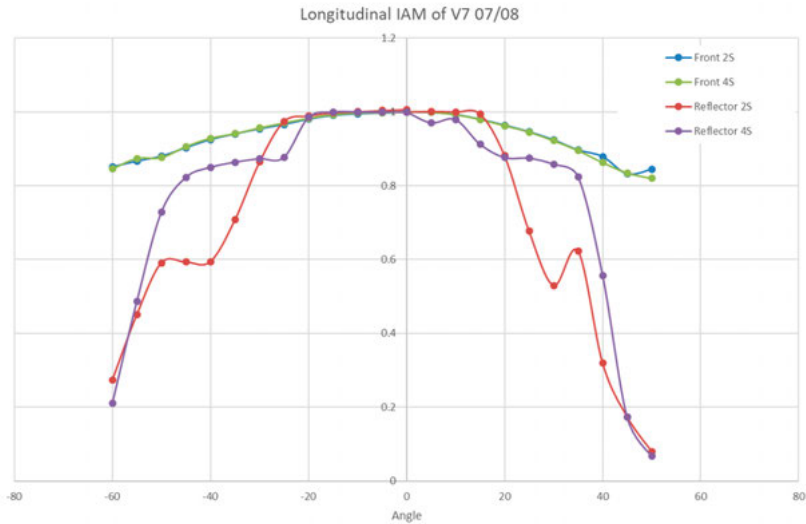


Figure 110. Longitudinal IAM of the V7 prototype collector.

Figure 111 shows the longitudinal IAM of the V8 prototype collector. It can be observed that the front side of the receivers perform similarly, as expected. On the reflector side of the receiver, it can be observed that the receiver with 5 cells on the edge string has a slightly steeper initial efficiency drop when compared to the receiver with 4 cell edge strings, which corresponds to the additional cell being bypassed by the diode. However, this also means that the 5 cell receiver only has the second power drop later. Overall, this does not have a very large impact in the performance.

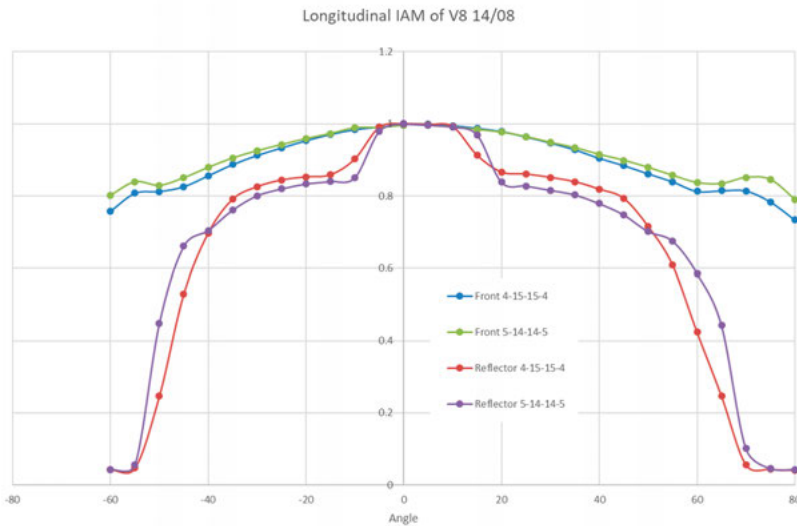


Figure 111. Longitudinal IAM of the V7 prototype collector.

Figure 112 illustrates the transversal IAM of the reflector sides of both V7 and V8 prototype collectors. All collectors have a very steep drop around the point of normal incidence, when the reflector becomes out of focus and no longer re-directs the light towards the receiver.

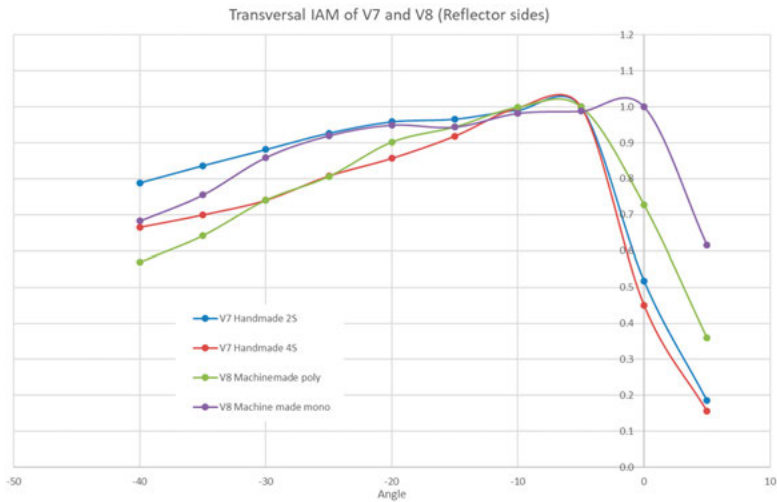


Figure 112. Transversal IAM comparison of reflectors sides of V7 and V8.

Figure 113 shows a test to the reliability of the electrical power obtained from the V8 prototype collector. In order for the measurements to be comparable, the power was normalized to 25°C and 1000W/m<sup>2</sup>.

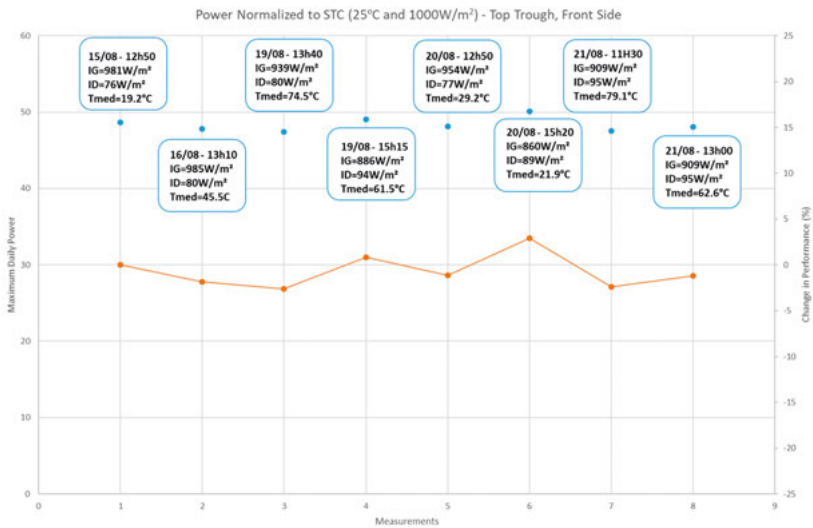


Figure 113. Power normalized to STC for the front side of the top trough of V8.

The power remained relatively stable during the measurements, oscillating around +/- 2 % of the initial power measurement. In opposition, V7 and V6, showed decreases in power soon after exposure to sun, in particular if the collector reached higher temperatures. This was due to the red silicon (encapsulating the cells) being stiffer and not being able to protect the cells from the thermal expansion of the receiver. The variation found was considered to be within the measurement error and thus the V8 collector shows no impact in performance even after being exposed to higher temperatures, such as 80 °C. This indicates that the cell encapsulation with the transparent silicon in V8 is sufficient to cope with the thermal expansion of the aluminium receiver.

Figure 114, presents the same information for the bottom trough of V8, which displayed a similar total variation of less than 5% in total.

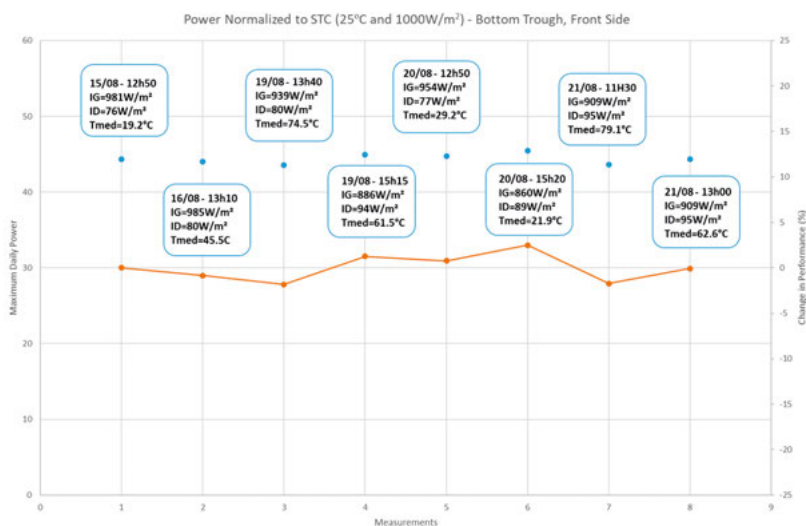


Figure 114. Power normalized to STC for the front side of the bottom trough of V8.

Figure 115 and 116 illustrate the electrical performance of the reflector side of both trough for the V8 collector prototype. Due to the high concentration around the focal line, the performance of the reflector side is at a greater risk of than the front side where there is no concentration. Still, the power variation of both reflector sides showed a similar total variation to the top sides of around 5% of the initial measurement, which indicates that the transparent silicone is able to successfully protect the solar cells from the daily temperature variations to which the C-PVT collector is exposed.

In order to further complement these measurement, the collector was left under stagnation for a period of one month and re-measured having displayed similar power output variations ranging to about 7% of the initial measurement value. This further solidifies the expectation that the V8 C-PVT collector will be able to sustain its electrical performance over time.

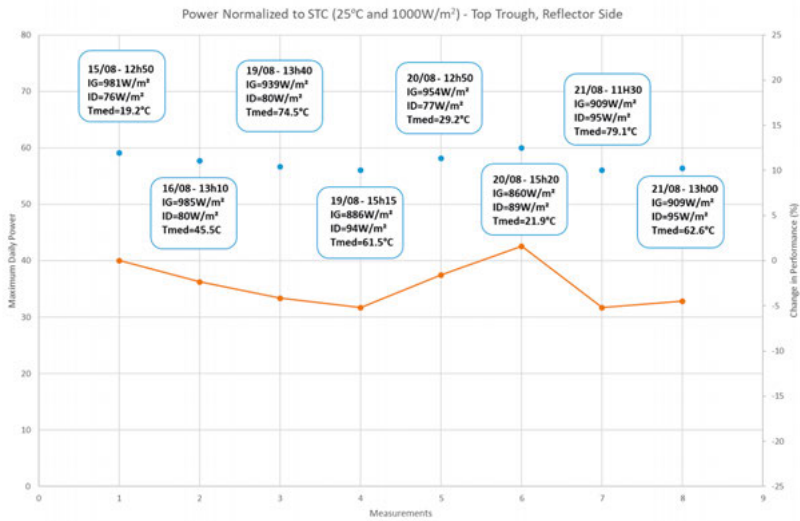


Figure 115. Power normalized to STC for the reflector side of the top trough of V8.

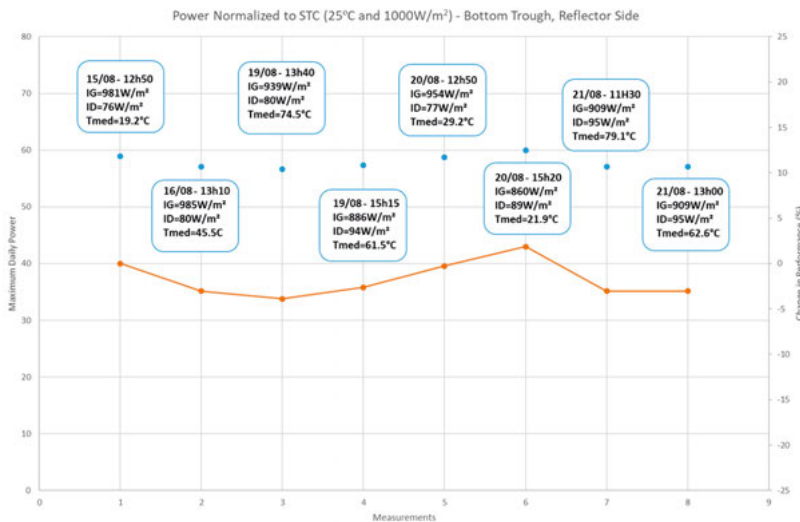


Figure 116. Power normalized to STC for the reflector side of the bottom trough of V8.

Lastly, Figure 117 shows the thermal and electrical performance of the top through of the V8 prototype collector, while operating at an average temperature of 45 °C. The thermal performance during this day peaked at 240 W, meaning that the whole collector would have an output of about 480W. It is also noteworthy that the electrical performance of the front side is overperforming the reflector side over most of the day, highlighting that the cell string layout

with 4 cell strings is superior to the one with only 2 cell strings in terms of annual output.

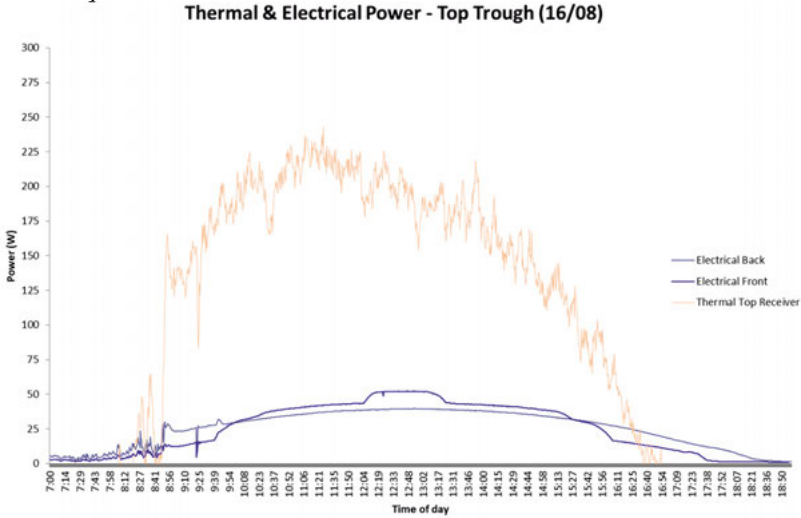


Figure 117. Thermal and electrical power of the top trough of V8 at  $T_{med} = 45 \text{ }^{\circ}\text{C}$ .

## 6.7 Paper VI: Testing at Dalarna University of 2016

### 6.7.1 Methodology

A new version of the Solarus Power Collector (V9) designed and installed at the solar laboratory of Dalarna University as shown in Figure 118. This collector was tested using the Quasi-Dynamic Testing (QDT), following the ISO 9806:2013.

The process for studying the collector performance was as follows: identifying the key parameters in the QDT equation, setting up the test sequence according to the QDT methodology, verifying the usability of the test system for conducting QDT by testing a generic solar thermal flat plate collector, testing and characterizing a novel concentrating PVT collector, and finally comparing and analyzing the results to draw conclusions.

The thermal collector model under the QDT equation was adapted from the ISO 9806:2013.

$$\frac{\dot{Q}}{A} = F'(\tau\alpha)K_{\theta b}(\theta_L, \theta_T)G_b + F'(\tau\alpha)K_{\theta d}G_d - c_1(t_m - t_a) - c_2(t_m - t_a)^2 - c_3u(t_m - t_a) + c_4(E_L - \sigma T_a^4) - c_5 \frac{dt_m}{dt} - C_6uG \quad \text{Eq. 40}$$



Figure 118. The Solarus Power Collector installed at Dalarna University

The test rig possesses an advanced hydraulic circuit that is capable of sustaining testing conditions for two separate collectors and is schematically compatible with the recommended circuit layout as specified by the ISO 9806:2013 standard.

All test measurements values are obtained using a data acquisition device, which is connected to a computer that logs the measurements every 10 seconds. Figure 119 shows a schematic of the data measurement and logging system.

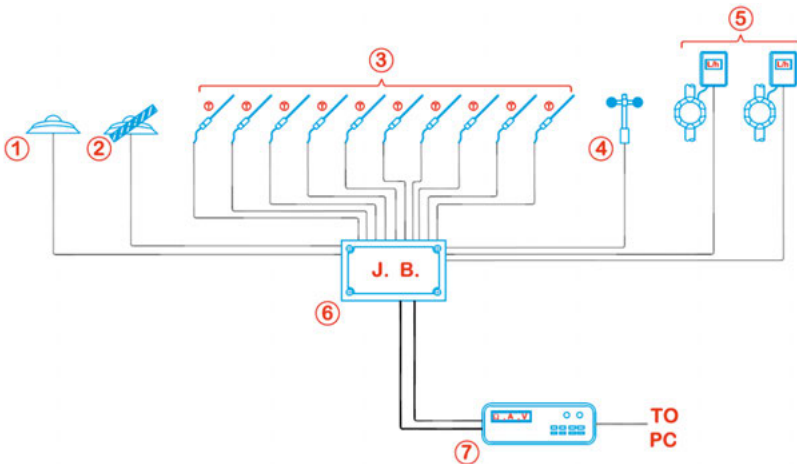


Figure 119. Data measurement and logging system.

Table 36 lists the details of the temperature and flow regulation system.

Table 36. Details of temperature and flow regulation system.

Description	Manufacturer	Model	Relevant Info
1 Pyranometer	Kipp & Zonen	CM11	Industry standard for monitoring and logging solar irradiance.
2 Pyranometer with shading ring	Kipp & Zonen	CM11	Sensitivity $7 \mu\text{V} \cdot \text{W}^{-1} \cdot \text{m}^{-2} - 14 \mu\text{V} \cdot \text{W}^{-1} \cdot \text{m}^{-2}$ Non-linearity $<0.2 \%$ .
3 Temperature sensors	Unknown	PT100	4 wire RTD sensor, individually calibrated
4 Wind Speed sensor	Thies Clima	N/A	Accuracy $\pm 0.5 \text{ m} \cdot \text{s}^{-1}$ Resolution $<0.1 \text{ m} \cdot \text{s}^{-1}$ Range $0.5 \text{ m} \cdot \text{s}^{-1} - 50 \text{ m} \cdot \text{s}^{-1}$
5 Flow Sensors	Krohne	IFC 300	Electromagnetic flow sensor Accuracy $\pm 0.3 \%$ of mean value
6 Junction Box	-	-	-
7 Data logging device	Agilent Technologies	34972A	Highly sophisticated programmable data measurement and export device capable of high-resolution voltage, current, and resistance measurements simultaneously with PC interface for logging

A dedicated temperature and flow regulation control panel is used to regulate the operational set-values as shown in Figure 120. It offers the possibility to control the pump speed, and the heating and cooling elements, in order to achieve the required test boundaries dictated by the standard.

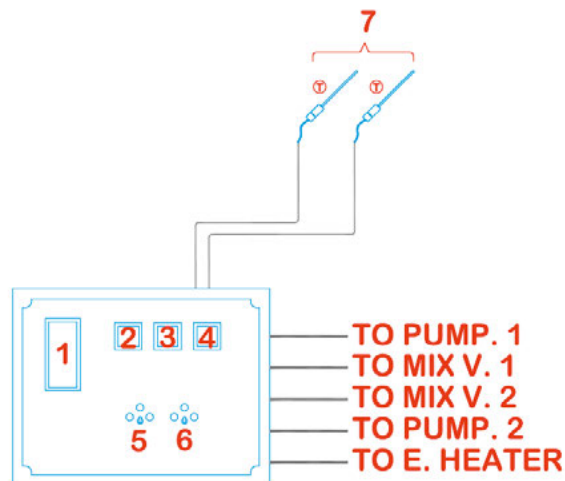


Figure 120. Temperature and flow regulation system.

Table 37 lists the details of the temperature and flow regulation system, including manufacturer, model and other information.



Table 37. Details of temperature and flow regulation system.

Description	Manufacturer	Model	Relevant Info
1 Pump control panel	Danfoss	2216e	Frequency drive pump controller regulating the primary pump (Pump. 1) flow rate
2 Heater control unit	Eurotherm	2216e	PID controller regulating operation of the system's electrical heating elements based on a temperature set point, temperature signal is taken from an RTD sensor located in line after the heating element.
3 Control unit – cooling circuit 1	Eurotherm	2216e	PID controller regulating operation of the system's borehole cooling pump (Pump. 2) and mixing valve (Mix V. 1) based on a temperature set point, temperature signal is taken from an RTD sensor located in line after the cooling circuit heat exchanger.
4 Control unit – cooling circuit 2	Eurotherm	2216e	Unused heat pump cooling circuit controller
5 Mixing valve – cooling circuit 1	–	–	Electrically actuated mixing valve controlled by the borehole cooling control unit to regulate the coolant fluid flow from the borehole.
6 Mixing valve – cooling circuit 2	–	–	Unused heat pump cooling circuit mixer
7 Temperature sensors	Unknown	PT100	2 RTD sensor, one after the heating element, and one after cooling circuit 1

In order to test the parameter characterization of the flat plate collector, the power generated is plotted against the power calculated from the formulated model. The results of both are in harmony indicating the success in the parameter characterization. These results were as expected and also validate the test rig and our procedure. This is confirmed and illustrated in Figure 121.

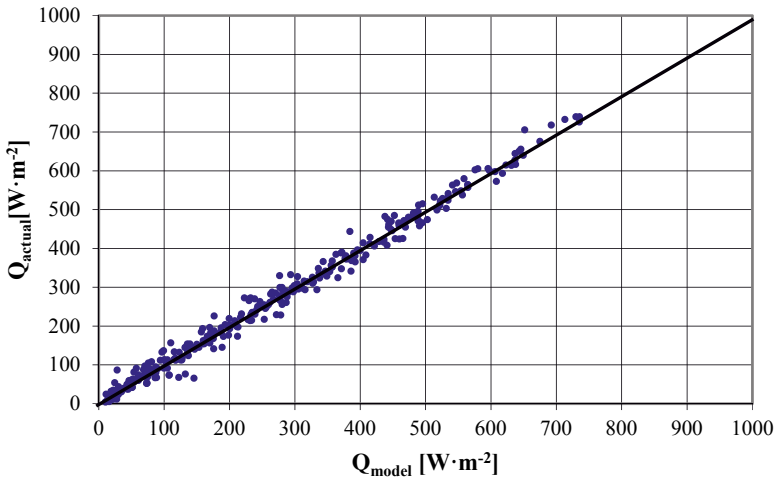


Figure 121. Actual measured production to model predicted production for a flat plate solar thermal collector.

Coefficients  $C_4$  and  $C_6$ , were omitted as per the recommendation of the standard or glazed collectors. On the other hand, coefficient  $C_2$  (the temperature dependence of heat losses) is usually essential in the model unless it comes out as statistically insignificant even with enough data points at elevated testing temperature, in that case the standard permits omitting it and the multi linear regression (MLR) is repeated without including its data.

Coefficient  $C_3$  could have been omitted initially, but it was attempted to include its data points, and they proved to be statistically significant to be include in the model, even though it possesses a relatively high standard deviation.

The same procedure was then applied to the Solarus Power Collector (PC) which is illustrated in Figure 122. Although with a higher standard deviation, the power output from both the formulated model and measured the values were congruent. Hence, it can be concluded that the parameter characterization was successful.

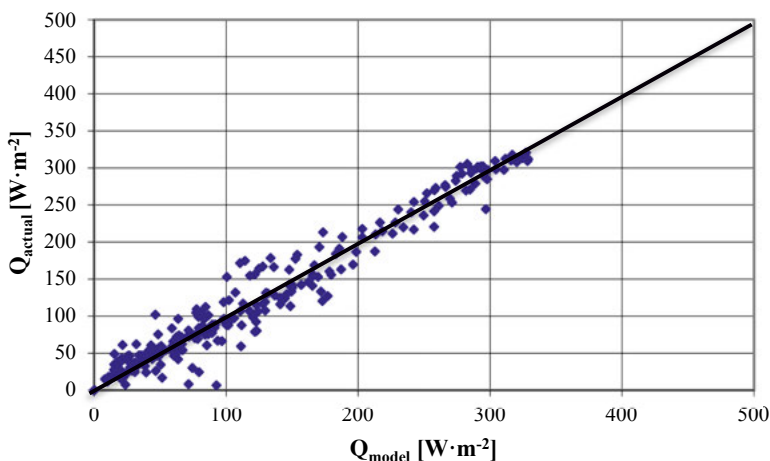


Figure 122. Actual measured production to model predicted production (PC).

Furthermore, the power production obtained using the parameters of QDT and the parameters from the testing conducted by the Applied Energy solar test Lab (AEL) in Cyprus ( $\eta=0.496$ ,  $a_1=3.155\text{W}/\text{m}^2\text{K}$ ,  $a_2=0.022\text{W}/\text{m}^2\text{K}^2$ ) was plotted and is shown in Figure 123. Comparison conditions assumed at  $1000\text{W}/\text{m}^2$  hemispherical irradiance, no diffuse,  $3\text{m}/\text{s}$  wind speed, and normal incidence angle. The results in this comparison are also in congruence.

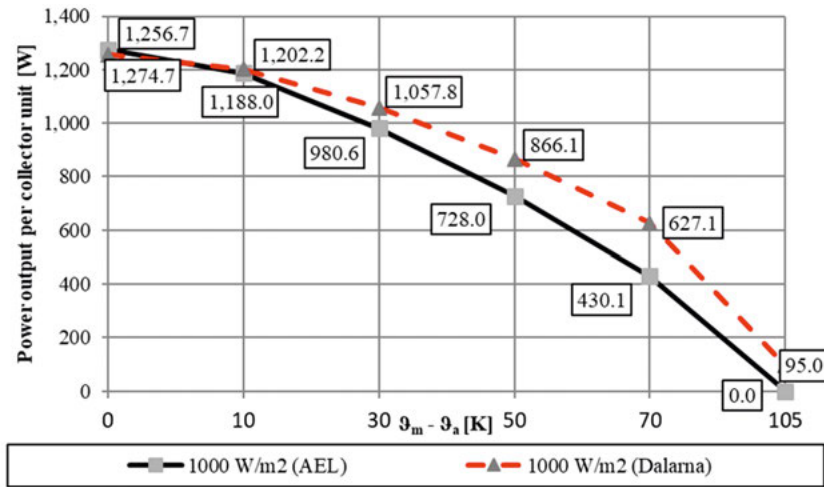


Figure 123. Actual measured production to model predicted production (PC).

## 6.8 Paper V: C-PVT with a wedge receiver

### 6.8.1 Methodology

As part of a Swedish-Iranian cooperation project, a C-PVT collector featuring a wedge PVT receiver has been designed. The PVT receiver holds 24 quarter-size monocrystalline PV cells connected in series (hand-soldered), on each receiver side. The receiver has been placed 41 mm above the center section of the parabolic reflector geometry and makes an angle of 20° between the two receiver copper plates. The solar collector trough is characterized by an aperture of 323 mm and a parabolic reflector depth of 144 mm, as shown in Figure 124.

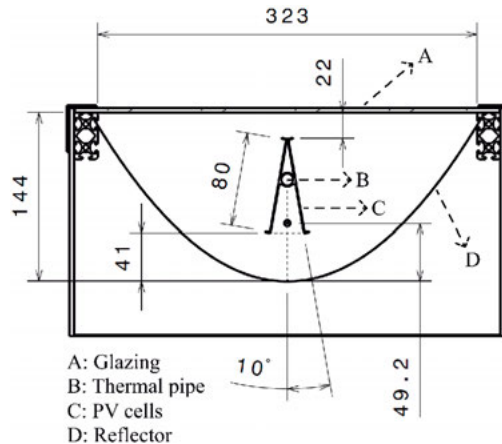


Figure 124. Cross-section (with dimensions in millimeters and degrees) view of the parabolic trough solar collector with a wedge PVT receiver.

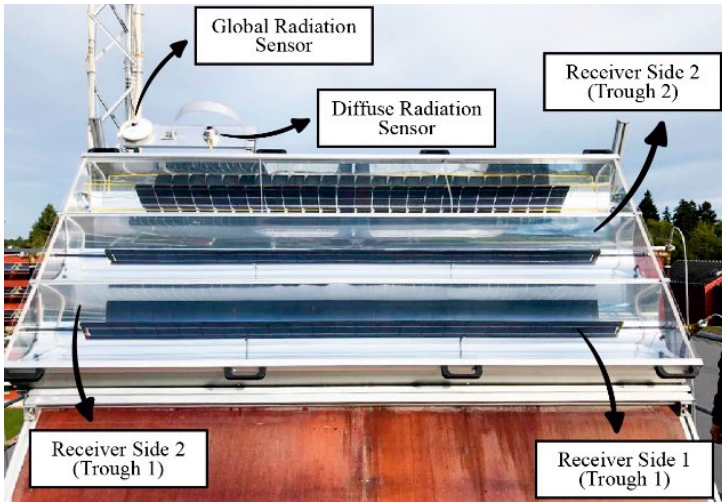


Figure 125. Solar collector test apparatus for the transversal electrical IAM testing procedure with both pyranometers for global and diffuse radiation measurements.

The collector was then installed at the HiG solar laboratory, as shown in Figure 125. Two days, one at the end of July and another in August, have been selected to provide a better understanding of the daily performance of the C-PVT solar collector for the two troughs (1-bottom and 2-top) and receiver sides (1 and 2), as well as, the importance of the collector tilt angle in the overall performance of the C-PVT solar collector. Therefore, Figure 126 presents a profile view of the wedge PVT receiver in regards to the solar radiation incidence angle for a collector tilt of  $42^\circ$  for the 28<sup>th</sup> July (A) and the 27<sup>th</sup> August (B) at noon.

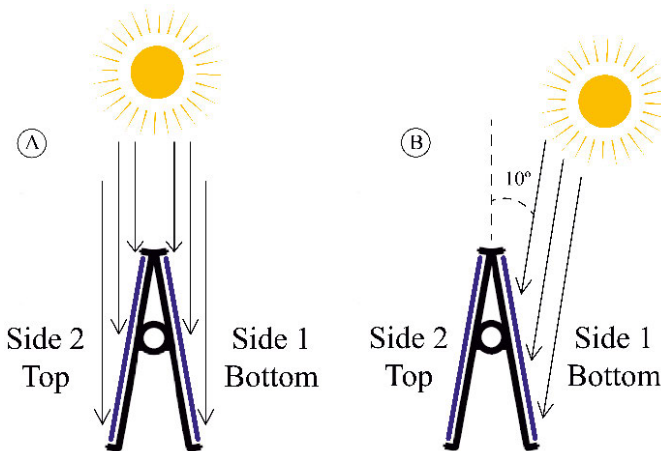


Figure 126. Solar radiation incidence angle for a collector tilt of  $42^\circ$  for the 28<sup>th</sup> July (A) and the 27<sup>th</sup> August (B) at noon.

## 6.8.2 Collector Testing Results

The optical efficiency from thermal measurements is dependent on the geometry, transmittance of the glazing, the reflectance of the reflector and the absorptance of the PV cells. Figure 127 shows the measured instantaneous daily thermal efficiency, relative to the global radiation for two similar troughs, with a time-steps of 10 minutes.

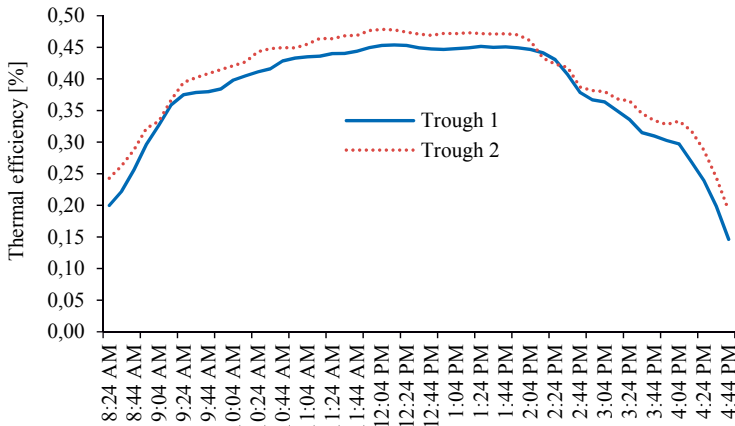


Figure 127. Instantaneous thermal efficiency diagram of the C-PVT system. The collector is south oriented and placed in the east-west direction at a tilt of  $42^\circ$ , with an HTF temperature of  $56^\circ\text{C}$  on the 27<sup>th</sup> of August.

The minor misalignment displayed in Figure 127 (from trough 1 with  $\eta_{max}=45\%$  and 2 with  $\eta_{max}=48\%$ ) is due to the fact that the cable from receiver side 1 (trough 2) was unattached from the PV cell string and no electric power was generated, which will lead to higher thermal efficiencies, as no electric power is generated the thermal production will be higher. Furthermore, the measurements were taken with an HTF average temperature of  $56^\circ\text{C}$ , which increases the losses.

The effective projected solar height determines the optimum tilt angle of a surface facing south for the given time of the year. The effective solar height for the 27<sup>th</sup> of August is fairly constant between 11:44 am and 1:44 pm, which explains the also fairly constant thermal efficiency around noon, in Fig. 14.

Additionally, from the instantaneous thermal efficiency diagrams with a fairly constant irradiation pattern (between  $850$  and  $982\text{ W/m}^2$ ), it is possible to attain the thermal optical efficiency diagram from experimental data, which is presented in the following Figure. 128, for both troughs 1 and 2.

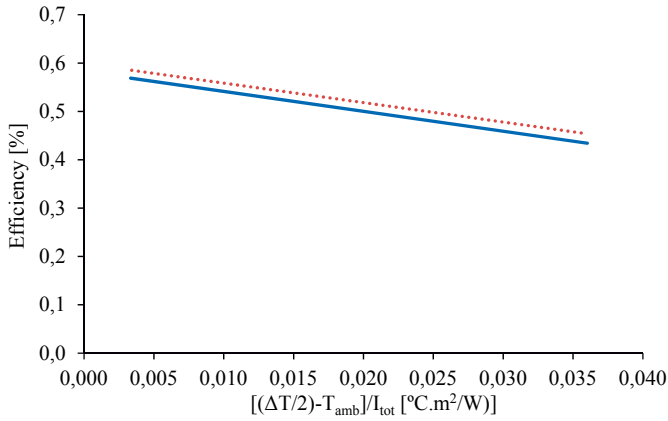


Figure 128. Experimental efficiency for trough 1-bottom (solid blue line) and 2-top (dashed orange line).

From the slope of the linear regression diagram shown in Figure 128, it is possible to extract the first-order heat loss coefficient  $U_l$  (W/m<sup>2</sup>.°C) of 4.1 and 4.0 W/m<sup>2</sup>.°C ( $R^2 = 0.996$ ) for both trough 1-bottom and 2-top, respectively. Moreover, a thermal optical efficiency of 58.3 % has been achieved for trough 1-bottom, which leads to a thermal peak efficiency of around 50.3 % if electricity is being produced. Additionally, a thermal optical efficiency of 59.9 % (i.e. thermal peak efficiency of 52.2 %, if electricity is generated) is achieved for trough 2-top. As previously stated, only receiver side 2 is electrically operational, therefore it is comprehensible that trough 2-top achieved a slightly higher optical efficiency of around +2.7 %<sub>rel</sub> than trough 1.

The electrical IAM has been obtained from the incidence angle, global irradiation (W/m<sup>2</sup>) during clear weather, and electrical power per unit of area (W/m<sup>2</sup>). Fig. 129 presents the normalized experimental electrical IAM for the longitudinal direction.

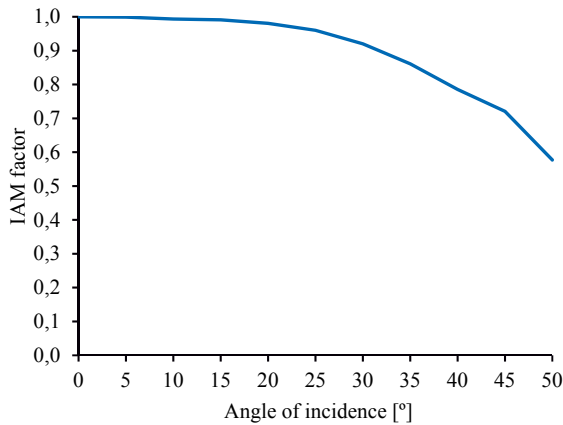


Figure 129. Normalized experimental electrical IAM (combined receiver side 1-bottom and 2-top, from trough 1-bottom), longitudinal direction.

Furthermore, Figure 130 presents the normalized experimental electrical transversal IAM diagram for both receiver side 1-bottom and 2-top (trough 1-bottom). It has a maximum deviation of 9.2 % between both receiver sides, which can be explained due to a possible misalignment of the PVT receiver, which automatically leads to a minor deviation.

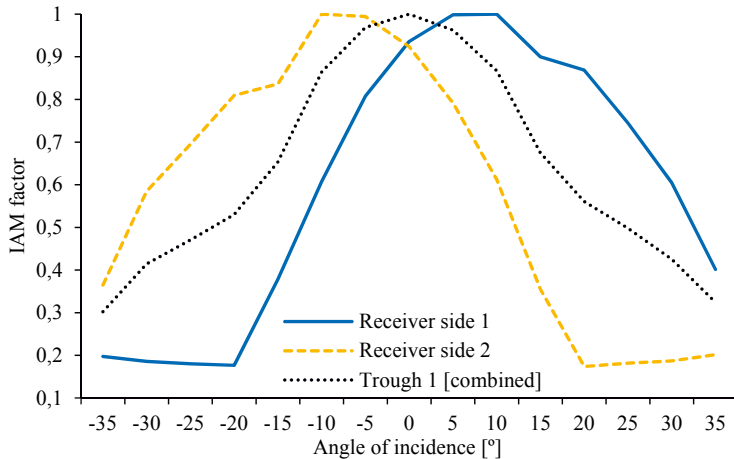


Figure 130. Normalized experimental electrical IAM (receiver side 1-bottom, 2-top and the combined trough 1-bottom) in the transversal direction.

As expected, the transversal IAM is far more sensitive than the longitudinal IAM, which is explained by the narrow acceptance angle of around  $10^\circ$  (outside of which the drop in efficiency is more pronounced). Additionally, Figure 130 also illustrates that the electrical peak efficiency of each receiver side is not reached at normal incidence (typically at  $0^\circ$ ), as in a standard flat PVT module, but between  $5\text{-}10^\circ$  due to the tilt angle between the two receiver sides. This leads to around 8 % losses at normal incidence due to the large angle of incidence at the absorber. The findings presented in this section are in line with the study presented by Koronaki and Nitsas (2018), which states that low-concentrator solar collectors are highly sensitive to high incident angles.

### 6.8.3 Conclusions

The measurement results made on the wedge C-PVT solar collector allowed the following conclusions:

- An overall electrical peak efficiency of 8 % has been achieved.
- The thermal optical efficiency reached 58.3 % and 59.9 % for trough 1 and 2, respectively.
- First-order heat loss coefficients of  $4.1$  and  $4.0 \text{ W/m}^2\cdot^\circ\text{C}$  were attained for trough 1 and 2, respectively.
- The electrical transversal IAM for each receiver side reached the electrical peak efficiency at  $10^\circ$ .
- The half-acceptance angle is around  $10^\circ$ .

- The design concept has been successful in reducing the electrical peak power at normal incidence and thus, lower the stress and high radiation intensity to which the solar cells are exposed at normal incidence.

## **6.9 The RES4Build DM Collector**

### **6.9.1 *RES4Build project***

RES4Build is a 5 M€ H2020 project pushed forward by diverse consortium with 15 partners from 8 countries. RES4Build aims to develop renewable-energy-based solutions for decarbonising the energy used in buildings. The project approach is flexible, so that the solutions are applicable to a wide variety of buildings, new or renovated, tailored to their size, their type and the climatic zones of their location. In the heart of the RES4Build solution lies an innovative multi-source heat pump with a cascading configuration, including a magnetocaloric (bottom cycle) and a vapour compression heat pump (top cycle) which is coupled with a C-PVT collector that is being designed by MG Sustainable Engineering AB.

The heat pump will be integrated with other technologies in tailor-made solutions that suit the specific needs of each building and its owners/users. These technologies are to be selected on a case-by-case basis from a mix of standard equipment available in the market and from novel components that will be specifically explored within the project. The novel components include innovative C-PVT collectors and borehole thermal energy storage. For all solutions, advanced modelling and control approaches will be developed and will be integrated in a Building Energy Management System. This will allow the users to select their objectives and to optimise the use of the system accordingly, thus activating demand response exploiting the full value of their demand flexibility. The project adopts a co-development approach, where the end-users and other relevant stakeholders are engaged in an interactive and iterative process, resulting in a co-designed RES4Build system that meets technical and non-technical user and installer requirements. In parallel, a full life cycle assessment and life cycle economics analysis is being carried out, showing from an early stage the real impact of each proposed design.

The main system components are the PVT collectors for producing heat and electricity and the dual-source (air or water) heat pump for heating and cooling. The system is intended for a multi-family residential building with the same concept also applicable in other types of buildings, such as single-family houses and offices after some modifications. The heating and cooling modes are illustrated in Figure 131, along with the main system components and their connections.



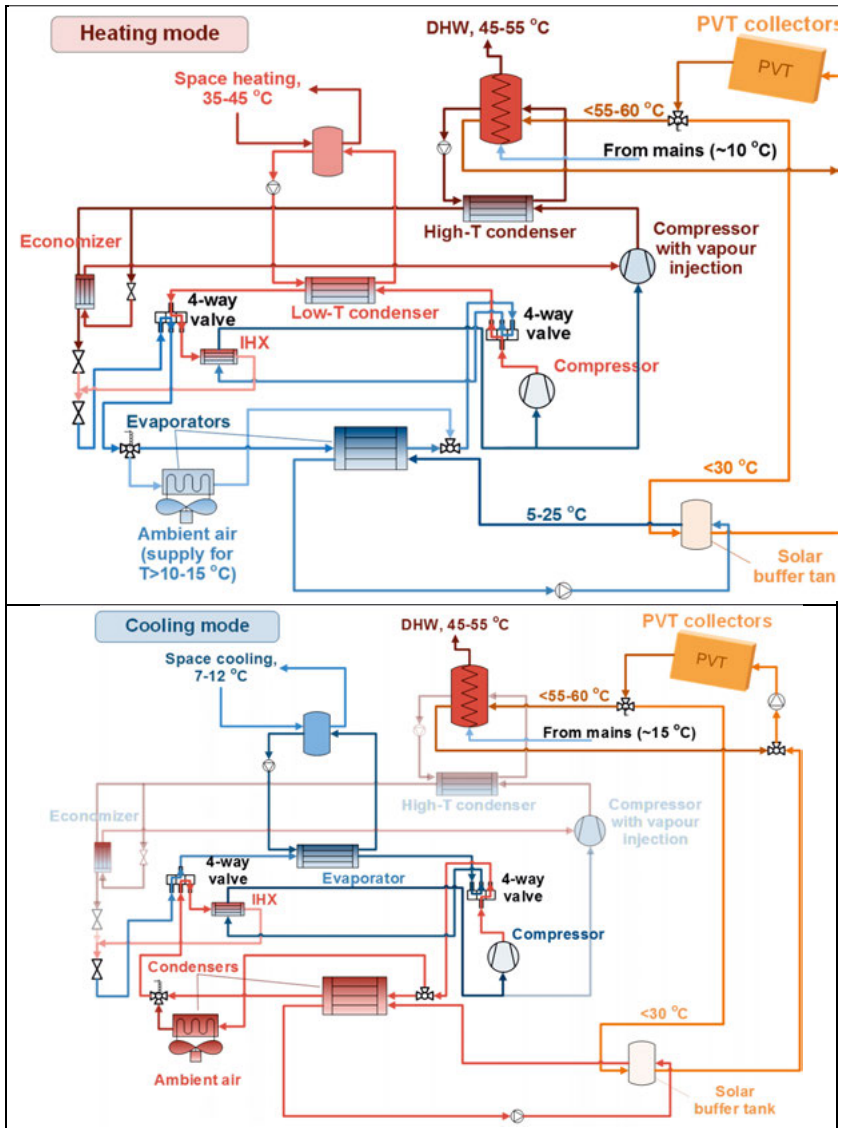


Figure 131. System operation at heating mode (top) and at cooling mode (bottom), including the main system components.

MG Sustainable Engineering AB responsibility within this project is to develop, test and deliver a new C-PVT collector design. The new design is to feature a novel reflector geometry that is suitable for PVT collectors at all latitudes and provides an increased output, as well as, an improved receiver with an improved thermal conductivity between the cell and the HTF. This last task is detailed in more detail in section 5, including the novel H-Pattern design.

### 6.9.2 Construction of the DM collector (V10 & V11)

The Double MaReCo (DM) is a symmetric CPC reflector geometry that is specifically designed for PVT collectors with the goal of increasing the annual output at all latitudes. A Solidworks rendering of the C-PVT collector, featuring the DM reflector geometry, is shown in Figure 132 and 133. The reflector geometry is fully detailed in the raytracing chapter 7.3.

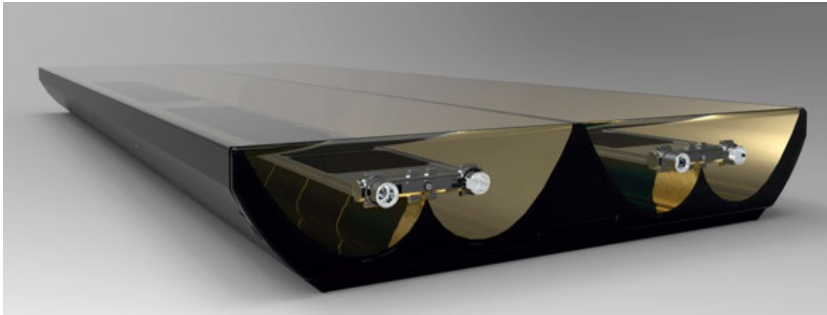


Figure 132. Solidworks rendering of the C-PVT collector with the DM reflector geometry.

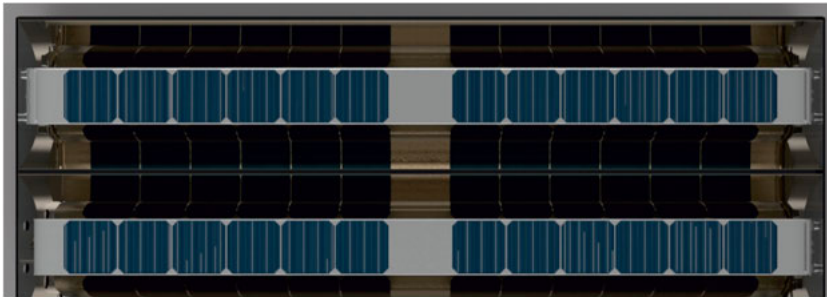


Figure 133. Solidworks rendering a top view of the C-PVT collector with the DM reflector geometry.

During the RES4Build project, the team at MG Sustainable Engineering AB built several prototype DM C-PVT prototype collectors, some of which have already been delivered to the Greek partner for testing.

Figures 134 and 135 show the construction of the second DM C-PVT prototype at Gävle University.



Figure 134. Two steps of the construction process of the DM C-PVT collector.

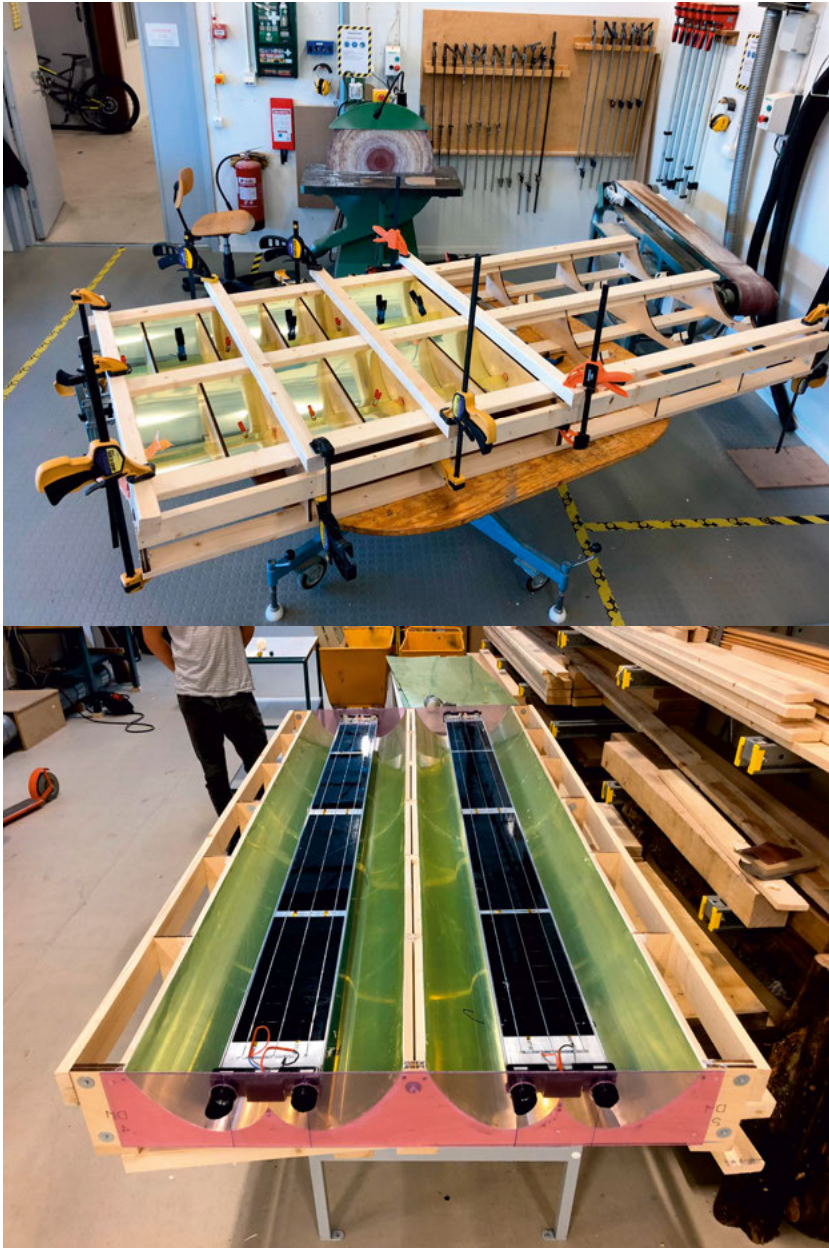


Figure 135. Two steps of the construction process of the DM C-PVT collector.

Figure 136 displays the third DM C-PVT collector version, which was delivered to the partners for collector testing and installation in Greece and Denmark.



*Figure 136.* Two steps of the construction process of the DM C-PVT collector.

Figure 137 display the final DM C-PVT collector that was produced under the RES4Build project and delivered to the partners for testing and installation.



*Figure 137.* The final version of the DM C-PVT.

Figure 138 shows a side by side view of DM C-PVT collector that was produced under the RES4Build project and the Solarus Power Collector.



*Figure 138. Side by Side view of the PC and the DM C-PVT.*

The list below highlights the three most significant advantages of the DM C-PVT over the former PC collector design:

- Thinner design that is easier to transport and install;
- Symmetric design that fits better demand profile for most applications;
- Higher annual outputs than the PC, especially on the electrical side.

### **6.9.3 New Solar Laboratory at Gävle University**

Within the RES4Build project, the University of Gävle decided to invest on a new solar laboratory. Figure 139 and 140 shows the schematic and experimental schematic setup that has been used for both electrical and thermal measurements, being able to log inlet, outlet and ambient temperature, pressure, flow rate, as well as global and diffuse solar radiation.

The test setup apparatus consists of a solar collector closed-loop and a domestic hot water open-loop. Furthermore, the solar collector loop relates to the HTF flowing between the collector and heat exchanger, supplied by a fixed flow rate. A mixture of 80 % of pure water and 20 % of ethylene glycol (with a heat capacity of 2200 J/Kg.K) is used as HTF with a heat capacity of 3813 J/Kg.K.

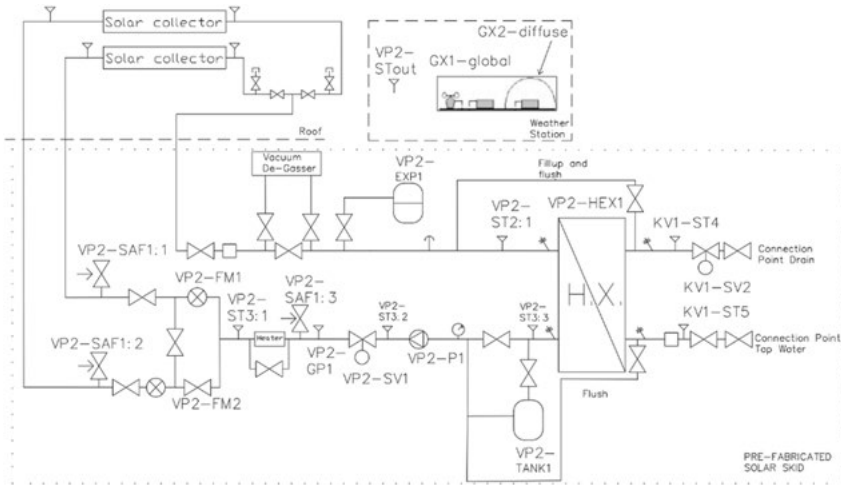


*Figure 139.* Technical drawing of the hydraulic rig composed by several temperature and pressure sensors, a heat exchanger, a vacuum degasser, expansion vessel, mixing tank (for a more homogeneous temperature), as well as a heater for constant inlet temperature.

The test rig apparatus consists of a hydraulic and electric circuit designed for performance characterization (both electrical and thermal) of any kind of domestic solar collector.



*Figure 140.* Hydraulic rig apparatus station with a pumping station for adjusting the temperature of the heat transfer fluid and fixing the flow rate equipped with several pneumatic valves and mixing circuits.



For thermal performance characterization, the inlet collector temperature was kept constant for each measurement period (in order to assess the efficiency), and the outlet collector temperature was measured to characterize the thermal behaviour of the collector. The closed-loop is composed of the following components:

- Programmable Logic Controller: All regulation and control is done by an Abelko Webmaster Pro/Ultrabase PLC system, which allows for remote control of the system.
- Automated Flow Control: The flow is controlled through a Proportional Integral Derivative (PID) regulated and a frequency-controlled pump, which allows the user to set the desired flow rate and automatically adjust to any in pressure drop.
- Collector Inlet Temperature Control: The incoming hot water from the solar collectors is first cooled by tap water (through a heat exchanger) to a temperature slightly below the desired collector inlet temperature. The water is stored in a 10L tank for buffering and then heated to the desired temperature with a 4.5 kW heater from Relek Produktion AB.
- Temperature Measurement/ Thermal performance characterization: PT100s are used to measure inlet and outlet temperatures of thermal collectors, as well as ambient temperature. The inlet and outlet temperature sensors have been installed against the flow, thus creating turbulence within the pipe and therefore yields more accurate measurements.
- Vacuum Degasser: For accurate measurement and results, the circuit must be completely free of air. Therefore, a degasser has been installed as it allows the flow to go through a chamber of lower pressure where air bubbles increase in size and are subsequently removed. Water that is free of air will naturally absorb any incoming air from the circuit and therefore the system eventually will be completely air-free, even in places where the flow is too low to physically move the trapped air bubbles.
- Insulated stainless steel piping: All piping in the test rig is made out of stainless steel pipes which decreases the pressure drop and significantly reduces the possibility of corrosion.

The solar collector test facility is composed of a hydraulic and electric circuit designed for domestic solar collector thermal and electrical performance characterization. For both electrical and thermal performance characterization, several testing measurement equipment has been used, such as two KippZonen (CMP3 for diffuse and CMP6 for global radiation shown in Figure 141) pyranometers (installed in the same plane as the solar collector), IV tracer, ambient and HTF temperature sensors, and flowmeters.



Figure 141. CMP3 and CMP6 solar radiation sensors for both global and diffuse radiation, respectively.

Table 38 presents both the thermal and electrical measurement equipment accuracy:

Table 38. Thermal and electrical measurement equipment and respective accuracy deviation accordingly to manufacturer datasheets.

Thermal measurement equipment	Value	Deviation
Flow rate $\dot{m}$ [L/m]	0.5-10	$\pm 1.5\%$
Temperature interval $\Delta T$ [ $^{\circ}\text{C}$ ]	0-90	$\pm 0.04\%$
Pressure interval $\Delta P$ [Bar]	Up to 6	$\pm 1.5\%$
Heater [ $^{\circ}\text{C}$ ]	10-90	$\pm 0.04\%$
Pressure transmitter [Bar]	6	$\pm 1\%$
Electrical measurement equipment	Data	Deviation
Pyranometer CMP3 [ $\text{W}/\text{m}^2$ ]	Up to 2000	$\pm 1.5\%$
Pyranometer CMP6 [ $\text{W}/\text{m}^2$ ]	Up to 2000	$\pm 1\%$
I-V Tracer [I] [V]	-	$0.1\%$

The testing equipment is connected to a CR1000 datalogger from Campbell Scientific (presented in Fig. 40) that monitors, records and processes the data with time-step measurements of 30 sec. All the measurements were then treated as 10-minute average data to compress and increase data accuracy.



Figure 142. Solar laboratory analysis station.

#### 6.9.4 Test results from the DM collector

The DM C-PVT solar collector has been installed and evaluated in the outdoor testing laboratory at Gävle University (Sweden) with a variable south-oriented collector tilt angle depending on the nature of the tests.

The collector has been mounted and fastened on the solar collector stand with the inlet and outlet pipes (from one side of the collector) connected to the hydraulic pumping station as shown in Figure 143.



Figure 143. The DM C-PVT collector installed at the HiG solar laboratory. (V11)

Table 39. Main parameters for solar studied collectors study, per gross area.

RES4BUILD (CPVT)		
	Value	Unit
$\eta_{0,\text{hem}}$	0.504	-
$\eta_{0,\text{b}}$	0.543	-
$\alpha_1$	3.87	W/m <sup>2</sup> K
$\alpha_2$	0.026	W/m <sup>2</sup> K <sup>2</sup>
$\eta_{\text{elect}}$	10.6	%
Solarus PC (CPVT)		
	Value	Unit
$\eta_{0,\text{b}}$	0.52	-
$\alpha_1$	3.8	W/m <sup>2</sup> K
$\alpha_2$	0.014	W/m <sup>2</sup> K <sup>2</sup>
$\eta_{\text{elect}}$	9.1	%
Weissman (flat-plate ST)		
	2 <sup>nd</sup> Order	Unit
$\eta_{\text{th}}$	0.82	-
$\alpha_1$	4.4	W/m <sup>2</sup> K
$\alpha_2$	0.02	W/m <sup>2</sup> K <sup>2</sup>
TrinaSolar (PV)		
$\eta_{\text{elect}}$	19.2	%

As intended, the measurement results confirmed a performance improvement of the RES4Build DM C-PVT solar collector in comparison to the Solarus PC featuring a MaReCo geometry.

The overall peak efficiency was increased by 5.5%<sub>rel</sub> (per gross area). Furthermore, the heat loss coefficient for the RES4Build collector increased (when compared with the Solarus PC) due to the lower concentration factor (i.e. higher heat losses), however on the other hand, the IAM profiles (shown below) showed the biggest improvement of all the parameters that have been measured. as the RES4Build reflector geometry revealed to be substantially less sensitive to high longitudinal incidence angles than the Solarus PC, and thus increasing the overall yearly energy yields.

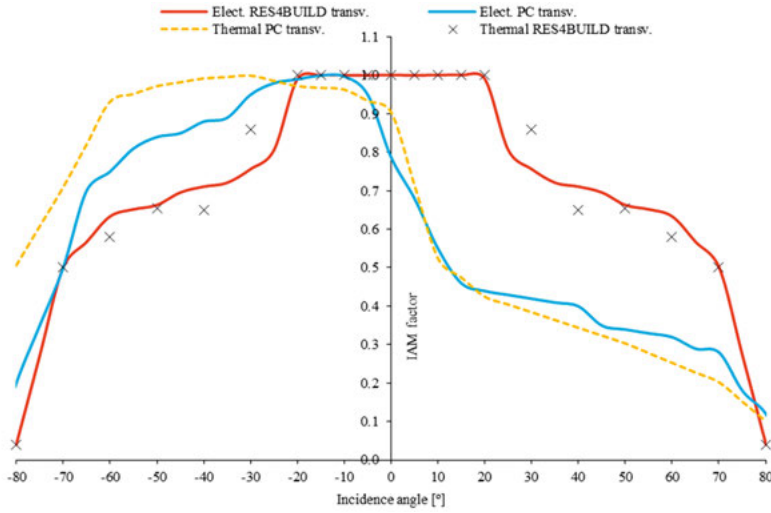


Figure 144. Transversal electrical and thermal IAM for both Solarus PC and the RES4Build DM C-PVT solar collector.

### 6.9.5 Output simulations based on the measured results

The RES4Build team has carried out measurement simulations using simulation tool developed by Solarus that is suitable for asymmetric concentrating PVT. A detailed assessment has been carried out to evaluate the required installation area for three different locations (Fayoum, Athens and Stockholm) for each technology (CPVT and PV+T).

#### Annual energy yield assessment results for Fayoum, Egypt:

The results of the performance of the difference systems are presented in Table 40:

Table 40. Production per square meter (gross area) per month for Fayoum (Egypt), for an HTF of 45 °C, 55 °C and 65 °C. Both the flat plate and PV module have 0.5 m<sup>2</sup>, which will give an overall installation area of 1 m<sup>2</sup> when combined.

	Year total [kWh/m <sup>2</sup> ]			Year total [kWh/m <sup>2</sup> ]		
	45 °C	55 °C	65 °C	45 °C	55 °C	65 °C
	P <sub>thermal</sub>	P <sub>thermal</sub>	P <sub>thermal</sub>	P <sub>electric</sub>	P <sub>electric</sub>	P <sub>electric</sub>
<i>Weissman 200FM</i>	332	265	203	-	-	-
<i>TrinaSolar AllMax Plus</i>	-	-	-	107	103	100
<i>RES4BUILD</i>	426	308	200	164	158	151
<i>Solarus PC</i>	411	302	206	117	112	107

Within the study of the electrical and thermal performance, a parallel study has been conducted on non-uniform solar irradiation profile distributions on the

selected symmetric low concentration PVT solar collector design concept, which is detailed in the raytracing chapter.

Figure 145 shows a comparison of the annual energy yield of different systems. It is important to note that the RES4Build and the Solarus PC refers to a system with 1 m<sup>2</sup> of concentrating photovoltaic thermal (one collector producing both heat and electricity), while PV + T refers to a system with two separate solar technologies, photovoltaics and thermal, namely 0.5 m<sup>2</sup> of PV panels and 0.5 m<sup>2</sup> of solar thermal collectors. This way, we can compare the output of 1 m<sup>2</sup> of the two CPVT collector versions the alternative of 1m<sup>2</sup> of PV + T.

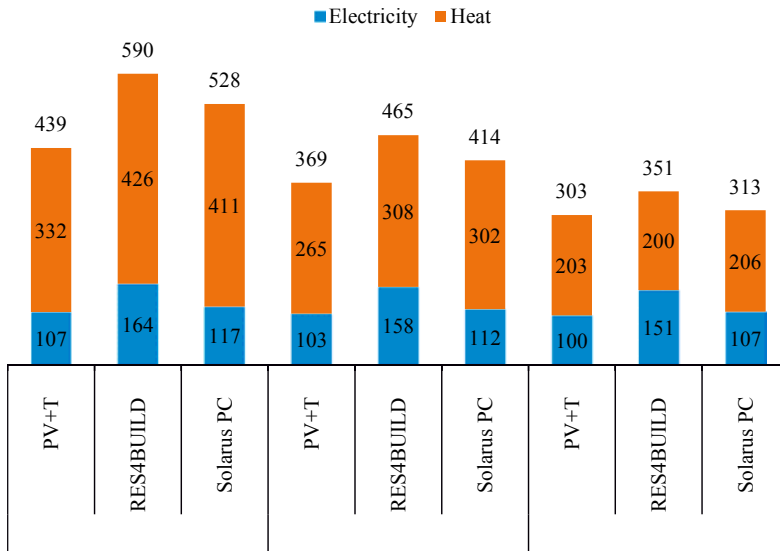


Figure 145. Yearly energy yield comparison per square meter for Fayoum, Egypt.

The PV+T system and the RES4BUILD solar collector have been considered with a collector tilt of 25°, whereas the Solarus PC has been installed with a collector tilt of 15°. These are the ideal tilts for maximizing annual output.

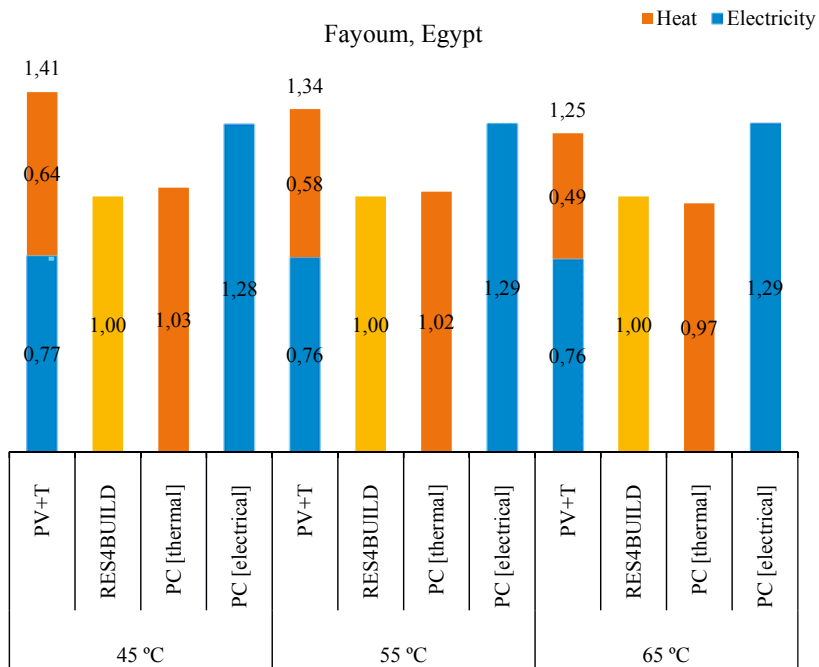


Figure 146. Required installation area to produce the same energy yield (thermal and electrical) as the RES4BUILD solar collector (Fayoum, Egypt).

The results of this study show that the RES4Build PVT collector is able to deliver the same energy yield (both thermal and electrical) making use of less collector area than a standard PV+T system. In fact, in order for the PV+T system to be able to deliver the same overall energy yield (both thermal and electrical) of the PVT collector, the PV+T system requires an additional area of +0.41 m<sup>2</sup> (at 45 °C), +0.34 m<sup>2</sup> (at 55 °C) and +0.25 m<sup>2</sup> (at 65 °C), which highlights the potential of PVT technology. At 45 °C, the Solarus collector to meet the electrical and thermal production of the RES4BUILD needs more +0.28 m<sup>2</sup> and +0.03 m<sup>2</sup> of installed area, respectively. For 55 °C, it needs more +0.29 m<sup>2</sup> and +0.02 m<sup>2</sup>, whereas for 65 °C needs +0.29 m<sup>2</sup> and -0.03 m<sup>2</sup> of installed area for electricity and heat, respectively.

### Annual energy yield assessment results for Athens, Greece

Simulations were carried out for Athens, Greece. The PV+T system and the RES4BUILD solar collector have been considered with a collector tilt of 35°, whereas the Solarus PC has been installed with a collector tilt of 20°. All collectors are at an optimal tilt for maximum annual production. The output results of the simulation are shown in Table 41 and can be visualized in Figure 147 and 148.

Table 41. Production per square meter (gross area) per month for Athens (Greece), for an HTF of 45 °C, 55 °C and 65 °C. Both the flat plate and PV module have 0.5 m<sup>2</sup>, which will give an overall installation area of 1 m<sup>2</sup>.

	Year total [kWh/m <sup>2</sup> ]			Year total [kWh/m <sup>2</sup> ]		
	45 °C	55 °C	65 °C	45 °C	55 °C	65 °C
	P <sub>thermal</sub>	P <sub>thermal</sub>	P <sub>thermal</sub>	P <sub>electric</sub>	P <sub>electric</sub>	P <sub>electric</sub>
<i>Weissman 200FM</i>	352	291	235	-	-	-
<i>TrinaSolar AllMax Plus</i>	-	-	-	115	112	108
<i>RES4BUILD</i>	356	257	170	154	148	142
<i>Solarus PC</i>	346	258	181	109	104	99

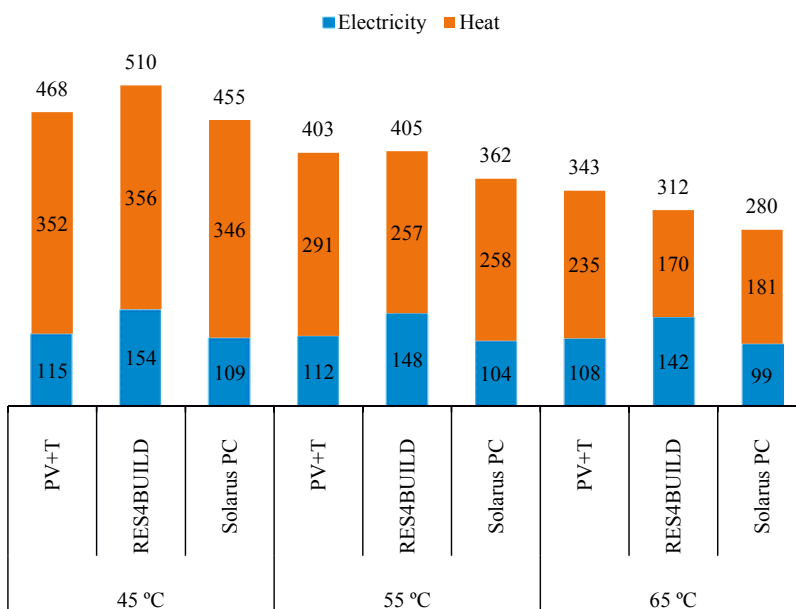


Figure 147. Yearly energy yield comparison per square meter for Athens, Greece.



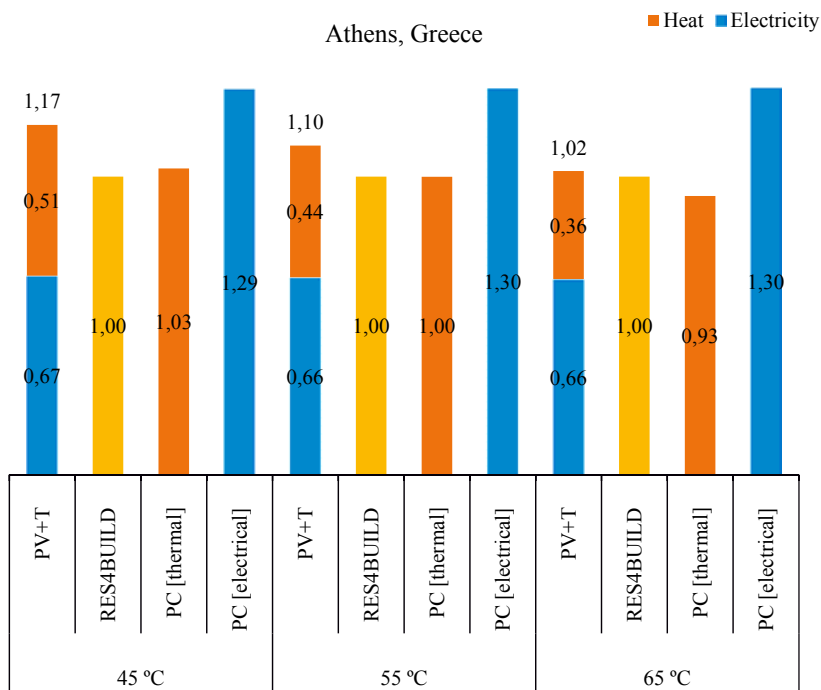


Figure 148. Required installation area to produce the same energy yield (thermal and electrical) as the RES4BUILD solar collector (Athens).

For Athens, the PV+T system needs an additional area of +0.17 m<sup>2</sup> (at 45 °C), +0.1 m<sup>2</sup> (at 55 °C) and +0.02 m<sup>2</sup> (at 65 °C) than the RES4Build solar collector, despite needing less square meters for each individual technology (e.g. PV and flat-plate). For 45 °C, the Solarus collector to meet the electrical and thermal production of the RES4BUILD needs more +0.29 m<sup>2</sup> and +0.03 m<sup>2</sup> of installed area, respectively. For 55 °C, it needs +0.30 m<sup>2</sup> for electricity, whereas for 65 °C needs +0.30 m<sup>2</sup> and -0.07 m<sup>2</sup> of installed area for electricity and heat, respectively.

**Annual energy yield assessment results for Stockholm, Sweden:**

The PV+T system and the RES4BUILD solar collector have been considered with a collector tilt of 45°, whereas the Solarus PC has been installed with a collector tilt of 40°. The output results of the simulation are shown in Table 42 and can be visualized in Figure 149 and 150.

Table 42. Production per square meter (gross area) per month for Stockholm (Sweden), for an HTF of 45 °C, 55 °C and 65 °C. Both the flat plate and PV module have 0.5 m<sup>2</sup>, which will give an overall installation area of 1 m<sup>2</sup>.

	Year total [kWh/m <sup>2</sup> ]			Year total [kWh/m <sup>2</sup> ]		
	45 °C	55 °C	65 °C	45 °C	55 °C	65 °C
	P <sub>thermal</sub>	P <sub>thermal</sub>	P <sub>thermal</sub>	P <sub>electric</sub>	P <sub>electric</sub>	P <sub>electric</sub>
<i>Weissman 200FM</i>	110	80	54	-	-	-
<i>TrinaSolar AllMax Plus</i>	-	-	-	56	54	52
<i>RES4BUILD</i>	113	64	29	95	91	88
<i>Solarus PC</i>	115	70	38	70	67	64

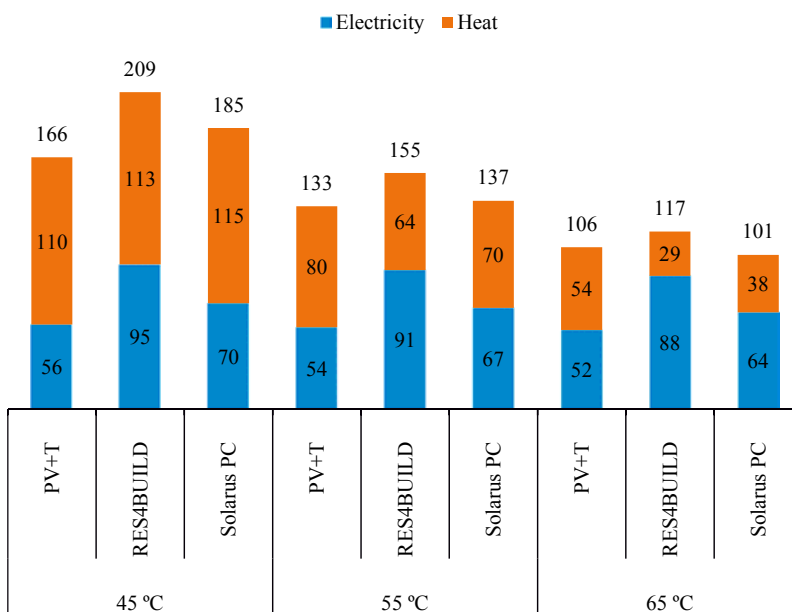


Figure 149. Yearly energy yield comparison per square meter for Stockholm, Sweden.

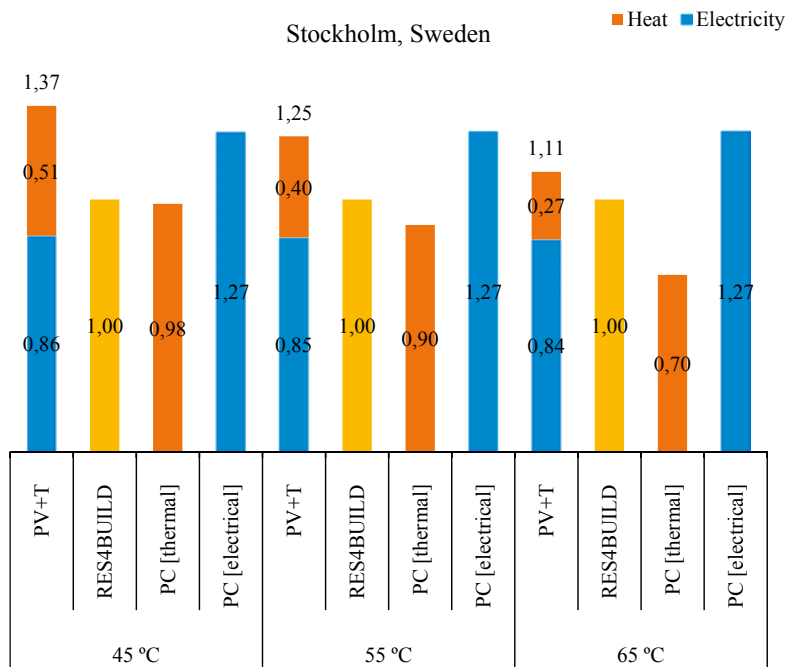


Figure 150. Required installation area to produce the same energy yield (thermal and electrical) as the RES4BUILD solar collector (Stockholm).

For Stockholm, the PV+T system needs an additional area of +0.37 m<sup>2</sup> (at 45 °C), +0.25 m<sup>2</sup> (at 55 °C) and +0.11 m<sup>2</sup> (at 65 °C) than the RES4Build solar collector, despite needing less square meters for each individual technology (e.g. PV and flat-plate) to reach the same thermal and electrical output. For 45 °C, the Solarus PC to meet the electrical and thermal production of the RES4BUILD needs +0.27 m<sup>2</sup> and -0.02 m<sup>2</sup> of installed area, respectively. For 55 °C, it needs +0.27 m<sup>2</sup> and -0.1 m<sup>2</sup>, whereas for 65 °C needs +0.27 m<sup>2</sup> and -0.3 m<sup>2</sup> of installed area for electricity and heat, respectively.

## 6.10 Testing in Cyprus, Portugal and Switzerland

### 6.10.1 Methodology and results

Eight prototype collectors were designed and constructed by the team at Solarus during 2018 and 2019. These collectors were sent to testing institutes such as the National Laboratory for Energy and Geology (LNEG) in Portugal, the Institute for Solar Technology (SPF) in Switzerland, and the Applied Energy Laboratory (AEL) in Cyprus.

The eight prototypes all use the Solarus collector box that features the asymmetric MaReCo reflector geometry. Furthermore, all prototypes also use the Solarus aluminium receiver. A description of the prototypes is presented below in Table 43:

Table 43. Description of the 8 prototypes build by the Solarus team

Name	Prototype Description
<b>1S: Sputtered</b>	Front side: PVT (standard Solarus receiver). Reflector side: Sputtered selective surface instead of the PVT receiver with the silicone encapsulated PV cells.
<b>1S: Inlay</b>	Front side: PVT (standard Solarus receiver). Reflector side: glued selective surface instead of the PVT receiver with the silicone encapsulated PV cells.
<b>PVT: 1.0 certified</b>	Standard Solarus Power Collector
<b>T: Sputtered</b>	Thermal only collector that uses the Solarus receiver with sputtered selective surface
<b>T: Black Anodized</b>	Thermal only collector that is anodized with a black non-selective surface
<b>PVT: 1.0 preliminary</b>	Standard Solarus Power Collector with a new PCB unit for connecting the solar cells and housing the diodes.
<b>T: Inlay</b>	Thermal only collector that uses the Solarus receiver with glued selective surface
<b>SPF T</b>	Front side: PVT (standard Solarus receiver). Reflector side: glued selective surface instead of the PVT receiver with the silicone encapsulated PV cells.

Table 44 describes the thermal properties of the eight prototypes.

Table 44. Thermal properties of the 8 solar collector prototypes:

Version	Name	$\eta_0$	$a_1$	$a_2$
<b>V12</b>	<b>1S: Sputtered</b>	0.583	3.088	0.011
<b>V13</b>	<b>1S: Inlay</b>	0.549	2.880	0.012
<b>V14</b>	<b>PVT: 1.0 certified</b>	0.523	3.779	0.014
<b>V15</b>	<b>T: Sputtered</b>	0.671	1.725	0.024
<b>V16</b>	<b>T: Black Anodized</b>	0.514	4.313	0.016
<b>V17</b>	<b>PVT: 1.0 preliminary</b>	0.496	3.155	0.022
<b>V18</b>	<b>T: Inlay</b>	0.656	1.790	0.013
<b>V19</b>	<b>SPF T</b>	0.676	2.300	0.0055

Lastly, Figure 151 illustrates the difference in performance between the different prototype collectors. As expected the anodized thermal collector performed substantially worse than the remaining thermal collectors. The other three thermal collectors are fairly similar in performance and thus production cost will be the main driver when selecting which version to put in production. The PVT preliminary and certified have, as expected, very similar in performance. As for the 1S PVT prototypes, that have the top side with solar cells

and the reflector side with thermal only, they displayed a fairly similar performance with the sputtered version performing slightly better.

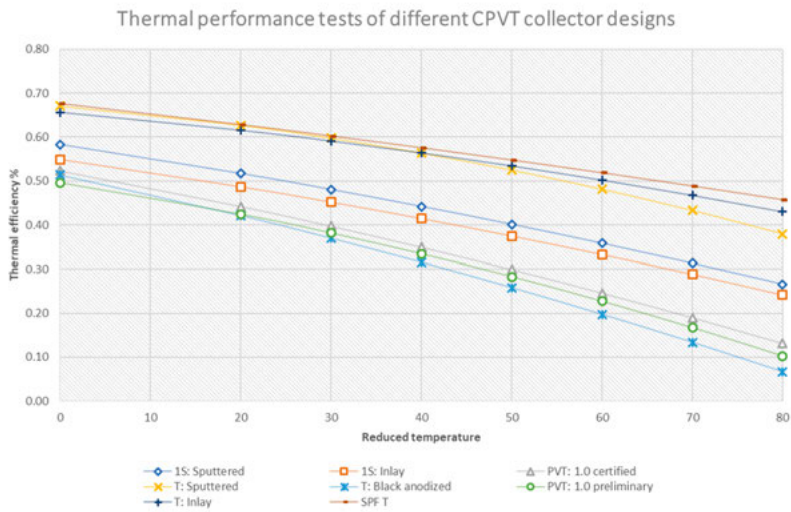


Figure 151. The thermal efficiency curve of the 8 solar collector prototypes.

## 7 RayTracing Simulations with Tonatiuh

### 7.1 Method

#### 7.1.1 *Tonatiuh and Matlab*

The Monte Carlo method uses the principles of geometrical optics as a statistical method to acquire a complete and statistically viable analysis of an optical system. Several different Monte Carlo ray tracing software exist and they are powerful tools in the design and analysis of solar concentrating systems. This thesis uses mainly Tonatiuh software although the author has also conducted some simulations in Soltrace in Paper 14 [68] and later also on OTSUN.

Tonatiuh is an open-source software specially developed for optical simulation of solar concentrating systems. The program generates rays that simulate the sun and calculate the intersections of these rays with system surfaces. The sun light is defined by the sun position, i.e., the elevation and the azimuth. These two parameters can also be calculated as a function of the day, the hour, the latitude and the longitude.

The main advantage of Tonatiuh resides in the possibility to write a script for parametrical simulations. This script allows launching several simulations and saving the results. With a script, it is possible to simulate an entire year by using loops in the script. A disadvantage of Tonatiuh is not having the possibility to conduct post-processing analysis of the results. Therefore, in order to extract the data, Matlab was used to sort and analyze large amounts of values rapidly. This is because once a simulation is done, the Tonatiuh software exports the results either as binary file (.dat) or as SQL database file (.sql).

Each simulation consists of 10,000 solar rays that are sent in the direction of the collector and whose intersection points are calculated, in order to obtain the total power from the photons that is reaching each side of the receiver. For each annual simulation, the power is calculated at each hour (i.e., in total 24 simulations per day, 8,760 simulations per year) with an accuracy of 10,000 rays. The sun shape follows a pillbox distribution, i.e., the solar intensity is the same on each point of the sun's disk, as shown in Figure 152.

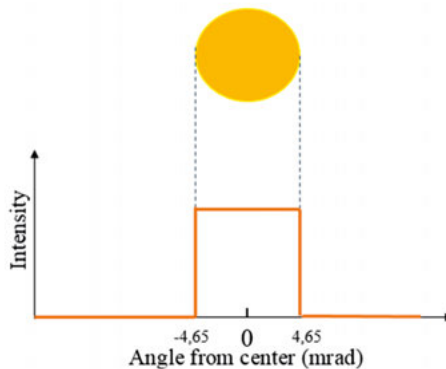


Figure 152. Illustration of the pillbox sun shape.

The parameter of this flat distribution is the half-angle width of 4.65 mrad to mimic the sun. Additionally, the irradiance is always set at 1,000 W/m<sup>2</sup> and the weather is not considered. Simulations were made for the latitude and longitude for various locations, with many studies being conducted based on the following locations: Gävle in Sweden (60°N, 17°E) and at the equator (0°N, 17°E). Figure 153 describes the ray-tracing simulation method:

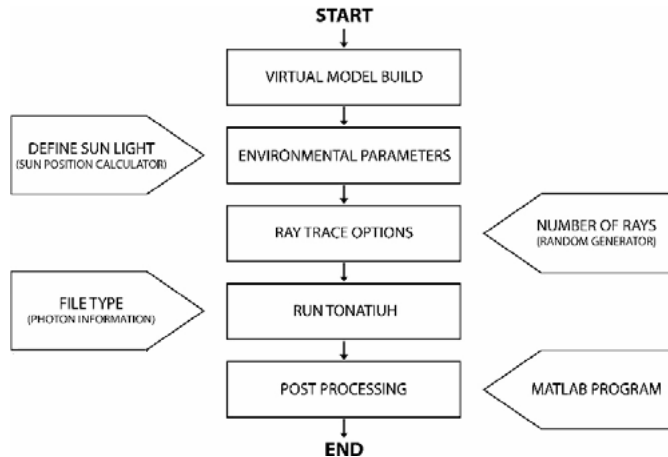


Figure 153. Ray-tracing simulation steps.

### 7.1.2 Optical properties

The simulated solar collector uses reflector material made of anodized Aluminium with a total solar reflectance of 95% (measured according to norm ASTM891-87) according to Alanod. The glass cover of the collector is made of anti-reflection coated low iron glass with solar transmittance of 95 % at normal incidence angle and a refractive index of 1.52 (measured following the norm ISO9050 for solar thermal, according to the producer SunArc). The solar transmittance of the plastic gables is 91 % and its refractive index is 1.492. Each material has been defined with a slope error of 2mrad to account for macroscopic defects. It was assumed that the light reaching the receivers is fully absorbed.

### 7.1.3 Software limitations

Regarding the software used for the sets of simulations, some limitations existed:

- Tonatiuh simulates the apparent movement of the “sun” around the collector as a full 360° in longitudinal directions over a day. This meant that we had to set a time for sunrise and sunset, in order to avoid having output during the night. The exact time of the sunset and sunrise differs throughout the year and in the different locations. Since Tonatiuh is only able to store 24 values (one per hour), it was necessary to set the sunset and the sunrise by hours instead of by minute, which leads to a slight inaccuracy.

However, this error is not significant since the energy output at low angles is significantly lower when compared with the values at midday and since the time period is never longer than 30 minutes.

- No meteorological data has been inserted in the ray tracing simulation tool. Some climates have over 50 % diffuse irradiation which considerably changes the results. Currently the simulations are conducted for one fully sunny year.

#### 7.1.4 Incidence Angle Modifier

The Incidence Angle Modifier (IAM) is the angular dependence of the optical efficiency for a solar thermal collector and the angular dependence of the electric efficiency for a PV panel. The IAM can be expressed by the following equation 41.

$$IAM(\theta) = \frac{\eta(\theta)}{\eta(\theta=0)} \quad \text{eq. 41}$$

The Solarus C-PVT is asymmetrical with different optical properties along ( $\theta_L$ ) and ( $\theta_T$ ). The IAM of an asymmetrical collector ( $K(\theta_T, \theta_L)$ ) is usually given as the product of the transversal IAM  $K(\theta_T)$  and the longitudinal IAM  $K(\theta_L)$ , which can be expressed by equation 42.

$$K(\theta_T, \theta_L) = K(\theta_T) \times K(\theta_L) \quad \text{eq. 42}$$

$K(\theta_T)$  can be measured by doing collector testing or simulated by means of ray tracing, obtaining the efficiency while the angle of the beam irradiance is varying in the transversal plane and  $\theta_L=0$ .

$$K(\theta_T, \theta_{L=0}) = K(\theta_T) \times 1 \quad \text{eq. 43}$$

Likewise,  $K(\theta_L)$  can be measured or simulated by ray tracing by the same processes, but this time we obtain the efficiency while when the angle of the beam irradiance is varying in the longitudinal plane and  $\theta_T=0$ .

$$K(\theta_{T=0}, \theta_L) = 1 \times K(\theta_L) \quad \text{eq. 44}$$

Typically, the IAM is characterized in 5 degree intervals from -90 to +90, being that the most relevant angles are generally the ones closest to 0.

## 7.2 Simulation of an early CPVT prototype

Paper VI models the performance of an early Solarus C-PVT (version V4) in terms of solar radiation received. Both the Flux homogeneity and the 3D effective solar radiation are obtained.



### 7.2.1 *The impact of the different collector components in performance*

As a verification of the newly created collector model, the simulation was started with a simplified version of the actual collector design that only featured the reflector design and the absorber. This is illustrated by the left drawing in Figure 154, which is called Ideal with only the reflector and the receiver.

Following this, several additional features of the collector were added to the models in small incremental steps in complexity level until reaching a detailed copy of studied collectors. The final version was called accurate and can be seen on the right side of Figure 154. This process allowed not only verifying the model used but also to assess the impact of the different incremental steps on an annual received energy basis.

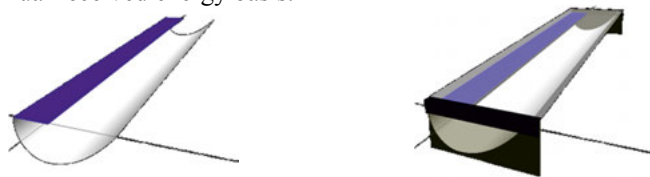


*Figure 154.* The modelled solar collector. The initial simple model was called Ideal (on the left) and the complex complete model was called accurate (on the right). The bifacial receiver is drawn in blue while the frame and plastic gables are drawn in black.

Figure 155 shows the impact in the annual received energy of each incremental change. The selected collector tilt was  $0^\circ$ . The shape on the top of Figure 155 shows the version that was modelled while the bars below describe the result.

The first shape is the simplest. The changes are then done gradually. The second shape includes an extension of the parabolic reflector while the third shape includes an extension of the circular reflector. The fourth shape includes the gap between the reflector and the absorber while the fifth includes the thickness of the absorber. The sixth shape includes the collector frame and the shading that it causes on the receiver over the year. The seventh shape includes a more accurate representation of the sun rays. For all versions, except for the last, the optical properties of the materials were set as ideal (reflectivity 100 %, transmittance 100 %, and no optical errors). The last version the collector has been simulated with all optical elements present.

The performance of the back and top sides of the receiver are constantly compared. For simplicity, the bottom side is called ‘concentrated side’ and the top side is called ‘flat side’ since it behaves almost like a flat plate. The green line in Figure 155 shows the received energy of both receivers and the numbers above show the variation to the shape called Ideal.

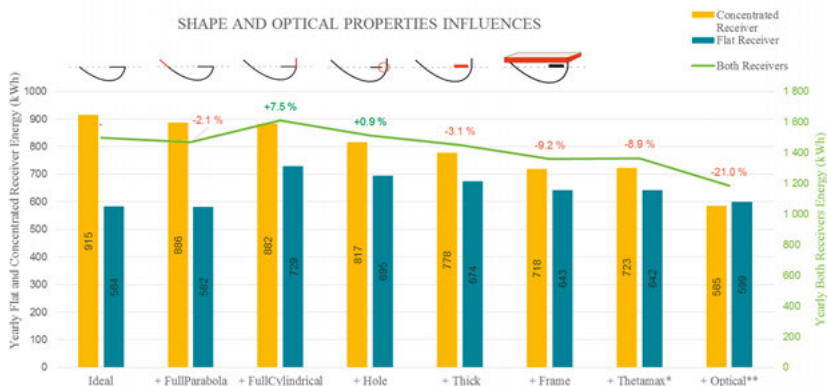


Figure 155. The impact of the different elements of the collector on performance on the annual energy receiver.

It was found that the small parabolic reflective extension leads to a small decrease (-2.1 %) due to shading effects on the concentrated side of the receiver when the sun is low. This does not affect the flat receiver.

However, the same increase in collector thickness also gives space for the extension of the cylindrical reflector which allows the flat side of the receiver to increase its yearly total power (+21 %), and so the total power of the whole collector. Overall having both extensions leads to an increase in power under these conditions (7.5 %). The space between the reflector and the receiver is big enough to affect the total power received on each side, leading to a significant decrease (-6.1 %) compared to the previous version. The fifth change is adding the thickness of the absorber, which decreases the total power received in both surfaces in the same way. This decrease happens because some light hits the sides of the receiver.

Adding a collector frame had a smaller impact than it was initially foreseen. The total power received on both receiver sides was reduced compared to the previous model. The concentrated side is, as expected, significantly more affected by this change. It must also be mentioned that adding the frame presents a much larger reduction in the PV than in the thermal part due to the series connection as discussed earlier. This reduction in electricity output will however become an increase in heat output.

Using a more accurate model of the sun increased slightly the total power received (seventh collector model). However, the biggest influence came when, on the last model, the optical properties of the material were added. As expected, the concentrated side of the absorber is far more affected by these properties due to the reflectivity of the anodized Aluminium and the fact that most of the time rays hit the reflector more than one time. The final difference between the first and last model is -21 %.

### 7.2.2 Influence of the tilt

The final version of the collector model (named accurate) was simulated for several tilt angles from 0° to 60°. The annual energy received was obtained and a power ratio power was established as defined by the equation below:

$$\text{Ratio power} = \frac{\text{Energy}_{\text{Concentrated receiver}} [\text{kWh/year}]}{\text{Energy}_{\text{both receivers}} [\text{kWh/year}]} \quad \text{eq. 45}$$

Whenever this ratio is above 50 %, it means that the concentrated receiver is performing better than the flat receiver. Figure 156 shows the yearly energy received for each side of the receiver and a power ratio which is defined by equation above.

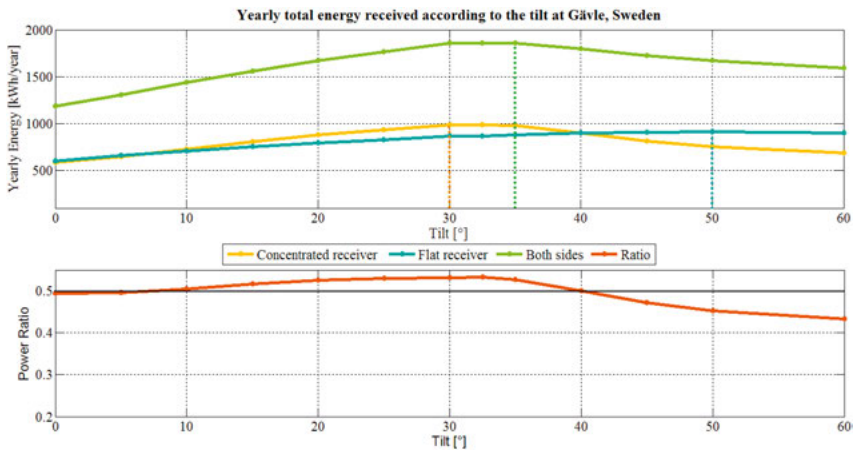


Figure 156. Influence of the tilt on the yearly energy received for each side of the receiver, in Gävle, Sweden.

The most important observation from Figure 156 is that on an annual basis, the total energy received by the concentrated side of the receiver is only 13 % above the front side, even for the best tilt for the concentrated side.

As expected, tilting the collector leads to a considerable increase in the total energy received on the receiver. Changing from a tilt of 0° to 35°, increases the power of both sides to 56 % compared to 0° tilt. Regarding the tilt that allows reaching the best performances, the two sides of the bifacial receiver behave differently: 30° for the concentrated side while the flat (or top) side performs best at 50°. The tilt that maximizes the annual received solar radiation for the whole collector is 35° for the latitude of Gävle. This is because the concentrated side is much more sensitive to the tilt variation than the flat side.

The ratio shows that between the tilts of 10° and 40°, the concentrated side receives more energy from the sun than the flat receiver. At tilts higher than 35°, the daily average power of the concentrated side starts to show large reductions during the summer days. Making an hour-by-hour observation, shows that the concentrated side receives sunlight only during a fraction of the day,

which greatly affects the daily average power in summer. For example, on the summer solstice with a tilt of  $30^\circ$ , the concentrated receiver sees sunlight between 9 AM and 3 PM, when the length of the day is 19 hours. This happens because of the reflector acceptance angle, as described in Chapter 1.

Figure 157 below shows both the daily maximum and average power that is received on each side of the receiver. At tilt  $30^\circ$ , the average power of the concentrated side is already showing a reduction in received power around the summer solstice. At a tilt of  $45^\circ$ , this cut-off is even more evident with the concentrated side of the receiver producing no power during the summer solstice due to the acceptance angle of the reflector geometry.

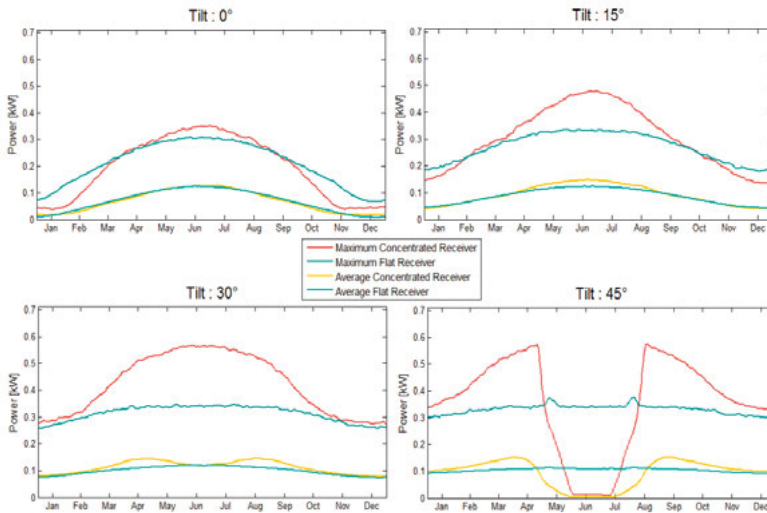


Figure 157. Daily maximum and average power received on each receiver side.

Figure 158 also shows the influence of tilt but this for the equator, instead of Gävle. On an annual basis, the total energy received by the concentrated side of the receiver is again only 13 % higher than the front side, similar to latitude  $60^\circ$ . One of the reasons for this is that in summer at  $60^\circ$  of latitude, although the sunlight lasts for 20 hours, the collector can only see a maximum of 12 hours because during the other eight hours the sun is behind the collector. It is important to note that this reflector geometry implies that the concentrated side of the receiver will not accept a large part of the incoming solar radiation either during summer or winter. At high latitudes, this does not mean that a high loss in annual performance since the winter has very little solar radiation however at low latitudes the summer and the winter generally have similar solar radiation.

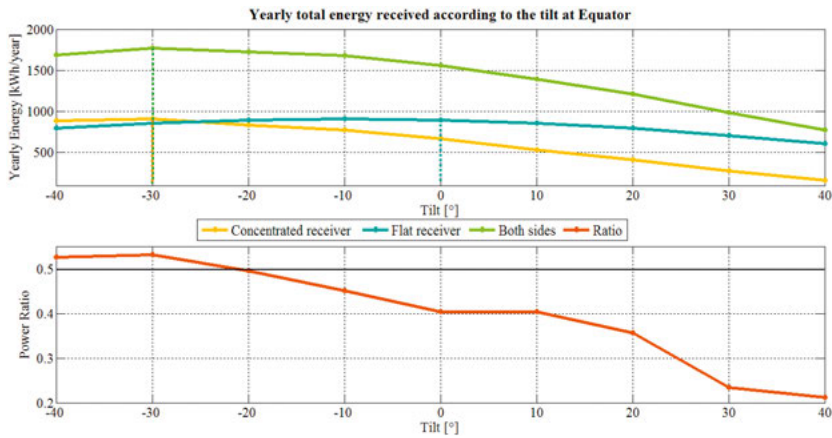


Figure 158. Influence of the tilt on the yearly energy received in each side of the receiver, in the Equator.

### 7.2.3 Flux Homogeneity

Obtaining homogeneous flux intensity on a receiver and on solar cells can improve the lifespan of the material. Additionally, non-homogenous light can reduce the collector performance, as described in several of the author's paper. In this way, it becomes important to characterize how the light is distributed in the receiver.

Figure 159 and 160 shows how the incoming sunlight is distributed on each side of the receiver. It must be noted that, in Figure 159, the surfaces plotted below are normalized in a 50x50 mesh for an easier reading of the results:

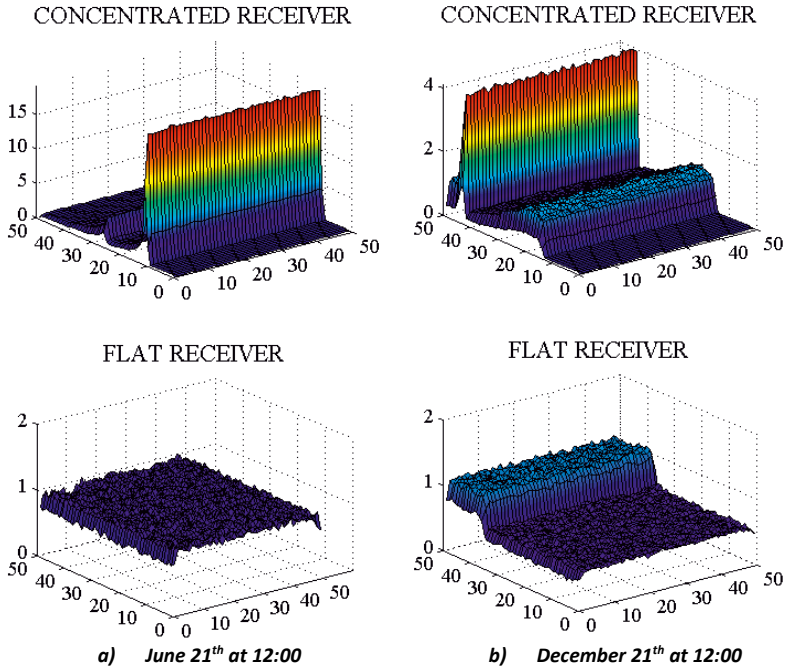


Figure 159. Light distribution on both sides of the receiver for the solstice days in Gävle, Sweden (for latitude = 60° and tilt=30°).

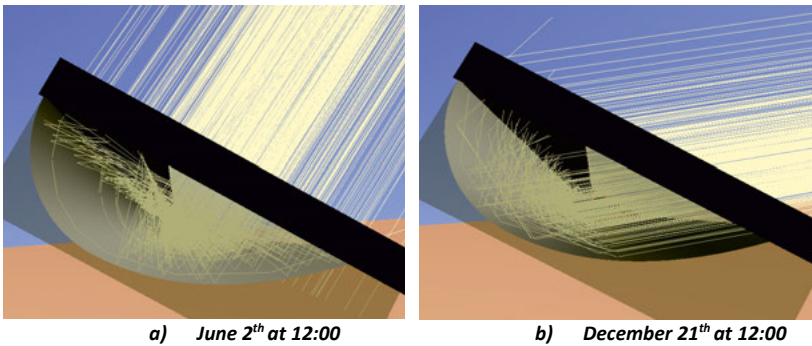


Figure 160. Illustrations from Tonatiuh showing the solar rays reaching the receiver (for latitude = 60° and tilt=30°).

Figure 160 above shows an illustration of the collector and incoming sun rays at different times of the year.

As expected, the flat side has an almost homogenous solar radiation distribution. Only the small extension of the circular reflector creates a small disruption on the homogeneity mainly around the winter solstice when the sun is low.

On the other hand, as expected the reflector focuses the light on a line, which moves depending on the incoming angle. This leads to a much higher concentration levels being reached in some parts of the receiver (around the parabola focus). Since the absorber is considerably larger than the focus area, at certain angles, there will be shading on parts of the concentrated receiver. The highest concentration factor that has been simulated for this geometry was 22 for a small duration of the day in a very small percentage of the area of the receiver, although the concentrating factor of the backside has only a concentrating factor of two. This is a high concentration factor that can potentially create durability issues and affect power production as detailed below:

- Temperature on the concentrated line raises and thus reduces cells efficiency as a whole;
- High light lead to high current in one of the three busbars of the cells which will lead to higher resistance losses;

#### 7.2.4 3D Effective solar radiation

Peak performance measurements are normally taken with exposure to the sun perpendicular to the collector plane. However, when the sun's rays reach the collector from a different angle, the performance changes. This can be explained by angular effects such as shown in Figure 161 or, for example, a decrease of absorption of the receiver at high incidence angles, shading effects caused by the collectors' frame and increase of the width of the solar image on the receiver.

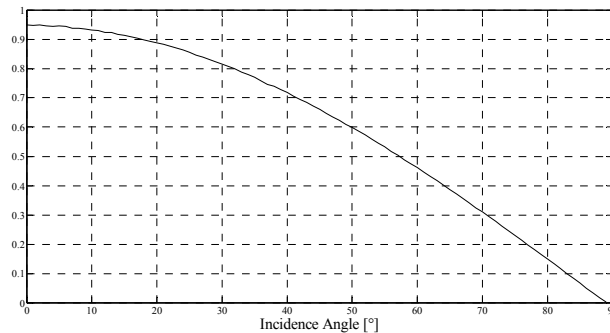


Figure 161. Transmittance times  $\cos(\theta)$  on an anti-reflecting treated glass cover (refraction index = 1.52).

The IAM is characterized by two angles: Transversal angle ( $\theta_t$ ) and longitudinal angle ( $\theta_l$ ), as can be seen in Figure 162. Figure 162 illustrates the transverse angle and the longitudinal angles of the collector and helps to understand how the effective solar radiation is obtained:

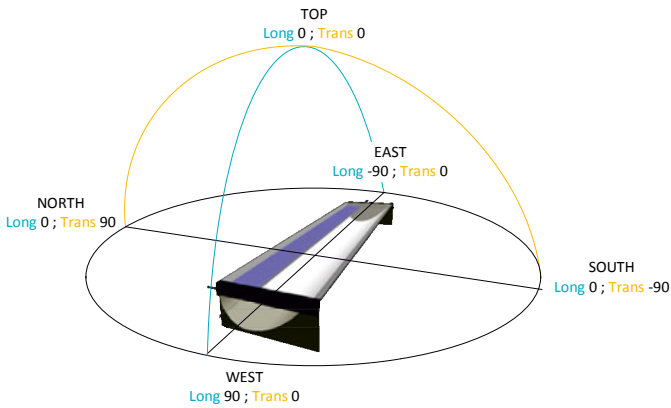


Figure 162. Representation of the longitudinal and transversal directions.

Figure 163 represents the 3D effective solar radiation, which corresponds to the coefficient of solar power for a given angle. In order to be able to measure this coefficient for different transversal and longitudinal angles, the collector was kept in the same position in one axis, while varying the other axis.

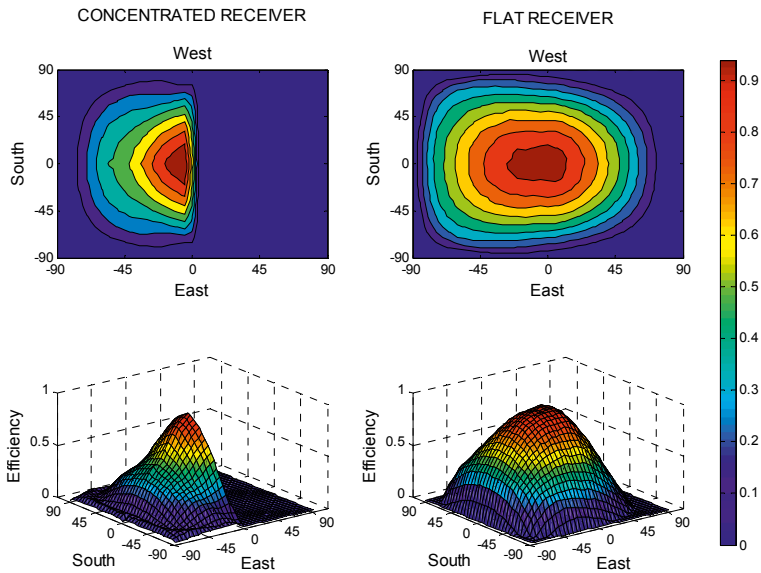


Figure 163. 3D effective solar radiation for the concentrated and flat receiver.

The output drop in the concentrated receiver around  $0^\circ$  is due to the acceptance angle of the reflector and is the most significant striking element shown by this figure.

Since light is reflected on the cylindrical extension to the flat receiver between  $-90^\circ$  to  $0^\circ$  in transversal, the effective solar radiation of the flat receiver side is also not symmetrical, almost close to it. This cylindrical extension also



shades a part of the receiver whenever the sun is between  $0^\circ$  and  $90^\circ$  in the transversal direction.

### 7.2.5 Conclusions

A numerical model was created that allows perform several simulations, which show the annual distribution of the light, in both the flat and the concentrated sides of the receiver. This analysis allows evaluating the merits of a reflector geometry. One of the advantages of using simulation is that varying the parameters (localization, tilt, collector components, etc.) is both faster and cheaper.

The main conclusions are listed below:

- The optical properties of the components affect significantly the performance of the collector. The concentrated side of the receiver is more influenced by these properties;
- The final model only performed 21% worse than the initial model with ideal properties;
- Strong non-uniformity of light was discovered, with large concentration factors at certain angles on the concentrated side. This can potentially create lifespan issues and affect the power production of the collector;
- The effective 3D solar power performance was characterized. For the concentrated side, a steep output reduction around  $0^\circ$  was found, which is due to the reflector's acceptance angle;
- Due to the acceptance angle, on an annual basis, the total energy received by the concentrated side of the receiver is only 13% above the flat side, even at the best angle for the concentrated side; this value is the same at latitude  $0^\circ$  or  $60^\circ$ . It is important to note that this value is reached for a perfect weather (assuming that all days are sunny). However, real conditions are not perfect and clouds exist. The performance of concentrating collectors is more affected by clouds than non-concentrating collectors. This is because beam light can be concentrated, but for diffuse radiation, only  $1/C$  of the total light on the aperture area is reflected. If the weather would be taken into account, it is expected that the front side of the receiver would produce more energy than the concentrated over the year. However, it is also important to note that there is a small concentration also on the front side at least for low angles, which reduces the value of the ratio.

### 7.3 Improved Reflector Geometries for C-PVTs

Paper VII explores several new reflector geometries that are more suitable for C-PVTs than the existing Solarus Power Collector design. An electrical and thermal performance evaluation of a symmetric truncated low concentration PVT solar collectors based on a CPC reflector geometry with a central transverse bifacial PVT receiver has been carried out, through a numerical ray tracing model software and a multi-paradigm numerical computing environment software. A simplified thermal (quasi-dynamic testing method for liquid heat-

ing collectors described in the international standard for solar thermal collectors ISO 9806:2017) and electrical performance models were employed to evaluate the CPVT design concepts. The evaluation was carried out for heating Domestic Hot Water (DHW) for a Single Family House (SFH) in Fayoum (Egypt), where energy yields between 351 and 391 kWh/m<sup>2</sup>/year have been achieved. The non-uniform solar irradiation assessment showed that the PV cells are exposed to high levels of radiation due to the specific reflector geometry. The study showed that the CPC geometries are sensitive to the shading effect, as partial shadowing is substantial for high incidence angles.

### 7.3.1 The DM reflector geometry

During this thesis, several reflector geometries have been created and analyzed. Paper VIII describes the process by which several variations of a reflector design called Double MaReCo (DM) has been created in conjunction with Diogo Cabral.

Winston and Hinterberger [69] demonstrated that an absorber of a two-dimensional ideal cylindrical concentrator does not need to have a horizontal flat receiver parallel to the collector aperture. Furthermore, an arbitrary absorber shape has been presented by Rabl [70], as well as different examples of ideal cylindrical concentrators as shown in Figure 164.

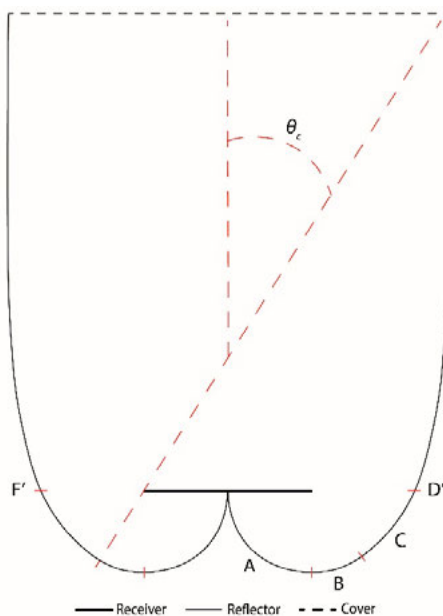


*Figure 164.* Cross-section view of the CPC reflector geometry design concept (commonly used for circular tube receivers), based on Rabl, divided into four main sections: A (90° arc-angle circular section); B (30° arc-angle circular section); C (parabola 1 section); D (parabola 2 section). Depending on the truncation, the position of the cover glass will vary along the extended parabola.  $\theta_c$  is the acceptance half-angle for the given reflector geometry.

Concentrators can be substantially truncated with very low losses of the entrance aperture. Note that truncation reduces concentration but not the acceptance half-angle [69].

Truncation was applied to decrease unnecessary shading and increase optical efficiencies and energy yields, therefore leading to a lower average number of reflections and to higher heat losses per aperture area [71] [33]. As this kind of collectors (with concentration factors below two) are introduced in the market, the collector depth (truncation point), and the maximum distance between the plane of the aperture and the reflector trough should be employed and minimized to facilitate building integration.

The design concepts were truncated for a collector depth of around 128 mm, as it was intended to have a short shadow length, which is expected to allow removing the diode system while maintaining a good performance. The general form of the design concepts (shown below) was created with both circular and parabola sections with their optical axis defining the accepted radiation interval. The reflector consists of three sections A, B, and C, which can vary in size depending on the design concept, employed. The radius of both sections A and B was set to 80 mm, slightly higher than the half of a full-size commercial PV cell width of 156 mm. This aims at minimizing the shadow effect, as well as to have the center of the circular section A slightly inside the edge of the PV cell. The shadow effect can be minimized by decreasing the depth of the reflector since the distance between the bottom receiver side and the bottom reflector will set the size of the shadow in the bottom solar cells. Furthermore, the relative shadow is set by the size of the PV cell, decreasing the losses in the remaining series-connected PV cells. Section C is characterised by a parabola section that limits the concentration factor as well as the insulation air gap.

A concentration factor on the bottom receiver side (receiver side facing the reflector) of 1.6 has been employed in all of the four geometry concepts, in order to have a very similar concentration factor as the LCPVT collector tested by Koronaki and Nitsas [72]. Furthermore, the PV cell string has a length of 2100 mm (comprising 12 full-size PV cells), and a receiver core with a length of 2310 mm, 165 mm of width, and a thickness ( $r$ ) of around 14.5 mm. The receiver placement has been kept constant with a gap between the top of the receiver and the glass of 33 mm. This gap has been implemented in order to reduce convection losses, as mentioned by Duffie and Beckman [21]. The collector and reflector length were set to 2310 mm, to cope with the shadow created by the lack of reflector in the longitudinal direction, as can be seen in Chapter 4.3. A low iron solar glass and a PMMA side gable protection with a thickness of 4 mm have been added to the collector design concept.

Carvalho et al. [71] presented the number of bounces for a CPC where acceptance radiation angles from  $0^\circ$  to  $90^\circ$  (CPC 1 and 3) have an average number of reflections of around 0.785. On the other hand, for acceptance radiation angles from  $0^\circ$  to  $120^\circ$  (CPC 2 and 4), the average number of bounces is set between 0.15 and 1.0, for a given concentration factor and specific truncation point.

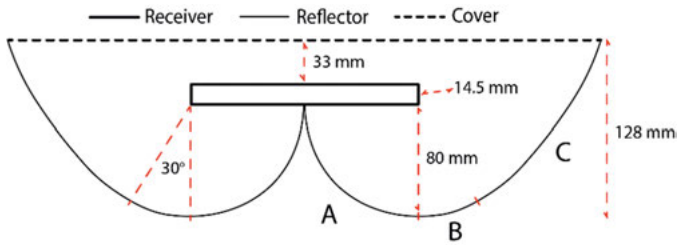


Figure 165. Cross-section view (with dimensions) of the general CPC 1 and 2 geometries. Circular section A and B with 80 mm radius and an air gap of 33 mm.

The circular section A and B are set by the acceptance half-angle of the geometry. Due to the implementation of truncation in the studied CPC design concepts, this circular section has been edited. CPC 1 has a circular section characterized by an arc angle of  $90^\circ$  and a radius of 80 mm centered on the bottom edge of the receiver edge.

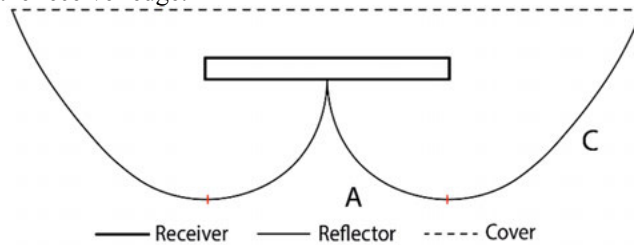


Figure 166. Cross-section view of the CPC 1 geometry: A ( $90^\circ$  circular section); C (parabola section).

On the other hand, CPC 2 has a circular section with a total arc angle of  $120^\circ$  (section A:  $90^\circ$ ; section B:  $30^\circ$ ), centered on the bottom edge of the receiver.

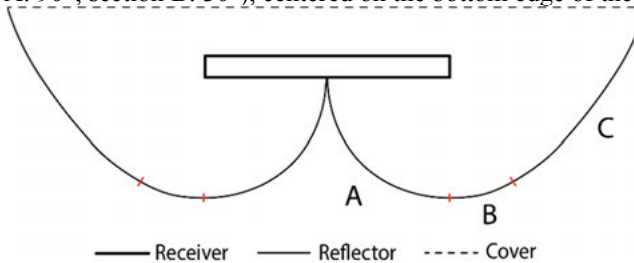


Figure 167. Cross-section view of the CPC 2 geometry: A ( $90^\circ$  circular section); B ( $30^\circ$  circular section); C (parabola section).

Regarding geometries CPC 3 and 4, a gap between the bottom receiver side and the mid reflector (middle of section A) was set to 24 mm. This design allows the light rays to pass through the center of the collector (between the bottom receiver side and reflector) being collected on the opposite side of the bottom receiver. This gap has two goals such as, distributing more evenly the

light rays and reducing the conduction losses between the receiver and the reflector. However, a downside is that this gap also allows some rays to escape (being reflected back to the outside), which reduces the optical efficiency for the collector at non-normal incidence angles. The circular section A has been shifted 24 mm downwards and rotated 30° towards section C (D' and F', respectively).

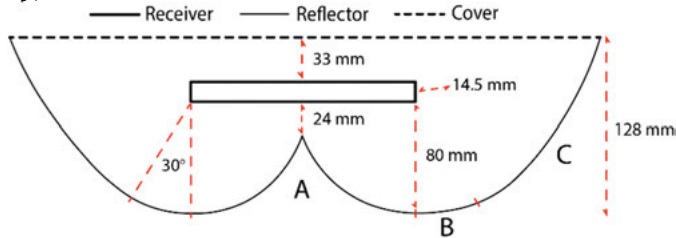


Figure 168. Cross-section view (with dimensions) of the general CPC 3 and 4 geometries. Circular section A and B with 80 mm radius, an air gap of 33 mm and an aperture area of 1 m<sup>2</sup>.

CPC 3 has a circular section A characterized by an arc angle of 77°, centered in the bottom edge of the receiver.

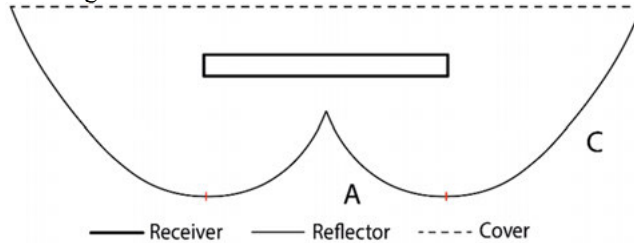


Figure 169. Cross-section view of the CPC 3 geometry: A (77° circular section); C (parabola section).

On the other hand, geometry CPC 4 has an arc angle (section A and B) of around 107° (section A: 77°; section B: 30°). The 30° arc angle employed in the circular section B, has the aim to compensate the Earth's declination ( $\pm 23.45^\circ$ ) so that the collector has a wider range of working hours.

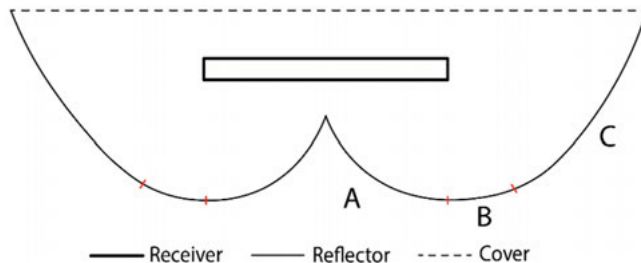


Figure 170. Cross-section view of the CPC 4 geometry: A (77° circular section); B (30° circular section); C (parabola section).

Incoming sunlight that reaches the collector aperture area at the adequate angle of incidence will be reflected into the receiver or circular section, while all incoming light with a negative incidence angle will be reflected out.

### 7.3.2 Comparison of Incidence Angle Modifiers

Paper VIII also features a detail comparison of the IAM of each reflector design. For all evaluated design in Paper VIII, the longitudinal profile is fairly similar for top and bottom. However, the top shows a considerably better transversal IAM than the bottom. Furthermore, the top side of the receiver acts like a standard PV panel, which means that the main difference between geometries lies in the transversal direction of the bottom side, which is carefully analyzed in the paper. The IAM of CPC 4, is shown in the Figure 171:

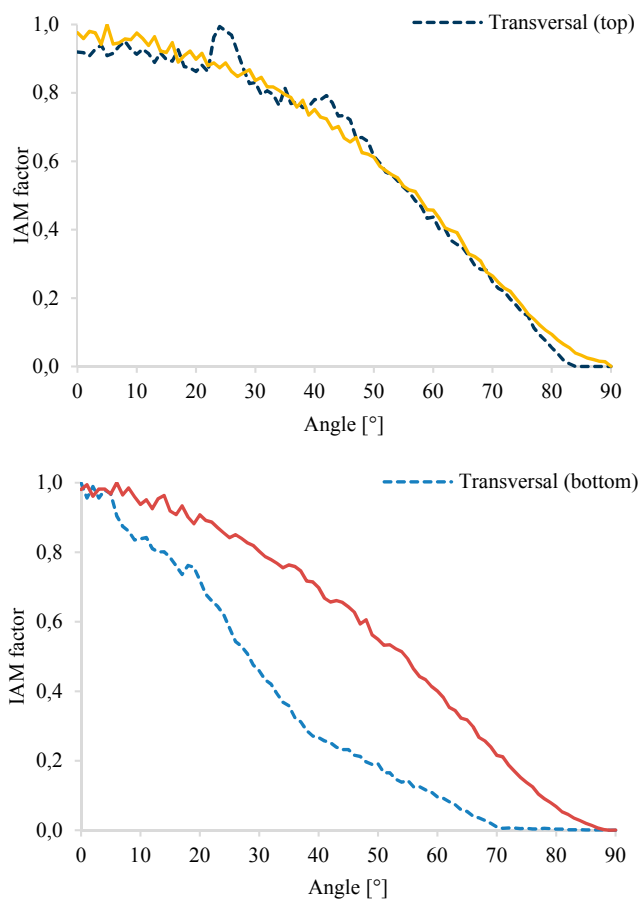


Figure 171. CPC 4 normalized IAM for normal incidence (for a reflector depth  $z$  of 128 mm and a receiver thickness  $r$  of 14.5 mm). Solid line: Longitudinal IAM; Dashed line: Transversal IAM.

Another important point to make is that all of these reflector designs were found to be more suitable for a low concentrating PVT than the current design of Solarus (MaReCo). The improvement in performance is more visible as we come to the equator.

The highest optical efficiency obtained was 46.3 %, while the lowest was 43.1 %.

### 7.3.3 Electrical and thermal yield

An evaluation focused on the thermal output of a DHW system for Single-Family Houses (SFH) in Fayoum (Egypt) was carried out for a range of temperatures between  $T_{in} = 40\text{ }^{\circ}\text{C}$  and  $T_{out} = 65\text{ }^{\circ}\text{C}$ . Several tilts have been simulated and the highest annual energy yield output has been obtained for a  $25^{\circ}$  tilt, which, as expected, is slightly below the  $29^{\circ}$  of latitude for Fayoum.

Energy yields between 351 and 377 kWh/m<sup>2</sup>/year were achieved, depending on the design concept, which represent a variation of 6.9% in the annual energy yield between the design concepts.

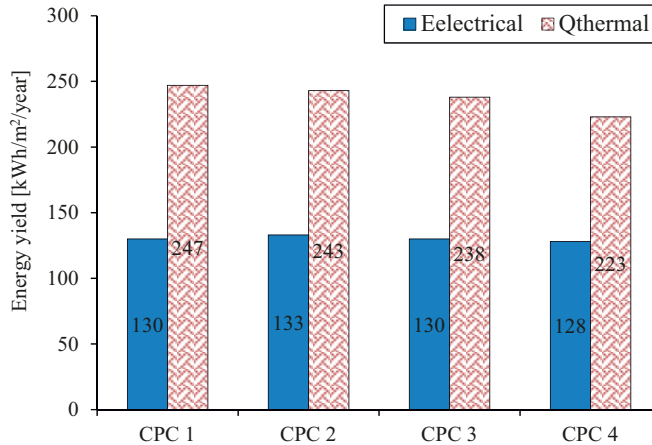


Figure 172. Annual electrical (solid fill, blue) and thermal (pattern fill, red) yield for a DHW/SFH system, for a range of temperatures between  $T_{in} = 40^{\circ}\text{C}$  and  $T_{out} = 65^{\circ}\text{C}$  (for a reflector depth  $z$  of 128 mm and a receiver thickness  $r$  of 14.5 mm).

Generally, CPC 3 and 4 achieved lower annual total yields, showing that the gap between the reflector (section A) and the bottom of the receiver does lead to a reduction in output. However, it is important to point out that the benefit from an increase in light uniformity over the receiver is not accounted in these simulations, due to the lack of literature to estimate the performance decrease associated with the increase of the non-uniformity of light in PV cells. Durability is another key issue whose potential benefits are difficult to estimate.

### 7.3.4 Evaluation of non-uniform illumination

The following study has been done for a constant reflector depth ( $z$ ) of 128 mm and a receiver thickness ( $r$ ) of 14.5 mm. The transversal angle was kept at  $0^\circ$  while the longitudinal was simulated for every  $15^\circ$  (from the normal of the solar collector to the cover glass). Then the process was repeated for a longitudinal angle fixed at  $0^\circ$ .

Figure 173 shows the different longitudinal irradiation profile distribution on the bottom receiver side, for different incidence angles and for all four reflector geometries. CPC 3 is the design that shows the highest concentration levels surpassing  $6.5 \text{ kW/m}^2$  while CPC 4 has the lowest levels concentration at just over  $4 \text{ kW/m}^2$ . All troughs clearly display the two focus lines for all angles.

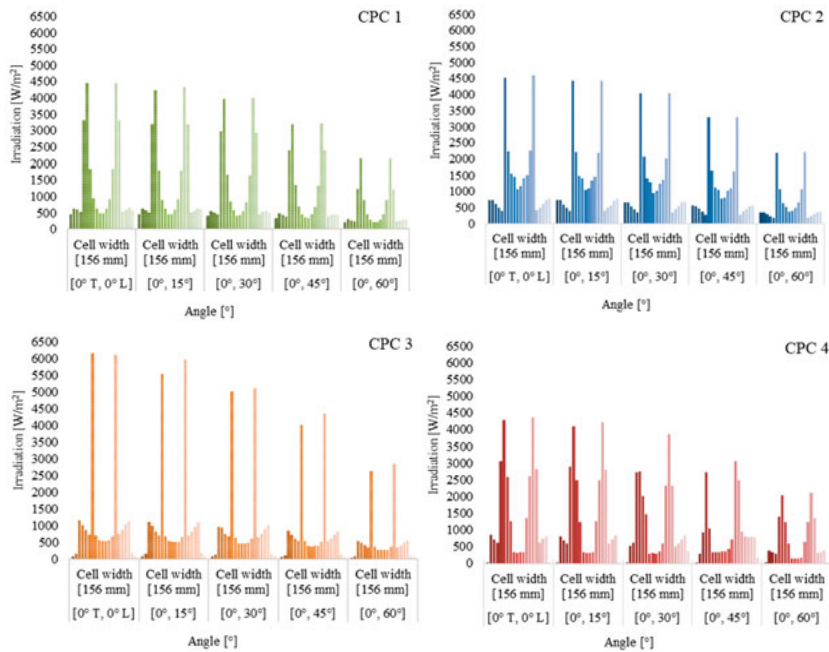


*Figure 173.* Irradiation profile distribution on the transversal (direction) cell plane (156 mm) for different incidence angles (i.e., variable longitudinal angle and constant transversal angle) (for a  $z$  of 128 mm and  $r$  of 14.5 mm).

Another important point is that comparing the above results with those of Paper VII (Chapter 7.2), where the Solarus MaReCo geometry is simulated, it is possible to conclude all DM reflector geometries vastly outperform the PC in terms of light uniformity. Since the PC reaches concentration levels of  $20 \text{ kW/m}^2$ , even the worse performing DM geometry outperforms the PC by a factor 3 in terms of light uniformity, which should prove significant in terms of reducing the thermal stress on the monocrystalline silicon PV cells.



For a constant longitudinal and variable transversal angles (figure shown in paper VIII), CPC4 once again shows lower sunlight intensity levels. This is especially relevant for the region of  $0^\circ \leq L \leq T$ , which gathers the most intense solar radiation levels and thus has the highest potential for damaging the solar cells as well as for creating high resistance loss that limit output.

A further analysis was also conducted at a string level, showing the longitudinal angle at which the limiting cells (colored in black) become shaded and thus produces less power than the rest of the cells in the string. This analysis is presented in the Figure 174.

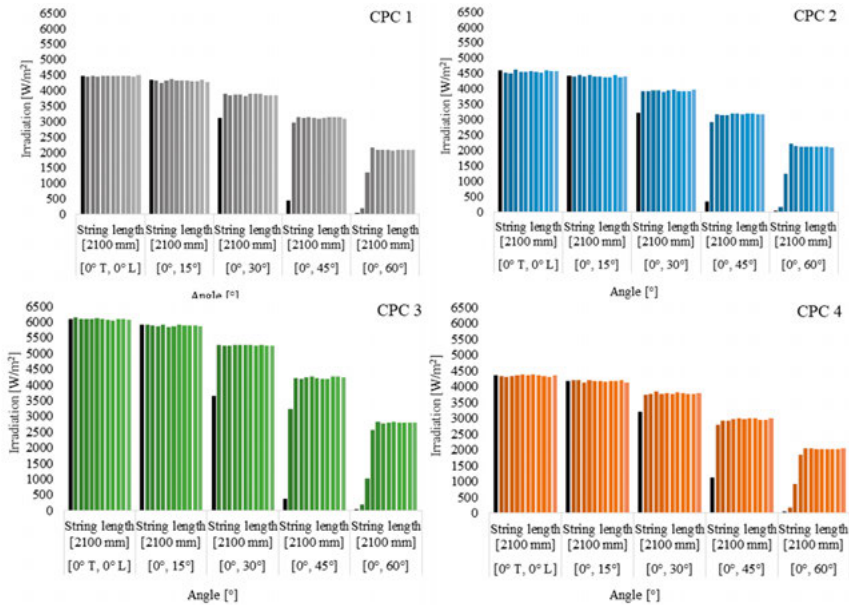


Figure 174. Irradiation profile distribution on the longitudinal (direction) string plane (2100 mm) for different incidence angles (i.e. variable longitudinal angle and constant transversal angle)

An analysis of Figure 174 shows that, for all reflector designs, all cells have the a similar illumination, when at an angle of  $0^\circ$  and  $15^\circ L$ , which means that no cell is limiting the power of the string. However, from  $30^\circ L$  onwards, the limiting cell (shown in black) starts to present a significantly lower illumination than the remaining cells in the string, which means that if there is no diode, this cell will be limiting the output of the whole string. This analysis allows quantifying the impact of the longitudinal shading on the whole string. The CPC reflector design number four is less sensitive to this type shading than the remaining designs. Furthermore, longitudinal shading would not occur, if there would be a reflector extending infinitely in the same direction as cell string.

At around  $60^\circ L$ , the first cell receives no illumination and the whole string will be producing almost no power unless there is a diode is in place.

Another important point to mention is that despite having a similar irradiation profile as the other three geometries, CPC 3 achieves higher irradiation intensities.

### 7.3.5 Conclusion

The goal of the studied designs is to maximize the incoming solar radiation that can be collected without the need for tracking while simultaneously reducing non uniform illumination, which has a potential to reduce the lifespan of the solar cells. In comparison to the MaReCo design, the DM possesses a symmetric reflector geometry with a low concentration factor which allows dividing the focal line into two, which lowers the impact on non-uniform illumination. Furthermore, the lower collector depth allows for reduced longitudinal shading, as show in the previous Chapter. This is particularly important for the electrical part of these PVT reflector design concepts.

Furthermore, the use of a symmetric reflector geometry allows higher annual outputs worldwide, matching better with the typical annual heat demand curves. A low concentration factor is necessary to avoid tracking

CPC 1 achieved the highest annual energy yields while CPC 4 achieved the lowest, although the difference in output is not very large at 1.6 % for the electrical performance and 10.7 % for the thermal output. This is due to the 24 mm gap, that causes part of the incoming reflected light to miss the reflector, thus leading to lower energy yields, with the electrical yield being far less sensitive than the thermal yield for the all the studied design concept variations. However, this happened, only because the partial shading on the PV cells has not been taken into account in the output simulations, otherwise, it would be expectable that the electrical yield is more sensitive than the thermal yield.

Overall, each of the four design concepts analyzed (and its multiple variations) show advantages and disadvantages. Based on the findings, the authors believe that CPC 2 showed to be the most promising geometry due to the combination between total illumination received and radiation profile on the bottom receiver. Furthermore, CPC 1 and 2 display a more uniform radiation distribution profiles than the remaining geometries, leading to lower maximum incident radiation, thus higher energy yields and lower level of cell stress, which ultimately means higher durability. Moreover, the study showed that the longitudinal direction is closely related to the shading effect, as partial shading is substantial at 30°. In this point, CPC 4 has the lowest shading on the first cell at 30°. This is especially important in array of PV cells without a diode to mitigate the impact of shading.

Comparing the DM design to the MaReCo Solarus PC design, it can be stated that there are large improvements in terms of reduction of non-uniform illumination (a factor 3 at least) and in terms of mitigation of shading (in particular longitudinal shading and the electrical output). Furthermore, the advantages of the DM vs the PC reflector geometry will increase as the collectors are deployed closer to the equations, as the winter solar radiation (and consequently the output) increases.

## 8 Overall Conclusions

This thesis analyses solar thermal, solar photovoltaic, and the combination of both of these technologies into a PVT collector. Additionally, concentration in PVT is also discussed.

Research Question 1: **How does the annual energy output ratio between PV and ST collectors vary around the world? What is relevant to consider when analyzing this ratio?**

A market survey has been conducted that assessed both price and performance of various standard domestic solar thermal and photovoltaic modules for 2013 and 2021. An annual energy output ratio between PV and ST calculated based on Winsun simulations, and plotted for 66 locations in the world map.

Comparing PV and ST only on the basis of panel performance, ST always yields a higher thermal annual output than the electrical output of PV for any location in the world. However, at higher latitudes, on average, this ratio becomes less favourable for ST, despite large variations being introduced by the local climate. Two main factors are responsible for this:

- The efficiency of a PV panel is reduced with increased air temperature, while for ST the opposite effect takes place;
- Under low intensity solar irradiance, the efficiency of a PV panel is maintained, while a solar thermal collector might not reach the required operating temperatures and have an output of zero.

It is important to keep in mind that PV produces electricity, which is more valuable than heat. Furthermore, solar thermal systems are more complex and thus its performance is more sensitive to the quality of the installation. Some additional conclusions can be drawn from the ratio:

- The ST to PV ratio was also calculated for ST operating temperatures of 30 °C and 80 °C. As expected, the ratio goes up for 30 °C (meaning that it is more favourable to ST) and goes down for 80 °C (meaning that it is less favourable for ST);
- All four maps show that for locations with low number of hours with high solar radiation intensity or low ambient temperature, the ratio goes down meaning that ST is producing less energy in relation to the PV;
- For latitudes lower than 66°, the ratio of flat plate at 50 °C to PV ranges from 1.9 to 4.5 while the ratio between vacuum tube at 50 °C and PV ranges from 3.1 to 4.8. These numbers can be an important tool when making the decision between PV and ST. However, it is important not to forget that the dimensioning of ST installations is of utmost importance in order to ensure that there is sufficient heat demand, so that the collectors

are working at a high efficiency, which is key to generate good revenue from projects;

Additionally, for all 66 locations, vacuum tubes with flat absorber normally outperform flat plate collectors per aperture area for temperatures of 50 °C and 80 °C. However, the price per aperture area of vacuum tube with flat absorber is also 32 % higher than flat plate. This means that, assuming that the installation cost is the same for both ST technologies, vacuum tubes should be preferred only if its annual output is higher than a flat plate annual output by 32 %. For a temperature of 30 °C, the flat plate is sometimes outperforming the vacuum tube with flat absorber, namely in warm locations;

**Research Question 2: What are the most important parameters that define PVT and C-PVT collectors?**

Solar collector characterization relies on two main testing methodologies: Quasi Dynamic Testing (QDT) and Steady State (SST). Each methodology has advantages and disadvantages as previously outlined.

During this thesis work, 30 different prototype collectors have been tested. In order to characterize the electrical output of a PVT collector, the defining parameters are peak electrical performance and temperature coefficient, while for the thermal part, one needs to consider the optical efficiency and the heat loss factor, which for collectors that operate at higher temperatures is often divided into first and second order heat losses.

For non-tracking concentrating panels the IAM, which characterizes the performance of the collector at different incoming angles, is of a critical parameter. In flat collector, this is not as important as flat panels display very little variation between themselves in this parameter. For tracking collectors, the IAM is not relevant, since the collector is always working at the best angle.

The IAM is different for electrical and thermal. This is further divided into longitudinal and transversal angular, which is especially relevant for asymmetric collectors.

**Research Question 3: How does PVT technology compare with standard PV and ST technologies?**

The main benefits of PVT collectors when compared to standard thermal and photovoltaic (PV) solar collectors are:

- The possibility of increasing cell efficiency by reducing the cell operating temperature, when heat is extracted at lower temperatures. In order for this to be achieved, it is fundamental that the panel design is able to transfer the heat from the cells to the cooling liquid efficiently and homogeneously;
- 1 m<sup>2</sup> of PVT provides higher annual output than an equivalent area of PV (0.5 m<sup>2</sup>) plus ST (0.5 m<sup>2</sup>);

- The production of one unit of PVT uses fewer raw materials than an equivalent area of thermal and photovoltaic panels. This is expected to enable a lower production cost per kWh of annually produced solar energy.
- Reduction of the module area, which enables the deployment of more installed capacity per roof area. This should also lower the installation costs.

The main disadvantages for PVTs are the higher complexity in both collector production and installation and the reduced market share since it requires customers that need both heat and electricity.

Table 45. *Advantages and disadvantages of PVT collectors (Vs T and PV).*

Topic	Advantage	Disadvantage
<b>Efficiency</b>	Most PVT designs yield a higher energy output per m <sup>2</sup> compared to PV and T, in particular for low temperatures. Possibility to increase electrical efficiency by cooling.	Heat has more value at high temperatures but this reduces electrical output.
<b>Collector Cost</b>	Fewer raw materials needed to obtain the same energy output	Early in the Technology curve. Cell Price has greatly decreased making PVT (and T) less attractive.
<b>Production Cost</b>	-	Increased complexity at production level
<b>Installation Cost / Reliability</b>	Lower installation cost can be achieved due to smaller area for the same output	Increased complexity at installation level
<b>Market</b>	-	Niche Market (require need for heat and electricity)

**Research Question 4: What are the advantages and disadvantages of using concentrating PVT solar collectors?**

Throughout this thesis, a total of 29 collectors have been tested. When comparing C-PVT with PVT, there are advantages and disadvantages. Concentration in PVTs can be used to reduce the usage of PV cells and thermal absorber material, but this carries a penalty due to increased optical losses. In the end, it is a balance between the positive effect of lowering the collector cost and the negative effect of decreasing the electrical output per square meter. The steep decrease in the price of silicon solar cell made the C-PV and CPVT concepts less popular. On the other hand, PVT collectors feature a more expensive receiver than traditional ST and PV, which enhances the benefit of concentration.

Concentration also helps to reduce the heat losses, as the hot absorber area becomes smaller. This way, concentration also allows higher temperatures to be achieved, although higher temperatures will reduce the efficiency of the solar cells. Heat at higher temperatures is generally more valuable. Some of the disadvantages of concentration are aesthetics (bulkier collector), lower power

density and higher stagnation temperatures, which leads to a more expensive component.

Two other less considered aspects are: 1) Weight, PVT collectors are heavier than ST, which in turn is heavier than PV. This can sometimes limit the number of roofs where installations can be deployed as well as requires more work for installation. 2) Modularity, PVT panels tend to have 1.6 m<sup>2</sup> while ST and PV generally have a 2.5 m<sup>2</sup>. Smaller panels are easier fit nicely into a roof with less dead areas.

Finally, although factors such as simplicity or aesthetics do play a role, the most important number in solar remains the cost per kWh of heat and electricity produced, including the installation cost.

Table 46: *Advantages and disadvantages of C-PVT collectors (vs PVT).*

Topic	Advantage	Disadvantage
<b>Electrical Output/ Cost</b>	Concentration can reduce the costs, as it increases the output per cell area	Concentration reduces output per glazed area
<b>Thermal Output/ Cost</b>	Concentration reduces heat losses and increases range of possible working temperatures	Higher stagnation temperatures (=more expensive materials or complex systems to cope)
<b>Product Complexity</b>	-	Concentration increases complexity
<b>Aesthetics</b>	-	Concentration can reduce aesthetic value

**Research Question 5: What are the challenges and requirements of solar cells encapsulation in PVT and CPVT collectors?**

The most critical part in the manufacture of a PVT collector is widely considered to be the receiver. A major technical design difficulty for PVT collectors is to find a material for encapsulating the solar cells that is able to effectively conduct the heat from the solar cells to the receiver while still maintaining a number of critical characteristics such as high electrical insulation, high transparency, low cost, ability to cope with thermal stress in order to protect the solar cells, resistance to moisture penetration, resistance to UV. These difficulties are even more pronounced in CPVT collectors, which face higher stagnation temperatures. Ensuring good thermal contact between solar cells and receiver, while being able to avoid cell cracking from thermal expansion and contraction are significant design considerations in PVT collector development. Improving cell-receiver thermal contact is performed by the choice of material and its method of application during the manufacturing process.

In addition to the aforementioned performance and cost considerations, another key aspect in solar collector design is durability. Solar collectors must survive at least 20 years outdoors with an acceptable power output reduction over the period in order for owners to be able to profit from the installation.

This carries long-term implications on UV and temperature resistance, for example.

The stagnation temperature of a collector is reached when the heat losses are equal to the energy received from the sun. This means that all incoming solar radiation is transferred to the surrounding environment either as heat losses. A particularly important disadvantage of concentration is the increase of the stagnation temperature, which can cause damage to the materials of the collector, in particular to the solar cells.

**Research Question 6: How can solar cells be encapsulated in PVT collectors? Can PVT and C-PVT collectors use a silicone encapsulation method? What are the advantages and disadvantages? How can these disadvantages be mitigated?**

The polymer EVA is the standard material for encapsulating solar cells in PV panels and it is today fairly cheap with high light transmission and good heat transfer coefficient. Additionally, the production processes are also highly developed. EVA encapsulation method can also be applied to low temperature PVTs. However, EVA starts to degrade between 80 to 120 °C, depending on the type of solar cell. This means that in order to be able to use EVA in a collector, one of two things must happen:

- 1) The collector has a very high heat loss factor, which means that the collector will either be used for very low temperature applications where the heat has reduced value or have reduced output in applications such as DHW;
- 2) The solar thermal system must include a heat dissipater in order to prevent the collector from being destroyed by reaching the stagnation temperature, which represents an additional cost and therefore an additional barrier for the introduction of PVT systems in the market.

A large number of the PVT collector designs in the market today feature insulation and an air gap between the glass and the receiver, so they easily exceed 80 °C. This means that, if these PVT designs are encapsulated with EVA, they will not withstand stagnation. Silicone encapsulation provides a solution to this problem.

Throughout this thesis period, several small scale receivers were design and built using different silicone based encapsulation techniques. This thesis presents an analysis of different techniques to encapsulate PV cells with silicone in solar concentrating photovoltaic thermal collects, and to the author's knowledge, it is this first peer-reviewed publication on this topic.

Using performance testing and electroluminescence analysis, Paper II proved that it is possible to construct C-PVT receivers that withstand temperatures up to 220 °C. Further studies to these issues are also conducted in Papers 10, 11, 16 and 19. Solarus has opted for the route of silicone encapsulation, which is a significant deviation from the industry standard.

Encapsulation with silicone provides a method to tackle not only the stagnation temperature, but also number of other issues critical for PVT and C-PVT such as electrical insulation, durability, light transmittance and protection of the PV cell against thermal expansion. However, there are also several disadvantages such as high material costs, low thermal conductivity and a production process on its early development stages.

A design to mitigate these disadvantages, called the H-pattern has been presented in this thesis. This design would increase electrical resistance reliability, while also increasing thermal conduction between the receiver and the cell as well as minimizing both cost and thermal stress from receiver expansion. This design features a cheap aluminium sheet with several H-shaped holes, which is expected to enable a very strong resistance to thermal expansion, which in turn allows the cells lay on the aluminium sheet greatly increasing the thermal conductivity (the silicone has about 1000 times lower heat conductivity than the aluminium sheet). This sheet would feature a very thin powder coating to ensure electrical insulation. Lastly, the presence of the aluminium sheet would greatly reduce the need for usage of silicone, which would also reduce material costs, as detailed in Chapter 5.5.

Lastly, as a result of the work within this thesis, two patents applications will be filled within the coming year. One is on a variation of the H-pattern design, and the other is a novel design for C-PVTs using bifacial solar cells and a unique method for cooling the solar cells.

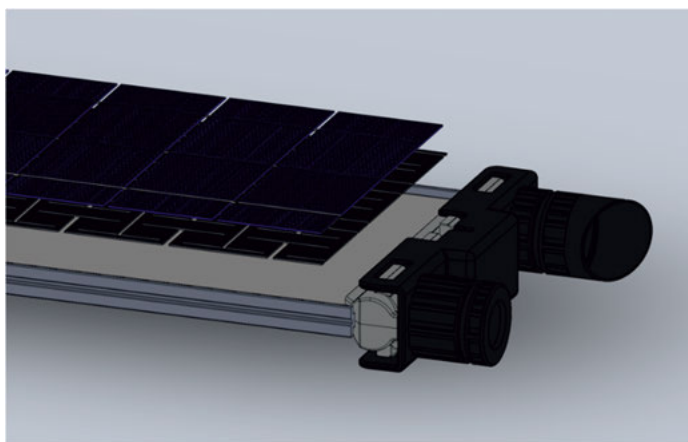


*Figure 175.* Solidwork drawing of the H-pattern integrated with the PVT receiver.



**Research Question 7: Can Tonatiuh be used for reflector design of a C-PVT? Which reflector geometry is the most suitable for a stationary low concentration factor C-PVT?**

For Paper VII, a Tonatiuh model of a MaReCo C-PVT was constructed. In order to process the data from Tonatiuh and Matlab code was created as well. A 3D based image of the effective radiation was obtained which showed that the current reflector design had a strong margin for improvement. Furthermore, a mapping of the uniformity of the incoming light was also been carried out, with local concentration factors reaching as high as 22 at certain times of the day.

This happens because the MaReCo reflector geometry is designed for matching the heat demand with the heat production at high latitudes, which is very skewed to the summer. In order to accomplish a more balance heat production, solar radiation is reflected away in the summer and focused onto the absorber in the remaining seasons. Although, this is a solid strategy for ST (for which the MaReCO reflector geometry was originally designed), this is not a good strategy for PVT, since you always want to maximize electricity production.

Throughout this thesis, several potential C-PVT reflector geometries have been studied and published in five papers. In Paper VIII, four reflector geometries have been developed with the goal of maximizing the incoming solar radiation that can be collected without the need for tracking, while simultaneously reducing non uniform illumination, in order to also increase solar cell lifespan. In comparison to the MaReCo design, the Double MaReCo (DM) reflector design possesses a symmetric reflector geometry, which divides the focal line in two and lowers the impact on non-uniform illumination. Furthermore, the reduction in collector depth also reduces longitudinal shading. This is particularly important for the electrical part of these PVT reflector design concepts.

Furthermore, the use of a symmetric reflector geometries allows higher annual outputs worldwide, matching better with the typical profile for annual heat demand. A low concentration factor is necessary to avoid tracking.

Overall, each of the four design concepts analyzed (and its multiple variations) show advantages and disadvantages. Based on the findings, the author believes that CPC 2 showed to be the most promising geometry for C-PVTs due to the combination between total illumination received and radiation profile on the bottom receiver.

Comparing the DM design to the MaReCo Solarus PC design, it can be stated that there are large improvements in terms of reduction of non-uniform illumination (a factor 3 at least) and in terms of mitigation of shading (in particular longitudinal shading and the electrical output) with an increase in annual output in the order of 15 %, depending on location and application. Furthermore, the advantages of the DM vs the PC reflector geometry will increase when the collectors are deployed closer to the equator, as the winter solar radiation (and consequently the output) increases.

**Research Question 8: What type of cell string layout is most suitable for a stationary low concentration C-PVT?**

Papers IV, 9, 16, 17, 18 analyze this issue from different perspectives. While flat PVTs require only very small diode numbers, typically three for each panel, similar to standard PV panels, the situation is not the same for C-PVT, as concentration inevitably causes uneven illumination. Shading is more critical for PV than ST, so Paper IV focuses its analysis on the electrical performance of a stationary low concentration C-PVT, and showcases clearly that the longitudinal shading is a concern for line concentrators. Additionally, several strategies for how to mitigate this shading are laid out, such as turning the cells 90° degrees or increasing the relation between cell size and distance between the cell and the reflector.

Diodes mitigate the impact of shading in series connected cells. From a performance standpoint, having a diode over each cells would be optimal, however this is not feasible from a cost or production process standpoint. The ideal cell string layout depends on the specific details, however an ideal number of string would be three to five strings. An uneven number of strings is preferable since it is a common issue than inverter efficiency is greatly reduced when the power becomes 50 % of the rated power. The work of paper IV was further consolidated with LTSpice simulations.

**Research Question 9: What types of PVT collectors exist and what is their potential market?**

PVT collectors can be considered a niche market of solar thermal in the sense that economically viable installations require applications with a demand for both heat and electricity, where generally, the heat demand is the limiting factor defining the maximum number of collectors that can be installed.

Several types of PVT collectors exist in the market. Based on the market studies carried out for this thesis, a possible classification of PVTs follows, in increasing order of operating temperature: 1) Air PVT; 2) Unglazed PVT; 3) Glazed PVT; 4) Low concentration stationary PVT, and 5) High concentration tracking PVT. This thesis focused on 2, 3 and predominantly on 4.

Air PVTs have the advantage of being cheap but have the drawback that air has a low specific heat and thus is not able to transport much heat. This type of collectors is suitable for very low temperature applications (5° above ambient temperature) such as heating or preheating the inlet air for heat pumps

Unglazed PVT have the advantage of low stagnation temperatures but the drawback that the heat produced is, like for air PVTs, of low value. Unglazed PVT collectors can provide low temperature applications (10° above ambient temperature) in swimming pool applications or DHW in warm countries.

Glazed PVTs using EVA have to tackle the issue of stagnation temperature but are able to enjoy much of the benefits of scale economy already achieve by PV and ST. This type of collectors can be used in DHW applications or low temperature industrial applications.

Low concentration stationary PVT collectors have a similar market to glazed PVTs but have to cope with lower IAMs performance, which needs to be compensated by a reduction of material cost.

High concentration tracking collectors typically uses high efficiency solar cells and can be used in applications such as SHIP (Solar Heat Industrial Process). A major advantage of this type of collectors is that concentration is in theory a good way to reduce collector costs. Some drawbacks of this type of collectors is that they are very complex and bulky with high stagnation temperatures, still fairly experimental, and benefit very little from the market standardization and cost reduction driven by today mainstream PV and domestic ST.

It is often said that PVT collectors should operate at low temperatures but this is not always necessarily true. This idea is mainly due to the overwhelming market dominance of Si cells that have a negative cell temperature coefficient and the fact that PVTs have no selective surface which means high heat losses. However, concentration allows not only to minimize the heat loss area but also to use a smaller number of solar cells, which are also being exposed to more sunlight and thus utilized more efficiently. Furthermore, other types of solar cells have different optimal working ranges, in the case of organic solar cells, this range is around 120 °C, very different for Si cells. Regardless, today, the young PVT market is mainly dominated by unglazed and glazed flat PVT collectors, which in the author's opinion mainly because they have easier systems to install.

In summary, a large array of different types of PVT collector designs exists and each presents different benefits and drawbacks. PVT collectors are essentially solar thermal collectors with PV cells on the absorber. While the PV market has mainly consolidated around one technology (Si cells), the ST market present a much wider range of technologies and much more fragmented market in terms of solar collector manufacturers.

**Research Question 10: Is a PVT better than separate PV + ST systems? Under which situations are PVT or C-PVT collectors a good choice? What can the future hold for the PVT market?**

PVT is a niche technology with a potential market that is considerably smaller than ST or PV. Regardless, on a world scale, this is still an enormous potential market.

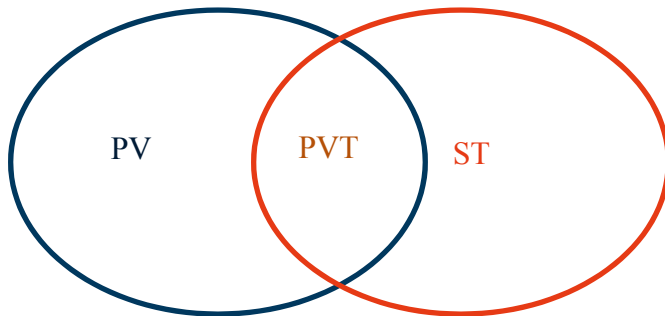


*Figure 176. Connection between ST, PV and PVT*

Annual output is extremely dependent of the type of system and the type of collector used, regardless 1 m<sup>2</sup> PVT collector should, under most cases, yield a higher output than 0.5 m<sup>2</sup> of PV and 0.5 m<sup>2</sup> of ST combined by an order of magnitude of about 30 % higher. However, the energy output does not provide the whole picture, cost is an essential part of the puzzle. Since PVT systems are in their infancy when compared to both PV and ST, collector production and installation are considerably higher. Regardless, in general, it is safe to say that PVT collectors have a potential to outperform PV and ST in applications where there is a limitation of available space to deploy the solar collectors.

In general, PV output increases in cold but sunny climates while ST benefits from warm climates and sunny climates. PVT collectors benefit even more than ST from warm climates, as these collectors can cool down the cells in warmer regions and tend to have a higher heat loss factors.

The author believes that PVT will play a role in the future world energy system, but the success of this technology is deeply connected to the capacity of the PVT industry to scale down its current system cost as well as being able to streamline/simplify its system design and installation. Another aspect that will have a significant impact in PVT market penetration is consistent access to funding options, which PV is now just starting to roll out through power purchasing agreements, but ST has not yet been able to roll out. The heat purchasing agreements are, in the author view, a critical step for both ST and PVT in the coming years.

For the past decade, ST has been continuously growing but at a considerably slower pace than PV. However, this can change, especially when one considers that electricity represents only 20 % of the current world energy consumption and the world will need to find a solution to supply both the 50 % of

heating and cooling and the 30 % of transport. Part of these 80 % will become electrified, a trend that is already ongoing with, for example, electric cars. However, in the author's opinion, it is highly unlikely that heating and cooling will all become electrical by 2100. This means that the world will need to find solutions for heating and cooling and ST is a natural option. Furthermore, despite great progress in electrical batteries, storage of heat is easier, cheaper and environmentally friendlier than storage of electricity. This is an advantage for both ST and PVT systems over PV. In this way, the future of the PVT technology will be closely dependent on the future of ST, as PVTs are, at the core, ST collectors that also feature PV cells.

## 9 References

1. D. Lüthi *et al.*, “High-resolution carbon dioxide concentration record 650,000–800,000 years before present,” *Nature*, vol. 453, no. 7193, pp. 379–382, May 2008, doi: 10.1038/nature06949.
2. I. Tattersall, “Human origins: Out of Africa,” *Proc. Natl. Acad. Sci.*, vol. 106, no. 38, pp. 16018–16021, Sep. 2009, doi: 10.1073/pnas.0903207106.
3. REN21, “RENEWABLES 2019 GLOBAL STATUS REPORT.” <https://www.ren21.net/gsr-2019> (accessed Mar. 16, 2021).
4. A. Zervos and C. Lins, *Renewables 2009 Global Status Report*. 2009.
5. A. Zervos and C. Lins, *Renewables 2016 Global Status Report*. 2016. Accessed: Jan. 08, 2018. [Online]. Available: <https://apps.uqo.ca/LoginSigparb/LoginPourRessources.aspx?url=http://www.deslibris.ca/ID/10091391>
6. L. Junfeng *et al.*, “Renewable Energy Policy Network for the 21st Century”.
7. S. Manju and N. Sagar, “Renewable energy integrated desalination: A sustainable solution to overcome future fresh-water scarcity in India,” *Renew. Sustain. Energy Rev.*, vol. 73, no. C, pp. 594–609, 2017.
8. C. S. Lai, Y. Jia, L. L. Lai, Z. Xu, M. D. McCulloch, and K. P. Wong, “A comprehensive review on large-scale photovoltaic system with applications of electrical energy storage,” *Renew. Sustain. Energy Rev.*, vol. 78, no. C, pp. 439–451, 2017.
9. A. Zervos and C. Lins, *Renewables 2017 Global Status Report*. 2017. Accessed: Jan. 08, 2018. [Online]. Available: <https://apps.uqo.ca/LoginSigparb/LoginPourRessources.aspx?url=http://www.deslibris.ca/ID/10091391>
10. A. Zervos and C. Lins, *Renewables 2014 Global Status Report*. 2014. Accessed: Jan. 08, 2018. [Online]. Available: <http://large.stanford.edu/courses/2014/ph240/singh1/docs/GSR2014.pdf>
11. R. Y. Shum, “Heliopolitics: The international political economy of solar supply chains,” *Energy Strategy Rev.*, vol. 26, p. 100390, Nov. 2019, doi: 10.1016/j.esr.2019.100390.
12. “Crystalline Silicon Photovoltaics Research | Department of Energy.” <https://www.energy.gov/eere/solar/crystalline-silicon-photovoltaics-research> (accessed Jan. 08, 2018).
13. P. Wawer, J. Müller, M. Fischer, P. Engelhart, A. Mohr, and K. Petter, “Latest Trends in Development and Manufacturing of Industrial, Crystalline Silicon Solar-Cells,” *Energy Procedia*, vol. 8, pp. 2–8, Jan. 2011, doi: 10.1016/j.egypro.2011.06.093.
14. S. Binetti, “Silicon based solar cells: Research progress and future perspectives,” in *7th IEEE International Conference on Group IV Photonics*, Sep. 2010, pp. 189–191. doi: 10.1109/GROUP4.2010.5643385.
15. T. Saga, “Advances in crystalline silicon solar cell technology for industrial mass production,” *NPG Asia Mater.*, vol. 2, no. 3, p. 96, Jul. 2010, doi: 10.1038/asiamat.2010.82.
16. Spork-dur, Monika and F. Mauthner, “Solar Heat Worldwide, IEA Solar Heating & Cooling Programme,” AEE INSTEC, Austria, 2017.

17. L. Carnot, *Principes fondamentaux de l'équilibre et du mouvement; par L. N. M. Carnot ...* de l'imprimerie de Crapelet, 1803.
18. M. A. Green, *Solar Cells: Operating Principles, Technology, and System Applications*. Englewood Cliffs, NJ: Prentice Hall, 1981.
19. Wagner, *Photovoltaik Engineering - Handbuch für Planung, Entwicklung | Andreas Wagner | Springer*. Accessed: Jan. 08, 2018. [Online]. Available: <https://www.springer.com/de/book/9783662486399>
20. S. R. Wenham, M. A. Green, M. E. Watt, and R. Corkish, Eds., *Applied Photovoltaics*, 2nd edition. London ; Sterling, VA: Routledge, 2006.
21. J. A. Duffie and W. A. Beckman, "Solar Engineering of Thermal Processes," in *Solar Engineering of Thermal Processes*, John Wiley & Sons, Inc., 2013, pp. i–xxvi. doi: 10.1002/9781118671603.fmatter.
22. "Physics of Solar Energy," *Wiley.com*. <https://www.wiley.com/en-us/Physics+of+Solar+Energy-p-9780470647806> (accessed Jan. 08, 2018).
23. J. Chen, "Physics of Solar Energy," *Wiley.com*. <https://www.wiley.com/en-us/Physics+of+Solar+Energy-p-9780470647806> (accessed Jan. 08, 2018).
24. E. Aguado, J. E. Burt, and J. Burt, *Understanding Weather and Climate, Third Edition*, 3 edition. Upper Saddle River, N.J: Prentice Hall, 2003.
25. O. Z. Sharaf and M. F. Orhan, "Concentrated photovoltaic thermal (CPVT) solar collector systems: Part I – Fundamentals, design considerations and current technologies," *Renew. Sustain. Energy Rev.*, vol. 50, no. Supplement C, pp. 1500–1565, Oct. 2015, doi: 10.1016/j.rser.2015.05.036.
26. G. Boyle, *Renewable Energy: Power for a Sustainable Future*, 3 edition. Oxford: Oxford University Press, 2012.
27. A. H. Jaaz, H. A. Hasan, K. Sopian, M. H. B. H. Ruslan, and S. H. Zaidi, "Design and development of compound parabolic concentrating for photovoltaic solar collector: Review," *Renew. Sustain. Energy Rev.*, vol. 76, pp. 1108–1121, Sep. 2017, doi: 10.1016/j.rser.2017.03.127.
28. R. Pujol-Nadal, V. Martínez-Moll, F. Sallaberry, and A. Moià-Pol, "Optical and thermal characterization of a variable geometry concentrator using ray-tracing tools and experimental data," *Appl. Energy*, vol. 155, pp. 110–119, 2015.
29. F. G. Braun, E. Hooper, R. Wand, and P. Zlocystsi, "DIW Berlin: Holding a Candle to Innovation in Concentrating Solar Power Technologies : A Study Drawing on Patent Data," Mar. 01, 2007. [https://www.diw.de/sixcms/detail.php?id=diw\\_01.c.371611.de](https://www.diw.de/sixcms/detail.php?id=diw_01.c.371611.de) (accessed Jan. 17, 2018).
30. R. Winston and W. T. Welford, *High Collection Nonimaging Optics - 1st Edition*. Academic Press. Accessed: Jan. 17, 2018. [Online]. Available: <https://www.elsevier.com/books/high-collection-nonimaging-optics/welford/978-0-12-742885-7>
31. M. Adsten, *Solar Thermal Collectors at High Latitudes Design and Performance of Non-Tracking Concentrators*, vol. PhD Thesis. Uppsala University, 2002.
32. J. S. Coventry, "A solar concentrating photovoltaic/thermal collector," The Australian National University, 2004. Accessed: Jan. 17, 2018. [Online]. Available: <https://openresearch-repository.anu.edu.au/handle/1885/46253>
33. M. Adsten, A. Helgesson, and B. Karlsson, "Evaluation of CPC-collector designs for stand-alone, roof- or wall installation," *Sol. Energy*, vol. 79, no. 6, pp. 638–647, Dec. 2005, doi: 10.1016/j.solener.2005.04.023.

34. J. Nilsson, "Optical Design and Characterization of Solar Concentrators for Photovoltaics," Lund University, 2005. [Online]. Available: [http://www.lth.se/fileadmin/energi\\_byggnadsdesign/images/Publikationer/Bok\\_EBD-T-05\\_6\\_G5\\_Johan\\_N.pdf](http://www.lth.se/fileadmin/energi_byggnadsdesign/images/Publikationer/Bok_EBD-T-05_6_G5_Johan_N.pdf)
35. J. Nilsson, R. Leutz, and B. Karlsson, *Micro-structured reflector surfaces for a stationary asymmetric parabolic solar concentrator*, vol. 91. Solar Energy Materials and Solar Cells, 2007. doi: 10.1016/j.solmat.2006.11.003.
36. O. Z. Sharaf and M. F. Orhan, "Concentrated photovoltaic thermal (CPVT) solar collector systems: Part II – Implemented systems, performance assessment, and future directions," *Renew. Sustain. Energy Rev.*, vol. 50, pp. 1566–1633, Oct. 2015, doi: 10.1016/j.rser.2014.07.215.
37. A. M. Ricaud, "Solar Cells Failure Modes and Improvement of Reverse Characteristics," in *Fourth E.C. Photovoltaic Solar Energy Conference*, Springer, Dordrecht, 1982, pp. 392–398. doi: 10.1007/978-94-009-7898-0\_64.
38. D. Rossi, M. Omaña, D. Giaffreda, and C. Metra, "Modeling and detection of hotspot in shaded photovoltaic cells," *IEEE Trans. Very Large Scale Integr. VLSI Syst.*, vol. 23, no. 6, pp. 1031–1039, 2015.
39. D. I. Paul, M. Smyth, A. Zacharopoulos, and J. Mondol, "The Effects of Non-uniform Illumination on the Electrical Performance of a Single Conventional Photovoltaic Cell," *International Journal of Photoenergy*, 2015. <https://www.hindawi.com/journals/ijp/2015/631953/abs/> (accessed Jan. 22, 2018).
40. "Solarus Sunpower Website," *Solarus*. <http://solarus.com/> (accessed Jan. 08, 2018).
41. D. Cabral, J. Costeira, and J. Gomes, "Electrical and thermal performance evaluation of a district heating system composed of asymmetric low concentration PVT solar collector prototypes," 2018, pp. 755–763. Accessed: May 24, 2021. [Online]. Available: <http://urn.kb.se/resolve?urn=urn:nbn:se:hig:diva-30563>
42. J. Fernandes, P. Alves, J. P. Torres, C. Fernandes, and P. Branco, *Energy efficiency of a PV/T collector for domestic water heating installed in Sweden or in Portugal: The impact of heat pipe cross-section geometry and water flowing speed*. 2017.
43. "Energy Revolution — Mara Prentiss." <https://www.hup.harvard.edu/catalog.php?isbn=9780674725027> (accessed Mar. 11, 2021).
44. L. Brand, A. Calvén, J. Englund, H. Landersjö, and P. Lauenburg, "Smart district heating networks – A simulation study of prosumers' impact on technical parameters in distribution networks," *Appl. Energy*, vol. 129, pp. 39–48, Sep. 2014, doi: 10.1016/j.apenergy.2014.04.079.
45. "Solar Thermal is NOT Dead," *GreenBuildingAdvisor*, Jul. 03, 2017. <https://www.greenbuildingadvisor.com/article/solar-thermal-is-not-dead> (accessed Mar. 16, 2021).
46. "Solar Water Heating: A Comprehensive Guide to Solar Water and Space Heating." <https://www.nhbs.com/solar-water-heating-book> (accessed Mar. 16, 2021).
47. "Best Research-Cell Efficiency Chart." <https://www.nrel.gov/pv/cell-efficiency.html> (accessed Mar. 16, 2021).
48. "ITRPV - VDMA." <https://itrpv.vdma.org/> (accessed Mar. 16, 2021).



49. “Renewable Power Generation Costs in 2019,” */publications/2020/Jun/Renewable-Power-Costs-in-2019*. */publications/2020/Jun/Renewable-Power-Costs-in-2019* (accessed Mar. 16, 2021).
50. M. A. Salam and S. A. Khan, “Transition towards sustainable energy production – A review of the progress for solar energy in Saudi Arabia,” *Energy Explor. Exploit.*, vol. 36, no. 1, pp. 3–27, Jan. 2018, doi: 10.1177/0144598717737442.
51. P. Korkmaz, F. Gardumi, G. Avgerinopoulos, M. Blesl, and U. Fahl, “A comparison of three transformation pathways towards a sustainable European society - An integrated analysis from an energy system perspective,” *Energy Strategy Rev.*, vol. 28, p. 100461, Mar. 2020, doi: 10.1016/j.esr.2020.100461.
52. J. R. Petit *et al.*, “Climate and atmospheric history of the past 420,000 years from the Vostok ice core, Antarctica,” *Nature*, vol. 399, no. 6735, p. 429, Jun. 1999, doi: 10.1038/20859.
53. B. K. Widyolar *et al.*, “Design, simulation and experimental characterization of a novel parabolic trough hybrid solar photovoltaic/thermal (PV/T) collector,” *Renew. Energy*, vol. 101, pp. 1379–1389, Feb. 2017, doi: 10.1016/j.renene.2016.10.014.
54. P. G. Charalambous, G. G. Maidment, S. A. Kalogirou, and K. Yiakoumetti, “Photovoltaic thermal (PV/T) collectors: A review,” *Appl. Therm. Eng.*, vol. 27, no. 2, pp. 275–286, Feb. 2007, doi: 10.1016/j.applthermaleng.2006.06.007.
55. P. Alves, J. F. P. Fernandes, J. P. N. Torres, P. J. Costa Branco, C. Fernandes, and J. Gomes, “From Sweden to Portugal: The effect of very distinct climate zones on energy efficiency of a concentrating photovoltaic/thermal system (CPV/T),” *Sol. Energy*, vol. 188, pp. 96–110, Aug. 2019, doi: 10.1016/j.solener.2019.05.038.
56. J. Gomes *et al.*, “Analysis of different C-PVT reflector geometries,” in *2016 IEEE International Power Electronics and Motion Control Conference (PEMC)*, Sep. 2016, pp. 1248–1255. doi: 10.1109/EPEPMC.2016.7752175.
57. P. Chaturvedi, B. Hoex, and T. M. Walsh, “Broken metal fingers in silicon wafer solar cells and PV modules,” *Sol. Energy Mater. Sol. Cells*, vol. 108, pp. 78–81, Jan. 2013, doi: 10.1016/j.solmat.2012.09.013.
58. U. Pettersson, P. Kovács, and B. Perers, “Improving the compatibility between steady state and quasi dynamic testing for new collector designs”.
59. J. Afonso, N. Mexa, and M. Carvalho, “Comparison between Steady State and Quasi -Dynamic test Method according to EN 12975 - Application to flat plate collectors .,” *Eurosun 2008*, 2008.
60. S. Fischer, W. Heidemann, H. Müller-Steinhagen, B. Perers, P. Bergquist, and B. Hellström, “Collector test method under quasi-dynamic conditions according to the European Standard EN 12975-2,” *Sol. Energy*, vol. 76, no. 1–3, pp. 117–123, 2004.
61. M. J. Carvalho, P. Horta, J. F. Mendes, M. C. Pereira, and W. M. Carbajal, “Incidence Angle Modifiers: A General Approach for Energy Calculations,” in *Proceedings of ISES World Congress 2007 (Vol. I – Vol. V)*, Springer, Berlin, Heidelberg, 2008, pp. 608–612. doi: 10.1007/978-3-540-75997-3\_112.
62. J. Gomes, N. Stenlund, S. Larsson, and B. Karlsson, “Development of a Hybrid MaReCo Solar Panel.” *Elforsk*, 2011.

63. H. Davidsson *et al.*, “Construction of Laboratories for Solar Energy Research in Developing Countries,” *Energy Procedia*, vol. 57, pp. 982–988, Jan. 2014, doi: 10.1016/j.egypro.2014.10.081.
64. G. Niko *et al.*, “Construction of a Small Scale Laboratory for Solar Collectors and Solar Cells in a Developing Country,” *Engineering*, vol. 5, no. 1, Art. no. 1, Jan. 2013, doi: 10.4236/eng.2013.51B014.
65. R. Bernardo, H. Davidsson, J. Gomes, and N. Gentile, “Solarus PVT Hybrid Collector- Test and evaluation of pre-series modules in Moçambique.” Lund University.
66. L. R. Bernardo, B. Perers, H. Håkansson, and B. Karlsson, “Performance evaluation of low concentrating photovoltaic/thermal systems: A case study from Sweden,” *Sol. Energy*, vol. 85, no. 7, pp. 1499–1510, Jul. 2011, doi: 10.1016/j.solener.2011.04.006.
67. L. R. Bernardo, H. Davidsson, and B. Karlsson, “Performance Evaluation of a High Solar Fraction CPC-Collector System,” *J. Environ. Eng.*, vol. 6, no. 3, pp. 680–692, 2011, doi: 10.1299/jee.6.680.
68. J. P. N. Torres *et al.*, “Effect of Reflector Geometry in the Annual Received Radiation of Low Concentration Photovoltaic Systems,” *Energies*, vol. 11, no. 7, Art. no. 7, Jul. 2018, doi: 10.3390/en11071878.
69. R. Winston and H. Hinterberger, “Principles of cylindrical concentrators for solar energy,” *Sol. Energy*, vol. 17, no. 4, pp. 255–258, Sep. 1975, doi: 10.1016/0038-092X(75)90007-9.
70. A. Rabl, “Comparison of solar collectors,” *Sol. Energy*, vol. 18 (2), 93-111..
71. M. J. Carvalho, M. Collares-Pereira, J. M. Gordon, and A. Rabl, “Truncation of CPC solar collectors and its effect on energy collection,” *Sol. Energy*, vol. 35, no. 5, pp. 393–399, Jan. 1985, doi: 10.1016/0038-092X(85)90127-6.
72. I. P. Koronaki and M. T. Nitsas, “Experimental and theoretical performance investigation of asymmetric photovoltaic/thermal hybrid solar collectors connected in series,” *Renew. Energy*, vol. 118, pp. 654–672, Apr. 2018, doi: 10.1016/j.renene.2017.11.049.

**Papers**

Associated papers have been removed in the electronic version of this thesis.

For more details about the papers see:

<http://urn.kb.se/resolve?urn=urn:nbn:se:hig:diva-35411>